Plasmonic Properties of Gold Nanorod-based Oligomers and Arrays

基於金納米棒組裝的寡聚體及陣列的表面等離子體共振特性研究

SHAO, Lei

邵磊

A Thesis Submitted in Partial Fulfilment

of the Requirements for the Degree of

Doctor of Philosophy

in

Physics

The Chinese University of Hong Kong

August 2013

Thesis/Assessment Committee

Professor XIAO, Xudong (Chair)
Professor WANG, Jianfang (Thesis Supervisor)
Professor ONG, Hock Chun Daniel (Committee Member)
Professor ROGACH, Andrey L. (External Examiner)

Abstract

Gold nanorods are preferred candidates for future plasmonic applications due to their synthetically adjustable plasmon energies and polarization-sensitive optical responses. By assembling Au nanorods into oligomers and arrays, we can greatly tune their plasmonic features, obtain more robust and reliable plasmonic structures, and therefore greatly extend their applications. In this thesis, I report on my studies on the plasmon coupling in Au nanorod oligomers, the use of graphene to mediate the plasmon coupling between Au nanocrystals, the comparison of plasmonic properties between lithographically-written and chemically-grown Au nanorods, and the fabrication of macro-scale colloidal Au nanorod arrays and their applications as refractive index sensors.

First, the plasmonic properties of Au nanorods can be tailored in a wide range by coupling them with other Au nanocrystals. The unique spectral characteristics, together with the ability to concentrate light, of coupled Au nanorod structures endow them with great potentials in applications ranging from biosensing and optics to metamaterials. To fully realize these potentials requires a thorough understanding of the plasmon coupling behavior. In this regard, our group has investigated the coupling in Au nanocube oligomers and Au nanorod homodimers. In this thesis, I have further performed systematic studies on the plasmon coupling in heterodimers composed of two different Au nanorods or one Au nanorod and one Au nanosphere.

Extensive simulations were performed to unravel the plasmon coupling in heterodimers of nanorods aligned along their length axes. The effects of the gap distance, plasmon energy, and nanorod end shape on the plasmon coupling were ascertained. I found that the plasmon coupling between two arbitrarily varying Au nanorods can be well described using a coupled mechanical oscillator model. The coupled plasmon energy can be easily, yet accurately predicted with a universal hyperbolic formula. The nanorod heterodimers also exhibit Fano interference, which

can be adjusted by controlling the gap distance and monomer plasmon energies.

I have also investigated the coupling between a Au nanorod and a small Au nanosphere approaching it. The plasmonic responses of the heterodimer, including Fano resonance, are remarkably sensitive to the nanosphere position on the nanorod, the gap distance, and the nanocrystal dimensions. Interestingly, the nanosphere dipole is found to rotate around the nanorod dipole to achieve favorable attractive interaction for the bonding dipole–dipole mode. The sensitive spectral response of the heterodimer to the spatial perturbation of the nanosphere offers an approach to designing plasmon rulers of two spatial coordinates for sensing and high-resolution measurements of distance changes.

Furthermore, the plasmon coupling can be modulated by an ultra-thin monolayer graphene. Coupled plasmonic structures can compress light energy into an ultra-small region, permitting a strong light–graphene interaction. Effective light modulation therefore can be realized by the graphene–metal hybrid plasmonic structures. I have explored the interaction between graphene and two different coupled plasmonic structures, including Au nanorod dimers and the Au film-coupled Au nanosphere structures. For nanorod dimers, no apparent spectral modulation can be acquired through graphene. By contrast, remarkable modulation on Au nanosphere scattering can be achieved by adding graphene into the cavity between the nanosphere and the supporting film. The graphene-loaded nanosphere antennas exhibit significant resonance redshifts, which can further be modulated when graphene screening effect is varied. This graphene-decorated plasmonic nanocavity not only pushes the optical response of graphene into the visible-to-near-infrared (NIR) region but also naturally exemplifies an electro-plasmonic system. These findings thus open an avenue on effectively operating graphene photonic devices in the visible-to-NIR range and pave a way for electrically controlling light by plasmonic structures.

In the end, practical applications of Au nanorods usually require their assembly into coupled or uncoupled macro-scale arrays. I have fabricated Au nanorod arrays by electron beam

lithography (EBL) and further developed a method to prepare macro-scale colloidal nanocrystal arrays. The plasmonic properties of Au nanorods prepared from these two different methods are compared. EBL-written Au nanorods suffer from a poor plasmonic performance. The chemical method, on the other hand, can achieve Au nanocrystals with excellent plasmonic properties. In particular, I have succeeded in directly depositing colloidal metal nanocrystals onto different substrates to form arrays. The resultant nanocrystal arrays are uniform and dense, with the single-layer absorbance value reaching 0.2 and the size up to one decimeter square. The refractive index sensitivities of the obtained Au nanorod arrays have also been characterized. The macro-scale metal nanocrystal arrays can overcome the poor stability of the colloidal solutions and the high cost of single-particle spectroscopy that hinders the practical applications of plasmonic nanocrystals for sensing. This method is expected to greatly facilitate the plasmonic applications that require the formation of large-area metal nanocrystal arrays.

I believe that the improved understanding on the plasmonic response of coupled Au nanorods, the exploration of using graphene to modulate the plasmon coupling, and the efforts towards the fabrication of macro-scale nanostructures in this thesis are important for designing and fabricating complex assemblies, hierarchical structures, and macroscopic materials out of noble metal nanocrystal building blocks, much similar to the formation of molecules and macroscopic materials out of atoms, with desired plasmon-derived functions. The results here will promote the applications of Au nanorods in optics, optoelectronics, and biotechnology.

摘要

金納米棒顆粒可以承載特殊的具有偏振激發依賴的表面等離子體共振激元。目前科學家們已經有成熟的工藝來很容易調控這種納米棒的表面等離子體共振能量，因而它們具有很好的應用前景。通過組裝成寡聚體和陣列，這些納米顆粒可以成形成更加穩定的表面等離子體共振結構，進一步地為其實用化鋪平道路。由于表面等離子體激元之間的相互耦合，金纳米棒的寡聚體和陣列擁有更加豐富的表面等離子體共振特性，因而也引起了科學家們的廣泛關注。在這篇論文中，我系統地研究了以金納米棒为单元的纳米颗粒寡聚体上的表面等離子體激元共振耦合性质，探索了利用石墨烯材料來調控這些共振特性，比較了化學方法和電子束刻蝕方法製備的金納米棒顆粒的表面等離子體共振特性的異同，而且進一步地發展了一種新的方法來利用化學合成的納米顆粒製備大面積的金納米棒顆粒陣列。

通過與其他的金屬納米顆粒的耦合，我們可以實現對金納米棒的表面等離子體激元性質的大範圍調控。這些耦合的金納米棒結構具有獨特的譜學特徵，可以將光能聚焦到一個極小的區域，因而它們在從生物傳感到光學超材料的很多領域都具有很大的發展潛力。為了充分發揮這些潛能，我們需要對表面等離子體的耦合行為進行透徹理解。在過去一段時間，我們實驗小組已經詳細研究過金納米立方體低聚物和金納米棒同種二聚體中的表面等離子體耦合效應。在這篇論文中，我進一步對由兩個不同的金納米棒或一個金納米棒和一個金納米球組成的異種二聚體的等離子體耦合系統進行深入的研究。

首先，我進行了大量的模擬計算，研究沿著長軸方向組裝的金納米棒二聚體的表面等離子體耦合行為，確定了顆粒間距、單體的表面等離子體共振能量、以及納米棒的端部形狀對等離激元耦合的影響。我發現，兩個任意的金納米棒之間的等離子體耦合效應可以用一個簡單的耦合諧振子模型來很好的描述。耦合過後新的等離子體共振能量可以通過一個簡單普適的公式來準確計算。金納米棒的異種二聚體還表現出法諾（Fano）共振效應，並且 Fano 共振可以通過調整顆粒間距和單體的等離激元能量來實現。

接下來，我也研究了一個金納米棒和一個接近它的金納米球之間的耦合。這種棒球二

聚體的表面等離子體響應對納米球相對納米棒的位置、顆粒間距、以及顆粒尺寸的依賴非常敏感。有趣的是，我發現在偶極子–偶極子成鍵模式下，納米球偶極子會繞著納米棒的偶極子旋轉，二者總是呈現出一種使體系能量較低的相互吸引的模式。這種棒球二聚體的光學響應對納米球的空間擾動極其靈敏，因而它提供了一個平臺來設計基於等離子體共振原理進行二維座標測量的納米尺子。

進一步的，我探索了利用單層石墨烯來調製金納米結構的等離子體耦合特性。因為表面等離子體共振耦合可以將光的能量會聚在一個超小的區域，因而它們可以顯著增強光與石墨烯的相互作用。利用這一點，我們可以實現基於石墨烯–貴金屬的複合納米結構的光調製。在論文中，我探討了石墨烯和兩種不同的等離子體耦合結構，即金納米棒二聚體–石墨烯，和金膜/金納米球耦合結構–石墨烯之間的相互作用。實驗發現，金納米棒二聚體和石墨烯的作用很弱，我們沒有觀測到明顯的調製效應。與之相對的，將石墨烯夾在金納米球和金膜之間則可以通過石墨烯實現對金納米球散射的顯著調製。這種石墨烯負載的納米球天線具有顯著的共振紅移，且紅移可以通過調製石墨屏蔽效應來控制。我們設計的這種金納米球-石墨烯-金膜結構不僅可以將石墨烯的光學響應調整至可見光到近紅外區域，而且也可以通過電來調控石墨烯，從而實現表面等離子體共振的電控調製。因此，我們的研究成果不僅有助於製備工作在可見光到近紅外波段的石墨烯光子器件，而且為製造實現電控表面等離子體光響應的納米結構鋪平了道路。

最後，為實現金納米棒的實際應用，我們需要製備它們的宏觀陣列。這種宏觀陣列可以通過電子束光刻（EBL）或是化學方法得到。我在論文中對比了這兩種不同方法製備的金納米棒的表面等離子體性質。EBL 製備得到的金納米棒的表面等離子體性質通常較差，而化學方法可以合成具有優良表面等離子體特性的金納米棒。我發展出一種新的方法來把化學水相合成的金納米棒直接沉積到不同的襯底上形成金納米棒陣列。這種方法得到的金納米晶陣列分佈均勻且排列緻密，單層陣列的消光值可以達到 0.2。我們可以單次在很短的時間內製備大到一平方分米大小的納米顆粒陣列。我們也測試了所製備的金納米棒陣列的對周圍環境的折射率靈敏度。宏觀尺度的金屬納米陣列可以克服膠體溶液穩定性差和單顆

粒光譜學方法成本高的缺點，因此十分有利於表面等離子體結構在檢測方面的實際應用。我們的方法會非常有助於那些需要大面積的金屬納米陣列才能實現的表面等離子體激元的應用。

總而言之，這篇論文中對表面等離子體耦合的深入探討，對用石墨烯來調控表面等離子體耦合結構響應的研究，以及利用膠體金納米顆粒製備大面積納米結構陣列的探索都將有助於將來設計製造更為複雜的表面等離激元複合結構和各種組件。正如原子形成分子進而組成宏觀結構一樣，我們的研究將為利用貴金屬納米晶作單元實現具有特定等離子體共振性質的宏觀結構（例如超材料）提供有益的幫助。我們的結論將推動金納米棒在光學，光電子學，以及生物技術方向的應用。

Acknowledgement

It is my great pleasure to thank many people whose help and suggestions are so valuable in completing this thesis.

First of all, this thesis would not have been possible without the valuable guidance, the always unconditional supports, and the great patience offered by my dear supervisor, Professor Jianfang Wang. Thank you so much, I even did not realize how lucky I am when I first entered the exciting research field of plasmonics under your guidance. In the passing five years (including my MPhil study), Professor Wang's childhood love for science, infectious enthusiasm about work, and rigorous attitude towards research have deeply impressed me. Many thanks for the precious opportunities, the valuable suggestions and unconditional supports you have provided. I feel lucky and proud to be your student. And I have tried and will try my best in my career to not let you down.

Also, I want to express my cordial gratitude to Professor Hai-Qing Lin. It is his instructions that made the theoretical model possible in this thesis. I really learnt a lot from the weekly discussions with him in the first three years after I came to CUHK. Later, the joint small seminar with his group, initiated by him, really helped me a lot, especially in pushing myself to read a lot of papers in profound topics. Special thanks should also be given to Professor Jianbin Xu for his great help in nanofabrication and the sharing of the knowledge in graphene.

Every project finished in this thesis is based on the close collaboration with my collaborators. I want to say thank you to Mr. Kat Choi Woo, Ms. Caihong Fang, Dr. Xiaomu Wang, Mr. Qifeng Ruan, and Dr. Huanjun Chen. Mr. Kat Choi Woo helped me a lot in doing FDTD simulations; Ms Caihong Fang did a lot of work in taking single nanostructure scattering

spectra for me; Dr. Xiaomu Wang is an expert in graphene experiments and the discussion and joint work with him is quite efficient; Mr. Qifeng Ruan helped me a lot in doing sample preparation and optical measurements; From Dr. Hunjun Chen, I have learnt a lot of experiment and simulation skills, which is indispensable for my research.

In addition, I want to deliver my thanks to the technicians in our department, and all the ladies in the general office for their kindness and efficient help.

Furthermore, I would like to extend my thanks to all present and previous group members in Professor Jianfang Wang's group. I really enjoy the happy time with the whole group.

Finally, I am forever indebted to my parents for their understanding, endless patience and encouragement whenever it is required.

Contents

List of Figures

List of Tables

Chapter 1

Introduction

I would like to start this thesis from a brief overview on the plasmonic properties of noble metal and their nanostructures. Plasmonics is a flourishing research field. Although theoretical descriptions for the basic concepts have been well-developed for a long time, new experimental surprises are being found almost day by day and novel applications of plasmonic structures are continuously being proposed, ranging from solar energy harvesting to cancer photothermal therapy. In this chapter, I will first briefly present the basic knowledge of the surface plasmon resonance supported by metals and their nanostructures (Section 1.1). Then I will focus on one of the most promising plasmonic structures, gold nanorods in Section 1.2. The preparation, plasmonic properties and applications of gold nanorods will be summarized. Further, I will put emphasis on plasmon coupling in Section 1.3, which is the interaction between plasmonic structures. It is the importance in the fundamental understanding of plasmon coupling and the great potential of coupled plasmonic structures in applications that motivated me to carry out my thesis research. A brief outline of the thesis is thereafter presented at the end of this chapter (Section 1.4).

1.1 Surface Plasmon Resonances of Noble Metals and Their Nanostructures

Noble metals are resistant to corrosion and oxidation in moist air and therefore they tend to be precious. Among noble metals, silver, gold, platinum, and palladium are especially important. They are also called precious metals and have been signs of wealth after their first extraction. The noble metals can support collective oscillations of their conduction band electrons on their

surfaces, which are referred to as surface plasmons. Just as water ripples travel along the surface of a pond after a stone is thrown into it, surface plasmons can be produced on metal-dielectric interface and propagate along the interface (Figure 1.1). Such propagating surface plasmons on metal surfaces are mixtures of the conduction electron oscillations and the accompanied oscillating electromagnetic fields.[1,2] They are also called surface plasmon polaritons. Under general conditions, surface plasmon polaritons can be explained in terms of classical electromagnetism. The history of the 'plasmonics' field has been more than a hundred years (Figure 1.2). Theoretical efforts to treat surface plasmon polaritons can be dated back to year 1899 A. C, when Sommerfeld and Zenneck published their works on electromagnetic surface waves on metal surfaces with finite conductivity.[3,4] In 1941, Fano related [5] these theoretical explanations with previous observations on Wood's anomalies (1902) [6] and Lord Rayleigh's work on diffractions of metal gratings (1907).[7] The bands of abnormally high or low intensities in the light diffracted by reflection metal gratings can therefore be related with surface plasmon polaritons on metal surfaces.

After being divided into fragments of sizes reaching down to ~100 nm, the precious metals become more 'precious', since their electronic, optical and catalytic properties are very different from their bulk counterparts. Most of these differences originate from the large surface area-to-volume ratio and the spatial confinement of the free electrons of noble metal nanocrystals (Figure 1.1).[8,9] In as early as 1847, Michael Faraday prepared such noble metal nanostructures, using phosphorus in CS_2 to reduce chloroaurate ($AuCl_4^-$) to obtain colloidal gold nanoparticles.[10] The colloidal nanoparticle solution exhibits a red color, quite different from that of bulk gold. Such unique optical responses of noble metal nanoparticles was not understood until 1908, when Mie published the analytical solution of Maxwell's equations for the scattering of electromagnetic radiation by spherical particles (also called Mie scattering).[11] Later, Gans extended the solution to the case of spheroidal particles under the electrostatic approximation.[12] By combining Mie or Gans solutions with noble metal dielectric functions described by Drude

model,[13] one can easily obtain the optical response of metal nanoparticles. Specifically, if the metal has dispersive dielectric properties, electromagnetic resonances will occur at some certain frequencies, giving rise to scattering or absorption maxima and different colors of the nanoparticles. I will discuss these calculations in details later in this thesis (Chapter 2). Interested readers can also refer to some text books for more information.[14,15]

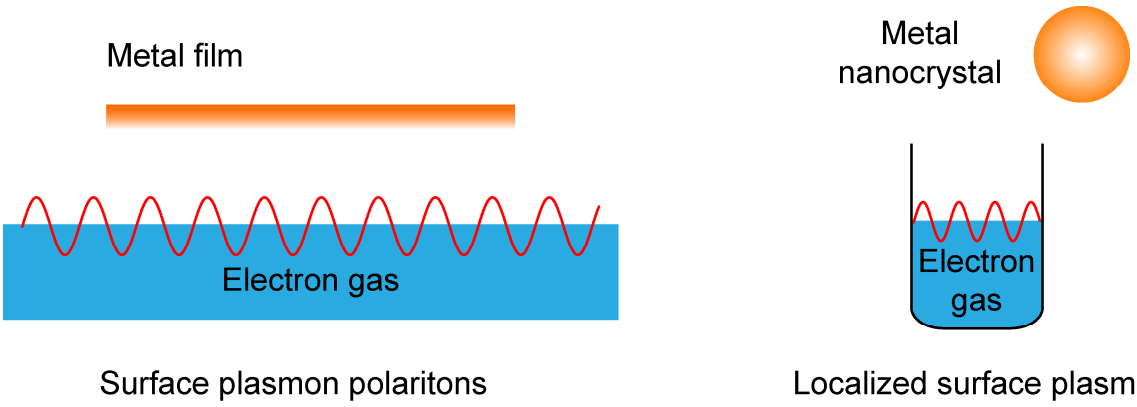

Figure 1.1 Schematic showing the surface plasmon polaritons supported on a metal surface and the localized surface plasmon on a metal nanocrystal.

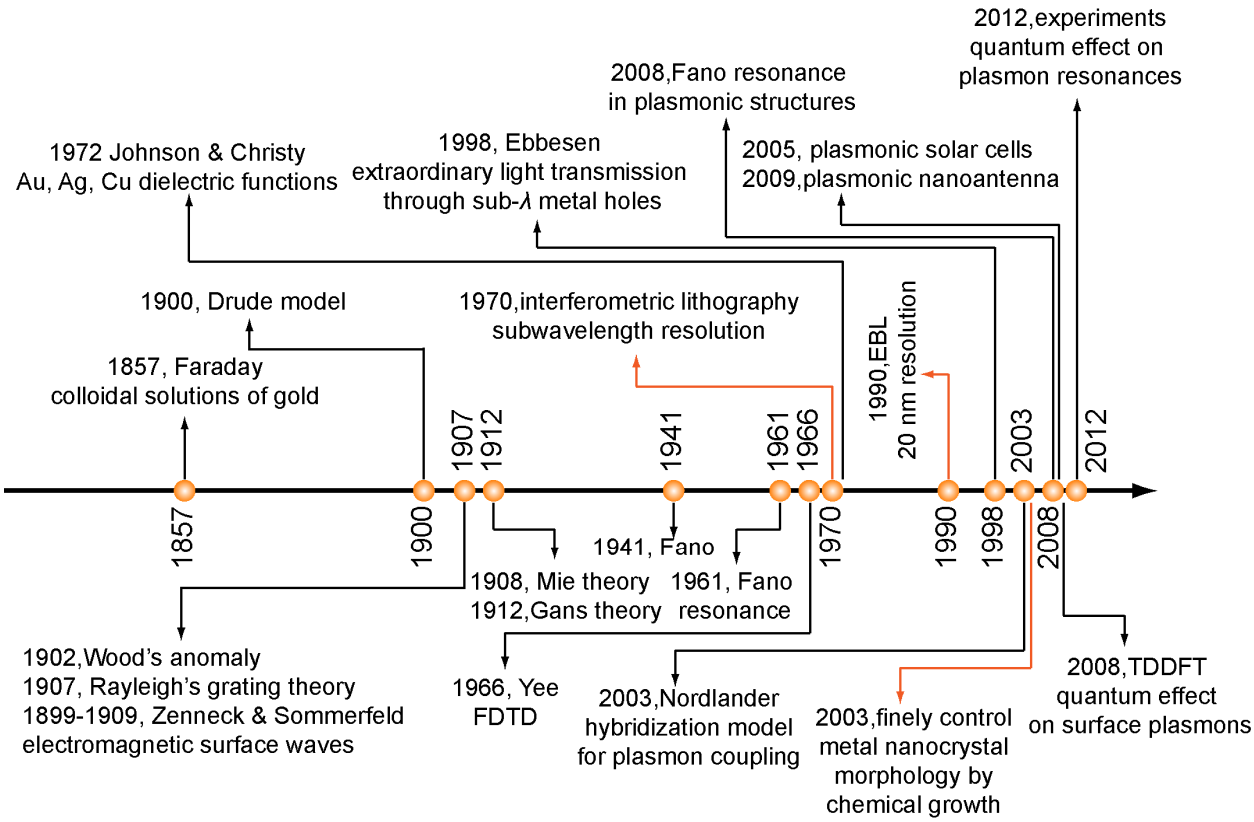

Figure 1.2 An overview of the research development of plasmonics since 1857.

Compared with their propagating counterparts, i.e. surface plasmon polaritons, localized surface plasmon resonances have some unique features. First, the localized nature of this type of resonances provides an effective way to directly convert far-field signals into near-field ones for light concentration and vice versa, to convert near-field energies into far-field radiations for characterizations and tests. The flat dispersion of localized surface plasmons supported by metallic nanoparticles (Figure 1.3) allows for their excitation by incident light over a wide range of angles.[14,16,17] Surface plasmon polaritons, however, cannot be excited directly by free-space light, since their dispersion relation $\omega(k)$ lies below that of free-space light (Figure 1.3). External setups are needed to overcome the momentum mismatches between free space light and surface plasmon polaritons. There are three main techniques to provide the missing momentum, including the use of prisms, the addition of topological defects on the surface, and the use of a periodic corrugation on the metal surface.[18] Second, coupled localized surface plasmons supported by metal nanostructures can avoid Ohmic losses resulting from resistive heating.[19] The Ohmnic loss is a severe problem in the propagation of surface plasmon polaritons.[2,19] Using gain media can partly solve this problem but will make the structure more complex.[21–23] Metal nanostructures, on the other hand, can minimize the metal volume and therefore their localized surface plasmons will substantially suppress the Ohmic loss.[8] Third, the localized surface plasmon wavelengths of noble metal nanocrystals are highly dependent on their shapes, sizes, compositions, and geometrical configurations. As a result, localized surface plasmon energies can be easily tuned over a wide range, from the violet to near-infrared regions.[8,24,25] Fourth, excitation of localized surface plasmons can extremely compress light into an ultrasmall vicinity of metal nanostructures, leading to a remarkable enhancement of near fields.[26] The accordingly greatly increased optical density of states enables strong light–matter interactions and boosts the developments of a variety of plasmon-enhanced spectroscopies,[27–30] plasmonic lasers,[31,32] and plasmon-driven nonlinear effects.[33,34]

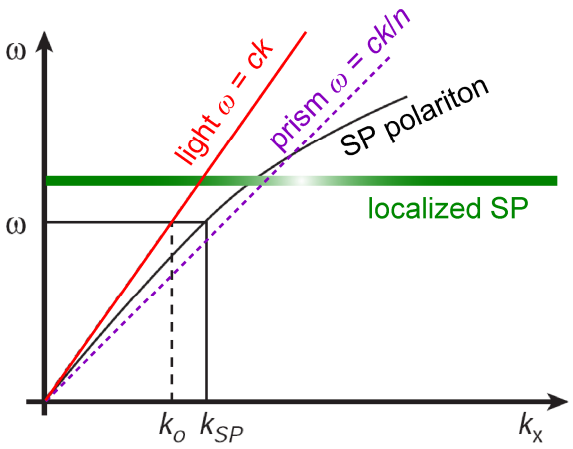

Figure 1.3 Dispersion relations of surface plasmon polariton, localized surface plasmon, free space light and light coupled into a prism, respectively.

Since 1990s, the research in the field of plasmonics has been expanding significantly. Figure 1.4 shows the increasing numbers of publications on plasmonics.[35] The rapid growth of the investigations in this field can be attributed to the following reasons. First, the progress in fabrication techniques enables scientists to prepare metal nanostructures with high resolutions and finely controlled morphologies. State-of-the-art electron-beam lithography (EBL) methods developed from semiconductor-integrated circuit industries can achieve nanostructures with at least 20-nm resolution from 1990 (Figure 1.2). From around 2003, various types of wet-chemistry methods have been developed to synthesize noble metal nanocrystals of different geometries. Here I list gold and silver nanostructures that can be readily produced by wet-chemistry approaches as examples. For gold, chemical methods can already produce high-purity nanospheres, nanorods, nanoplates, nanocubes, nanoshells, and anisotropic nanostructures with various protrusions.[8] For silver, chemical methods can yield high-purity nanospheres, nanocubes, tetrahedron nanocrystals, octahedron nanocrystals, nanobars, nanospheroids, right nanobipyramids, decahedron nanocrystals, nanorods, nanoplates, branched and hollow nanostructures.[24] Second, various types of high-sensitivity optical characterization techniques have been developed for measuring the plasmonic properties of noble metal nanostructures. Especially, single-particle dark-field scattering spectroscopy combined with SEM imaging is a powerful tool for investigating the plasmonic responses of individual metal

nanostructures.[36] Third, the development of numerical methods for simulating surface plasmons, and the rapid advance in computing power and speed have provided us powerful modeling tools to understand the plasmonic properties of metal nanostructures. The well-developed fabrication approaches, the improved characterization techniques, and the powerful modeling tools pave the way for studying the plasmonic properties of noble metal nanostructures. Most importantly, the wide range of potential applications drives more and more researchers to join in this research field. The 1998 paper by Ebbesen *et al.* on the extraordinary transmission of light through metallic nanohole arrays [37] triggered many to enter the field (Figure 1.2). Nowadays, localized surface plasmon resonances are proposed to be applied in high-efficiency thin-film solar cells,[38] high-resolution microscopy,[39] drug delivery,[9] high-density optical data storage,[40] environmental monitoring,[41] biosensing,[9] optical metamaterials,[42] photodynamic cancer cell treatment,[43] optical nanoantennas,[44–46] and surface plasmon-enhanced infrared photodetectors.[47]

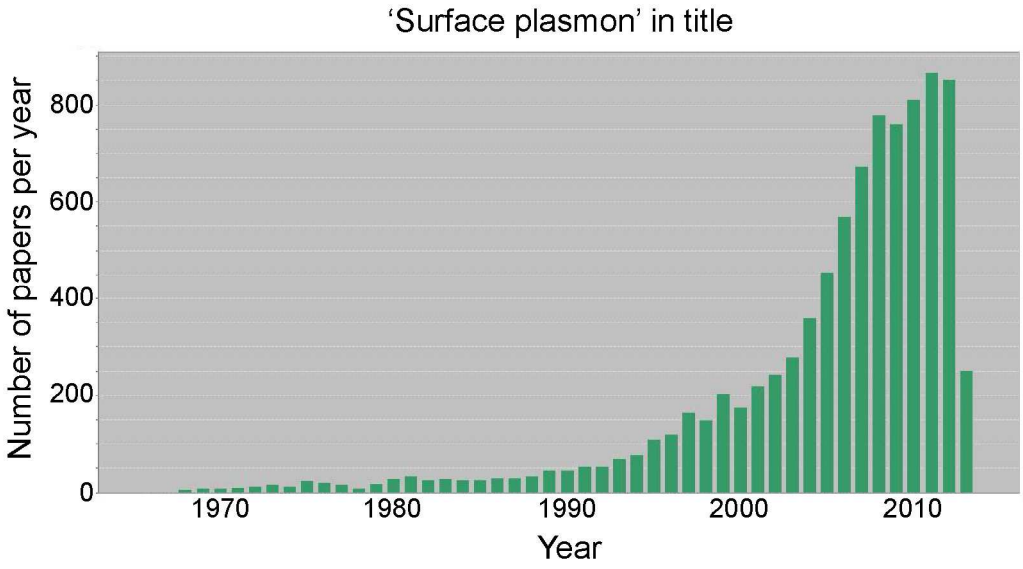

Figure 1.4 Increase in the number of publications on surface plasmon since 1956.

1.2 Gold Nanorods: Promising Candidates for Plasmonic Applications

One intriguing feature of Au nanocrystals is that their localized surface plasmon resonance

(LSPR) properties can be tailored by synthetically tuning their sizes and shapes.[8] Compared to other nanocrystals, Au nanorods offer significant advantages in this aspect. Au nanorods can support two plasmon modes. One is the longitudinal LSPR mode associated with the electron oscillations along the length axis, and the other is the transverse LSPR mode excited by light polarized along the transverse direction of the nanorod.[8,48] The plasmon wavelength of the longitudinal mode can be synthetically tuned across a broad spectral range, covering the visible and near-infrared regions, by tailoring the aspect ratio, that is, the ratio between the length and diameter (Figure 1.5a–c). In the spectral regions far from the interband transitions of gold, which are below ~590 nm, the plasmon damping is very small. Au nanorods can therefore exhibit huge electric field enhancements under resonant excitation (Figure 1.5d–f).[49] Such enhancements are mainly located in the regions around the two ends of the nanorods. Their magnitudes and distributions can also be tailored by varying the head shape. Furthermore, Au nanorods can be assembled into a number of superstructures in different geometries,[8,50–56] which results in even richer plasmonic properties owing to the anisotropic nature of Au nanorods. As a result, the LSPRs in Au nanorods have been vigorously pursued during the last decade.[8,9,48]

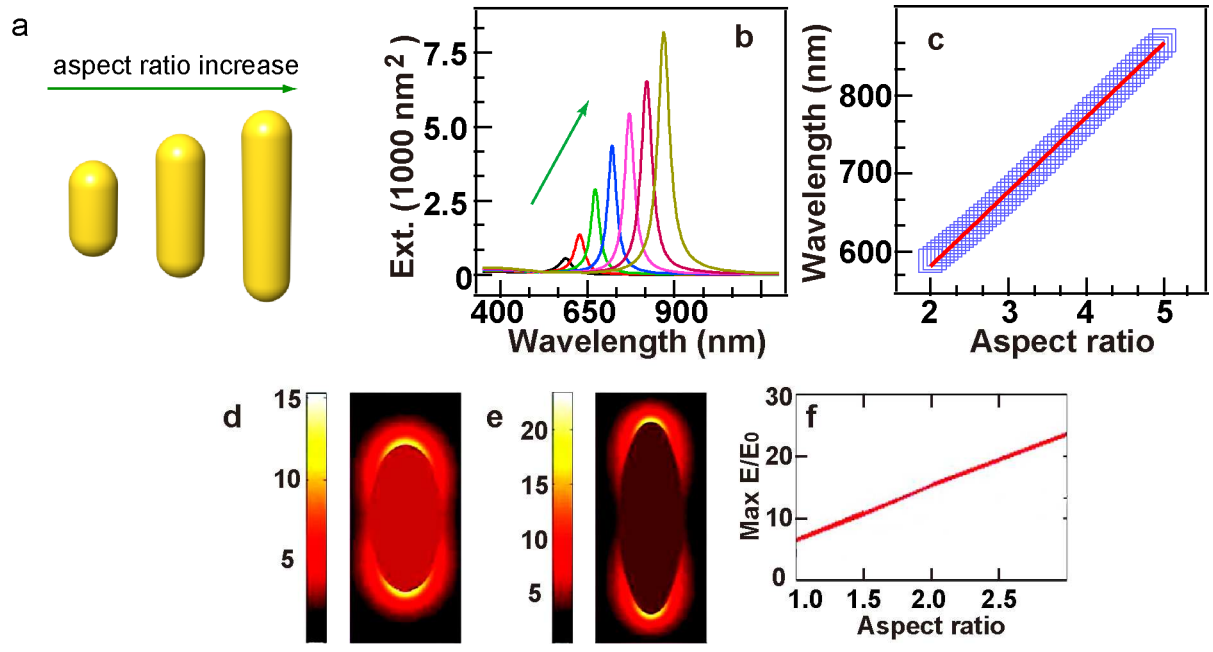

Figure 1.5 Dependence of the plasmonic properties of Au nanorods on the aspect ratio.[8] (a) Schematic showing Au nanorods with a fixed diameter but different aspect ratios. (b)

Dependence of the extinction spectra on the aspect ratio under the longitudinal excitation. The aspect ratio of the nanorod is changed from 1.5 to 6 while its diameter is fixed at 5 nm. In (a) and (b), the arrows indicate the increasing direction in the aspect ratio. (c) Dependence of the longitudinal plasmon wavelength on the aspect ratio. (d) Electric field enhancement contour [49] of a nanorod with an aspect ratio of 2. (e) Electric field enhancement contour [49] of a nanorod with an aspect ratio of 3. (f) Maximum electric field enhancement as a function of the aspect ratio at the longitudinal plasmon resonance.[49] All the results shown here are calculated with Gans theory, where the Au nanorod is modeled with a spheroid. The details of Gans theory will be introduced in Chapter 2.

The LSPR wavelength of Au nanorods is highly sensitive to the surrounding dielectric environment. Increase of the dielectric constant (or the refractive index) of the surrounding nanoenvironment can induce more polarization charges around the nanorod. Under external electromagnetic excitations, there will be an increased screening of the Coulombic restoring force that acts on the free electrons in the nanorod (Figure 1.6a). The reduced restoring force therefore results in a red shift in the plasmon resonance. From Figure 1.6b, we can clearly see that both the longitudinal and transverse plasmon modes red-shift as the refractive index is increased. The longitudinal plasmon shift follows a linear relationship with the refractive index (Figure 1.6c).[8] This linear relationship can be employed to design ultrasensitive biomedical sensors. The sensing performance can be reflected by the refractive index sensitivity, which is defined as the plasmon shift per refractive index unit (RIU). Both the polarizability (defined as the dipole moment of the entire particle, see Chapter 2 for the calculation details of the polarizability) and the shape of metal nanocrystals play important roles in the index sensitivity, as it is shown in Figure 1.6d.[57]

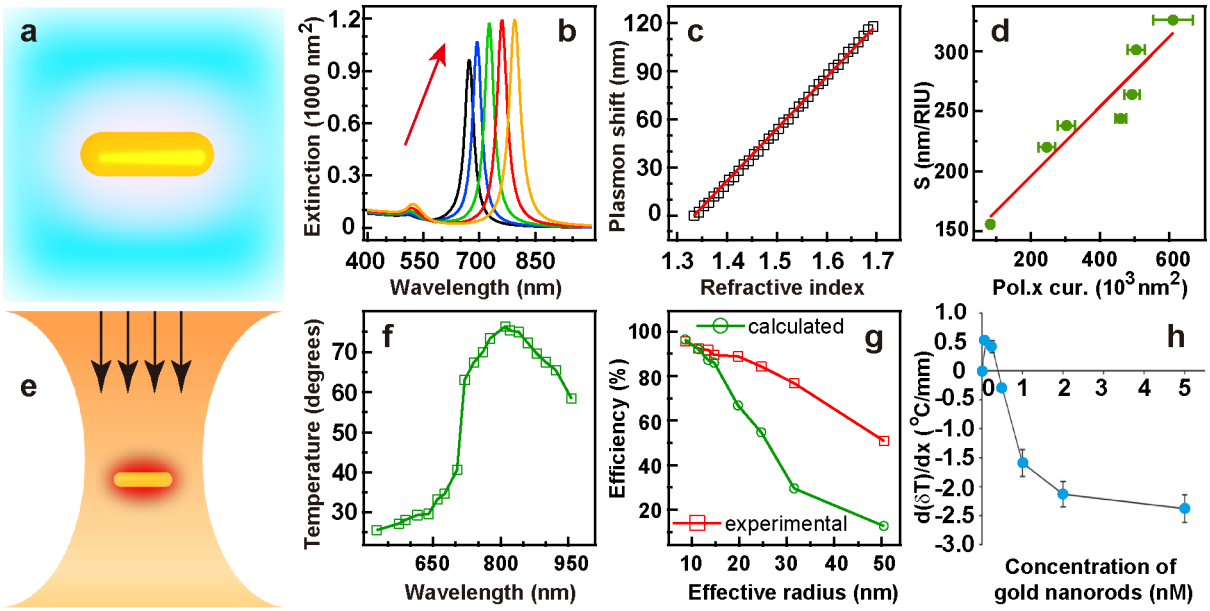

Figure 1.6 Refractive index dependent-plasmon resonances and plasmonic photothermal conversion properties of Au nanorods.[8] (a) Schematic of a Au nanorod immersed in a solution. (b) Calculated extinction spectra of a Au nanorod in solutions with different refractive indices. The nanorod has an aspect ratio of 3. The refractive index of the solution is increased from 1.3 to 1.7 at a step of 0.1. (c) Dependence of the longitudinal plasmon shift on the refractive index of the solution. (d) Refractive index sensitivity as a function of the product between the polarizability and the end curvature of elongated Au nanocrystals with different end shapes.[57] (e) Schematic showing the plasmonic photothermal conversion of a Au nanorod. (f) Dependence of the end temperature on the nanorod longitudinal plasmon wavelength.[61] (g) Dependence of the measured and calculated photothermal conversion efficiencies on the effective particle radius of Au nanorods.[61] (h) Effect of the Au nanorod concentration on the gradient of the temperature increase along the depth of the microcentrifuge tube containing Au nanorods.[62]

The extremely large absorption cross sections of Au nanorods at their LSPR wavelengths make them a promising material for photothermal conversion. The underneath mechanism is that decay of the plasmon resonances in Au nanorods through thermalization with the lattice will generate heat, which can thereby cause temperature rises in the surrounding environment (Figure 1.6e). The excellent photothermal conversion capability of Au nanorods enables them to be used for killing cancer cells,[58] controllably releasing gene[59] and delivering drugs.[60] The photothermal conversion of Au nanorods is governed by the competition between the radiative and non-radiative decays of their plasmon resonances. It will be the highest for Au nanorods with longitudinal plasmon wavelengths very close to the incident laser wavelength (Figure 1.6f).[61]

Au nanorods with smaller volumes have reduced radiative decay, and therefore exhibit higher photothermal conversion efficiencies (Figure 1.6g).[61] In real applications, the photothermal conversion performance is also dependent on the nanorod concentrations (Figure 1.6h).[62] The dose of Au nanorods, as well as the laser power, should be considered to achieve optimal curative effects in clinic applications.

1.3 Coupling between Surface Plasmons

When metallic nanocrystals are in close proximity, their localized surface plasmons will interact with each other and lead to intriguing properties such as spectral shifts and large electric field enhancements.[26] The interaction between localized surface plasmons is accompanied with the formation of new collective plasmon modes. Plasmon coupling can be well understood and predicted by the hybridization model raised in 2003,[63] similar to the case for the hybridization theory of molecular orbitals (Figure 1.7a). The details of the hybridizatiom model will be discussed in Chapter 2 of this thesis. After plasmon coupling, lower-energy bonding and higher-energy antibonding hybridized plasmon modes will be formed (Figure 1.7a–c).[64–66] Furthermore, near-field interactions enable the excitation of new plasmon modes, such as high-order electric multipolar and magnetic dipolar plasmon modes (Figure 1.7d).[67,68] The interferences between different plasmon modes thereafter result in several fascinating phenomena in coupled metal nanostructures, such as spectral splitting,[69] plasmonic Fano resonance (Figure 1.7e,f),[67,68,70] and electromagnetically induced transparency (Figure 1.8a,b).[42,71] Symmerty plays an important role in the excitation of the new high-order electric multipolar and magnetic dipolar plasmon modes. For example, in the plasmon coupling between two identical metal nanocrystals in a homodimer, usually only dipole–dipole bonding plasmon modes are active under light excitation. The dipole–dipole antibonding plasmon modes are 'dark' modes, since the net dipole of the entire system is zero and they can not be directly excited by electromagnetic plane waves. If the symmetry is broken, such plasmon modes can be excited,

enabling their interaction with the bright plasmon modes. For example, considering a nanoring structure composed of four coupled Au nanospheres, the nanoring can support both electric and magnetic dipolar plasmon modes.[68] The two modes do not interfere for symmetric nanorings (Figure 1.7e). After slight symmetry-breaking is introduced by using Au nanospheres of different sizes, interference between the electric dipolar and magnetic dipolar modes can be achieved, giving rise to a pronounced Fano resonance in the scattering spectrum (Figure 1.7f).

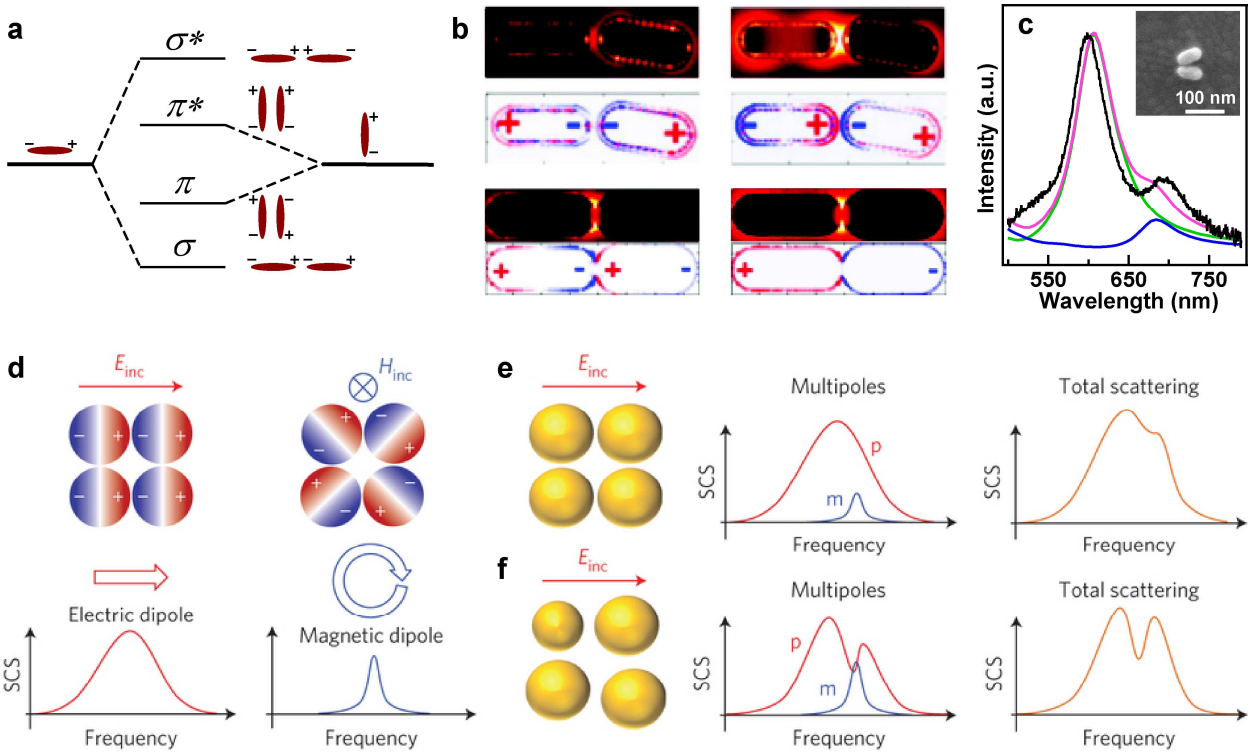

Figure 1.7 Plasmon coupling in noble metal nanostructures. (a–c) Plasmon coupling in Au nanorod dimers. (a) Electromagnetic analogy to molecular orbital theory: hybridization model showing the basic picture of the coupled longitudinal plasmon modes of end-to-end and side-by-side assembled Au nanorod homodimers.[64] (b) Calculated electric field enhancement contours (upper) and charge distributions (lower) of linear end-to-end nanorod homodimers at the antibonding mode, the bonding mode, the conductive coupled bonding mode, and the conductive coupled charge-transfer plasmon mode.[66] (c) Plasmon coupling in Au nanorod homodimers with the nanorod angle at ~30°. Scattering spectrum of an individual dimer was measured.[65] The two scattering peaks reveal the formation of the antibonding and bonding plasmon modes. (d–f) Illustration of the scattering response of plasmonic nanorings.[68] (d) Scatteirng cross-section (SGS) of a four-particle nanoring system excited by a time-varying electric field (left) and by a time-varying magnetic field (right). E_{inc} and H_{inc} represent the incident electric and magnetic fields, respectively. Colours indicate the charge distribution inside

each nanoparticle. (e,f) Scattering response of a symmetric nanoring (e) and when small asymmetries are introduced (f). Symmetry-breaking induces interference between the electric dipolar (p) and magnetic dipolar (m) modes, which gives rise to a pronounced Fano resonance in the scattering spectrum.

It is quite intriguing that we can observe Fano profiles in purely plasmonic systems,[72–77] since Fano profiles are typical spectral features arising from the coupling of a discrete state with a continuum.[78] When the plasmon modes of metallic nanocrystals interact with each other, the newly formed hybridized plasmon modes may have energy overlap and the interference between them can occur. The energy of the bright mode (which can be excited directly by light) will be transferred to the dark mode (which cannot be excited directly by light) at their overlapped resoancne frequencies, leading to the asymmetric profile in the scattering or extinction spectra and a dip in the scatting spectrum. Apart from their fundamental importance, Fano resonances in plasmonic media are of considerable interest in localized surface plasmon resonance sensing applications because they are extraordinarily sensitive to their local dielectric environment. The low scattering intensities associated with Fano resonances are potentially useful for plasmonic waveguide applications. Fano interference is also closely related to the electromagnetically induced transparency in plasmonic nanostructures (Figure 1.8a,b).[70,71]

Slight perturbation in coupled plasmonic structures can give rise to rich changes on light scattering and absorption spectra.[8] As shown in Figure 1.8c–h, the small change of the three dimensional displacement of the central Au nanorod in a coupled plasmonic structure will bring distinct spectral variations.[79] As a result, the coupled plasmonic structures can act as colormetric biosensing components,[80] plasmonic ruler for nanometer measurements,[79] and electromagnetically-induced transparency materials.[42,71]

Besides their unique spectral features, the plasmon coupling between metal nanocrystals can significantly increase the near field in the junction (Figure 1.7b, 1.8a).[8,26,65,66,71]. Intensity enhancements up to 10^6 have been theoretically predicted. The coupling between noble metal nanocrystals has therefore been employed for enhancing optical signals, including

second-harmonic generation (Figure 1.8i),[33] Raman scattering(Figure 1.8j),[28,81,82] fluorescence,[83] and two-photon photoluminescence,[84] and applied in photolithography,[85] two-photon polymerization,[86] and nanometric optical tweezers (Figure 1.8k).[87–89]

Closely spaced metallic nanorods can function as optical nanoantennas to link propagating radiation with confined optical fields [44–47,90,91]. The optical antenna can boost the efficiency of light–matter interactions and enable control of photophysical processes on the nanoscale. This has many foreseeable applications, such as high-resolution microscopy and spectroscopy, photovoltaics and photocatalysis, and solid-state lighting [92,93].

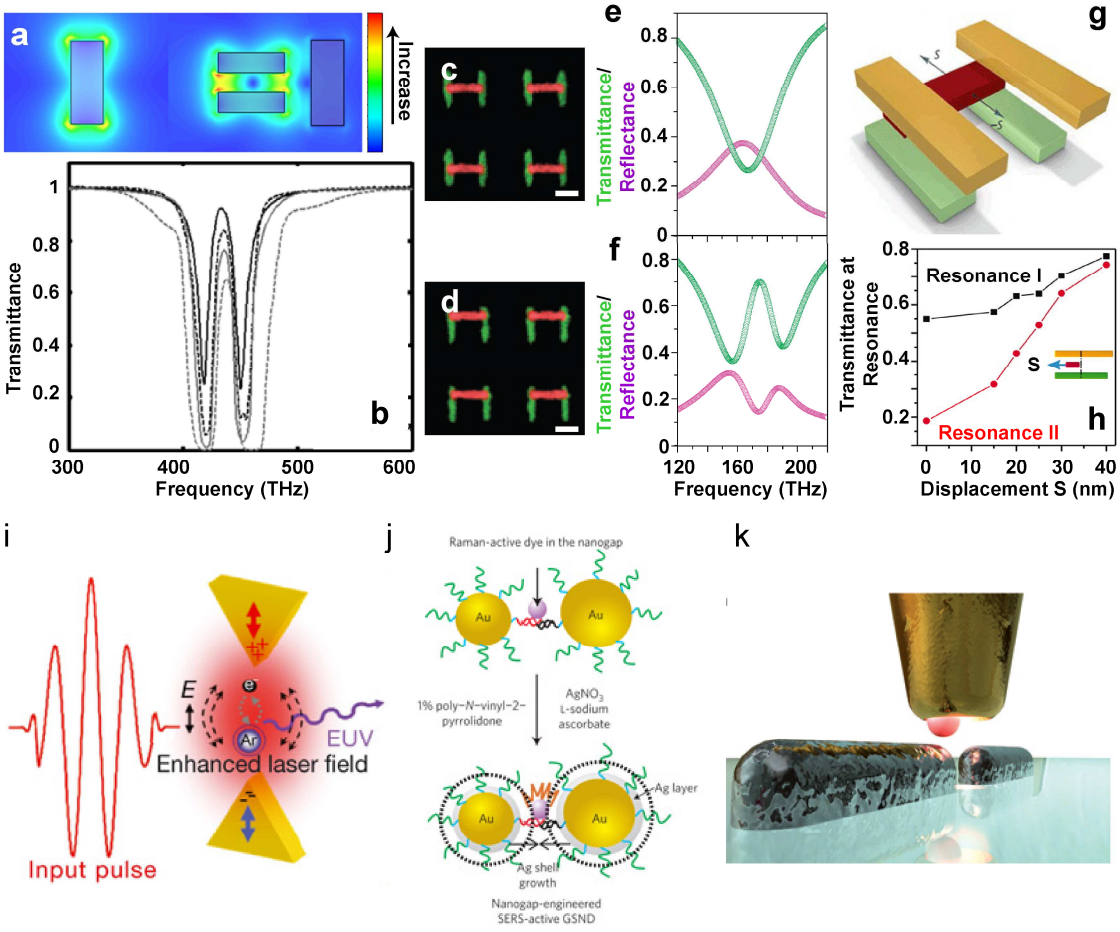

Figure 1.8 Applications of coupled plasmonic structures. (a–h) Metamaterials of distinct spectral responses made of Au nanorods. (a) Electromagnetic filed distributions of an uncoupled Au nanorod (left) and the building unit of the metamaterial (right) at the frequency of the transmission window.[71] (b) Transimission spectra of the metamaterials showing the electromagnetically induced transparency.[71] (c,d) False-color SEM images of the metamaterials made of Au nanorods. The scale bars are 200 nm.[79] (e,f) Transmittance and

reflectance spectra of the corresponding structures shown in (c) and (d), respectively.[79] (g) Schematic showing the three-dimensional plasmonic ruler.[79] (h) Evolution of the plasmonic resonances as a function of the displacement of the middle nanorod.[79] (i–k) Applications of coupled plasmonic structures by utilizing their extremely large near-field enhancements. (i) Plasmon field enhancement for high-harmonic generation.[33] (j) Surface-enhanced Raman scattering of coupled plasmonic nanostructures for single-molecule detection.[28] (k) Plasmonic nano-optical tweezers for positioning single emitters with nanoscale accuracy.[89]

There are so many applications based on the plasmon coupling of noble metal nanostructures that I cannot list all of them here. Interested readers can refer to some excellent reviews.[8,26]

1.4 Outline of Thesis

As stated above, the plasmonic properties of Au nanorods and their coupled structures are not only of fundamental importance, but also have potential applications in many areas. My research mainly focuses on the plasmonic properties of coupled Au nanostructures and Au nanocrystal arrays. In this thesis, I will study the plasmon coupling in Au nanorod heterodimers and Au nanorod–Au nanosphere heterodimers, the modulation of plasmon coupling in Au nanostructures with graphene, and the methods to build large-area Au nanocrystal arrays for their practical applications. The contents are organized as follows.

Chapter 2 will give an overview of the theoretical background of the localized surface plasmon resonances in noble metal nanocrystals and their coupling, including Maxwell electrodynamics, the solid state theory for describing the dielectric properties of noble metal nanostructures, analytical approaches for calculating the scattering/absorption responses of metal nanostructures, and several numerical techniques for calculating the plasmonic properties of noble metal nanostructures.

Experimental preparation methods, including both chemical and lithographical means, of Au nanostructures (mainly Au nanorods) will be presented in Chapter 3. Characterizaiton methods for measuring the plasmonic properties of noble metal nanostructures are also

described.

Chapter 4 and Chapter 5 give the details of my research on the plasmon coupling in Au nanorod-based oligomers, including Au nanrod heterodimers (Chapter 4) and Au nanorod–Au nanosphere heterodimers (Chapter 5). The coupling-induced spectral variation, plasmonic Fano resonance, and the potential applications of these structures are discussed in detail.

In Chapter 6, I will introduce my efforts to use graphene to mediate the plasmonic properties of coupled Au nanorod dimers and Au film-coupled Au nanosphere antennas. The interaction between graphene and Au nanorod dimers is found to be very weak due to the difficulty in placing graphene into the near-field hot spots. On the other hand, Au film-coupled Au nanosphere can effectively squeeze light into an ultrasmall cavity to promote light–graphene interactions. Significant spectral tuning of the film-coupled nanoantennas has been achieved by graphene.

Chapter 7 introduces my efforts to fabricate large-area plasmonic Au nanorood arrays. The plasmonic properties of Au nanorods fabricated by EBL and chemical growth methods are first compared and discussed. To overcome the poor plasmonic performance of EBL-written Au nanorods, I further developed a method to directly deposit colloidal metal nanocrystals onto different substrates to form uniform, dense arrays. The refractive index sensing performance of the obtained Au nanorod arrays is characterized.

Finally, conclusion will be given in Chapter 8.

References

[1] Brongersma, M. L.; Kik, P. G. *Surface Plasmon Nanophotonics.* Dordrecht: Springer, 2007.

[2] Maier, S. A. *Plasmonics: Fundamentals and Applications.* Springer Science+Business Media LLC, 2007.

[3] Sommerfeld, A. *Ann. der Physik und Chemie* **1899**, *67*, 233.

[4] Zenneck, J. *Ann. der Physik* **1907**, *23*, 846.

[5] Fano, U. *J. Opt. Soc. Am.* **1941**, *31*, 213.

[6] Wood, R. W. *Phil. Mag.* **1902**, *4*, 396.

[7] Lord Rayleigh. *Phil. Mag.* **1907**, *14*, 60.

[8] Chen, H. J.; Shao, L.; Li, Q.; Wang, J. F. *Chem. Soc. Rev.* **2013**, *42*, 2679.

[9] Huang, X. H.; Neretina, S.; El-Sayed, M. A. *Adv. Mater.* **2009**, *21*, 4880.

[10] Faraday, M. *Phil. Trans. R. Soc.* **1857**, *147*, 145.

[11] Mie, G. *Ann. der Physik* **1908**, *25*, 377.

[12] Gans, R. *Ann. der Physik* **1912**, *342*, 881.

[13] Drude, P. *Ann. der Physik* **1900**, *306*, 566.

[14] Kreibig, U.; Vollmer, M. *Optical Properties of Metal Clusters*. Springer, Berlin, 1995.

[15] Bohren, C. F.; Huffman, D. R. *Absorption and Scattering of Light by Small Particles*. John Wiley & Sons, Inc., 1983.

[16] Kreibig, U. *J. Phys. F: Metal Phys.* **1974**, *4*, 999.

[17] Special Issue: Optical Properties of Nanoparticles. *Appl. Phys. B* **2001**, *73*.

[18] Barnes, W. L.; Dereux, A.; Ebesen, T. W. *Nature* **2003**, *424*, 824.

[19] Maier, S. A. Kik, P. G.; Atwater, H. A.; Meltzer, S.; Harel, E.; Koel, B. E.; Requicha, A. A. G. *Nat. Mater.* **2003**, *2*, 229

[20] Ozbay, E. Plasmoincs: Merging Photonics and Electronics at Nanoscale Dimensions. *Scinece* **2006**, *311*, 189.

[21] Nezhad, M. P.; Tetz, K.; Fainman, Y. *Opt. Express* **2004**, *12*, 4072.

[22] Maier, S. A. *Opt. Commun.* **2006**, *258*, 295.

[23] Ambati, M.; Nam, S. H.; Ulin-Avila, E.; Genov, D. A.; Bartal, G.; Zhagn, X. *Nano Lett.* **2008**, *8*, 3998.

[24] Rycenga, M.; Cobley, C. M.; Zeng, J.; Li, W. Y.; Moran, C. H.; Zhang, Q.; Qin, D.; Xia, Y. N. *Chem. Rev.* **2011**, *111*, 3669.

[25] Cortie, M. B.; McDonagh, A. M. *Chem. Rev.* **2011**, *111*, 3713.

[26] Halas, N. J.; Lal, S.; Chang, W.-S.; Link, S.; Nordlander, P. *Chem. Rev.* **2011**, *111*, 3913.

[27] Ming, T.; Chen, H. J.; Jiang, R. B.; Li, Q.; Wang, J. F. *J. Phys. Chem. Lett.* **2012**, *3*, 191.

[28] Lim, D.-K.; Jeon, K.-S.; Kim, H. M.; Nam, J.-M.; Suh, Y. D. *Nat. Mater.* **2010**, *9*, 60.

[29] Schietinger, S.; Aichele, T.; Wang, H.-Q.; Nann, T.; Benson, O. *Nano Lett.* **2010**, *10*, 134.

[30] Kinkhabwala, A. Kinkhabwala, A.; Yu, Z. F.; Fan, S. H.; Avlasevich, Y.; Müllen, K.; Moerner, W. E. *Nat. Photonics* **2009**, *3*, 654.

[31] Noginov, M. A. Zhu, G.; Belgrave, A. M.; Bakker, R.; Shalaev, V. M.; Narimanov, E. E.; Stout, S.; Herz, E.; Suteewong, T.; Wiesner, U. *Nature* **2009**, *460*, 1110.

[32] Berini, P.; De Leon, I. *Nat. Photonics* **2011**, *6*, 16.

[33] Kim, S. Jin, J.; Kim, Y.-J.; Park, I.-Y.; Kim, Y.; Kim, S.-W. *Nature* **2008**, *453*, 757.

[34] Klein, M. W.; Enkrich, C.; Wegener, M.; Linden, S. *Science* **2006**, *313*, 502.

[35] ISI. Surface Plasmon Publication Statistics. http://apps.isiknowledge.com, May 2013.

[36] Slaughter, L.; Chang, W.-S.; Link, S. *J. Phys. Chem. Lett.* **2011**, *2*, 2015.

[37] Ebbesen, T. W.; Lezec, H. J.; Ghaemi, H. F.; Thio, T.; Wolff, P. A. *Nature* **1998**, *391*, 667.

[38] Atwater, H. A.; Polman, A. *Nat. Mater.* **2010**, *9*, 205.

[39] Kawata, S.; Inouye, Y.; Verma, P. *Nat. Photonics* **2009**, *3*, 388.

[40] Zijlstra, P.; Chon, J. W. M.; Gu, M. *Nature* **2009**, *459*, 410.

[41] Homola, J.; Yee, S. S.; Gauglitz, G. *Sensors and Actuators B: Chemical* **1999**, *54*, 3.

[42] Liu, N. Langguth, L.; Weiss, T.; Kästel, J.; Fleischhauer, M.; Pfau, T.; Giessen, H. *Nat. Mater.* **2009**, *8*, 758.

[43] Huang, X. H.; El-Sayed, I. H.; Qian, W.; El-Sayed, M. A. *J. Am. Chem. Soc.* **2006**, *128*, 2115.

[44] Ni, X. J.; Emani, N. K.; Kildishev, A. V.; Boltasseva, A.; Shalev, V. M. *Science* **2012**, *335*, 427.

[45] Curto, A. G.; Volpe, G.; Taminiau, T. H.; Kreuzer, M. P.; Quidant, R.; van Hulst, N. F. *Science* **2010**, *329*, 930.

[46] Novotny, L.; van Hulst, N. F. *Nat. Photonics* **2011**, *5*, 83.

[47] Knight, M. W.; Sobhani, H.; Nordlander, P.; Halas, N. J. *Science* **2011**, *332*, 702.

[48] Pérez-Juste, J.; Pastoriza-Santos, I.; Liz-marzán, L. M.; Mulvaney, P. *Coord. Chem. Rev.* **2005**, *249*, 1870.

[49] Zuloaga, J.; Prodan, E.; Nordlander, P. *ACS Nano* **2010**, *4*, 5269.

[50] Love, J. C.; Estroff, L. A.; Kriebel, J. K.; Nuzzo, R. G.; Whitesides, G. M. *Chem. Rev.* **2005**, *105*, 1103.

[51] Joseph, S. T. S.; Ipe, B. I.; Pramod, P.; Thomas, K. G. *J. Phys. Chem. B* **2006**, *110*, 150.

[52] Pramod, P.; Thomas, K. G. *Adv. Mater.* **2008**, *20*, 4300.

[53] Sun, Z. H.; Ni, W. H.; Yang, Z.; Kou, X. S.; Li, L.; Wang, J. F. *Small* **2008**, *4*, 1287.

[54] Liu, K.; Zhao, N. N.; Kumacheva, E. *Chem. Soc. Rev.* **2011**, *40*, 656.

[55] Nie, Z. H. Fava, D.; Kumacheva, E.; Zou, S.; Walker, G. C.; Rubinstein, M. *Nat. Mater.* **2007**, *6*, 609.

[56] Liu, K.; Nie, Z. H.; Zhao, N. N.; Li, W.; Rubinstein, M; Kumacheva, E. *Science* **2010**, *329*, 197.

[57] Chen, H. J.; Shao, L.; Woo, K. C.; Ming, T.; Lin, H.-Q.; Wang, J. F. *J. Phys. Chem. C* **2009**, *113*, 17691.

[58] Dickerson, E. B.; Dreaden, E. C.; Huang, X. H.; El-Sayed, I. H.; Chu, H. H.; Pushpanketh, S.; McDonald, J. F.; El-Sayed, M. A. *Cancer Lett.* **2008**, *269*, 57.

[59] Chen, C.-C.; Lin, Y.-P.; Wang, C.-W.; Tzeng, H.-C.; Wu, C.-H.; Chen, Y.-C.; Chen, C.-P.; Chen, L.-C.; Wu, Y.-C. *J. Am. Chem. Soc.* **2006**, *128*, 3709.

[60] Bikram, M.; Gobin, A. M.; Whitmire, R. E.; West, J. L. *J. Controlled Release* **2007**, *123*, 219.

[61]Chen, H. J. Shao, L.; Ming, T.; Sun, Z. H.; Zhao, C. M.; Yang, B. C.; Wang, J. F. *Small* **2010**, *6*, 2272.

[62] Jiang, B.; Kim, Y. S.; Choi, Y. D. *Small* **2011**, *7*, 265.

[63] Prodan, E.; Radloff, C.; Halas, N. J.; Nordlander, P. *Science* **2003**, *302*, 419.

[64] Jain, P. K.; Eustis, S.; El-Sayed, M. A. *J. Phys. Chem. B* **2006**, *110*, 18243.

[65] Shao, L. Woo, K. C.; Chen, H. J.; Jin, Z.; Wang, J. F.; Lin, H.-Q. *ACS Nano* **2010**, *4*, 3053.

[66] Slaughter, L. S.; Wu, Y.; Willingham, B. A.; Nordlander, P.; Link, S. *ACS Nano* **2010**, *4*, 4657.

[67] Fan, J. A.; Wu, C.; Bao, K.; Bao, J. M.; Bardhan, R. Halas, N. J.; Manoharan, V. N.; Nordlander, P.; Shvets, G.; Capasso, F. *Science* **2010**, *328*, 1135.

[68] Shafiei, F.; Monticone, F.; Le, K. Q.; Liu, X.-X.; Hartsfield, T.; Alù, A.; Li, X. Q. *Nat. Nanotechnol.* **2013**, *8*, 95.

[69] Liu, N.; Guo, H. C.; Fu, L. W.; Kaiser, S.; Schweizer, H.; Giessen, H. *Nat. Mater.* **2008**, *7*, 31.

[70] Luk'yanchuk, B.; Zheludev, N. I.; Maier, S. A.; Halas, N. J.; Nordlander, P.; Giessen, H.; Chong, C. T. *Nat. Mater.* **2010**, *9*, 707.

[71] Zhang, S.; Genov, D. A.; Wang, Y.; Liu, M.; Zhang, X. *Phys. Rev. Lett.* **2008**, *101*, 047401.

[72] Bachelier, G.; Russier-Antoine, I.; Benichou, E.; Jonin, C.; Del Fatti, N.; Vallée, F.; Brevet, F.-F. *Phys. Rev. Lett.* **2008**, *101*, 197401.

[73] Christ, A.; Martin, O. J. F.; Ekinci, Y.; Gippius, N. A.; Tikhodeev, S. G. *Nano Lett.* **2008**, *8*, 2171.

[74] Hao, F.; Sonnefraud, Y.; Van Dorpe, P.; Maier, S. A.; Halas, N. J.; Nordlander, P. *Nano Lett.* **2008**, *8*, 3983.

[75] Verellen, N.; Sonnefraud, Y. Sobhani, H.; Hao, F.; Moshchalkov, V. V.; Van Dorpe, P.; Nordlander, P.; Maier, S. A. *Nano Lett.* **2009**, *9*, 1663.

[76] Mirin, N. A.; Bao, K.; Nordlander, P. *J. Phys. Chem. A* **2009**, *113*, 4028.

[77] Brown, L. V.; Sobhani, H.; Lassiter, J. B.; Nordlander, P.; Halas, N. J. *ACS Nano* **2010**, *4*, 819.

[78] Fano, U. *Phys. Rev.* **1961**, *124*, 1866.

[79] Liu, N.; Hentschel, M.; Weiss, T.; Alivisatos, A. P.; Giessen, H. *Science* **2011**, *332*, 1407.

[80] Liu, J. W.; Lu, Y. *Nat. Protocol* **2006**, *1*, 246.

[81] Shegai, T.; Li, Z. P.; Dadosh, T.; Zhang, Z. Y.; Xu, H. X.; Haran, G. *Proc. Natl. Acad. Sci. USA* **2008**, *105*, 16448.

[82] Li, W. Y.; Camargo, P. H. C.; Lu, X. M.; Xia, Y. N. *Nano Lett.* **2009**, *9*, 485.

[83] Kinkhabwala, A.; Yu, Z. F.; Fan, S. H.; Avlasevich, Y.; Müllen, K.; Moerner, W. E. *Nat. Photonics* **2009**, *3*, 654.

[84] Ueno, K.; Juodkazis, S.; Mizeikis, V.; Sasaki, K.; Misawa, H. *Adv. Mater.* **2008**, *20*, 26.

[85] Sundaramuethy, A.; Schuck, P. J.; Conley, N. R.; Fromm, D. P.; Kino, G. S.; Moerner, W. E. *Nano Lett.* **2006**, *6*, 355.

[86]Ueno, K.; Juodkazis, S.; Shibuya, T.; Yokota, Y.; Mizeikis, V.; Sasaki, K.; Misawa, H. *J. Am. Chem. Soc.* **2008**, *130*, 6928.

[87] Grigorenko, A. N.; Roberts, N. W.; Dickinson, M. R.; Zhang, Y. *Nat. Photonics* **2008**, *2*,

365.

[88] Xu, H.; Käll, M. *Phys. Rev. Lett.* **2002**, *89*, 246802.

[89] Juan, M. L.; Righini, M.; Quidant, R. *Nat. Photonics* **2011**, *5*, 349.

[90] Mühlschlegel, P.; Eisler, H.-J.; Martin, O. J. F.; Hecht, B.; Pohl, D. W. *Science* **2005**, *308*, 1607.

[91] Schnell, M.; García-Etxarri, A.; Huber, A. J.; Crozier, K.; Aizpurua, J.; Hillenbrand, R. *Nat. Photonics* **2009**, *3*, 287.

Chapter 2

Theoretical Background

Surface plasmons are described as quanta of collective electron oscillations in quantum mechanics. To fully obtain the optical response of surface plasmons, the quantization of electromagnetic fields and investigation of electron–electron, electron–photon interactions are required.[1] However, very recent reports pointed out that we need to consider quantum mechanical effects only for metal nanoparticles with dimensions smaller than 10 nm [2,3] and for metal nanoparticle pairs with an interparticle distance smaller than 0.5 nm.[4,5] In most cases, the interaction of metals with electromagnetic fields can be firmly understood in a classical framework based on Maxwell's equations.[6] In classical electromagnetism theory, surface plasmons are surface waves confined at metal–dielectric interfaces, just as water ripples travel along the surface of a pond after a stone is thrown into it. The optical responses of metallic structures are fully determined by the dielectric properties of the metal and the dielectric, the boundary conditions of the interfaces, and the properties of the excitation light source. In this thesis, I will not extend my study to the quantum regime and all discussions will be restricted in the classical electromagnetism theory. As a result, I will first give a brief review on Maxwell's equations and the solid state theory for describing the dielectric properties of metals (Section 2.1 and 2.2) in this chapter. The electrodynamic theory for calculating the optical response of spherical nanoparticles and the quasi-static approximation approach will be given in the second part (Section 2.3). For coupled plasmonic structures, some simple models can provide intuitive physical pictures for understanding the complex plasmonic interactions. I will discuss theoretical models for treating coupled plasmonic structures, such as metal nanocrystal oligomers and

plasmonic arrays, in Section 2.4. However, these theoretical models are either only suitable for the calculation of some simplest coupled systems or inable to give quantitative description. Numerical methods are usually required. I therefore will discuss the numerical methods for calculating the plasmonic properties of metal nanostructures, especially the finite-difference time-domain method, in the last section of this chapter (Section 2.5).

2.1 Maxwell's Equations

As the basis for describing the electrodynamic processes in macroscopic systems (where quantum effects can be neglected), Maxwell's equations can be written as (the differential form):[7]

$$\nabla \cdot \mathbf{D} = \rho_{\mathrm{f}} \tag{2.1}$$

$$\nabla \cdot \mathbf{B} = 0 \tag{2.2}$$

$$\nabla \times \mathbf{E} = -\frac{\partial \mathbf{B}}{\partial t} \tag{2.3}$$

$$\nabla \times \mathbf{H} = \mathbf{j}_{\mathrm{f}} + \frac{\partial \mathbf{D}}{\partial t} \tag{2.4}$$

The electric field (**E**) and the magnetic field (**B**) are related by the above four partial differential equations, where ρ_{f} and $\mathbf{j}_{\mathrm{f}}$ are free charge density and free current density, respectively. In the case of the interaction between light and noble metal nanoparticles, the external (free) charge and current densities $\rho_{\mathrm{f}} = 0$ and $\mathbf{j}_{\mathrm{f}} = 0$. The electric displacement (**D**) and the magnetizing field (**H**) are determined by the polarization and magnetization properties of the system,

$$\mathbf{D} = \varepsilon_0 \mathbf{E} + \mathbf{P} \tag{2.5}$$

$$\mathbf{B} = \mu_0 \mathbf{H} + \mathbf{M} \tag{2.6}$$

where **P** and **M** are polarization (defined as the electric dipole moment per unit volume) and magnetization (defined as the magnetic dipole moment per unit volume), respectively. ε_0 and μ_0 are the permittivity and permeability of vacuum, respectively. In most cases we will discuss, the response of the system is linear and **P** and **M** can be written as,

$$\mathbf{P} = \varepsilon_0 \chi_e \mathbf{E} \tag{2.7}$$

$$\mathbf{M} = \mu_0 \chi_M \mathbf{H} \tag{2.8}$$

where χ_e is the dielectric susceptibility, describing the linear relationship between **P** and **E**. χ_M is the magnetic susceptibility and describes the linear relationship between **M** and **H**. For linear, isotropic, and nonmagnetic media, equations (2.5) and (2.6) therefore become

$$\mathbf{D} = \varepsilon_0 \mathbf{E} + \mathbf{P} = \varepsilon_r \varepsilon_0 \mathbf{E} \tag{2.9}$$

$$\mathbf{B} = \mu_0 \mathbf{H} + \mathbf{M} = \mu_r \mu_0 \mathbf{H} \tag{2.10}$$

where ε_r and μ_r are the relative permittivity and permeability, respectively. They are defined as:

$$\varepsilon_r = 1 + \chi_e \tag{2.11}$$

$$\mu_r = 1 + \chi_M \tag{2.12}$$

ε_r and μ_r are phenomenological parameters and are frequency-dependent. By combining equations (2.3), (2.4), (2.9) and (2.10), we can obtain the following equations describing the electromagnetic waves propagating in a linear media:

$$\nabla(\nabla \cdot \mathbf{E}(\mathbf{r},t)) - \nabla^2 \mathbf{E}(\mathbf{r},t) + \mu_0 \frac{\partial}{\partial t}[\nabla \times (\mu_r(\mathbf{r})\mathbf{H}(\mathbf{r},t))] = 0 \tag{2.13}$$

$$\nabla(\nabla \cdot \mathbf{H}(\mathbf{r},t)) - \nabla^2 \mathbf{H}(\mathbf{r},t) - \varepsilon_0 \frac{\partial}{\partial t}[\nabla \times (\varepsilon_r(\mathbf{r})\mathbf{E}(\mathbf{r},t))] = 0 \tag{2.14}$$

Given the spatially dependent $\varepsilon_r(\mathbf{r})$, $\mu_r(\mathbf{r})$, the boundary conditions, and the initial conditions, the electric and magnetic components of the electromagnetic wave in the system therefore can be fully determined by solving equations (2.13) and (2.14).

Another form of Maxwell's equations is based on the electric potential φ and magnetic potential **A**. φ and **A** are related with **E** and **B** in the following manner:

$$\mathbf{E}(\mathbf{r},t) = -\nabla \varphi(\mathbf{r},t) - \frac{\partial \mathbf{A}(\mathbf{r},t)}{\partial t} \tag{2.15}$$

$$\mathbf{B}(\mathbf{r},t) = \nabla \times \mathbf{A}(\mathbf{r},t) \tag{2.16}$$

Maxwell's equations turn out to be

$$\nabla^2\varphi(\mathbf{r},t)+\frac{\partial}{\partial t}(\nabla\cdot\mathbf{A}(\mathbf{r},t))=-\frac{1}{\varepsilon_{\mathrm{r}}(\mathbf{r})\varepsilon_0}\rho_{\mathrm{f}}(\mathbf{r},t) \tag{2.17}$$

$$-\nabla^2\mathbf{A}(\mathbf{r},t)+\varepsilon_0\varepsilon_{\mathrm{r}}(\mathbf{r})\mu_0\mu_{\mathrm{r}}(\mathbf{r})\frac{\partial\mathbf{A}(\mathbf{r},t)}{\partial t}+\nabla\left(\nabla\cdot\mathbf{A}(\mathbf{r},t)+\varepsilon_0\varepsilon_{\mathrm{r}}(\mathbf{r})\mu_0\mu_{\mathrm{r}}(\mathbf{r})\frac{\partial\varphi(\mathbf{r},t)}{\partial t}\right)=\mu_0\mu_{\mathrm{r}}(\mathbf{r})\mathbf{j}_{\mathrm{f}}(\mathbf{r},t) \tag{2.18}$$

in the Lorentz gauge, when

$$\nabla\cdot\mathbf{A}(\mathbf{r},t)+\varepsilon_0\varepsilon_{\mathrm{r}}(\mathbf{r})\mu_0\mu_{\mathrm{r}}(\mathbf{r})\frac{\partial\varphi(\mathbf{r},t)}{\partial t}=0 \tag{2.19}$$

Maxwell's equations (2.17) and (2.18) turn out to be a beautiful form

$$\left(\nabla^2-\varepsilon_0\varepsilon_{\mathrm{r}}(\mathbf{r})\mu_0\mu_{\mathrm{r}}(\mathbf{r})\frac{\partial}{\partial t}\right)\varphi(\mathbf{r},t)=-\frac{1}{\varepsilon_{\mathrm{r}}(\mathbf{r})\varepsilon_0}\rho_{\mathrm{f}}(\mathbf{r},t) \tag{2.20}$$

$$\left(\nabla^2-\varepsilon_0\varepsilon_{\mathrm{r}}(\mathbf{r})\mu_0\mu_{\mathrm{r}}(\mathbf{r})\frac{\partial}{\partial t}\right)\mathbf{A}(\mathbf{r},t)=-\mu_0\mu_{\mathrm{r}}(\mathbf{r})\mathbf{j}_{\mathrm{f}}(\mathbf{r},t) \tag{2.21}$$

$\varphi(\mathbf{r}, t)$ and $\mathbf{A}(\mathbf{r}, t)$ can be obtained by solving the above equations once $\varepsilon_{\mathrm{r}}(\mathbf{r})$, $\mu_{\mathrm{r}}(\mathbf{r})$, the boundary conditions, and the initial conditions are provided. We can extract $\mathbf{E}(\mathbf{r}, t)$ and $\mathbf{B}(\mathbf{r}, t)$ after solving $\varphi(\mathbf{r}, t)$ and $\mathbf{A}(\mathbf{r}, t)$. Equations (2.17), (2.18), (2.20), and (2.21) are quite useful for solving the electromagnetic radiation problems.

In particular, if a system is homogeneous and has no free charges, Maxwell's equations (2.13) and (2.14) are reduced to,

$$\nabla^2\mathbf{E}(\mathbf{r},t)-\varepsilon_0\varepsilon_{\mathrm{r}}\mu_0\mu_{\mathrm{r}}\frac{\partial^2\mathbf{E}(\mathbf{r},t)}{\partial t^2}=0 \tag{2.22}$$

$$\nabla^2\mathbf{H}(\mathbf{r},t)-\varepsilon_0\varepsilon_{\mathrm{r}}\mu_0\mu_{\mathrm{r}}\frac{\partial^2\mathbf{H}(\mathbf{r},t)}{\partial t^2}=0 \tag{2.23}$$

The Maxwell's equations are linear and have a general solution in the form of sum of many harmonic components. We assume that the time-harmonic solutions of equations (2.22) and (2.23) have a dependence on time as $\exp(-\mathrm{i}\omega t)$:

$$\mathbf{E}(\mathbf{r},t)=e^{-i\omega t}\cdot\mathbf{E}(\mathbf{r}) \tag{2.24}$$

$$\mathbf{H}(\mathbf{r},t)=e^{-i\omega t}\cdot\mathbf{H}(\mathbf{r}) \tag{2.25}$$

Equations (2.22) and (2.23) become

$$\nabla^2\mathbf{E}(\mathbf{r})+\varepsilon_0\varepsilon_{\mathrm{r}}\mu_0\mu_{\mathrm{r}}\omega^2\mathbf{E}(\mathbf{r})=0 \tag{2.26}$$

$$\nabla^2\mathbf{H}(\mathbf{r})+\varepsilon_0\varepsilon_{\mathrm{r}}\mu_0\mu_{\mathrm{r}}\omega^2\mathbf{H}(\mathbf{r})=0 \tag{2.27}$$

In the frame of classical electrodynamics, surface plasmon resonance-related problems of different metal nanostructures can be regarded as the solutions of Maxwell's equations (2.13)–(2.14) or (2.17)–(2.18) with different dielectric properties, on different boundary conditions and under different excitation conditions. Since noble metals (Au, Ag, Pd, and Pt) are nonmagnetic, their relative permittivities are vitally important for their plasmonic performances. I then therefore will focus on ε_{r} of noble metals in the following part.

2.2 Dielectric Functions of Noble Metals

At metallic interfaces, external stimuli will induce both internal charge density ρ and current density **j**. ρ is closely related with the polarization **P**:

$$\nabla\cdot\mathbf{P}=-\rho \tag{2.28}$$

Charge conservation requires

$$\nabla\cdot\mathbf{j}=-\partial\rho/\partial t \tag{2.29}$$

The internal charge and current densities are therefore linked *via*

$$\mathbf{j}=\frac{\partial\mathbf{P}}{\partial t} \tag{2.30}$$

From the definition of the conductivity σ, we have

$$\mathbf{j}=\sigma\cdot\mathbf{E} \tag{2.31}$$

By incorporating equations (2.28)–(2.31) into Maxwell's equations, the complex permittivity of nonmagnetic metals (from now on called the dielectric function) can be written as

$$\varepsilon_{\mathrm{r}}=1+i\frac{\sigma(\omega)}{\varepsilon_0\omega} \tag{2.32}$$

At high frequencies, we have

$$\sigma=\sigma'+i\sigma'' \tag{2.33}$$

The dielectric function becomes

$$\varepsilon_r = 1 + i\frac{\sigma(\omega)}{\varepsilon_0\omega} = \left(1 - \frac{\sigma''(\omega)}{\varepsilon_0\omega}\right) + i\frac{\sigma'(\omega)}{\varepsilon_0\omega} = \varepsilon' + i\varepsilon'' \tag{2.34}$$

The dissipation mechanisms resulting from the induced internal currents and the non-zero resistivity of metals are all included in the imaginary part ε''. The modulus of ε_r determines the magnitude of the polarization while the phase of ε_r reflects the phase lag of the metal's response to the external field. For semiconductors or metals, the responses of the bound valence electrons are lumped into the static dielectric constant ε', while the responses of the conduction electrons are represented by ε'' (or σ'). As a result, a full description of ε' and ε'' requires the use of quantum theories for solids, where the many-body electron–electron interaction and electron–lattice interaction should be taken into consideration. At optical frequencies, ε_r of a specific material can also be experimentally determined by measuring the complex refractive index $\tilde{n}(\omega)$ defined as

$$\tilde{n} = n + i\kappa \tag{2.35}$$

The refractive index n and the extinction coefficient κ of thin films can be obtained from the reflectivity spectra measurement by ellipsometry. The complex dielectric function ε_r therefore can be calculated by

$$\varepsilon_r = \tilde{n}^2 \tag{2.36}$$

2.2.1. Free Electron Drude Model

The full description of the dielectric functions of metals by quantum theories is difficult. However, a plasma model (Drude Model) can successfully describe the optical properties of metals over a wide frequency range in a very simple way.[8–10] In this model the conduction electrons are treated as free electron gas. They move against a fixed background of positive ion cores. An effective mass m of each electron is used to take the band-structure correction into consideration.[11] The electrons oscillate in response to the applied electromagnetic field. Their

motion is damped via collisions with the lattice, which occur with a characteristic frequency $\gamma = 1/\tau$. τ is known as the relaxation time of the free electron gas. The electron–electron collision-induced interactions are neglected in this model.

The equation of motion for an electron subjected to an external electric field ***E*** is,

$$m\ddot{\mathbf{r}} + m\gamma\dot{\mathbf{r}} = -e\mathbf{E} = -e\mathbf{E}_0 e^{-i\omega t} \tag{2.37}$$

where **r** is the displacement of the electron, ω is the frequency of light and E_0 is its amplitude. A typical time-harmonic steady-state solution of this equation is

$$\mathbf{r}(t) = \mathbf{r}_0 e^{-i\omega t} \tag{2.38}$$

Equation 2.37 turns out to be

$$-m\omega^2\mathbf{r}_0 - im\omega\gamma\mathbf{r}_0 = -e\mathbf{E}_0 \tag{2.39}$$

The solution is

$$\mathbf{r} = \frac{e\mathbf{E}}{m(\omega^2 + i\gamma\omega)} \tag{2.40}$$

The microscopic polarization $\mathbf{P} = -ne\mathbf{r}$, where n is the number of electrons per unit volume. The electric displacement

$$\mathbf{D} = \varepsilon_0\mathbf{E} + \mathbf{P} = \varepsilon_0(1 - \frac{\omega_p^2}{\omega^2 + i\gamma\omega})\mathbf{E} \tag{2.41}$$

$\omega_p^2 = \frac{ne^2}{\varepsilon_0 m}$ is defined as the volume plasma frequency of the free electron gas. Hence, the relative dielectric function of the free electron gas becomes:

$$\varepsilon_r(\omega) = 1 - \frac{\omega_p^2}{\omega^2 + i\gamma\omega} \tag{2.42}$$

$$\omega_p = \sqrt{\frac{ne^2}{\varepsilon_0 m}} \tag{2.43}$$

2.2.2. Real Metals

For real metals, such as gold and silver, which are important in the field of plasmonics, the

free electron Drude model should be adjusted by taking into account the following two aspects.

First, the conduction electrons are dominated by the electrons in the *s* band of the noble metals. In addition to the behavior of free *s* electrons, the contribution of the bound electrons is not negligible, especially at high frequencies ($\omega >> \omega_p$) [6]. The filled *d* band close to the Fermi surface under an external electric field causes a highly polarized environment. This residual polarization due to the positive background of the ion cores can be described by adding the microscopic polarization to the following term: $\mathbf{P}_\infty = \varepsilon_0(\varepsilon_\infty - 1)\mathbf{E}$, thus the electric displacement becomes

$$\mathbf{D} = \varepsilon_0\mathbf{E} + \mathbf{P}_\mathrm{f} + \mathbf{P}_\infty = \varepsilon_0(\varepsilon_\infty - \frac{\omega_\mathrm{p}^2}{\omega^2 + i\gamma\omega})\mathbf{E} \tag{2.44}$$

The dielectric function is thus transformed into

$$\varepsilon_\mathrm{r}(\omega) = \varepsilon_\infty - \frac{\omega_\mathrm{p}^2}{\omega^2 + i\gamma\omega} \tag{2.45}$$

The background dielectric constant ε_∞, the effective mass *m*, and the relaxation constant γ can be acquired by fitting the Drude model to the experimentally determined dielectric data of metals.[11−13] The values of the parameters for Au, Ag, and Cu could be found in a related thesis.[14] The validity of the Drude model can also be examined by comparing the calculated and measured dielectric functions. For Au, the Drude model agrees excellently with the experimentally obtained dielectric function in the low-energy (below ~2 eV) part.

Second, when photon energies reach the threshold of transitions between electronic bands, the validity of the Drude model breaks down. For instance, the interband transition from *d*-band below the Fermi surface to *sp*-band becomes important for gold when photon energies are higher than 1.8 eV. [10] Indeed, the energy threshold for Au interband transitions lies at ~2.4 eV and is preceded by an absorption tail starting at about 1.8 eV. The main consequences of these processes are an increased damping and competition between the two excitations at visible frequencies.

The interband transitions can be described using the classical picture of a bound electron

with resonance frequency ω_L. A Lorentz oscillator model, which is usually employed for describing resonance absorption, can be applied to account for the interband transition contribution. The equation of motion of an electron turns out to be

$$m\ddot{\mathbf{r}} + m\gamma_L\dot{\mathbf{r}} + m\omega_L^2\mathbf{r} = -e\mathbf{E} \tag{2.46}$$

The solution therefore will be modified by adding a Lorentz oscillator term:[15,16]

$$\varepsilon_r(\omega) = \varepsilon_\infty - \frac{\omega_p^2}{\omega^2 + i\gamma\omega} + \frac{A_L}{\omega_L^2 - \omega^2 - i\gamma_L\omega} \tag{2.47}$$

Usually more than one interband transitions exist in real metals. These interband transitions involve different energy bands. To model $\varepsilon_r(\omega)$ accurately, a number of equations in the form of equation (2.46) have to be solved, leading to the addition of Lorentz-oscillator terms to the dielectric function deducted in the Drude model. The dielectric function becomes

$$\varepsilon_r(\omega) = \varepsilon_\infty - \frac{\omega_p^2}{\omega^2 + i\gamma\omega} + \sum_i \frac{A_i}{\omega_i^2 - \omega^2 - i\gamma_i\omega} \tag{2.48}$$

Mathematically, a sum over an infinite number of Lorentz functions can reproduce any well-behaved function that obeys the Kramers–Kronig relation, e.g. the dielectric function of metals.[17] It has been proven that the addition of two to five Lorentz-oscillator terms (i = 2~5) are enough to well reproduce the dielectric functions of Au and Ag.[16–19]

2.2.3. Noble Metal Nanostructures

All the models presented above are for bulk materials. When the dimension decreases to nanoscale, size-dependent effect must be taken into account.[20] When the sizes of noble metal nanocrystals are comparable to the electron mean free path, which is 38 nm for gold,[21] electrons would be strongly scattered by the particle surface, resulting in the increment of the electron relaxation rate in the Drude model:[22]

$$\gamma(R) = \gamma_0 + A\upsilon_F / R \tag{2.49}$$

where γ_0 is the free electron relaxation rate, υ_F is the Fermi velocity of the electrons in the metal

(1–2 nm/fs for most of metals at room temperature),[11] R is the effective radius of the particle (defined as the radius of a sphere having the same volume with the nanoparticle), and A represents the loss of coherence due to the scattering that is related to the surface chemistry. Typical values for A range from 0.1 to 0.7. For the Lorentz terms, they account for the bound electrons in the metal, which will not undergo the surface scattering. Therefore the relaxation rates in the Lorentz terms will not change.

When particles become smaller than 10 nm, especially when their sizes are less than 2 nm, the energy spacing in the energy band caused by quantization and splitting exceeds the thermal energy of 26 meV at room temperature [2,3,23]. As a result, quantum theory should be applied to rigorously describe the electron behavior. The dielectric function of noble metals must further be modified by including the contributions from the transitions between different quantum energy levels.

After obtaining the dielectric functions, the plasmonic performance of noble metal nanostructures can be predicted by solving Maxwell's equations under specific boundary conditions and initial conditions.

2.3 Mie Theory

Gustav Mie worked out the exact analytical solution for calculating the electrodynamic response of particles with a spherical shape.[24] The solutions take the form of an analytical infinite series of vector spherical harmonics. Maxwell's equations (2.26) and (2.27), and their boundary conditions are linear. As a result only the fundamental vector spherical harmonics solutions are considered. The general solutions can be obtained by superposing these fundamental solutions. Consider that a plane wave with a specific frequency and polarization is incident on a homogeneous, isotropic sphere of radius a and refractive index n_s. The sphere is surrounded by a homogeneous medium with refractive index n_m. The standard approach for searching for the solution to equations (2.26) and (2.27) is by first expanding the incident

electromagnetic field, the scattered field, and the field inside the sphere into infinite series of vector spherical harmonics with unknown coefficients. These coefficients can then be determined by fulfilling the boundary conditions on the surface of the sphere. Thereafter the near-field distribution, the far-field distribution, and the angular distribution of the scattering can be obtained.

In detail, solving Maxwell's equation (2.26) is equivalent to solving the following equations of a vector function **M**:[10,15]

$$\nabla^2\mathbf{M} + k^2\mathbf{M} = 0 \tag{2.50}$$

$$\nabla \cdot \mathbf{M} = 0 \tag{2.51}$$

where $k^2 = \omega^2\varepsilon_0\varepsilon_r\mu_0\mu_r$. The vector function **M** can be constructed by a scalar function ψ and an arbitrary constant vector **c**:

$$\mathbf{M} \equiv \nabla \times (\mathbf{c}\,\psi) \tag{2.52}$$

The definition of **M** by equation (2.52) naturally satisfies equation (2.51), since the divergence of the curl of any vector function vanishes. From the identification of **M** by equation (2.52), we have:

$$\nabla^2\mathbf{M} + k^2\mathbf{M} = \nabla \times \left[\mathbf{c}\left(\nabla^2\psi + k^2\psi\right)\right] \tag{2.53}$$

Therefore, **M** satisfies the vector wave function (2.5.0) if ψ is a solution to the following scalar wave function:

$$\nabla^2\psi + k^2\psi = 0 \tag{2.54}$$

Since **E** and **H** are not independent in Maxwell's equations:

$$\nabla \times \mathbf{E} = i\omega\mu_r\mu_0\mathbf{H} \tag{2.55}$$

$$\nabla \times \mathbf{H} = -i\omega\varepsilon_r\varepsilon_0\mathbf{E} \tag{2.56}$$

Once we obtain the solution of **E**, we can calculate **H**. Accordingly we can define another vector function **N**:

$$\mathbf{N} \equiv \frac{\nabla \times \mathbf{M}}{k} \tag{2.57}$$

The problem of solving Maxwell's equations turns out to be the problem of finding the vector functions **M** and **N**, which therefore is the simpler problem of finding solutions to the scalar wave equation (2.54). ψ can be called the generating function for the vector harmonics **M** and **N**.

The choice of ψ is dictated by whatever symmetry might exist in the problem. Here we discuss the calculation of the electrodynamic response of a spherical particle. We as a result choose ψ that satisfies equation (2.54) in spherical polar coordinates (r, θ, ϕ). If we choose

$$\mathbf{M} = \nabla \times (\mathbf{r}\psi) \tag{2.58}$$

where **r** is the radius vector, then **M** is a solution to the vector wave function (2.50). The scalar wave equation (2.54) in spherical polar coordinates is

$$\frac{1}{r^2}\frac{\partial}{\partial r}\left(r^2 \frac{\partial \psi}{\partial r}\right) + \frac{1}{r^2 \sin\theta}\frac{\partial}{\partial \theta}\left(\sin\theta \frac{\partial \psi}{\partial \theta}\right) + \frac{1}{r^2 \sin\theta}\frac{\partial^2 \psi}{\partial \phi^2} + k^2 \psi = 0 \tag{2.59}$$

The solutions to equation (2.59) are as follows:

$$\psi_{emn} = \cos m\phi \cdot P_n^m(\cos\theta) \cdot z_n(kr) \tag{2.60}$$

$$\psi_{omn} = \sin m\phi \cdot P_n^m(\cos\theta) \cdot z_n(kr) \tag{2.61}$$

$P_n^m(\cos\theta)$ are the associated Legendre functions of the first kind of degree n and order m, where $n = m, m+1, \ldots$[25] z_n is any of the four spherical Bessel functions j_n, y_n, $h_n^{(1)}$, or $h_n^{(2)}$. Because of the completeness of the functions $\cos m\phi$, $\sin m\phi$, $P_n^m(\cos\theta)$, and $z_n(kr)$, any function that satisfies the scalar wave equation can be expanded as an infinite series of equations (2.60) and (2.61). The vector harmonics $\mathbf{M}_{emn}$, $\mathbf{M}_{omn}$, $\mathbf{N}_{emn}$ and $\mathbf{N}_{omn}$ can therefore be acquired from ψ_{emn} and ψ_{omn}. A plane wave can be expanded in spherical harmonics as follows:

$$\mathbf{E}_i = E_0 \sum_{n=1}^{\infty} i^n \frac{2n+1}{n(n+1)} \left(\mathbf{M}_{o1n}^{(1)} - i\mathbf{N}_{e1n}^{(1)}\right) \tag{2.62}$$

The superscript (1) of the vector spherical harmonics **M** and **N** denotes that the radial dependence function z_n is j_n. The expansions of the internal and the scattered fields are

$$\mathbf{E}_l = E_0 \sum_{n=1}^{\infty} i^n \frac{2n+1}{n(n+1)} \left(c_n \mathbf{M}_{o1n}^{(1)} - i d_n \mathbf{N}_{e1n}^{(1)} \right) \tag{2.63}$$

$$\mathbf{E}_s = E_0 \sum_{n=1}^{\infty} i^n \frac{2n+1}{n(n+1)} \left(i a_n \mathbf{N}_{o1n}^{(3)} - b_n \mathbf{M}_{e1n}^{(3)} \right) \tag{2.64}$$

respectively. The superscript (3) of the vector spherical harmonics **M** and **N** denotes that the radial dependence function z_n is $h_n^{(1)}$. a_n, b_n, c_n, and d_n are unknown coefficients to be calculated from the boundary conditions. a_n and b_n are the most important, from which we can determine the scattering properties of the sphere. The two coefficients are obtained according to the following expressions:

$$a_n = \frac{m\psi_n(mx)\psi'_n(x) - \psi_n(x)\psi'_n(mx)}{m\psi_n(mx)\xi'_n(x) - \xi_n(x)\psi'_n(mx)} \tag{2.65}$$

$$b_n = \frac{\psi_n(mx)\psi'_n(x) - m\psi_n(x)\psi'_n(mx)}{\psi_n(mx)\xi'_n(x) - m\xi_n(x)\psi'_n(mx)} \tag{2.66}$$

where

$$x = ka \tag{2.67}$$

$$m = n_s / n_m \tag{2.68}$$

ψ_n and ξ_n are Riccati-Bessel functions and are expresses as

$$\psi_n(\rho) = \rho \cdot j_n(\rho) \tag{2.69}$$

$$\xi_n(\rho) = \rho \cdot h_n^{(1)}(\rho) \tag{2.70}$$

After obtaining the electric and magnetic fields in and outside the sphere, we can calculate the absorption cross section (C_{abs}), the scattering cross section (C_{sca}), and the extinction cross section (C_{ext}) as follows:[10,15,24]

$$C_{sca} = \frac{2\pi}{k^2} \sum_{n=1}^{\infty} (2n+1) \left(|a_n|^2 + |b_n|^2 \right) \tag{2.71}$$

$$C_{ext} = \frac{2\pi}{k^2} \sum_{n=1}^{\infty} (2n+1) \mathrm{Re}(a_n + b_n) \tag{2.72}$$

$$C_{abs} = C_{ext} - C_{sca} \tag{2.73}$$

In practical calculations, the infinite summations in equations (2.71) and (2.72) are usually

truncated to a particular *n* value, which is dependent on the radius of the sphere.

In 1908, when Mie wrote his classic paper, he was interested in explaining the colorful features of colloidal gold solutions. To date, the interest in Mie theory becomes much broader, ranging from interstellar dust, near-field optics and plasmonics to engineering subjects like optical particle characterization.[26] Mie theory is still being applied in many areas. Similar methods to analytically solve Maxwell's equations have been successfully developed for multiple spheres, core–shell spherical structures, and infinite cylinders.[26] The calculation based on Mie theory is exact and time-efficient. The Mie codes in Fortran, Matlab, C++, Mathematica, and even on-line Java application can be easily found. It is therefore quite convenient to use such codes to calculate the plasmonic responses of spherical metal nanoparticles.

2.4 Quasi-Static Approximation

Mie theory is applicable for spherical particles. For non-spherical particles, the solutions for equations (2.26) and (2.27) are very complicated. No analytical solutions without any approximations have been worked out. However, when a particle is much smaller than the wavelength of light in the surrounding medium, quasi-static approximation is effective for calculating the optical response of particles.[15] In this case, the phase of the harmonically oscillating light field is practically constant over the enitire particle volume. As a result, the spatial field distribution can be solved by considering the simplified problem of a particle in an electrostatic field. The harmonic time dependence can then be added to the solution by multiplying a phase term. Maxwell's equations are then changed into Laplace's equations

$$\nabla^2 \mathbf{E}(\mathbf{r}) = 0 \tag{2.74}$$

$$\nabla^2 \mathbf{H}(\mathbf{r}) = 0 \tag{2.75}$$

Small particles can therefore be treated as dipoles and their scattering and absorption can be calculated. Considering a spherical particles, simple analysis shows that its dipole moment α (also called polarizability in plasmonics), absorption and scattering cross sections can be

expressed as functions of the radius *a*:[10,15]

$$\alpha = 4\pi a^3 \frac{\varepsilon_s - \varepsilon_m}{\varepsilon_s + 2\varepsilon_m} \tag{2.76}$$

$$C_{abs} = k\,\mathrm{Im}(\alpha) = 4\pi k a^3\,\mathrm{Im}\left(\frac{\varepsilon_s - \varepsilon_m}{\varepsilon_s + 2\varepsilon_m}\right) \tag{2.77}$$

$$C_{sca}(\omega) = \frac{k^4}{6\pi}|\alpha|^2 = \frac{8}{3}\pi k^4 a^6 \left|\frac{\varepsilon_s - \varepsilon_m}{\varepsilon_s + 2\varepsilon_m}\right|^2 \tag{2.78}$$

where ε_s and ε_m are the dielectric functions of the sphere and the surrounding medium. The obtained absorption and scattering cross sections from quasi-static approximation have the same expressions as those for the cross sections given from the first terms in Mie theory (equations (2.71)–(2.73)). This agreement in turn verifies the effectiveness of quasi-static approximation. For small nanoparticles, the first term dominates the summations in equations (2.71) and (2.72).[14]

Most metal nanocrystals employed in experiments are non-spherical. Gans has investigated the scattering characteristics of ellipsoidal, including both oblate and prolate spheroidal particles, by solving Laplace's equations in the ellipsoidal coordinate system under quasi-static approximation.[15,27] The dipole moment, absorption and scattering cross sections of an ellipsoidal object can be expressed as follows

$$\alpha_j = 4\pi abc \frac{\varepsilon_s - \varepsilon_m}{3\varepsilon_m + 3L_j(\varepsilon_s - \varepsilon_m)}, (j = \mathrm{x,y,z}) \tag{2.79}$$

$$C_{abs,j} = k\,\mathrm{Im}(\alpha_j) \tag{2.80}$$

$$C_{sca,j}(\omega) = \frac{k^4}{6\pi}|\alpha_j|^2 \tag{2.81}$$

a, *b*, and *c* are the three semiaxes of the ellipsoid. We assume that $a \geq b \geq c$. The parameter *j* stands for the different axes, the parameter L_j is the depolarization factor, which can be calculated *via*,

$$L_j = \frac{abc}{2}\int_0^\infty \frac{dq}{\left(a_j^2+q\right)\left\{\left(q+a^2\right)\left(q+b^2\right)\left(q+c^2\right)\right\}^{1/2}}, \left(j = \mathrm{x,y,z}; a_j = a,b,c\right) \tag{2.82}$$

For spheroids, a special class of ellipsoids that have two axes of an equal length, L_j can be written in the following analytical expressions:

For prolate spheroid (cigar-shaped, a > b = c):

$$L_\mathrm{x} = \frac{1-e^2}{e^2}\left(-1+\frac{1}{2e}\ln\frac{1+e}{1-e}\right) \tag{2.83}$$

$$L_\mathrm{y} = L_\mathrm{z} = \left(1-L_\mathrm{x}\right)/2 \tag{2.84}$$

$$e^2 = 1-\frac{b^2}{a^2} \tag{2.85}$$

For oblate spheroid (pancake-shaped, a = b > c):

$$L_\mathrm{x} = L_\mathrm{y} = \frac{g(e)}{2e^2}\left[\frac{\pi}{2}-\tan^{-1}g(e)\right]-\frac{g^2(e)}{2} \tag{2.86}$$

$$L_\mathrm{z} = 1-2L_\mathrm{x} \tag{2.87}$$

$$g(e) = \left(\frac{1-e^2}{e^2}\right)^{1/2} \tag{2.88}$$

$$e^2 = 1-\frac{c^2}{a^2} \tag{2.89}$$

We always have

$$L_\mathrm{x} + L_\mathrm{y} + L_\mathrm{z} = 1 \tag{2.90}$$

The extinction cross sections can be calculated by summing up the absorption and the scattering cross sections:

$$C_{\mathrm{ext},\,j} = C_{\mathrm{abs},\,j} + C_{\mathrm{sca},\,j} \tag{2.91}$$

Spherical particles are a special case for ellipsoidal particles, where L_x = L_y = L_z =1/3. Equations (2.79)–(2.81) and (2.91) have been widely used in the calculations of the plasmonic properties of Au and Ag nanorods and nanodisks., which can be treated as prolate and oblate spheroids,

respectively.

According to equation (2.79), we can plot the absolute value and phase of α against ω. The polarizability α experiences a resonant enhancement under the condition that $\left|\varepsilon_{\mathrm{m}}+L_j\left(\varepsilon_{\mathrm{s}}-\varepsilon_{\mathrm{m}}\right)\right|$ is a minimum, which for the case of small or slowly varying Im[ε_{s}] (the imaginary part of ε_{s}) around the resonance simplifies to

$$\mathrm{Re}\left[\varepsilon_{\mathrm{s}}(\omega)\right]=-\frac{1-L_j}{L_j}\varepsilon_m \tag{2.92}$$

This relationship is called the Fröhlich condition and the associated mode (in an oscillating field) is called the dipolar surface plasmon of a metal nanoparticle. For spherical particles, the Fröhlich condition turns out to be:

$$\mathrm{Re}\left[\varepsilon_{\mathrm{s}}(\omega)\right]=-2\varepsilon_m \tag{2.93}$$

In conclusion, the optical response of a small metallic nanoparticle (sphere or ellipsoid) can be described by its polarizability α under quasi-static approximation:

$$\alpha=(1+\kappa)\varepsilon_0 V\frac{\left(\varepsilon_{\mathrm{s}}-\varepsilon_{\mathrm{m}}\right)}{\left(\varepsilon_{\mathrm{s}}+\kappa\varepsilon_{\mathrm{m}}\right)} \tag{2.94}$$

where V is the volume of the particle and κ is a shape factor that incorporates the dependence of the polarizability on the geometry. The localized surface plasmon resonance occurs when α becomes maximal at the frequency ω_{sp}, at which:

$$\mathrm{Re}\left(\varepsilon_{\mathrm{s}}\left(\omega_{\mathrm{sp}}\right)\right)=-\kappa\varepsilon_{\mathrm{m}} \tag{2.95}$$

When the dielectric function is expressed by the Drude model (equation (2.45)), the resonance frequency can then be calculated:

$$\omega_{\mathrm{sp}}=\sqrt{\frac{{\omega_{\mathrm{p}}}^2}{\varepsilon_\infty+\kappa\varepsilon_{\mathrm{m}}}+\gamma^2} \tag{2.96}$$

since $\gamma<<\omega_{\mathrm{sp}}$,

$$\omega_{sp} \approx \sqrt{\frac{\omega_p^2}{\varepsilon_\infty + \kappa\varepsilon_m}} \tag{2.97}$$

From equation (2.95), we can see that the real part of the metal dielectric function governs the frequency position of the electron oscillation resonance. The imaginary part determines the broadening and absorptive dissipation of the resonance due to the damping and dephasing of the electron oscillations[28].

The above solution for spheroids is usually called *Gans theory* since Richard Gans first published the solution for gold particles in 1912.[27] Nanorods, though having a cylindrical shape, are often treated as prolate spheroids. Thus the optical responses of gold nanorods in our experiments can be evaluated by analytical expressions. Most metal nanocrystals we encountered during experiments have dimensions below 100 nm and are much smaller than the light wavelength. Quasi-static approximation therefore can give satisfactory results for these nanocrystals illuminated with visible/near-infrared radiations.[6] For larger particles, quasi-static approximation is not valid since the phase change of the driving field over the particle volume cannot be neglected. As a result, Maxwell's equations should be solved rigorously.

2.5 Theoretical Treatments for Plasmon Coupling

When two metal nanocrystals are placed in a close proximity to, but not in contact with each other, the plasmon resonances carried by the two nanocrystals will interact to form different collective plasmon modes.[29–33] The optical responses of coupled nanostructures are strongly affected by the interparticle interactions and usually large electric field enhancements can occur [28,34]. As a simple prototypical model system for the study of localized surface plasmon coupling, nanoparticle dimers are often studied. In this section, I will discuss the usually employed theoretical approaches for treating plasmon coupling between two metal nanocrystals. First I will briefly introduce an analytical model, the hybridization model, which works under quasi-static approximation. Then I will present some simplified models that I will employ in this

thesis. In the end, I will talk about a coupled dipole model for collective plasmons in periodic plasmonic arrays.

2.5.1 Hybridization Model

The interaction between plasmons supported by particles of arbitrary shapes cannot be easily solved. For small particles separated far enough, their interactions are essentially of a dipolar nature. In a first approximation, such particle ensembles can be treated as an ensemble of interacting dipoles. However, when the interparticle gap distance is small compared with the particle size, the dipolar approximation breaks down.[35] Peter Nordlander *et al.* have developed a plasmon hybridization method to solve the plasmon coupling problem for complex plasmonic structures since 2003.[29,31,36–38] It is an analytical theoretical method that can provide an intuitive physical picture of coupled plasmons in complex nanostructures, such as metal nanocrystal oligomers. In the hybridization model, the plasmon modes of a complex nanostructure can be written in terms of the interactions between the plasmons of each elementary metal component. The formation of the hybridization plasmon modes in a coupled plasmonic structure is in rigorous analogy with the molecular orbital generation in the molecular orbital theory. The latter has been thoroughly studied quantum mechanically from the hybridization of individual atomic wave functions.

In the plasmon hybridization model, the oscillation of electrons can be solved by assuming the electron gas as an incompressible, irrotational fluid of uniform electron density n_0. The 'fluid' is confined to a uniform positive background having a dielectric permittivity ε_∞. The electron fluid deformations can be described by its velocity field $\mathbf{v}(\mathbf{r})$ representing the velocity $\mathbf{v}$ of a volume element at position $\mathbf{r}$. Incompressible deformation fields can be expressed as the gradients of scalar potentials that satisfy Laplace equation, since the deformation fields are passive (incompressible). Given the geometry of the system, one can trivially find a complete set of such scalar potentials, denoted as $\phi_\mu(\mathbf{r})$, where μ is an index that labels individual basis

functions. For example, μ would be equal to the multipolar indices (l, m) for a sphere and parallel wave vector for a planar surface. If $|i\mu>$ is referred to as a primitive plasmon mode on nanoparticle i with an associated velocity field $\mathbf{v}_{i\mu}(\mathbf{r})$

$$\mathbf{v}_{i\mu}(\mathbf{r}) = \nabla\phi_{i\mu}(\mathbf{r}) \tag{2.98}$$

an arbitrary deformation of the incompressible electron fluid can as a result be written as

$$\mathbf{v}(\mathbf{r}) = \sum_{i\mu}\frac{d}{dt}A_{i\mu}(t)\nabla\phi_{i\mu}(\mathbf{r}) \tag{2.99}$$

$A_{i\mu}(t)$ describes the spatial displacement of the primitive plasmon $|i\mu>$. Since the electron liquid is incompressible, the deformations only result in surface charges. The surface charges induced by primitive plasmon mode $|i\mu>$ can be determined from the continuity equation:

$$\sigma_{i\mu}(\mathbf{s},t) = -n_0 e A_{i\mu}\nabla\phi_{i\mu}(\mathbf{s})\cdot\mathbf{e}_s \tag{2.100}$$

s is a point on the metal surface and $\mathbf{e}_s$ is its normal unit vector pointing to the outward of the metal surface. In the presence of metallic background polarizabilities and any other background dielectrics (e.g. embedding media, dielectric particles/layers), the primitive plasmon mode $|i\mu>$ will induce extra screening charges on the metal structure surface. The screened surface charge has a distribution $\tau_{i\mu}(\mathbf{r})$.

In a complex geometry like nanoparticle oligomers or a nanoparticle with disconnected surfaces, the primitive plasmon modes interact with each other through the Coulomb potential. They are no longer the eigenmodes of the system. All interactions are assumed to be linear. To obtain the normal modes, one further assumes that all modes have harmonic motions and looks for self-sustained solutions, which are finite amplitude modes that exist without external applied fields. The kinetic and potential energies of the primitive plasmons $|i\mu>$ can be calculated from their velocity fields $\mathbf{v}_{i\mu}(\mathbf{r})$ and screened charge distributions $\tau_{i\mu}(\mathbf{r})$. The potential energy of the coupled system will contain nondiagonal elements due to the coupling of different $|i\mu>$ brought by Coulomb interactions. By constructing and diagonalizing the Lagrangian for the coupled system, one can determine the new eigenmodes, which are superpositions of the individual $|i\mu>$.

When external electric fields are applied, the equation of motion for the system can be written, from which the optical absorption of the complex coupled nanostructure can be directly calculated.

This hybridization method provides a simple and conceptually straightforward understanding of how the plasmon resonances in a multi-component structure arise from the plasmon modes of their individual components. This approach has now been successfully utilized for the analysis of plasmonic systems with specific geometries, such as metal nanosphere dimers,[31,39] nanoshells and their dimers,[29,40] nanospheroid dimers,[37] substrate-coupled nanospheres,[36] and nanostars.[41]

2.5.2 Simplified Models for Coupled Plasmonic Nanocrystal Dimers

The aforementioned intuitive hybridization model can analytically solve the plasmon coupling problem. However, its calculation is quite difficult for nanostructures that do not have specific geometries. Fortunately, some very simple models can also give good qualitative, even semi-quantitative descriptions for the plasmon coupling between metal nanoparticles.

The first simple model is the coupled dipole model, in which each nanoparticle is treated as a dipole under quasi-static approximation.[32,42] For a nanoparticle dimer, the simplified model can be seen in Figure 2.1. Under an externally applied electric field $\mathbf{E}_0$, the electric dipole moment of each nanoparticle is given by

$$\mathbf{p}_i = \varepsilon_0 \varepsilon_m \boldsymbol{\alpha}_i \cdot \mathbf{E}_i \tag{2.101}$$

In equation (2.101), $\boldsymbol{\alpha}_i$ is the polarizability matrix of the nanoparticle *i*, which can be expressed analytically for nanoparticles having some specific geometries, as we have introduced in section 2.4. $\mathbf{E}_i$ is the total electric field applied on the nanoparticle *i*. It is a sum of $\mathbf{E}_0$ and the field contributed from the electric dipole of the other nanoparticle. It can be expressed by

$$\mathbf{E}_i = \mathbf{E}_0 + \gamma \frac{3(\mathbf{p}_j \cdot \mathbf{e}_{ji})\mathbf{e}_{ji} - \mathbf{p}_j}{4\pi\varepsilon_0\varepsilon_m d^3}, \quad j \neq i \tag{2.102}$$

where d is the center-to-center distance between the two nanoparticles, $\mathbf{e}_{ji}$ is the unit vector pointing from the center of the nanoparticle j to the center of the nanoparticle i, and γ is a coefficient introduced to modify the dipole–dipole interaction. The introduction of the modifying coefficient is to account for the substrate effect, multipolar contribution, finite-size effect, and charge redistribution. The latter three factors usually become considerable as the spacing between metal nanocrystals is very small.[32,35,43] The dipole moment of each nanoparticle can thereafter be calculated by solving equations (2.101) and (2.102). Summing up the dipole moment components of the two nanoparticles yields the dipole moment of the entire dimer system. We can then therefore obtain the absorption and scattering responses of the coupled plasmonic system from the total dipole moment.

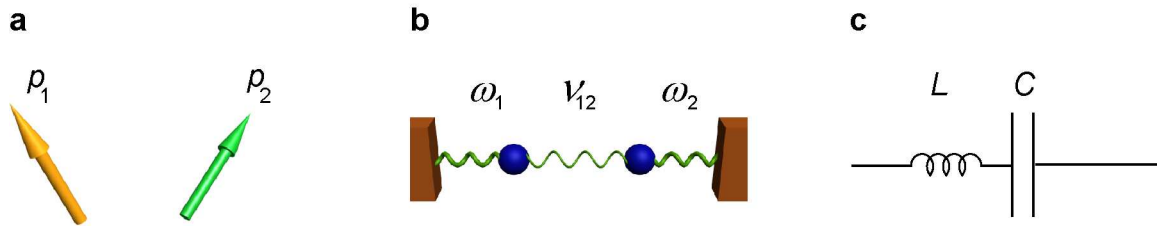

Figure 2.1 Schematic showing the coupled dipole model (a), the coupled harmonic oscillator model (b), and the resonant-circuit model for the description of plasmon coupling between metal nanoparticles.

The second simple model is the coupled harmonic oscillator model (Figure 2.1b). This model can be used to understand the coupled plasmon modes in Au nanoparticle dimers,[44,45] electromagnetically induced transparency,[46] and Fano resonance in Au nanoparticle–silica layer–Au layer core–shell–shell nanostructures.[47] In the coupled harmonic oscillator model, the plasmon coupling in nanoparticle dimers is modeled as the interaction between two oscillators. The primitive plasmon modes of the two nanoparticles before coupling are treated as two mechanical oscillators with frequencies ω_1 and ω_2, respectively. The two oscillators interact through one spring with an interacting strength v_{12} (or a coupling constant α_0). When the coupled plasmonic system is driven by an external electromagnetic field **E**, we can accordingly describe the driven stimuli with a periodic harmonic force $F(t) = Fe^{i\omega t}$ in the interacting mechanical

oscillator model. Assume that the oscillator with energy of ω_1 is driven by $F(t)$, the equations of motion of the two oscillators are

$$\ddot{x}_1 + \gamma_1 \dot{x}_1 + \omega_1^2 x_1 + \nu_{12} x_2 = F e^{i\omega t} \tag{2.103}$$

$$\ddot{x}_2 + \gamma_2 \dot{x}_2 + \omega_2^2 x_2 + \nu_{12} x_1 = 0 \tag{2.104}$$

where x_i specifies the displacement from the respective equilibrium position of the oscillators and γ_i represents the friction coefficient accounting for the energy dissipation of each oscillator. The equations can be solved in the form $x_i = c_i e^{i\omega t}$ and the scattering power of the system is expressed by $P(\omega) = |\ddot{x}_1 + \ddot{x}_2|^2$. As a result, the scattering spectra of the coupled plasmonic system can be calculated from the interacting oscillator model. The resonance energies of the coupled plasmonic system can thereafter be determined from the scattering spectrum. We can also obtain the resonance energies more easily by describing the coupled-oscillator system using the Lagrangian L. In the absence of dissipation,

$$L = T - V = \frac{1}{2}\dot{x}_1^2 + \frac{1}{2}\dot{x}_2^2 - \frac{1}{2}\omega_1^2 x_1^2 - \frac{1}{2}\omega_2^2 x_2^2 + \alpha_0 x_1 x_2 \tag{2.105}$$

where T and V denote the kinetic and potential energies. The dots represent the time derivatives of the displacements. The Lagrangian equations of motion are given as [48]:

$$\frac{d}{dt}\left(\frac{\partial L}{\partial \dot{x}_i}\right) - \frac{\partial L}{\partial x_i} = 0 \tag{2.106}$$

The solutions of equation (2.106) are in the form of linear combinations of harmonics $e^{i\Omega t}$, where the eigenoscillation frequencies Ω are given by the determination equation:

$$\det\begin{bmatrix} \omega_1^2 - \Omega^2 & -\alpha_0 \\ -\alpha_0 & \omega_2^2 - \Omega^2 \end{bmatrix} = 0 \tag{2.107}$$

The determination equation has two solutions

$$\Omega^2 = \frac{(\omega_1 + \omega_2)^2}{4}\left[1 + \left(\frac{\omega_1 - \omega_2}{\omega_1 + \omega_2}\right)^2 \pm 2\sqrt{\left(\frac{\omega_1 - \omega_2}{\omega_1 + \omega_2}\right)^2 + \frac{4\alpha_0^2}{(\omega_1 + \omega_2)^4}}\right] \tag{2.108}$$

These two solutions indicate the energies of the coupled plasmon modes. The coupling constant

α_0 (or ν_{12}) usually cannot be known in advance and should be determined from fitting.

The third simple model is the resonant-circuit model (Figure 2.1c). In this model, a simplest *L*–*C* circuit consisting of one inductor and one capacitor is used to model the coupled nanoparticle pairs. The dielectric gap with a separation of *d* between the two metal nanoparticles has a capacitance of *C*. The inductance of the entire structure is assumed to be *L*. *C* and *L* are both functions of the gap distance (*d*), the dielectric functions of the medium (ε_m) and the metal (ε_s). As a result they are both frequency-dependent:

$$C(\lambda) = C(d, \varepsilon_m, \varepsilon_s(\lambda)) \tag{2.109}$$

$$L(\lambda) = L(d, \varepsilon_m, \varepsilon_s(\lambda)) \tag{2.110}$$

The function forms are dependent on the geometry. The resonance wavelength, denoted as λ_r, in the resonant circuit model can be expressed as,

$$\lambda_r = 2\pi c\sqrt{L(\lambda_r)C(\lambda_r)} \tag{2.111}$$

where *c* is the vacuum speed of light. By solving equations (2.109)–(2.111), we can deduce that at the resonance wavelengths of the coupled structure, the following equation yields:

$$\varepsilon_s(\lambda) = F(\lambda) \tag{2.112}$$

F(λ) can be determined from equation (2.111). As a result, by plotting the curves of $\varepsilon_s(\lambda)$ and $F(\lambda)$ *versus* λ in the same graph, we can easily locate the resonance wavelengths of coupled plasmonic structures.

2.5.3 Coupled Dipole Model for Collective Plasmons of Periodic Plasmonic Arrays

The collective plasmons of periodic arrays can be described using the coupled dipole model as[49]

$$\alpha^* = \frac{1}{1/\alpha - S} \tag{2.113}$$

where α^* and α are the polarizabilities of the collective plasmon and each nanoparticle, respectively. *S* is expressed as

$$S = \sum_{n \neq m} \left[\frac{(1 - ikr_{mn})(3\cos^2 \theta_{mn} - 1) e^{ikr_{mn}}}{r_{mn}^3} + \frac{k^2 \sin^2 \theta_{mn} e^{ikr_{mn}}}{r_{mn}} \right] \quad (2.114)$$

where $\mathbf{r}_{mn}$ (r_{mn}= $|\mathbf{r}_{mn}|$) is the vector from the mth to nth particle, θ_{mn} is the angle between $\mathbf{r}_{mn}$ and the polarization of the incident light. k is the wave vector. The coupled dipole model is suitable for arrays composed of highly symmetric building units under normal incidence. For units with complex shapes and multiple nanoparticles, there are no analytical expressions for their polarizabilities. In addition, the model fails when the nanoparticle size approaches the light wavelength, where multipoles have to be taken into account. In these cases, numerical techniques are required to acquire the plasmonic responses of particle arrays.

2.6 Numerical Methods for Simulating the Plasmon Resonance Properties of Metal Nanostructures

Mie theory and its extension can give analytical solutions for spheres, spheroids, core–shell spherical particles, and infinite cylinders. Maxwell's equations for metal nanostructures with arbitrary shapes cannot be solved. Since metal nanoparticles are often assembled together for building plasmonic devices, accurate description of their plasmonic properties is very important for their applications. Although the exact Mie theory can be extended to multiple spheres, it cannot help for nanostructures of other geometries. The analytical hybridization model can give quantitative description of coupled plasmonic nanostructures but is limited to specific structure geometries and usually requires quasi-static approximation. The simplified models mentioned above can give us simple physical pictures for understanding the complicated plasmon coupling in real plasmonic structures. But they cannot provide quantitative descriptions. As a result, other than analytical approaches, numerical methods are required, since the latter can provide powerful tools for calculating the optical response of objects with arbitrary shapes and the coupled plasmonic features in complicated metal nanostructures.

Two main types of numerical methods are usually empolyed for electrodynamic

calculations. One is carried out in the frequency domain. Discrete dipole approximation (DDA) and the coupled dipole method (CDM) are two typical examples of this type [50,51] In these methods, an arbitrarily shaped particle is treated as a three-dimensional assembly of dipoles on a cubic grid located at positions $\mathbf{r}_j$ (j = 1, … , M). Each dipole cell is assigned a complex polarizability α. α can be computed from the complex dielectric function of the bulk material and the number of dipoles in a unit volume. The electromagnetic scattering problem is then solved on the basis of this array of the point dipoles. Each dipole has a polarization $\mathbf{P}_j=\alpha_j\mathbf{E}_j$, where $\mathbf{E}_j$ is the total electric field at $\mathbf{r}_j$. It consists of the incident wave plus the contribution of the other M–1 dipoles, which means that it is a function of $\mathbf{P}_l$ ($l \neq j$). We then therefore construct M linear vector equations with M unknown vectors $\{\mathbf{P}_j\}$. By solving the M linear equations, all the M polarizations can be obtained and the scattering, absorption, and extinction cross sections of the object can be evaluated accordingly. The basic idea of discrete dipole approximation was introduced by DeVoe in 1964.[52] The retardation effect caused by the phase difference at different points is naturally included in the above analysis of the electric field at $\mathbf{r}_j$ contributed by other dipoles. The open source codes are available for this calculation. However, the major drawback of this method is that it rely on linear algebra. Redundant calculations have to be performed to find the inverse of the $M \times M$ matrix. The computational complexity becomes more pronounced when one tries to improve the accuracy of the calculations by increasing the numbers of the dipoles employed to approximate continuum target objects. Typically, there are 10^6 electromagnetic unknowns.[13] Other frequency domain methods include the T-matrix method,[53] finite element method (FEM),[54] and boundary element method (BEM).[55,56] Interested readers may refer to some excellent reviews[57,58] to find more details about these methods.

The other type of numerical methods is performed in both the time and frequency domains. The finite-difference time-domain (FDTD) method is the most widely used one of this type.[13,59,60] FDTD was first developed by Yee in 1966.[61] It is an explicit time marching

algorithm used to solve Maxwell's curl equations on a discretized spatial grid. The FDTD method is so powerful that it can be used for studying both the near- and far-field electromagnetic responses of heterogeneous materials of arbitrary geometries. The approach has successfully been applied to many nanosystems in the past.[13,16,62–65]

When Maxwell's differential equations are examined, it can be seen that the change in the **E**-field in time depends on the change in the **H**-field across space. This results in the basic FDTD time-stepping relation that, at any point in space, the updated value of the **E**-field in time is dependent on the stored value of the **E**-field and the numerical curl of the local distribution of the **H**-field in space. Similarly, at any point in space, the updated value of the **H**-field in time depends on the stored value of the **H**-field and the numerical curl of the local distribution of the **E**-field in space. Iterating the updates of both **E** and **H** results in a marching-in-time process wherein sampled-data analogs of the continuous electromagnetic waves under consideration propagate in a numerical grid stored in the computer memory.

The key point in the FDTD method is to replace all the derivatives in Maxwell's equations with finite discrete grids. The Yee cell is the basic element of an interlocked Cartesian computational grid. In a rectangular unit of the Yee lattice, each **E**-field vector component is located midway between a pair of **H**-field vector components, and conversely. Figure 2.2 shows a typical Yee cell, with (*i*, *j*, *k*) representing a specific grid point in the space. Therefore each **E** and **H** are offset in both the space and time, allowing one to use the central differences and making the algorithm second-order accurate. For example, the one-dimensional discrete form of Maxwell's equations can be expressed as,

$$\varepsilon(k)E_x^{n+1}(k) = \varepsilon(k)E_x^{n}(k) - \frac{\Delta t}{\Delta z}\left[H_y^{n+1/2}\left(k+\frac{1}{2}\right) - H_y^{n+1/2}\left(k-\frac{1}{2}\right)\right] \tag{2.115}$$

$$\mu\left(k+\frac{1}{2}\right)H_y^{n+1}\left(k+\frac{1}{2}\right) = \mu\left(k+\frac{1}{2}\right)H_y^{n-1/2}\left(k+\frac{1}{2}\right) - \frac{\Delta t}{\Delta z}\left[E_x^{n}(k+1) - E_x^{n}(k)\right] \tag{2.116}$$

where *k* is the spatial coordinate and the superscript *n* denotes time. From equations (2.115) and (2.116), it is straightforward to obtain **E** and **H** iteratively. The **E**-field and **H**-field updates are

staggered so that **E**-field updates are conducted midway during each time step between successive **H**-field updates, and conversely. We can therefore acquire the **E** and **H** distributions in the simulation region at any time step. The solutions to Maxwell's equations are then obtained. The frequency-related properties such as the scattering, absorption, and extinction spectra can be further calculated through Fourier transformation.[59,60,66] The Yee lattice has proven to be very robust and remains at the core of many current FDTD software constructs. The explicit time-stepping scheme avoids the need to solve simultaneous equations. Usually many thousands of time steps are required to complete a simulation.

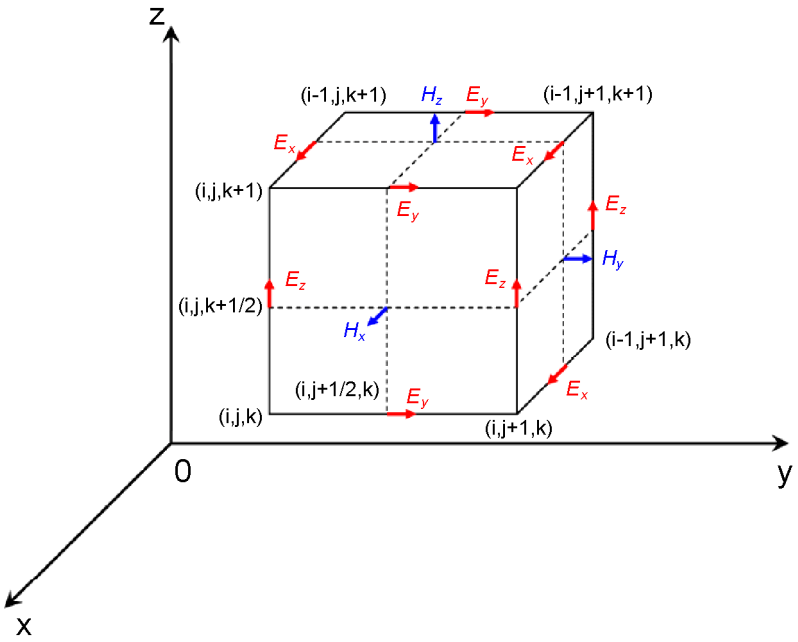

Figure 2.2 Schematic showing a standard Cartesian Yee cell used for FDTD. The distribution of electric and magnetic field vector components can be easily observed.

In practical calculations, the simulation region is limited. A perfectly matched layer (PML) technique is usually employed to model the propagation of electromagnetic waves in infinite space. Numerically, the PML technique is to place a boundary around the simulated object. This boundary can totally absorb the electromagnetic energy.

FDTD techniques have emerged as a primary means for computationally modeling many scientific and engineering problems that deal with the interaction between electromagnetic waves

and material structures. It is preferred for the investigation of the temporal response of an object and also powerful in the simulations of complicated structures. The accuracy of FDTD calculations is determined by the size of the grid and the time step. The use of a smaller grid size and time step can improve the calculation, but will consume much more calculation time and memories. However, compared with other numerical techniques, FDTD has at least the following three advantages: (1) We do not need to derive a geometry-specific equation for every new system we want to investigate. Modeling them is reduced to grid generation. Previously uninvestigated and potentially complex geometries do not require new formalisms. (2) The time marching aspect of FDTD allows one to make direct observations of both near- and far-field values of the electromagnetic fields and at any time during the simulation. The ability to visualize the time evolution of electromagnetic fields provides new insight into the dynamics of the system under study. (3) Although usually up to 10^9 electromagnetic unknowns are involved in the calculations,[13] the method is easily parallelizable due to the local nature of finite differences. Calculations of large and complex objects can be achieved by employing powerful clusters containing many different computers in a reasonable time.

Several excellent commercial packages can be found for FDTD technique-based numerical calculations of electrodynamic processes.[67−70] Convenient use of such well-developed softwares has not only greatly facilitated us to further our understanding on the plasmonic features of noble metal nanostructures, but also significantly promoted the design of novel photonic and plasmonic devices. In my thesis research, I adopted Lumerical Solutions software FDTD Solutions 8.5 to perform all electrodynamic simulations, to help in understanding the novel physical phenomena in coupled plasmonic structures.

References

[1] Jacob, Z.; Shalaev, V. M. *Science*, **2011**, *334*, 463.

[2] García de Abajo, F. J. *Nature* **2012**, *483*, 417.

[3] Scholl, J. A.; Koh, A. L.; Dionne, J. A. *Nature* **2012**, *483*, 421.

[4] Esteban, R.; Borisov, A. G.; Nordlander, P.; Aizpurua, J. *Nat. Commun.* **2012**, *3*, 825.

[5] Savage, K. J.; Hawkeye, M. M.; Esteban, R.; Borisov, A. G.; Aizpurua, J.; Baumberg, J. J. *Nature* **2012**, *491*, 574.

[6] Maier, S. A. *Plasmonics: Fundamentals and Applications.* Springer Science+Business Media LLC, 2007.

[7] Jackson, J. D. *Classical Electrodynamics.* John Wiley & Sons, Inc., 1962.

[8] Drude, P. *Ann. der Physik* **1900**, *306*, 566.

[9] Kittel, C. *Introduction to Solid State Physics*. 8th ed. John Wiley & Sons, Inc, c2005.

[10] Kreibig, U.; Vollmer, M. *Optical Properties of Metal Clusters*. Springer–Verlag: Berlin, 1995.

[11] Ashcroft, N. W.; Mermin, N. D. *Solid State Physics*. New York: Holt, Rinehart and Winston, 1976.

[12] Johnson, P. B.; Christy, R. W. *Phys. Rev. B.* **2012**, *483*, 421.

[13] Oubre, C.; Nordlander, P. *J. Phys. Chem. B* **2004**, *108*, 17740.

[14] Chen, H. J. *Localized Surface Plasmon Resonances of Gold Nanocrystals: Refractive Index Sensitivity, Plasmon Coupling, and Photothermal Conversion.* Ph.D Thesis, Department of Physics, The Chinese University of Hong Kong. 2010.

[15] Bohren, C.; Huffman, D. *Absorption and Scattering of Light by Small Particles*. Johy Wiley & Sons, Inc, 1983.

[16] Hao, F.; Nordlander, P. *Chem. Phys. Lett.* **2007**, *446*, 115.

[17] Moskovits, M.; Srnová-Šloufová, I.; Vlčková, B. *J. Chem. Phys.* **2002**, *116*, 10435.

[18] Vial. A.; Grimault, A.-S.; Macías, D.; Barchiesi, D.; de la Chapelle, M. L. *Phys. Rev. B* **2005**, *71*, 085416.

[19] Laroche, T.; Girard, C. *Appl. Phys. Lett.* **2006**, *89*, 233119.

[20] Link, S.; El-Sayed, M. A. *J. Phys. Chem. B* **1999**, *103*, 4212.

[21] Heinrich, B.; Tserkovnyak, Y.; Woltersdorf, G.; Brataas, A.; Urban, R.; Bauer, G. E. W. *Phys. Rev. Lett.* **2003**, *90*, 187601.

[22] Kreibig, U. *J. Phys. F: Metal Phys.* **1974**, *4*, 999.

[23] Link, S.; El-Sayed, M. A. *Int. Rev. Phys. Chem.* **2000**, *19*, 409.

[24] Mie. G. *Ann. Phys.* **1908**, *25*, 377.

[25] Courant, R.; Hilbert, D. *Methods of Mathematical Physics.* Julius Springer, Berlin, 1937.

[26] Hergert, W.; Wriedt, T. *The Mie Theory*. Springer-Verlag Berlin Heidelberg, 2012.

[27] Gans, R. *Ann. der Physik* **1912**, *342*, 881.

[28] Jain, P. K.; El-Sayed, M. A. *Chem. Rev. Lett.* **2010**, *487*, 153.

[29] Prodan, E.; Radloff, C.; Halas, N. J.; Nordlander, P. *Science* **2003**, *302*, 419.

[30] Gluodenis, M.; Foss, Jr. C. A. *J. Phys. Chem. B* **2002**, *106*, 9484.

[31] Nordlander, P.; Oubre, C.; Prodan, E.; Li, K.; Stockman, M. I. *Nano Lett.* **2004**, *4*, 899.

[32] Shao, L.; Woo, K. C.; Chen, H. J.; Jin, Z.; Wang, J. F.; Lin, H.-Q. *ACS Nano* **2010**, *4*, 3053.

[33] Halas, N. J.; Lal, S.; Chang, W.-S.; Link, S.; Nordlander, P. *Chem. Rev.* **2011**, *111*, 3913.

[34] Ghosh, S. K.; Pal, T. *Chem. Rev.* **2007**, *107*, 4797.

[35] Gunnarsson, L.; Rindzevicius, T.; Prikulis, J.; Kasemo, B.; Käll, M.; Zou, S. L.; Schatz, G. C. *J. Phys. Chem. B* **2005**, *109*, 1079.

[36] Nordlander P.; Prodan, E. *Nano Lett.* **2004**, *4*, 2209.

[37] Willingham, B.; Brandl, D. W.; Nordlander, P. *Appl. Phys. B* **2008**, *93*, 209.

[38] Bao, K. *Plasmon Hybridization in Real Metals.* Ph.D Thesis, Department of Physics and Astronomy, Rice University. 2012.

[39] Brown, L. V.; Sobhani, H.; Lassiter, J. B.; Nordlander, P.; Halas, N. J. Heterodimers: *ACS Nano* **2010**, *4*, 819.

[40] Lassiter, J. B.; Aizpurua, J.; Hernandez, L. I.; Brandl, D. W.; Romero, I.; Lal, S.; Hafner, J.

H.; Nordlander, P.; Halas, N. J. *Nano Lett.* **2008**, *8*, 1212.

[41] Hao, F.; Nehl, C. L.; Hafner, J. H.; Nordlander, P. *Nano Lett.* **2007**, *7*, 729.

[42] Shegai, T.; Chen, S.; Miljković, V. D.; Zengin, G.; Johansson, P.; Käll, M. *Nat. Commun.* **2011**, *2*, 481.

[43] Tabor, C.; van Haute, D.; El-Sayed M. A. *ACS Nano* **2009**, *3*, 3670.

[44] Woo, K. C.; Shao, L.; Chen, H. J.; Liang, Y.; Wang, J. F.; Lin, H.-Q. *ACS Nano* **2011**, *5*, 5976.

[45] Shao, L.; Fang, C. H.; Chen, H. J.; Man, Y. C.; Wang, J. F.; Lin, H.-Q. *Nano Lett.* **2012**, *12*, 1424.

[46] Garrido Alzar, C. L.; Martinez, M. A. G.; Nussenzveig, P.; *Am. J. Phys.* **2002**, *70*, 37.

[47] Mukherjee, S.; Sobhani, H.; Lassiter, J. B.; Bardhan, R.; Nordlander, P.; Halas, N. J. *Nano Lett.* **2010**, *10*, 2694.

[48] Goldstein, H. *Classical Mechanics*. Addision Wesley, Reading MA, 1950.

[49] Zhao, L. L.; Kelly, K. L.; Schatz, G. C. *J. Phys. Chem. B* **2003**, *107*, 7343.

[50] Draine, B. T.; Flatau, P. J. *J. Opt. Soc. Am. A* **1994**, *11*, 1491.

[51] Markel, V. A. *J. Mod. Opt.* **1993**, *40*, 2281.

[52] DeVoe, H. *J. Chem. Phys*. **1964**, *41*, 393.

[53] Waterman, P. C. *Proc. IEEE* **1965**, *53*, 803.

[54] Gilbert, S.; George, F. *An Analysis of The Finite Element Method*. Prentice Hall, 1973.

[55] García de Abajo, F. J.; Howie, A. *Phys. Rev. Lett.* **1998**, *80*, 5180.

[56] García de Abajo, F. J.; Howie, A. *Phys. Rev. B* **2002**, *65*, 115418.

[57] Wriedt, T. *Part. Part. Syst. Charact.* **1998**, *15*, 67.

[58] Yurkin, M. A.; Hoekstra, A. G. *J. Quant. Spectrosc. Radiat. Transfer* **2007**, *106*, 558.

[59] Taflove, A. *Computational Electrodynamics: the Finite-Difference Time-domain Method*. Artech House Boston, 1995.

[60] Sulivan, D. M. *Electromagnetic Simulation Using the FDTD Method*. IEEE Press, Piscataway, NJ, 2000.

[61] Yee, K. *IEEE Trans. Antennas Propag.* **1966**, *AP-14*, 302.

[62] Chen, H. J.; Sun, Z. H.; Ni, W. H.; Woo, K. C.; Lin, H.-Q.; Sun, L. D.; Wang, J. F.; Yan, C. H. *Small*, **2009**, *5*, 2111.

[63] Ni, W. H.; Kou, X. S.; Yang, Z.; Wang, J. F. *ACS Nano* **2008**, *2*, 677.

[64]Liu, Y.; Cheng, H.; Liao, L.; Zhou, H. L.; Bai, J. W.; Liu, G.; Liu, L. X.; Huang, Y.; Duan, X. F. *Nat. Commun.* **2011**, *2*, 579.

[65] Falk, A. L.; Koppens, F. H. L.; Yu, C. L.; Kang, K.; de Leon Snapp, N.; Akimov, A. V.; Jo, M.-H.; Lukin, M. D.; Park, H. *Nat. Phys.* **2009**, *5*, 475.

[66] FDTD Solutions Reference Guide, Release 8.5. Lumerical Solutions, Inc, Canada, 2013.

[67] OptiFDTD Software, Optiwave, Inc., Ottawa, Canada.

[68] FDTD Solutions Software, Lumerical, Inc., Vancouver, Canada.

[69] FDTD Solutions™, Breault Research Organization, Tucson AZ, United States.

[70] EZ-FDTD+ Software, Electromagnetic Simulation Company, Four Oaks NC, United States.

Chapter 3

Preparation of Gold Nanorods and Characterization Techniques

The samples used in this thesis research include both chemically grown colloidal Au nanorod solutions and electron-beam lithographically fabricated Au nanorod structures. Au nanospheres of different sizes synthesized by wet-chemistry methods have also been employed. In this chapter, I will first present the description of the seed-mediated wet-chemistry method for growing Au nanorods as well as nanospheres (Section 3.1). Then I will introduce the electron-beam lithography technique for fabricating Au nanostructures in Section 3.2. In Section 3.3, I will briefly review the experimental methods for examining the morphology and plasmonic properties of Au nanostructures. The characterization techniques include electron microscopies, UV–visible–NIR spectrophotometry, and single-nanostructure scattering imaging and spectroscopy.

3.1 Growth of Gold Nanorods by Wet-Chemistry Methods

A detailed description of the methods for the direct growth and shape/size tuning of Au nanorods can be found in our recent review.[1] Generally, two growth approaches, bottom-up and top-down methods, are utilized to obtain Au nanorods. For bottom-up methods, Au nanocrystals are obtained by reducing aqueous Au salts with reducing agents, such as sodium borohydride, ascorbic acid, and small Au clusters, under different external stimuli. To acquire elongated Au nanorods, one has to resort to a template. The template serves to confine the growth of Au along one direction during the reduction. People have developed techniques for

growing colloidal Au nanorods in solutions in the presence of various surfactants, among which cetyltrimethylammonium bromide (CTAB) is the most common. Surfactants serve as the stabilizing agents to prevent the aggregation of the nanorods. They can also form micelles to direct the longitudinal growth of Au nanorods. These micelles are referred to as 'soft templates'. The exact roles of surfactants in the formation of Au nanorods are still unknown.

Seed-mediated growth is the most commonly employed method utilizing 'soft templates' for growing Au nanorods (Figure 3.1). It was developed independently by Murphy *et al.* and El-Sayed *et al.*[2–4] Nearly monodisperse Au nanorods with very high yields and uniformity can be obtained using the seed-mediated growth method. In a typical growth, small Au nanoparticle seeds with a size ~1.5 nm are first prepared by reducing chloroauric acid with sodium borohydride ($NaBH_4$) in an aqueous CTAB solution. A certain amount of the seed solution is then added into the growth solution, which is obtained by reducing Au(III) complex ions to Au(I) complex ions with ascorbic acid in an aqueous CTAB solution. The added seeds thereafter catalyze the further reduction of Au(I) complex ions to form Au nanorods. The yields of the nanorods from the seed-mediated growth method can be up to 99%. In addition, the size and shape of acquired Au nanorods can be tailored by carefully adjusting the growth conditions, such as the composition of the surfactant, the pH of the growth solution, the amounts of the reagents, the growth temperature, and the structure of the seeds, in the seed-mediated growth process. Au nanospheres can be obtained in a similar way.

For the growth of Au nanorods in this thesis, the seed solution was made by injecting a freshly prepared, ice-cold aqueous $NaBH_4$ solution (0.01 M, 0.6 mL) into an aqueous mixture composed of $HAuCl_4$ (0.01 M, 0.25 mL) and CTAB (0.1 M, 9.75 mL), followed by rapid inversion mixing for 2 min. The resultant seed solution was kept at room temperature for more than 2 hours before use. The growth solution was made by the sequential addition of aqueous $HAuCl_4$ (0.01 M, 2 mL), $AgNO_3$ (0.01 M, 0.4 mL), HCl (1.0 M, 0.8 mL), and ascorbic acid (0.1 M, 0.32 mL) solutions into an aqueous CTAB (0.1 M, 40 mL) solution. The resultant solution

was mixed by swirling for 30 s. The seed solution was diluted by 10 times with deionized water and 0.04–0.12 mL of the diluted seed solution was injected into the growth solution. The resultant reaction solution was gently mixed by inversion for 2 min and then left undisturbed overnight. The obtained nanorods had a longitudinal plasmon resonance wavelength (LPRW) ranging from 681 to 715 nm.[5] Figure 3.2 a and b shows the TEM image and the extinction spectrum of the Au nanorods grown from 0.1 mL diluted seed solution.

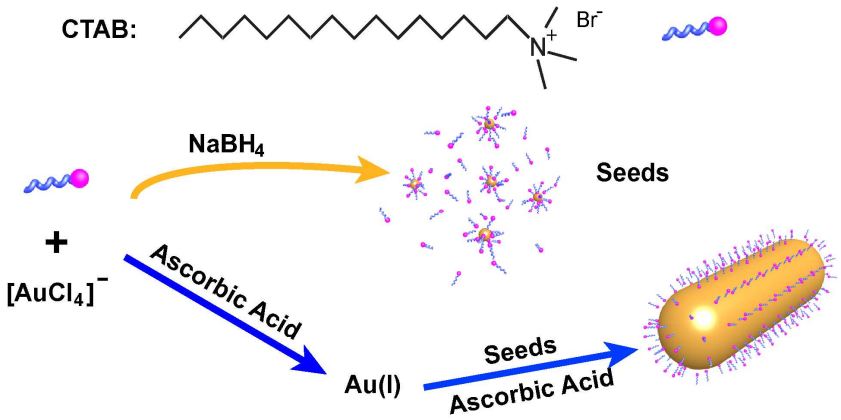

Figure 3.1 Schematic illustration of the seed-mediated method for the growth of Au nanorods.

Au nanospheres were prepared following a similar seed-mediated procedure. Specifically, the seed solution was made by injecting a freshly prepared, ice-cold $NaBH_4$ solution (0.01 M, 0.6 mL) into an aqueous mixture composed of $HAuCl_4$ (0.01 M, 0.25 mL) and CTAB (0.1 M, 9.75 mL) under stirring. Stirring was continued for 3 hours. The resultant seed solution was brown. The growth solution was made by adding aqueous $HAuCl_4$ (0.01 M, 4 mL) and deionized water (190 mL) into an aqueous CTAB (0.1 M, 9.75 mL) solution. The resultant growth solution was mixed by swirling for 30 s. Ascorbic acid (0.1 M, 15 mL) and the seed solution (0.12 mL) obtained in the first step were sequentially added into the growth solution under vigorously stirring. The resultant reaction solution was left undisturbed for 5–8 hours. The obtained nanospheres had a diameter ~24 nm and can be kept for more than 6 months. For the synthesis of larger Au nanospheres, the acquired 24-nm nanosphere solution was employed as the new seed for a second-step growth. The new growth solution was prepared by adding aqueous $HAuCl_4$

(0.01 M, 15 mL) into an aqueous cetyltrimethylammonium chloride (CTAC, 0.1 M, 300 mL) solution. Ascorbic acid (0.1 M, 7.5 mL) and the 24-nm nanosphere solution of different volumes were sequentially added into the new growth solution under vigorously stirring at 45 °C. After ~2-hour reaction under stirring, Au polyhedrons with different diameters were obtained. The size of the Au polyhedrons was determined by the 24-nm seed amount. The addition of 4 mL of the 24-nm seed solution would result in 326.5 mL of ~170-nm Au polyhedron solution. Au nanospheres with a ~160-nm diameter therefore could be obtained by adding aqueous $HAuCl_4$ (0.01 M, 2 mL) into the 170-nm Au polyhedrons solution (326.5 mL) to slightly oxidize the polyhedrons to round their edges. Figure 3.2 b and c show the extinction spectrum and the SEM image of the as-grown ~160-nm Au nanospheres.

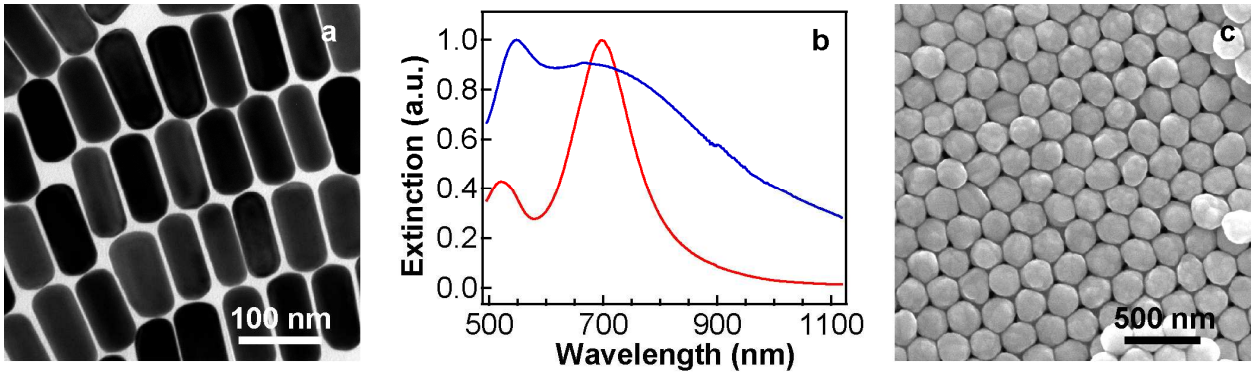

Figure 3.2 Seed-mediated growths of Au nanorods and nanospheres. a) TEM image of Au nanorods with a dimension of (111 ± 7) nm × (50 ± 4) nm. The Au nanorods were grown from 0.1-mL diluted seed solutions. b) Extinction spectra of the as-grown Au nanorods (red) and Au nanospheres (blue) shown in (a) and (c) respectively. c) SEM image of Au nanospheres with a diameter of (155 ± 9) nm.

3.2 Fabrication of Gold Nanorod Arrays by Electron-Beam Lithography

Although the bottom-up wet-chemistry methods can give monodisperse Au nanorods with high uniformity, they suffer from several disadvantages that hinder their potential device applications.[1] First, selective placement of Au nanorods at desired locations on substrates by bottom-up methods has been very difficult owing to the random nature of the reduction of Au ions and the deposition of Au atoms in reaction solutions. Second, the shape and size of Au

nanorods vary among different batches, even though the growths follow the same procedures. This variation will affect their optical and catalytic properties and applications. Third, there are extreme difficulties in placing Au nanorods into large-area, ordered arrays with bottom-up methods. Top-down approaches are therefore developed as a complementary means to the preparation of Au nanorods. Top-down methods have the merit of producing homogeneous Au nanorods with controlled particle geometries and regular inter-particle arrangements, which is valuable for quantitative characterization as well as device applications.

The electron-beam lithography (EBL) technique is one of the most popular top-down methods for the fabrication of nanostructures.[1,6] Compared with traditional optical lithographical techniques, EBL is able to create extremely fine structures. The electron beam spot size is much smaller than the diffraction limit of light and as a result a very high resolution can be achieved. Currently, the EBL technique is widely used for photo-mask production and research into quantum effects and other novel physics phenomena at very small dimensions. When fabricating Au nanostructures, EBL writing is employed to make masks (Figure 3.3). A layer of gold is then deposited on the substrate that is covered with the mask through physical methods, such as thermal, electron-beam evaporation, or sputtering. Au nanorods are obtained after the lift-off process.

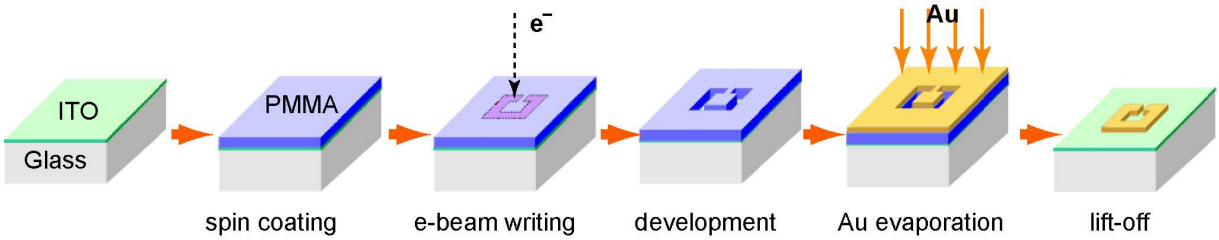

Figure 3.3 Schematic illustration of the electron-beam lithography technique for the fabrication of Au nanostructures.

As shown in Figure 3.3, in our experiments, poly(methyl methacrylate) (PMMA, 2% 950K PMMA in anisole) was first spin-coated on cleaned and prebaked (150 °C, 30 min) ITO substrates at a speed of 1600 rpm for 40 s to form a 100-nm thick resist layer. After a post bake (200 °C, 2 min), the 100-nm PMMA coated substrates were under e-beam exposure in an Elionix

ELS7800 electron-beam lithography system at a dosage of 1000 μC/cm^2 (80 kV, 100 pA). The exposed samples were developed in 1:3 (v/v) MIBK:IPA mixture solution (–18 °C) for 60 s and rinsed in IPA (room temperature) for another 30 s. The masks therefore were obtained. In the end, an adhesive Cr layer (4.5 nm) and Au layer (40 nm) were thermally evaporated at a speed of 0.4 nm·min^{-1} onto the PMMA/ITO substrate sequentially. After removing the PMMA layers by acetone, Au nanostructures with designed patterns were obtained on the ITO substrates. By utilizing the EBL technique, I have successfully fabricated Au nanorods, nanodisk, and cross antenna patterns on ITO substrates (Figure 3.4).

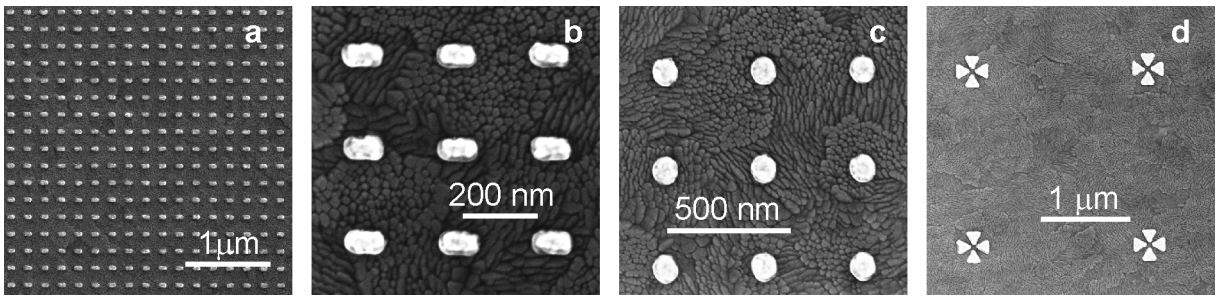

Figure 3.4 Au nanostructures fabricated by the electron-beam lithography technique on ITO substrates. a) SEM image of Au nanorod array patterns. b) Zoomed-in SEM image of the Au nanorod array. c) SEM image of Au nanodisks. d) SEM image of Au cross nanoantennas.

The sizes of the nanorods fabricated using the EBL methods are limited by the resolution of the lithography technique. Nowadays, state-of-the-art electron-beam lithography systems can produce Au nanorods of diameters ranging from ~10 nm to several hundred nanometers.[7] However, the top-down EBL method is usually time-consuming and has high costs, which makes it impractical for the fabrication of Au nanorod structures on large scales. In addition, the nanorods obtained from vacuum deposition techniques are usually composed of polycrystalline nanoparticles, which will degrade their plasmonic properties due to electron scattering at grain boundaries. These shortcomings prevent top-down methods from practical device applications and limit them mostly to fundamental research.

3.3 Characterization Techniques

The experimental methods employed for the characterization of the geometric and optical properties of Au nanostructures are described here. The optical properties of the Au nanocrystal colloidal solutions were studied by measuring their extinction spectra. The measurements were performed on a Hitachi U-3501 UV–visi mble/NIR spectrophotometer with 1 cm quartz cuvettes. Specifically, the extinction of nanostructure ensembles can be determined by the measurement of the transmissivity *T*:[8]

$$T = \frac{I}{I_0} = \exp(-N\sigma_{\text{ext}} l) \tag{3.1}$$

Where I and I_0 are the transmitted power and the incident power, N is the particle concentration of the nanostructures, σ_{ext} is the extinction cross section of a single nanostructure, and l is the interaction length. The UV/visible/NIR spectrophotometer can measure directly the extinction:

$$\text{Extinction} = -\log_{10}\left(\frac{I}{I_0}\right) = \frac{N\sigma_{\text{ext}} l}{\ln(10)} = n \cdot \varepsilon \cdot l \tag{3.2}$$

n is the molar concentration of nanostructures and ε is the molar extinction coefficient. The values of ε for some nanostructures have ready been reported. We can also calculate ε from the value of the extinction cross section obtained from analytical calculations or simulations. Therefore, the molar concentration of nanocrystals can be known from their extinction spectra.

Scanning electron microscopy (SEM), low- and high-magnification transmission electron microscopy (TEM) were used to characterize the geometrical properties of Au nanocrystals. SEM images were taken on an FEI Quanta 400 FEG microscope. Low-magnification TEM imaging was performed on an FEI CM120 microscope at 120 kV. High-resolution characterization was carried out on an FEI Tecnai F20 microscope.

The optical properties of each single Au nanostructure were investigated with the help of a home-built single-particle scattering imaging and spectroscopy system.[8] All samples are first deposited on conductive ITO substrate, which enables the characterization of Au nanostructures with both SEM and dark-field imaging. The scattering properties of individual Au nanostructures

were then measured on a dark-field optical microscope (Olympus BX60) that was integrated with a quartz–tungsten–halogen lamp (100 W), a monochromator (Acton SpectraPro 2300i), and a charge-coupled device camera (Princeton Instruments Pixis 512B). The camera was thermoelectrically cooled to −70 °C during measurements. A dark-field objective (100×, numerical aperture: 0.80) was employed for both illuminating ITO substrates with the white excitation light and collecting the scattered light. The scattered light from individual nanostructures was corrected by first subtracting the background spectra taken from the adjacent regions without Au nanocrystals and then dividing them with the calibrated response curve of the entire optical system. A pattern-matching method developed by Chen *et al.*[9,10] was utilized to locate the same nanostructures on their scattering and SEM images so that the scattering spectrum of each nanostructure could be correlated with its geometrical structure (Figure 3.5). This method is illustrated by comparing the SEM image shown in Figure 3.5b and the scattering image shown in Figure 3.5c. The spatial distributions of the features in both images are nearly the same, except that there are some extra bright spots caused by the scattering of dust particles in the dark-field image. Considering there are more than 20 spots in both images, the geometry and the scattering spectrum of the same nanostructure can be unambiguously characterized by SEM and dark-field spectroscopy, respectively.

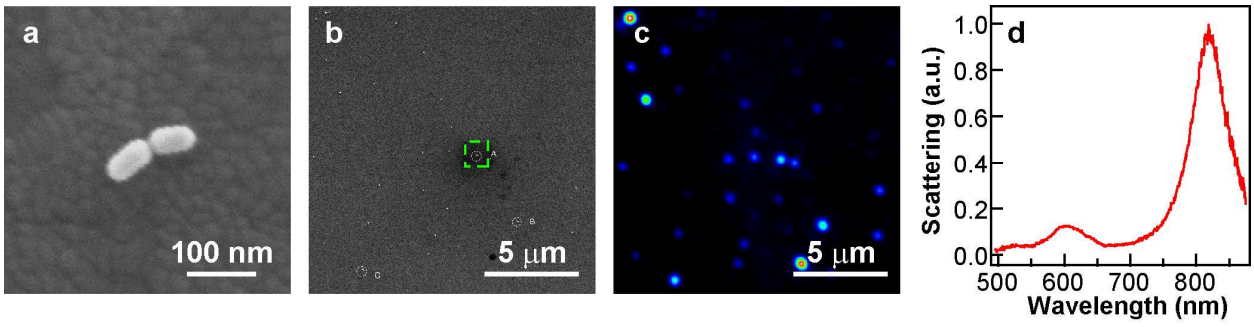

Figure 3.5: Pattern-matching method employed to measure the scattering properties of single Au nanostructures. (a) Enlarged SEM image showing the Au nanostructure indicated by the capital letter 'A' in (b). (b) SEM image of the Au nanostructures on an ITO substrate. (c) Dark-field scattering image taken from the same area as (b). (d) Dark-field scattering spectrum of the Au nanostructure shown in (a).

References

[1] Chen, H. J.; Shao, L.; Li, Q.; Wang, J. F. *Chem. Soc. Rev.* **2013**, *42*, 2679.

[2] Gole, A.; Murphy, C. J. *Chem. Mater.* **2004**, *16*, 3633.

[3] Nikoobakht, B.; El-Sayed, M. A. *Chem. Mater.* **2003**, *15*, 1957.

[4] Jana, N. R.; Gearheart, L.; Murphy, C. J. *Adv. Mater.* **2001**, *13*, 1389.

[5] Ming, T.; Kou, X. S.; Chen, H. J.; Wang, T.; Tam, H.-L.; Cheah, K.-W.; Chen, J.-Y.; Wang, J. F. *Angew. Chem. Int. Ed.* **2008**, *47*, 9685.

[6] Maier, S. A.; Kik, P. G.; Atwater, H. A.; Meltzer, S.; Harel, E.; Koel, B. E.; Requicha, A. A. G. *Nat. Mater.* **2003**, *2*, 229.

[7] Koh, A. L.; McComb, D. W.; Maier, S. A.; Low, H. Y.; Yang, J. K. W. *J. Vac. Sci. Technol., B* **2010**, *28*, C6O45.

[8] Ni, W. H. *Plasmonic Spectroscopy of Metallic Nanostructures.* Ph. D Thesis, Department of Physics, The Chinese University of Hong Kong. 2008.

[9] Chen, H. J.; Sun, Z. H.; Ni, W. H.; Woo, K. C.; Lin, H.-Q.; Sun, L. D.; Yan, C. H.; Wang, J. F. *Small* **2009**, *5*, 2111.

[10] Shao, L.; Woo, K. C.; Chen, H. J.; Jin, Z.; Wang, J. F.; Lin, H.-Q. *ACS Nano* **2010**, *4*, 3053.

Chapter 4

Energy-Resolved Plasmon Coupling in Gold Nanorod Dimers

As I have introduced in Chapter 1, when two metal nanocrystals are placed in a close proximity, the properties of their surface plasmons change dramatically.[1–6] Up to now, a great number of intensive investigations have been made to understand,[4,7–23] and engineer [24,25] the coupling between plasmonic nanocrystals. In most of the previous works, the research emphasis has focused on the role of the spatial arrangement, especially the inter-particle spacing, on the plasmon coupling. Specifically, for the nanocrystal homodimers comprising two identical components, the fractional plasmon wavelength shifts have been found by either experimental or computational means to decay nearly exponentially with the gap separation.[4,12,13] The decay length is found to be around 0.2–0.3 times the characteristic size of isolated nanocrystal and will not change with the nanocrystal size, shape, metal type or medium dielectric constant.

Heterodimers of metal nanocrystals exhibit richer plasmon coupling behaviors than homodimers because their symmetry breaking leads to the formation of new plasmon modes. The interaction between broad superradiant “bright” plasmon modes and narrow subradiant “dark” modes, can give rise to Fano-like interference in asymmetric plasmonic nanostructures.[26,27] When plasmonic Fano resonance occurs, an asymmetrical Fano profile with a clear Fano minimum that results from a destructive interference appears on the spectral responses. This plasmonic Fano interference phenomenon can not only further our understanding on light–matter interactions at the nanoscale below light’s diffraction limit but also offer tremendous potential for developing various plasmonic devices. Fano resonance has so far been

observed in several types of metal nanocrystal heterodimers.[28–30] The symmetry breaking in heterodimers plays an important role in the generation of Fano interference. The unique properties of Fano resonance have been utilized for creating nanoscale sensors with improved performance,[31] fabricating metamaterials with very narrow and nearly full-transparency windows,[32] and realizing various active operations, such as optical switching[30] and electro-optical modulation.[33]

Gold nanorods are preferred candidates for future plasmonic applications. Controllable plasmonic coupling between Au nanorods can provide adjustable resonance frequencies as well as remarkable optical field concentration and thereby is highly desirable for the development of high-efficiency optical antennas,[34] ultrasensitive biosensors, and high-performance quantum emitters. Tuning the plasmon coupling can be realized either by varying the inter-particle spacing or by adjusting the plasmon energies of the nanorod components in the dimer. The latter can result in tunable coupled-plasmon energy while the gap distance remains unchanged. This controllability will be advantageous to applications that require simultaneously large local field enhancements and variable plasmon energies. As a result, there exists a strong need to evaluate the coupled plasmon energies in the design of plasmonic structures and devices out of plasmon-coupled Au nanorods. The plasmon-hybridization model has been developed for the determination of the coupled plasmon energies of both homo- and heterodimers of metal nanorods,[6,16] but it only works in the quasi-static limit, as I have introduced in Chapter 2 of this thesis. In a recent study, the effect of the symmetry breaking on the plasmon coupling in Au nanorod dimers has been examined.[35] At a maintained gap distance, the coupled plasmon energy has been found to be strongly dependent on the plasmon energy of each nanorod monomer. During my MPhil study, I have also measured the coupled plasmon energies of the dimers composed of mismatched Au nanorods.[5,36] An anticrossing behavior has been observed in the plasmon coupling energy diagram. Despite these previous efforts and in contrast to the occurrence of a number of studies on the distance dependence of the plasmon coupling,

simple and reliable means have not been found for the determination of the coupled plasmon energies of Au nanorod dimers. The coupled plasmon energies of Au nanorod dimers are strongly dependent on both the plasmon energies of and the gap distance between the nanorod monomers. The interplay of these two dependences makes the accurate prediction of the coupled plasmon energies rather challenging.

In this chapter, I will present my systematic study on the energy diagrams of the plasmon coupling between Au nanorods that are aligned along their length axes using the finite-difference time-domain (FDTD) simulation method. The coupled plasmon energy has been investigated as a function of the plasmon energy of the nanorod monomer, the nanorod end shape, and the gap distance between the nanorod monomers. I have found that all of the coupling energy diagrams can be collapsed onto one universal scaling curve. I further employed a theoretical model based on two interacting mechanical oscillators to understand the plasmon coupling in Au nanorod dimers. The universal scaling behavior in the energy diagrams of coupled Au nanorods will be discussed in detail in Section 4.1. Moreover, the asymmetric nanorod heterodimers are found to exhibit Fano resonance. The parameters obtained from fitting the scattering spectra with the Fano profile are dependent on the relative plasmon energies of the nanorod monomers and the interparticle gap distance. The symmetry breaking induced Fano resonances will be discussed in Section 4.2. All the contents of this chapter have been published in *ACS Nano* in 2011.[37]

4.1 Universal Scaling in the Energy Diagram

During the simulations, Au nanorods were modeled as cylinders with differently shaped end-caps. Each Au nanorod had a radius R of 10 nm. The total length of the nanorod L was varied from 20 to 100 nm. The aspect ratio L/(2R) was therefore varied from 1 to 5. Such sizes are typical for chemically synthesized colloidal Au nanorods.[38] The nanorods were placed in a linear end-to-end configuration to form dimers, because colloidal Au nanorods tend to assemble in a linear end-to-end manner in liquids.[39–45] The gap distance between the two nanorods was

also variable. The dielectric function of gold was described by the Drude model with parameters chosen to match the experimental dielectric data as close as possible. The refractive index of the surrounding medium was first set to be 1.33, which is the refractive index of water. For our simulations, 0.5 nm spatial discretization was used in the gap region and 1 nm grids were applied in other regions. The excitation light was polarized along the length axis of the nanorod, which is also the axis of rotational symmetry of the dimer system. The transverse polarized light was not taken into account, since the plasmon resonance excited by such polarization is very weak in comparison to the longitudinal plasmon resonance for typically sized Au nanorods.[5,35] Figure 4.1a shows the calculated scattering spectra of two Au nanorod monomers as examples. The nanorods are capped with hemispheres at their ends. The aspect ratios of the two nanorods are 3.5 and 5, respectively. Their scattering spectra exhibit sharp peaks at 781 and 956 nm, respectively, which are ascribed to the longitudinal plasmon resonance wavelengths of the nanorods. The calculated longitudinal plasmon wavelengths exhibit a linear dependence on the aspect ratios of the nanorods (Figure 4.1b). This linear dependence is in agreement with previous experimental findings.[5,17,46] I have also listed the longitudinal plasmon energies of the au nanorods with varying aspect ratios in Table 4.1. We can then vary the longitudinal plasmon energy of the Au nanorod by changing the aspect ratio. In addition, because maximum scattering occurs when the localized plasmon resonances of metal nanocrystals are resonantly excited, the plasmon energies were obtained from the peak wavelengths of the calculated scattering spectra of the Au nanorod monomers and dimers in our study.

Table 4.1 Aspect Ratios and Corresponding Longitudinal Plasmon Energies (eV) of Au Nanorods with Hemispherical Ends in water

aspect ratio	1	1.5	2	2.5	3	3.5	4	4.5	5
plasmon energy	2.466	2.251	2.016	1.860	1.715	1.587	1.477	1.381	1.297

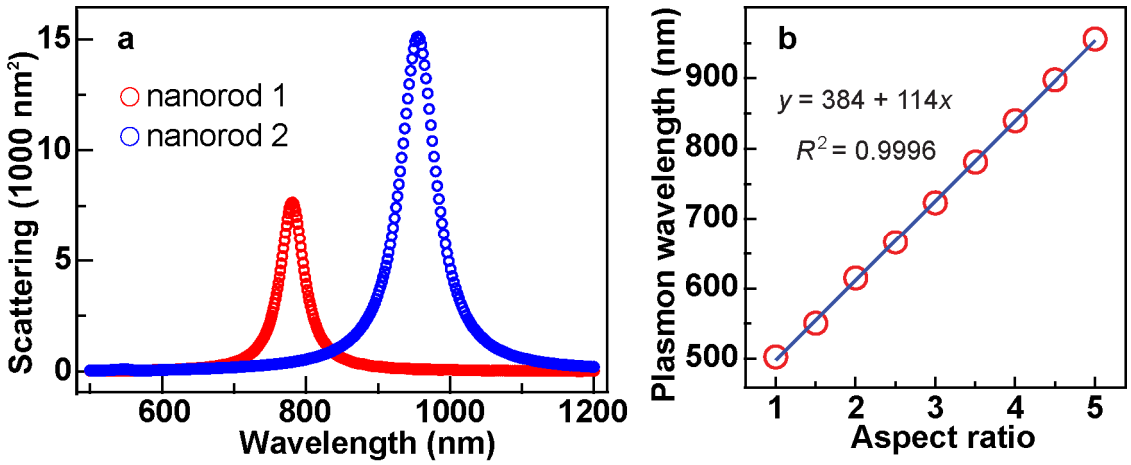

Figure 4.1 Scattering of individual Au nanorods. (a) Scattering spectra of two differently sized Au nanorods with hemispherical ends in water. The aspect ratios of the nanorods 1 and 2 are 3.5 and 5, respectively. (b) Longitudinal plasmon resonance wavelength versus the aspect ratio of the nanorod monomers with hemispherical ends. The line is a linear fitting. The inset gives the parameters obtained from the fitting.

Figure 4.2 shows the calculated scattering spectra of the plasmon-coupled Au nanorod dimers. There are two homodimers and one heterodimer (Figure 4.2, inset). The gap distances in all of the dimers are set at d = 7 nm. When the homodimers are formed from the nanorods with aspect ratios of 3.5 and 5, the plasmon resonance peaks red-shift to 845 and 1047 nm, respectively, due to the capacitive attraction between the two nanorods. The plasmon coupling between two identical nanorods can be well understood on the basis of the hybridization model.[6,16] The red-shifted hybridized plasmon mode in the nanorod homodimers is known as a hybridized bonding mode. Owning to the symmetry of the structure, the corresponding antibonding one cannot be excited by far-field light. It is known as a “dark” mode. When the two different nanorods are placed together to form the heterodimer, a weak scattering peak in the shorter-wavelength region, in addition to the strong scattering peak in the longer-wavelength region, is produced. The two scattering peaks are positioned at 770 and 989 nm, respectively. The higher-energy peak is induced by the symmetry breaking in the heterodimer. A detailed discussion about it will be presented later in this chapter. I first examined how the coupled-plasmon energy of the bonding mode is dependent on the nanorod monomers. In my previous experimental study,[5,36] an anticrossing behavior has been observed in the plasmon

coupling energy diagram of Au nanorod dimers. Due to the experimental limitations, only one coupling energy diagram at a particular gap distance has been obtained. FDTD simulations allow the parameters involved in the plasmon coupling to be varied over a large parameter space. My coworkers and I therefore carried out systematic FDTD simulations in order to gain a deeper understanding on the plasmon coupling behavior in Au nanorod dimers.

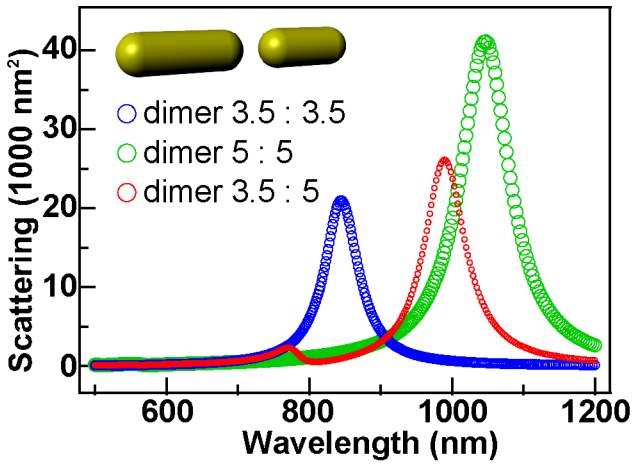

Figure 4.2 Scattering spectra of the plasmon-coupled Au nanorod dimers in water. The gaps between the two nanorods in all three dimers are 7 nm. The inset shows schematically the heterodimer.

In our simulations, we fixed the plasmon energy of one nanorod and varied that of the other. For Au nanorods with hemispherical ends, the plasmon energy of a nanorod monomer varies from 2.466 to 1.297 eV when the aspect ratio is changed from 1 to 5 (Table 4.2). An aspect ratio of 1 for a nanorod with hemispherical ends corresponds to a nanosphere. A plasmon coupling energy diagram for a representative nanorod dimer is given in Figure 4.3a. For this example, the plasmon energy, E_{fixed}, of one nanorod is fixed at 1.715 eV (red circles). The gap distance is set at d = 1 nm. As the plasmon energy of the other nanorod is gradually increased (black circles), the coupled-plasmon energy of the dimer also increases (blue circles). It is always smaller than the plasmon energies of the two nanorod monomers. The increase saturates asymptotically toward the plasmon energy of the fixed nanorod. The coupling energy diagram therefore exhibits an anticrossing behavior. This anticrossing behavior is maintained when E_{fixed} is varied from 1.297 to 2.466 eV, as shown in Figure 4.3b. The saturation limit of the coupled-plasmon energy

gets larger with increasing E_{fixed}. The numerical values of the coupled-plasmon energies for all of the dimers are supplied in Table 4.2.

Table 4.2 Energies (eV) of the Plasmon Coupling between Two Au Nanorods with Hemispherical Ends at a Gap Distance of 1 nm in water

	1[a]	1.5	2	2.5	3	3.5	4	4.5	5
1[b]	2.036	1.973	1.877	1.752	1.639	1.523	1.422	1.335	1.259
1.5	1.973	1.903	1.813	1.706	1.599	1.491	1.399	1.315	1.242
2	1.877	1.813	1.738	1.657	1.558	1.462	1.375	1.297	1.225
2.5	1.752	1.706	1.657	1.584	1.506	1.425	1.349	1.274	1.207
3	1.639	1.599	1.558	1.506	1.451	1.384	1.317	1.251	1.187
3.5	1.523	1.491	1.462	1.425	1.384	1.335	1.283	1.225	1.167
4	1.422	1.399	1.375	1.349	1.317	1.283	1.239	1.193	1.144
4.5	1.335	1.315	1.297	1.274	1.251	1.225	1.193	1.155	1.115
5	1.259	1.242	1.225	1.207	1.187	1.167	1.144	1.115	1.083

[a]In the topmost row are the aspect ratios for one nanorod in the dimer. [b]In the leftmost column are the aspect ratios for the other nanorod in the dimer. This is also applicable for Tables 4.3–4.5.

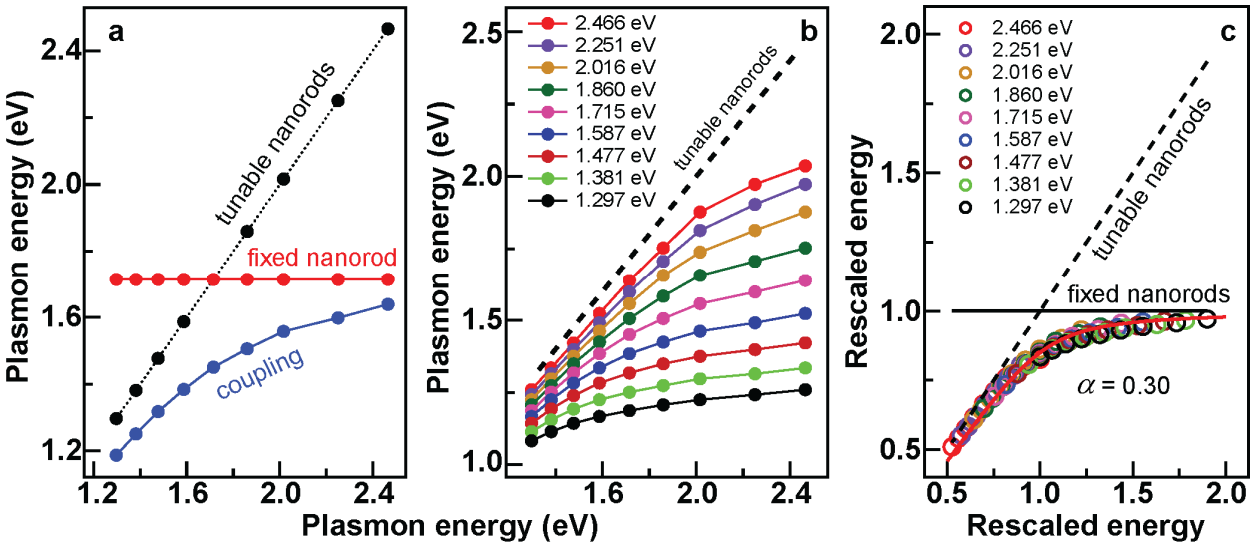

Figure 4.3 Energy diagrams of the plasmon coupling between Au nanorods with hemispherical ends at a fixed gap distance of 1 nm in water. (a) Plasmon coupling between one nanorod with a

fixed aspect ratio and another nanorod with varying aspect ratios. The blue, black, and red circles represent the coupled plasmon energy, plasmon energy of the varying nanorod, and plasmon energy of the fixed nanorod, respectively. The three energies are plotted as functions of the plasmon energy of the varying nanorod. (b) Coupled plasmon energy curves obtained when the aspect ratio of the fixed nanorod is set at different values. The corresponding plasmon energies of the fixed nanorods are given in the inset. The horizontal lines for the fixed nanorods are omitted for clarity. (c) Rescaled energy diagram of the plasmon coupling between variously sized nanorods from (b). The coefficient of determination for the fitting is $R^2 = 0.9996$.

One of our aims in this study is to find out whether and how the plasmon coupling between variously sized Au nanorods can be unified with a simple scaling relationship. Interestingly, we found that all of the anticrossing energy diagrams collapse into one if both the plasmon energies of the nanorod monomers and the coupled-plasmon energies are divided by their corresponding E_{fixed} (Figure 4.3c). The universal rescaled energy diagram might result from the fact that the plasmon coupling strength is mainly determined by the gap distance. Once a gap distance is given, the strength of the electromagnetic interaction between the nanorods will be fixed. Figure 4.3c shows that the universal diagram has two asymptotes. One is the inclined line with a slope of 1 (dashed line), and the other is the horizontal line (black line). We therefore utilized a hyperbolic function to describe the rescaled coupled-plasmon energies

$$y = 0.5(x+1) - 0.5\sqrt{(x-1)^2 + \alpha^2} \tag{4.1}$$

In equation (4.1), x and y are the rescaled energy values on the horizontal and vertical axis, respectively. There is only one fitting parameter, α, in the equation. When α = 0.30, the hyperbolic equation fits very well the universal energy diagram, with a coefficient of determination of $R^2 = 0.9996$.

The effect of the inter-particle gap distance on the plasmon coupling between Au nanorods was next considered. We performed the FDTD calculations of the Au nanorod dimers with the two monomers having varying plasmon energies and spaced apart at d = 3, 5, and 7 nm, respectively. The calculated coupled-plasmon energy values are listed in Tables 4.3, 4.4, and 4.5. At each gap distance, all of the coupling energy diagrams are collapsed onto one (Figure 4.4a).

In addition, we also calculated the coupled-plasmon energies of the nanorod dimers with a gap distance of 7 nm immersed in media having varying refractive indices. The results (Table 4.6 and Figure 4.4b) show that the plasmon coupling energy diagrams obtained for different refractive indices also collapse universally onto one curve. Therefore, the effect of the index of the surrounding medium can also be included in the energy rescaling. In this study, we focus on the plasmon coupling behavior of the nanorod dimers in water. The rescaled anticrossing energy diagrams can be well fitted with the hyperbolic function given above. The parameter α/coefficient of determination R^2 obtained from the fitting are 0.20/0.9998, 0.16/0.9998, and 0.14/0.9999 for d = 3, 5, and 7 nm, respectively. α is seen to decrease as d is increased. A close examination of Figure 4.3c and Figure 4.4a indicates that the coupling-induced plasmon shift also decreases with increasing gap distances. The decreased plasmon shift is attributed to the reduced capacitive coupling between the nanorods. We therefore reason that the fitting parameter α is dependent on the plasmon coupling strength.

Table 4.3 Energies (eV) of the Plasmon Coupling between Two Au Nanorods with Hemispherical Ends at a Gap Distance of 3 nm in water

	1	1.5	2	2.5	3	3.5	4	4.5	5
1	2.283	2.147	1.976	1.816	1.680	1.558	1.451	1.358	1.277
1.5	2.147	2.068	1.941	1.790	1.662	1.544	1.436	1.346	1.268
2	1.976	1.941	1.860	1.747	1.636	1. 523	1.422	1.335	1.257
2.5	1.816	1.790	1.747	1.686	1.596	1.497	1.404	1.323	1.248
3	1.680	1.662	1.636	1.596	1.538	1.462	1.381	1.306	1.233
3.5	1.558	1.544	1.523	1.497	1.462	1.410	1.349	1.286	1.219
4	1.451	1.436	1.422	1.404	1.381	1.349	1.309	1.257	1.199
4.5	1.358	1.346	1.335	1.323	1.306	1.286	1.257	1.219	1.172
5	1.277	1.268	1.257	1.248	1.233	1.219	1.199	1.172	1.141

Table 4.4 Energies (eV) of the Plasmon Coupling between Two Au Nanorods with Hemispherical Ends at a Gap Distance of 5 nm in water

	1	1.5	2	2.5	3	3.5	4	4.5	5
1	2.338	2.187	1.996	1.831	1.691	1.570	1.460	1.367	1.286
1.5	2.187	2.103	1.970	1.813	1.680	1.558	1.451	1.358	1.277
2	1.996	1.970	1.909	1.784	1.662	1.546	1.439	1.349	1.271
2.5	1.831	1.813	1.784	1.720	1.633	1.523	1.425	1.341	1.262
3	1.691	1.680	1.662	1.633	1.573	1.494	1.407	1.326	1.254
3.5	1.570	1.558	1.546	1.523	1.494	1.445	1.381	1.309	1.239
4	1.460	1.451	1.439	1.425	1.407	1.381	1.338	1.286	1.225
4.5	1.367	1.358	1.349	1.341	1.326	1.309	1.286	1.248	1.199
5	1.286	1.277	1.271	1.262	1.254	1.239	1.225	1.199	1.167

Table 4.5 Energies (eV) of the Plasmon Coupling between Two Au Nanorods with Hemispherical Ends at a Gap Distance of 7 nm in water

	1	1.5	2	2.5	3	3.5	4	4.5	5
1	2.373	2.205	2.007	1.839	1.700	1.573	1.465	1.370	1.288
1.5	2.205	2.152	1.987	1.825	1.689	1.567	1.460	1.364	1.283
2	2.007	1.987	1.935	1.805	1.677	1.558	1.451	1.358	1.277
2.5	1.839	1.825	1.805	1.744	1.651	1.544	1.439	1.349	1.271
3	1.700	1.689	1.677	1.651	1.596	1.512	1.425	1.341	1.262
3.5	1.573	1.567	1.558	1.544	1.512	1.468	1.399	1.326	1.254
4	1.465	1.460	1.451	1.439	1.425	1.399	1.358	1.303	1.239
4.5	1.370	1.364	1.358	1.349	1.341	1.326	1.303	1.265	1.216
5	1.288	1.283	1.277	1.271	1.262	1.254	1.239	1.216	1.184

Table 4.6 Plasmon Energies (eV) of the Varying Nanorod Monomers and the Nanorod Dimers in Different Media[a]

aspect ratio	monomer $n = 1$[b]	dimer $n = 1$	monomer $n = 1.2$	dimer $n = 1.2$	monomer $n = 1.4$	dimer $n = 1.4$	monomer $n = 1.6$	dimer $n = 1.6$
1	–	2.029	–	1.824	2.424	1.648	2.319	1.495
1.5	2.466	2.018	2.323	1.814	2.184	1.638	2.047	1.485
2	2.314	2.004	2.143	1.799	1.979	1.621	1.830	1.468
2.5	2.170	1.977	1.977	1.770	1.803	1.590	1.652	1.439
3	2.043	1.927	1.840	1.720	1.663	1.542	1.509	1.391
3.5	1.917	1.847	1.708	1.638	1.532	1.460	1.381	1.313
4	1.803	1.751	1.592	1.540	1.416	1.367	1.271	1.226
4.5	1.704	1.666	1.495	1.458	1.325	1.290	1.186	1.151
5	1.623	1.584	1.416	1.377	1.249	1.213	1.114	1.081

[a]The ends of the nanorods are hemispherical. The gap distance is 7 nm. The aspect ratio of the fixed nanorod is 3. [b]*n* represents the refractive index of the surrounding medium.

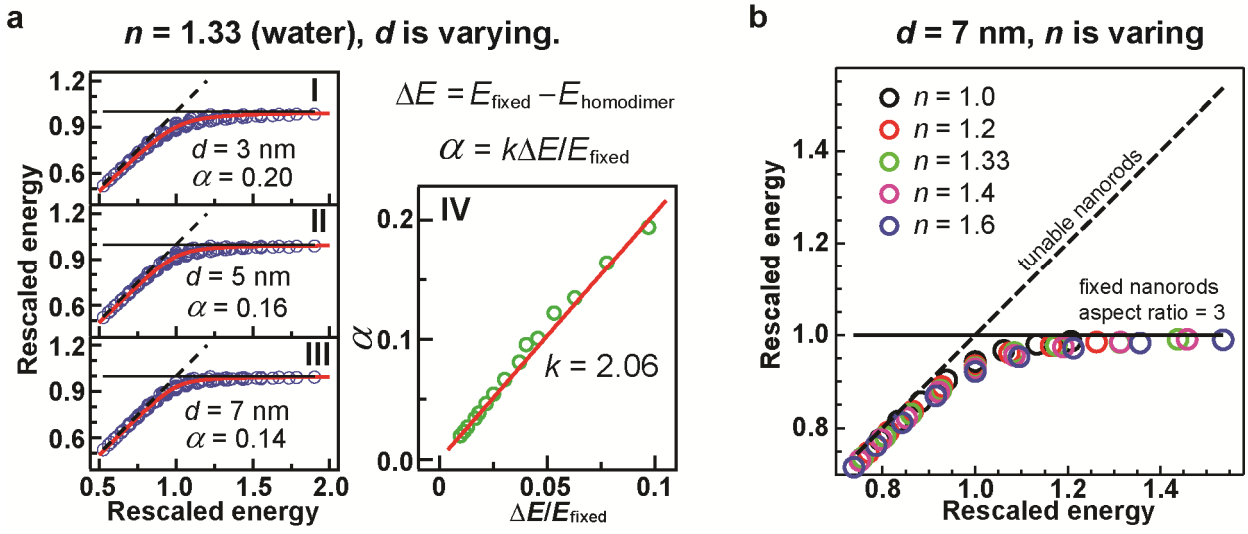

Figure 4.4 Effects of gap distance and medium refractive index on the rescaled energy diagrams of the plasmon coupling between nanorods with hemispherical ends. (a) (I–III) Rescaled energy diagrams of the plasmon coupling between nanorods with hemispherical ends at different gap distances in water (n = 1.33). The coefficients of determination for the fittings are 0.9998, 0.9998, and 0.9999, respectively. (IV) Fitting parameter α as a function of the fractional plasmon energy

shift $\Delta E/E_{fixed}$. The coefficient of determination for the linear fitting is $R^2 = 0.9963$. (b) Rescaled energy diagrams of the plasmon coupling between Au nanorods with hemispherical ends in different media. The fixed Au nanorod has an aspect ratio of 3, and the gap distance is fixed at 7 nm.

The fractional plasmon shift is directly related to the plasmon coupling strength. In order to ascertain how α changes with the fractional plasmon shift, we carried out the FDTD simulations on Au nanorod dimers with the gap distance between the two nanorods varied from 2 to 24 nm at a step of 2 nm. For each gap distance, since the results above have shown that all of the coupling energy diagrams can be rescaled onto a universal curve, we fixed the plasmon energy of one nanorod at E_{fixed} = 2.016 eV and changed the plasmon energy of the other nanorod. All of the as-calculated coupled-plasmon energies are listed in Table 4.7. They were thereafter subjected to the rescaling and hyperbolic fitting so that α could be determined. We then plotted α as a function of $\Delta E/E_{fixed}$ (Figure 4.4IV), where ΔE is the difference between E_{fixed} and the coupled-plasmon energy of the corresponding homodimer $E_{homodimer}$. For the data points shown in Figures 4.3c and 4.4I–III, there are many different E_{fixed} values. If all of the energy diagrams at each gap distance follows exactly the universal hyperbolic equation, then $E_{homodimer}/E_{fixed}$ and therefore $\Delta E/E_{fixed} = 1 - E_{homodimer}/E_{fixed}$ are fixed for different E_{fixed} values. α is seen to be proportional to $\Delta E/E_{fixed}$. A linear fitting gave a proportionality constant of k = 2.06 and a coefficient of determination of R^2 = 0.9963. The proportional relationship between α and $\Delta E/E_{fixed}$ supports our above argument that α can be interpreted as a measure of the plasmon coupling strength of Au nanorod dimers.

Table 4.7 Energies (eV) of the Plasmon Coupling between One Au Nanorod with Its Aspect Ratio Fixed at 2 (E_{fixed} = 2.016 eV) and the Other Au Nanorod with Varying Aspect Ratios at Varying Gap Distances[a]

gap (nm)[b]	2	4	6	8	10	12	14	16	18	20	22	24
1[c]	1.955	1.990	2.004	2.011	2.014	2.017	2.021	2.021	2.024	2.024	2.024	2.024
2	1.821	1.890	1.924	1.941	1.955	1.966	1.973	1.979	1.983	1.990	1.993	1.997
3	1.613	1.651	1.672	1.682	1.689	1.693	1.696	1.700	1.703	1.703	1.707	1.707
4	1.406	1.434	1.444	1.455	1.458	1.465	1.465	1.468	1.468	1.472	1.472	1.472
5	1.247	1.265	1.275	1.281	1.284	1.287	1.290	1.291	1.291	1.293	1.293	1.294

[a]The ends of the nanorods are hemispherical. [b]In the topmost row are the gap distances between the two nanorods in the dimers. [c]In the leftmost column are the aspect ratios of the varied nanorod in the dimers.

We also studied how the end shape of Au nanorods affects the plasmon coupling between Au nanorods. Previous studies have shown that the end curvature affects the longitudinal plasmon energy of Au nanorods.[5] Au nanorods with flat (Figure 4.5a, inset) and sharp ends (Figure 4.5b, inset) were considered. The sharp end was modeled with a hemi-prolate spheroid, with the length of the major axis being twice that of the minor axis. The major axis is aligned along the length axis of the nanorod. For both types of the nanorods, the gap distances were set to be 1, 3, 5, and 7 nm, and the aspect ratio of one nanorod monomer was kept at 3 to reduce the computational load. The plasmon energies of the nanorod monomers and dimers are provided in Tables 4.8 and 4.9 for the flat and sharp ends, respectively. Figure 4.5a and b show the rescaled energy diagrams when the gap distance is 1 nm. The energy diagrams can also be well fitted with equation (4.1). The obtained values for α are 0.46 and 0.27 for the flat and sharp ends, respectively. Taken together with the α value of 0.30 for the nanorods with hemispherical ends at d = 1 nm (Figure 4.3c), the results indicate that blunter ends leads to larger plasmon shifts for a given inter-particle gap distance. This is understandable because the capacitive coupling

between Au nanorods with blunter ends is stronger. Similar to the case of the nanorods with hemispherical ends, α also varies in proportion to $\Delta E/E_{fixed}$ for both types of the end shapes as the gap distance is changed (Figure 4.5c,d). The proportionality constants obtained from linear fitting are both 1.95. These results reveal that the hyperbolic function described by equation 4.1 is suitable for predicting the coupled-plasmon energies of the dimers of Au nanorods with different end shapes. The fitting parameter α is directly proportional to $\Delta E/E_{fixed}$. The proportionality constant is approximately equal to 2, irrespective of the end shape of Au nanorods.

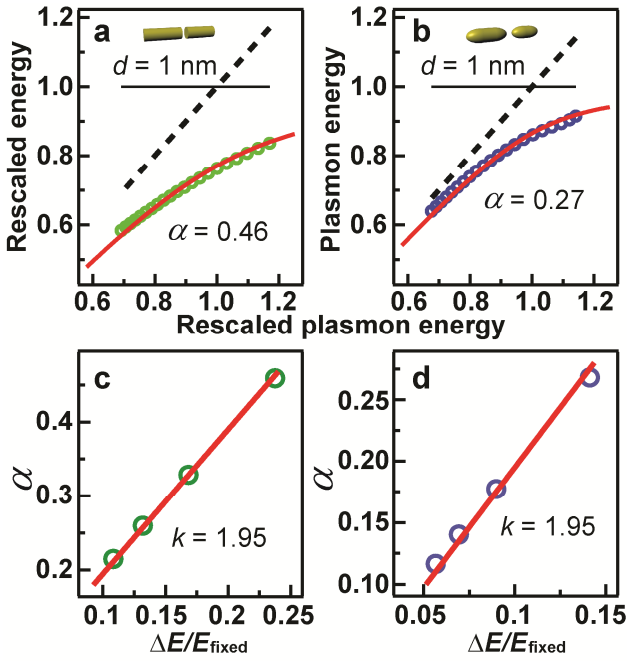

Figure 4.5 Effect of nanorod end shape on the plasmon coupling between Au nanorods. (a,b) Rescaled energy diagrams of the plasmon coupling between nanorods with flat and sharp ends, respectively. The insets show schematically the two types of dimers. The gap distances are both 1 nm. The coefficients of determination for the two fittings are 0.9999 and 0.9989. (c,d) Fitting parameter α as a function of $\Delta E/E_{fixed}$ for the flat and sharp nanorod dimers, respectively. The coefficients of determination for the fittings are 0.9999 and 0.9988, respectively.

Table 4.8 Plasmon Energies (eV) of One Monomer Nanorod with Varying Aspect Ratios and the Energies (eV) of the Plasmon Coupling between One Au Nanorod with Its Aspect Ratio Fixed at 3 (E_{fixed} = 1.601 eV) and the Other Au Nanorod with Varying Aspect Ratios[a]

aspect ratio	monomer	dimer 1 nm[b]	dimer 3 nm[b]	dimer 5 nm[b]	dimer 7 nm[b]
2	1.872	1.339	1.438	1.488	1.518
2.2	1.812	1.315	1.418	1.472	1.505
2.4	1.755	1.291	1.398	1.454	1.489
2.6	1.701	1.267	1.377	1.434	1.471
2.8	1.650	1.244	1.355	1.413	1.451
3	1.601	1.221	1.332	1.390	1.428
3.2	1.555	1.198	1.308	1.366	1.403
3.4	1.512	1.176	1.284	1.341	1.377
3.6	1.471	1.154	1.261	1.316	1.350
3.8	1.432	1.133	1.237	1.290	1.323
4	1.394	1.112	1.213	1.264	1.296
4.2	1.358	1.092	1.190	1.239	1.269
4.4	1.324	1.072	1.167	1.214	1.242
4.6	1.293	1.053	1.145	1.189	1.216
4.8	1.263	1.035	1.123	1.165	1.190
5	1.233	1.017	1.102	1.142	1.166
5.2	1.205	0.999	1.081	1.120	1.142
5.4	1.179	0.982	1.061	1.098	1.119
5.6	1.153	0.965	1.042	1.077	1.098
5.8	1.129	0.950	1.023	1.057	1.076
6	1.106	0.934	1.005	1.037	1.055

[a]The ends of the nanorods are flat. [b]The numbers indicate the gap distances.

Table 4.9 Plasmon Energies (eV) of One Monomer Nanorod with Varying Aspect Ratios and the Energies (eV) of the Plasmon Coupling between One Au Nanorod with Its Aspect Ratio Fixed at 3 (E_{fixed} = 1.764 eV) and the Other Au Nanorod with Varying Aspect Ratios[a]

aspect ratio	monomer	dimer 1 nm[b]	dimer 3 nm[b]	dimer 5 nm[b]	dimer 7 nm[b]
2	2.007	1.610	1.693	1.720	1.737
2.2	1.972	1.592	1.682	1.710	1.728
2.4	1.925	1.573	1.669	1.698	1.717
2.6	1.872	1.555	1.652	1.685	1.703
2.8	1.818	1.536	1.631	1.668	1.687
3	1.764	1.515	1.606	1.642	1.665
3.2	1.712	1.492	1.574	1.613	1.634
3.4	1.662	1.465	1.545	1.575	1.596
3.6	1.614	1.438	1.515	1.542	1.557
3.8	1.568	1.411	1.481	1.507	1.522
4	1.525	1.383	1.445	1.469	1.484
4.2	1.483	1.356	1.412	1.433	1.445
4.4	1.444	1.328	1.380	1.398	1.409
4.6	1.406	1.301	1.348	1.366	1.375
4.8	1.371	1.273	1.317	1.333	1.342
5	1.337	1.247	1.287	1.302	1.311
5.2	1.304	1.221	1.258	1.272	1.280
5.4	1.273	1.196	1.230	1.243	1.251
5.6	1.244	1.171	1.204	1.216	1.223
5.8	1.215	1.148	1.178	1.189	1.196
6	1.188	1.125	1.153	1.164	1.170

[a]The ends of the nanorods are sharp. [b]The numbers indicate the gap distances.

Equation (4.1) is purely mathematical. We tried to translate the rescaled energies back into the physical parameters involved in the plasmon coupling in the Au nanorod dimers in order to gain the underlying physics. If E_1 and E_2 are used to represent the plasmon energies of the fixed and varying nanorod monomers, respectively, the coupled-plasmon energy E_{12} can be obtained from equation (4.1) as

$$E_{12} = \frac{1}{2}(E_1 + E_2) - \frac{1}{2}\sqrt{(E_1 - E_2)^2 + [2(E_1 - E_{11})]^2} \tag{4.2}$$

where E_{11} is the coupled-plasmon energy of the homodimer composed of the fixed nanorods. The term $E_1 - E_{11}$ in equation (4.2) represents the contribution from the plasmon coupling. Due to the exchangeability between the two nanorod monomers in a dimer, the second term under the square root in equation (4.2) can be replaced with $[2(E_2 - E_{22})]^2$. However, the plasmon coupling strength is also affected by the size and shape of the nanorod although it is predominantly determined by the gap distance, as revealed by our FDTD simulations. The rescaled energy diagrams are seen to deviate slightly from the hyperbolic curve. As a result, the coupled-plasmon energy E_{12} values calculated from $E_1 - E_{11}$ and $E_2 - E_{22}$ are not exactly the same. To reduce the error, we replace the term $E_1 - E_{11}$ with the average of $E_1 - E_{11}$ and $E_2 - E_{22}$, which gives

$$E_{12} = \frac{1}{2}(E_1 + E_2) - \frac{1}{2}\sqrt{(E_1 - E_2)^2 + [(E_1 - E_{11}) + (E_2 - E_{22})]^2} \tag{4.3}$$

The largest error in the coupled-plasmon energies calculated with equation (4.3) in comparison with the FDTD simulation results is 3.8%. Equation (4.3) therefore provides an analytical expression for the evaluation of the coupled-plasmon energy between any two Au nanorods that are placed adjacently in a linear end-to-end manner, once the plasmon energies of the corresponding nanorod monomers and homodimers that have the same gap distance are obtained in the same dielectric environment. The quick and reliable estimation of the coupled-plasmon energies between Au nanorods will facilitate the plasmonic applications of Au nanorods in biotechnology and optics.

We further employed a theoretical model based on two coupled mechanical oscillators to help in understanding the plasmon coupling in Au nanorod dimers. The model has been

introduced in Chapter 2. In this study, the coupled-plasmon modes of Au nanorod dimers can be modeled as two mechanical oscillators with frequencies ω_1 and ω_2. The two oscillators interact through one spring with a coupling constant of α_0. In the absence of dissipation, the coupled-oscillator system can be described by the Lagrangian

$$L = T - V = \frac{1}{2}\dot{x}_1^2 + \frac{1}{2}\dot{x}_2^2 - \frac{1}{2}\omega_1^2 x_1^2 - \frac{1}{2}\omega_2^2 x_2^2 + \alpha_0 x_1 x_2 \tag{4.4}$$

where T and V denote the kinetic and potential energies, x_1 and x_2 are the displacements from the equilibrium positions of the oscillators in a one-dimensional system, and the dots represent the time derivatives of the displacements. The Lagrangian equations of motion are given as

$$\frac{d}{dt}\left(\frac{\partial L}{\partial \dot{x}_i}\right) - \frac{\partial L}{\partial x_i} = 0 \tag{4.5}$$

The solutions to equation (4.5) are in the form of a linear combination of harmonics. A determinant equation can be generated by inserting the solutions into equation (5). Two solutions for the eigen oscillation frequency Ω are obtained by solving the determinant equation. Because the lower-energy coupled-plasmon mode was considered in our above discussion of the coupled-plasmon energies, the smaller eigen frequency solution is taken. It is given by

$$\Omega^2 = \frac{(\omega_1 + \omega_2)^2}{4}\left\{\left[1 - \sqrt{\left(\frac{\omega_1 - \omega_2}{\omega_1 + \omega_2}\right)^2 + \frac{4\alpha_0^2}{(\omega_1 + \omega_2)^4}}\right]^2 - \frac{4\alpha_0^2}{(\omega_1 + \omega_2)^4}\right\} \tag{4.6}$$

By using Taylor expansion, the eigen frequency of the coupled-oscillator system Ω can be expressed as

$$\Omega = \frac{\omega_1 + \omega_2}{2} - \frac{1}{2}\sqrt{(\omega_1 - \omega_2)^2 + \frac{4\alpha_0^2}{(\omega_1 + \omega_2)^2}} - \delta \tag{4.7}$$

The first two terms in equation (4.7) have nearly the same form as equation (4.3), which was obtained through the hyperbolic fitting. The second term under the square root in equation (4.7) involves the coupling constant, α_0, of the spring connecting the two oscillators. It represents the perturbation of the coupling to the total energy of the coupled-oscillator system. In the nanorod

dimer system, the term bringing the plasmon coupling into the total energy is represented by $[(E_1 - E_{11}) + (E_2 - E_{22})]^2$. The coupling strength between the two nanorods is therefore related to the difference in the plasmon energies of the nanorod monomers and the corresponding homodimers. If we let the corresponding terms in equations (4.3) and (4.7) be equivalent to each other, $\delta\Omega$ in equation (4.7) is estimated to the first order from our FDTD simulation data to be smaller than 3.5%. As a result, the δ term in the coupled-plasmon energy of the Au nanorod dimer is neglected. The above reasoning indicates the usefulness of the coupled-oscillator model in understanding the coupled-plasmon energy between Au nanorods.

Equation (4.3) can be employed to calculate the coupled-plasmon energies between variously sized Au nanorods if the plasmon energies of the nanorod monomers and the corresponding homodimers having the same gap distance are known. The longitudinal plasmon energies of Au nanorod monomers can be determined either spectroscopically or from the linear dependence of the longitudinal plasmon wavelength on the nanorod aspect ratio.[5,17,46] We then need to find out the coupled-plasmon energies of two identical Au nanorods that are aligned linearly. Previous studies[4,12,13] have shown that the coupled-plasmon wavelength between two identical metal nanoparticles can be described using an empirical universal scaling law

$$\frac{\Delta\lambda}{\lambda} = \beta e^{-\left(\frac{d/D}{\tau}\right)} \tag{4.8}$$

where λ is the plasmon wavelength of the individual metal nanoparticle, $\Delta\lambda$ is the plasmon wavelength shift arising from the plasmon coupling, d is the gap distance, D is the diameter of the nanoparticle, τ is the decay constant, and β is the maximum fractional plasmon wavelength shift. The decay constant τ has been found to be within 0.2–0.3, irrespective of the metal type, the nanoparticle size and shape, and the surrounding medium. This empirical scaling law has also been applied to Au nanorods that are linearly aligned.[17,21] However, due to the geometrical anisotropy of nanorods, the fitting of the data points for Au nanorods with equation (4.8) is not as well as that for Au and Ag nanoparticles.

We performed the FDTD calculations to determine the plasmon shift $\Delta\lambda/\lambda$ as a function of the gap distance d for homodimers of Au nanorods that have hemispherical ends and different aspect ratios (Figure 4.6). We first used equation (4.8) to fit the obtained data points, with the nanorod length treated as the characteristic size. However, for the aspect ratio from 1 to 4, the β and τ values obtained from the fitting vary in the ranges of 0.13–0.16 and 0.18–0.28, respectively. These results suggest that equation (4.8) is not good enough for predicting the coupled-plasmon wavelengths of various Au nanorod homodimers. In order to have a more universal equation, we reasoned that the coupled-plasmon energy is determined by the competition between the inter-particle near-field interaction and the intra-particle Coulombic restoring force on the displaced electron cloud.[14] We therefore replaced the term d/D in equation (4.8) with $(V_{gap}/V_{nanorod})^{1/3}$, where V_{gap} and $V_{nanorod}$ denote the volumes of the gap region and nanorod, respectively. Because the volume ratio is approximately equal to d/L, with L being the nanorod length, the exponential equation can then be expressed as

$$\frac{\Delta\lambda}{\lambda} = \beta e^{-(d/L)^{1/3}/\tau} \tag{4.9}$$

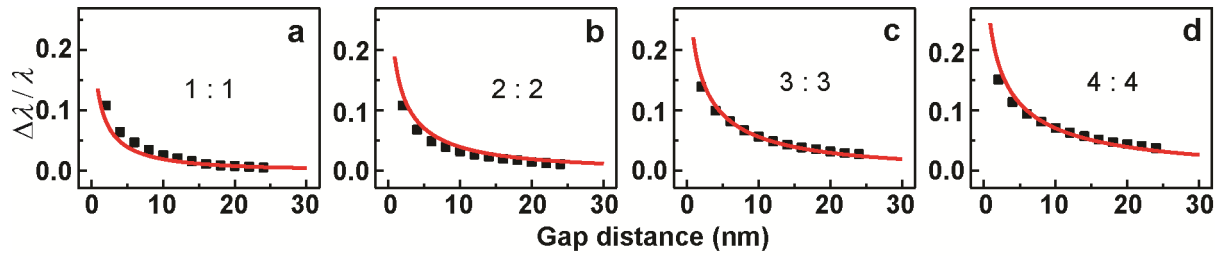

Figure 4.6 Gap-dependent fractional plasmon shifts in the homodimers of Au nanorods capped with hemispheres. The aspect ratios of the nanorods are (a) 1, (b) 2, (c) 3, and (d) 4. The coefficients of determination for the fittings are 0.9305, 0.9630, 0.9932, and 0.9859, respectively.

Figure 4.6 displays the calculated fractional plasmon shift as a function of the gap distance for different nanorod homodimers and the curves obtained from the fitting with equation (4.9). The coefficients of determination for all of the fittings are comparable to those for the fittings with equation (4.8). More importantly, all of the fittings give one set of β and τ at 0.67 and 0.22,

respectively. The decay constant τ is very close to the values obtained previously for metal nanoparticles and nanorods.[4,12,13,17,21]

With equation (4.9), we can calculate the coupled-plasmon energies of Au nanorod homodimers, and subsequently estimate the coupled-plasmon energies of heterodimers composed of arbitrarily sized Au nanorods using the hyperbolic formula given in equation (4.3).

4.2 Symmetry Breaking Induced Fano Resonances

Figure 4.2 shows a blue-shifted weak scattering peak, in addition to the red-shifted strong peak, for the nanorod heterodimer. The weak scattering peak does not exhibit an anticrossing behavior in the plasmon coupling energy diagram. There is also a dip, which is located at the lower-energy side of the weak scattering peak. The weak scattering peak and the dip must arise from the symmetry breaking in the heterodimer because none of Au nanorod homodimers exhibits such features. The appearance of the scattering peak agrees with previous experimental findings observed by us[5] and others.[35] The peaks on the calculated scattering spectra of the heterodimers have an asymmetric line shape, which signifies the Fano resonance.[27] The Fano resonance typically involves a broadband excitation light source, a superradiant and a subradiant mode. The Fano profile is generated from the destructive interference between the two modes.[27]

In plasmonics, different coupled plasmon modes can be identified from corresponding spatial charge distributions. We therefore first calculated the charge distributions at different scattering energies for a heterodimer of Au nanorods with hemispherical ends in order to ascertain the coupled-plasmon modes that are involved in the Fano resoannce. The two nanorods have aspect ratios of 3.5 and 5. When they are placed together to form a heterodimer, the calculated scattering spectrum exhibits a weak peak at 1.610 eV (i), a dip at 1.533 eV (ii), and a strong peak at 1.254 eV (iii, Figure 4.7a). In comparison, the longitudinal plasmon energies of the two nanorod monomers are 1.587 and 1.297 eV, respectively (Figures 1a and 4.7b). The

calculated charge distributions (Figure 4.7c) reveal that the strong scattering peak (iii) is contributed by the dipole–dipole bonding plasmon mode. At the positions of the weak scattering peak (i) and the dip (ii), the electron oscillation in the longer nanorod is mainly quadrupolar and slightly dipolar, and that in the shorter nanorod is dipolar. In order to obtain the hybridization energy diagram for the nanorod heterodimer, we also calculated the energies of the dipolar and quadrupolar plasmon modes of the longer nanorod by employing a dipole instead of a plane wave as the excitation source. The dipole source provides a non-uniform electromagnetic field. It can excite both the bright dipolar mode and the dark quadrupolar mode in the nanorod. Two peaks are seen on the obtained absorption spectrum of the longer nanorod (Figure 4.7b, red). The charge distributions (Figure 4.7c) at these two peaks show that the lower- (II) and higher-energy peaks (I) arise from the dipolar and quadrupolar plasmon mode, respectively. These two modes hybridize with the dipolar mode of the shorter nanorod to give the dipole–dipole and dipole–quadrupole bonding modes, as shown by the hybridization energy diagram in Figure 4.7a. The entire heterodimer therefore possesses a mixture of the hybridized dipole–dipole bonding and dipole–quadrupole bonding modes. The dipole–dipole bonding mode is superradiant. Its spectral profile extends to the energy region of dipole–quadrupole bonding mode, as revealed by the charge distributions. The dipole–quadrupole bonding mode is subradiant. The destructive interference between the superradiant and subradiant modes gives rise to the asymmetric Fano profile of the scattering spectrum. The weak scattering peak in the nanorod heterodimers arises from the Fano resonance instead of the dipole–dipole antibonding mode. Therefore it does not exhibit an anticrossing behavior in the plasmon coupling energy diagram.

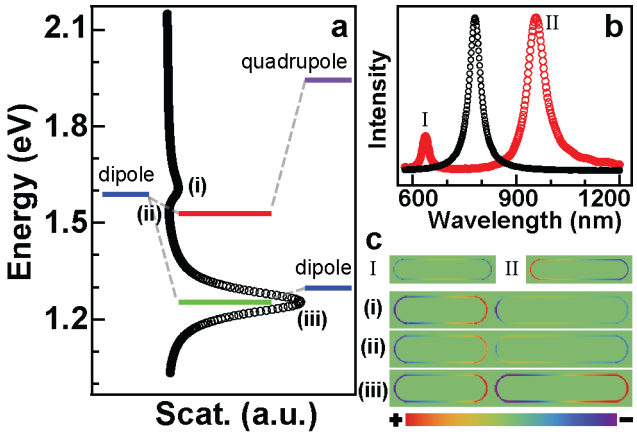

Figure 4.7 Plasmon hybridization in Au nanorod heterodimers. (a) Scattering spectrum and the plasmon hybridization diagram for a nanorod heterodimer. The nanorods have hemispherical ends. Their aspect ratios are 3.5 and 5. The gap distance is 7 nm. (i) and (iii) indicate the wavelengths of the two peaks, and (ii) indicates the valley between them. (b) Scattering spectrum of the shorter nanorod monomer (black) excited by a plane wave and the absorption spectrum of the longer nanorod monomer (red) excited by a dipole source. The absorption spectrum of the longer nanorod was calculated by replacing the shorter nanorod in the heterodimer with the dipole source at the center. In this way, both the quadrupolar (I) and dipolar (II) modes of the longer nanorod can be excited. (c) Charge distributions of the plasmon modes of the longer nanorod and hybridized plasmon modes in the heterodimer on the central cross sections of the nanorods.

The asymmetric profiles of the calculated scattering spectra of the nanorod heterodimers can be well fitted by a phenomenological model in the form[47–50]

$$C_{\mathrm{sca}}(\omega)=\left|a_r+\sum_{j=1,2}\frac{-b_j\Gamma_j e^{i\varphi_j}}{\hbar\omega-E_j+i\Gamma_j}\right|^2 \tag{4.10}$$

where C_{sca} represents the scattering signal, ω is the angular frequency, a_r denotes the background contribution, b_j, Γ_j, φ_j, and E_j represent the amplitude, line width, phase, and energy of each eigenmode, respectively, and $\hbar$ is the Planck's constant divided by 2π. In our study, we consider only two plasmonic eigenmodes. One is the dipole–dipole bonding mode (denoted by the subscript 1), and the other is the dipole–quadrupole bonding mode (denoted by the subscript 2).

The Fano profile is strongly dependent on the plasmon energy difference and the gap distance between the two nanorod monomers. Figure 4.8a shows the calculated scattering spectra of four representative nanorod heterodimers with the aspect ratio of one nanorod fixed at 5. Figure 4.8b shows the four representative spectra between the nanorods with aspect ratios of 3.5

and 5 at varying gap distances. In Figure 4.8a, as the aspect ratio of the varying nanorod becomes smaller and thus the dipolar plasmon energy of the nanorod becomes larger, both the dipole–dipole and dipole–quadrupole bonding modes shift to higher energies. At the same time, the intensity of the higher-energy scattering peak relative to that of the lower-energy one first grows larger and then gets smaller. In Figure 4.8b, as the gap distance is gradually reduced, the higher-energy scattering peak gets weaker relative to the lower-energy one.

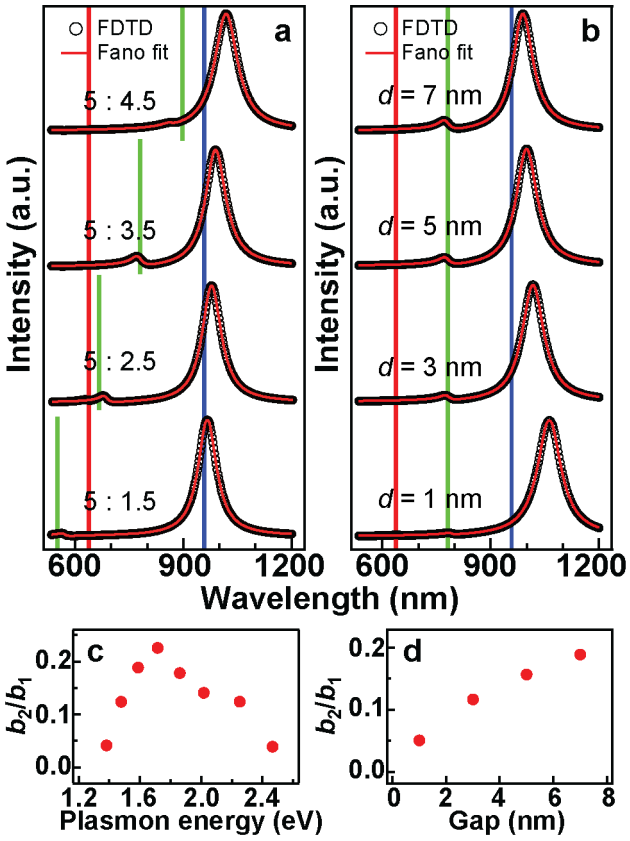

Figure 4.8 Fano resonances in Au nanorod heterodimers. (a) Fitting of the normalized scattering spectra of different Au nanorod heterodimers with the Fano profile. (a) The aspect ratio of one nanorod is fixed at 5, and that of the other nanorod is varied from 1 to 5. The gap between the two nanorods is 7 nm. (b) The aspect ratios of the two rods are fixed at 3.5 and 5. The gap is varied from 1 to 7 nm. The blue and red vertical bars indicate the dipolar and quadrupolar resonance positions of the longer nanorod, respectively, and the green ones indicate the dipolar resonance positions of the shorter nanorods. (c) Ratio of the amplitudes of the two eigenmodes obtained from the fitting versus the plasmon energy of the nanorod with varying aspect ratios. (d) Ratio of the amplitudes versus the gap distance between the two nanorods. The nanorods have hemispherical ends.

We fitted all of the calculated scattering spectra with the phenomenological model described in equation (4.10). The parameters obtained from the fitting are provided in Tables 4.10 and 4.11. We found that the amplitude ratio, b_2/b_1, between the two plasmon eigenmodes can be utilized to describe the Fano interference strength. The closer the ratio is to 1, the more noticeable the asymmetric Fano profile will become and thereby the stronger the interference (Figure 4.9). We therefore extracted b_2/b_1 and plotted them as a function of the plasmon energy of the varying nanorod in Figure 4.8c and as a function of the gap distance in Figure 4.8d. Figure 4.8c reveals that the 5 : 3.5 heterodimer has the largest b_2/b_1 ratio and therefore the most distinct Fano resonance. The first increase and then decrease in the amplitude ratio is believed to result from the shift of the dipolar mode (1.297–2.466 eV, Table 4.1) of the shorter nanorod from the red side to the blue side of the quadrupolar mode (1.944 eV, Figure 4.7b) of the longer nanorod. This shift causes the variation in the interference behavior between the two hybridized modes. Moreover, for the 5 : 3.5 nanorod heterodimer, the Fano line shape becomes clearer as the gap distance is gradually increased (Figure 4.8d). The b_2/b_1 ratio is essentially determined by the relative strengths between the dipole–dipole and dipole–quadrupole bonding modes around their overlapping spectral region. The relative strengths of the two bonding modes are in turn affected by the gap distance and the aspect ratios of the nanorod monomers, the latter of which determine the energy levels before the hybridization. The variations of the b_2/b_1 ratios observed in our study reflect the interplay of the different factors on the Fano interference strength.

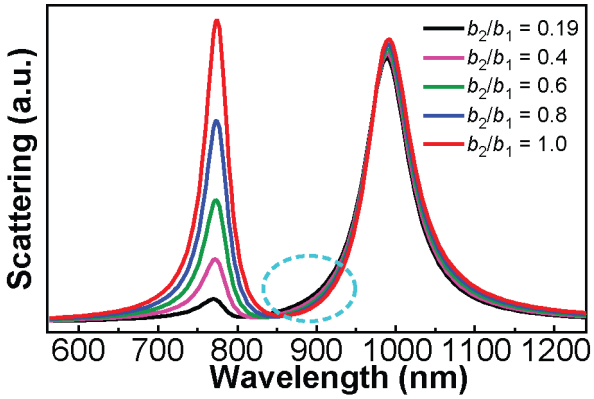

Figure 4.9 Fano profiles calculated at varying b_2/b_1 ratios. The curve for b_2/b_1 = 0.19 corresponds to the scattering spectrum of the 5 : 3.5 nanorod heterodimer shown in Figure 4.8 at

a gap of 7 nm. b_2 was changed while the other parameters were fixed to obtain varying b_2/b_1 ratios. The spectral region indicated with the circle shows that the lower-energy peak becomes more asymmetric as the amplitude ratio gets larger.

Table 4.10 Parameters Obtained from Fitting the Scattering Spectra of Different Nanorod Heterodimers at a Fixed Gap Distance with the Phenomenological Model[a]

	5 : 4.5[b]	5 : 4	5 : 3.5	5 : 3	5 : 2.5	5 : 2	5 : 1.5	5 : 1
a_r	6.8616	6.1621	-5.5232	-5.0664	-4.9352	-4.2632	-4.5167	4.8088
b_1	191.08	175.56	161.08	149.95	141.78	135.20	130.46	127.11
φ_1	3.0951	3.0926	6.2226	6.2190	6.2413	6.2286	6.2692	3.2164
E_1	1.2166	1.2388	1.2533	1.2633	1.2707	1.2770	1.2824	1.2874
Γ_1	0.046210	0.044981	0.043716	0.042764	0.042098	0.041561	0.041270	0.041088
b_2	7.9619	21.779	30.378	33.840	25.278	19.041	16.195	4.9688
φ_2	3.6309	3.3321	0.21881	0.23731	0.074293	0.28980	6.0296	1.9018
E_2	1.4392	1.5033	1.5968	1.7057	1.8212	2.0475	2.1794	2.1237
Γ_2	0.030074	0.033790	0.036469	0.033727	0.037493	0.038204	0.044354	0.22516

[a]The ends of the nanorods are hemispherical, and the gap distance is 7 nm. [b]In the topmost row are the aspect ratios of the two nanorods in each heterodimer.

Table 4.11 Parameters Obtained from Fitting the Scattering Spectra of a Nanorod Heterodimer at Varying Gap Distances with the Phenomenological Model[a]

	7 nm[b]	5 nm	3 nm	1 nm
a_r	-5.5232	-5.7462	6.1045	-6.6401
b_1	161.08	164.86	169.51	174.99
φ_1	6.2226	6.2269	3.0905	6.2411
E_1	1.2533	1.2402	1.2186	1.1663
Γ_1	0.043716	0.043867	0.043900	0.043314
b_2	30.378	25.800	19.744	8.8514
φ_2	0.21881	0.22907	3.3845	0.23152
E_2	1.5968	1.5950	1.5902	1.5721

Γ_2	0.036469	0.035021	0.032309	0.022777

[a]The ends of the nanorods are hemispherical, and the aspect ratios of the two nanorods in the heterodimer are 3.5 and 5. [b]In the topmost row are the gap distances.

4.3 Summary

In this chapter, we have made a systematic investigation through FDTD calculations on the plasmon coupling energy diagrams of the dimers of Au nanorods that have varying aspect ratios and different capping ends. The nanorods are placed in a linear end-to-end manner. Their gap distance is also varied. All of the energy diagrams exhibit an anticrossing behavior. They can be rescaled into one universal curve and thereby described with a simple hyperbolic scaling formula. A model based on two coupled mechanical oscillators has been employed to assist in understanding the hyperbolic scaling law. Moreover, the symmetry breaking in Au nanorod heterodimers induces unambiguously a Fano profile in their scattering spectra. The calculated charge distributions reveal that the Fano resonance results from the interactions between the different plasmon eigenmodes in the nanorod heterodimers. The spectral position of the obtained Fano dip and the relative amplitudes between the interfering plasmon eigenmodes are found to be dependent on the aspect ratios of the nanorod monomers and the gap distance. From our point of view, the discovered hyperbolic scaling law will be applicable for the capacitive plasmon coupling between Au nanorods that have diameters of ~5–50 nm and lengths of ~10–200 nm. Such a range covers the sizes of typical colloidal Au nanorods that are prepared chemically. Quantum tunneling will take effect when the gap distance is less than ~1 nm, and phase retardation will cause the excitation of multipolar plasmon modes and the hybridization of different plasmon modes for larger metal nanocrystals. Our results will be very useful in predicting the coupled-plasmon energies of Au nanorod dimers for their applications in plasmon-enhanced spectroscopies, biological sensing, and nanoantennas. In addition, the

variability of the Fano profiles in Au nanorod heterodimers offers an approach for the design of the Fano resonance, which can lead to new switchable metamaterials.

Reference

[1] Kreibig, U.; Althoff, A.; Pressmann, H. *Surf. Sci.* **1981**, *106*, 308.

[2] Quinten, M.; Kreibig, U.; Schonauer, D.; Genzel, L. *Surf. Sci.* **1985**, *156*, 741.

[3] Rechberger, W.; Hohenau, A.; Leitner, A.; Krenn, J.; Lamprecht, B.; Aussenegg, F. *Opt. Commun.* **2003**, *220*, 137.

[4] Su, K.-H.; Wei, Q.-H.; Zhang, X.; Mock, J. J.; Smith, D. R.; Schultz, S. *Nano Lett.* **2003**, *3*, 1087.

[5] Shao, L.; Woo, K. C.; Chen, H. J.; Jin, Z.; Wang, J. F.; Lin, H.-Q. *ACS Nano* **2010**, *4*, 3053.

[6] Prodan, E.; Radloff, C.; Halas, N. J.; Nordlander, P. *Science* **2003**, *302*, 419.

[7] Ghosh, S. K.; Pal, T. *Chem. Rev.* **2007**, *107*, 4797.

[8] Halas, N. J., Lal, S., Chang, W.-S., Link, S., Nordlander, P. *Chem. Rev.* **2011**, *111*, 3913.

[9] Gluodenis, M.; Foss, C. A. Jr. *J. Phys. Chem. B* **2002**, *106*, 9484.

[10] Nordlander, P.; Oubre, C.; Prodan, E.; Li, K.; Stockman, M. I. *Nano Lett.* **2004**, *4*, 899.

[11] Atay, T.; Song, J.-H.; Nurmikko, A. V. *Nano Lett.* **2004**, *4*, 1627.

[12]Gunnarsson, L.; Rindzevicius, T.; Prikulis, J.; Kasemo, B.; Käll, M. Zou, S.; Schatz, G. C. *J. Phys. Chem. B* **2005**, *109*, 1079.

[13] Jain, P. K.; Huang, W.; El-Sayed, M. A. *Nano Lett.* **2007**, *7*, 2080.

[14] Jain, P. K.; El-Sayed, M. A. *J. Phys. Chem. C* **2008**, *112*, 4954.

[15] Lassiter, J. B.; Aizpurua, J.; Hernandez, L. I.; Brandl, D. W.; Romero, I.; Lal, S.; Hafner, J. H.; Nordlander, P.; Halas, N. J. *Nano Lett.* **2008**, *8*, 1212.

[16] Willingham, B.; Brandl, D. W.; Nordlander, P. *Appl. Phys. B* **2008**, *93*, 209.

[17] Funston, A. M.; Novo, C.; Davis, T. J.; Mulvaney, P. *Nano Lett.* **2009**, *9*, 1651.

[18] Zuloaga, J.; Prodan, E.; Nordlander, P. *Nano Lett.* **2009**, *9*, 887.

[19] Chen, M.-W.; Myroshnychenko, V.; Chen, C. H.; Deng, J.-P.; Mou, C.-Y.; de Abajo, F. J. G. *Nano Lett.* **2009**, *9*, 399.

[20] Aćimović, S. S.; Kreuzer, M. P.; González, M. U.; Quidant, R. *ACS Nano*, **2009**, *3*, 1231.

[21] Tabor, C.; Haute, D. V.; El-Sayed, M. A. *ACS Nano*, **2009**, *3*, 3670.

[22] Yang, S.-C.; Kobori, H.; He, C.-L.; Lin, M.-H.; Chen, H.-Y.; Li, C.; Kanehara, M.; Teranishi, T.; Gwo, S. *Nano Lett.*, **2010**, *10*, 632.

[23] Huang, J.-S.; Kern, J.; Geisler, P.; Weinmann, P.; Kamp, M.; Forchel, A.; Biagioni, P.; Hecht, B. *Nano Lett.*, **2010**, *10*, 2105.

[24] Merlein, J.; Kahl, M.; Zuschlag, A.; Sell, A.; Halm, A.; Boneberg, J.; Leiderer, P.; Leitenstorfer, A.; Bratschitsch, R. *Nat. Photon.*, **2008**, *2*, 230.

[25] Huang, F.; Baumberg, J. J. *Nano Lett.* **2010**, *10*, 1787.

[26] Fan, J. A.; Wu, C.; Bao, K.; Bao, J. M.; Bardhan, R. Halas, N. J.; Manoharan, V. N.; Nordlander, P.; Shvets, G.; Capasso, F. *Science* **2010**, *328*, 1135.

[27] Luk'yanchuk, B.; Zheludev, N. I.; Maier, S. A.; Halas, N. J.; Nordlander, P.; Giessen, H.; Chong, C. T. *Nat. Mater.* **2010**, *9*, 707.

[28] Bachelier, G.; Russier-Antoine, I.; Benichou, E.; Jonin, C.; Del Fatti, N.; Vallée, F.; Brevet, P.-F. *Phys. Rev. Lett.* **2008**, *101*, 197401.

[29] Sheikholeslami, S.; Jun, Y.; Jain, P. K.; Alivisatos, A. P. *Nano Lett.* **2010**, *10*, 2655.

[30] Brown, L. V.; Sobhani, H.; Lassiter, J. B.; Nordlander, P.; Halas, N. J. *ACS Nano* **2010**, *4*, 819.

[31] Liu, N.; Weiss, T.; Mesch, M.; Langguth, L.; Eigenthaler, U.; Hirscher, M.; Sönnichsen, C.; Giessen, H. *Nano Lett.* **2010**, *10*, 1103.

[32] Liu, N.; Langguth, L.; Weiss, T.; Kästel, J.; Fleischhauer, M.; Pfau, T.; Giessen, H. *Nat. Mater.* **2009**, *8*, 758.

[33] Sámson, Z. L.; MacDonald, K. F.; De Angelis, F.; Gholipour, B.; Knight, K.; Huang, C. C.; Di Fabrizio, E.; Hewak, D. W.; Zheludev, N. I. *Appl. Phys. Lett.* **2010**, *96*, 143105.

[34] Alù, A.; Engheta, N. *Nat. Photon.*, **2008**, *2*, 307.

[35] Slaughter, L. S.; Wu, Y.; Willingham, B. A.; Nordlander, P.; Link, S. *ACS Nano* **2010**, *4*, 4657.

[36] Shao, L. *Angle-, Energy- and Position-Resolved Plasmon Resonance Coupling between Gold Nanocrystals.* Mphil. Thesis, Department of Physics, The Chinese University of Hong Kong, 2008.

[37] Woo, K. C.; Shao, L.; Chen, H. J.; Liang, Y.; Wang, J. F.; Lin, H.-Q. *ACS Nano* **2011**, *5*, 5976.

[38] Chen, H. J.; Shao, L.; Li, Q.; Wang, J. F. *Chem. Soc. Rev.* **2013**, *42*, 2679.

[39] Sun, Z. H.; Ni, W. H.; Yang, Z.; Kou, X. S.; Li, L.; Wang, J. F. *Small* **2008**, *4*, 1287.

[40] Sudeep, P. K.; Joseph, S. T. S.; Thomas, K. G. *J. Am. Chem. Soc.* **2005**, *127*, 6516.

[41] Zhang, S. Z.; Kou, X. S.; Yang, Z.; Shi, Q. H.; Stucky, G. D.; Sun, L. D.; Wang, J. F.; Yan, C. H. *Chem. Commun.* **2007**, 1816.

[42] Chang, J.-Y.; Wu, H. M.; Chen, H.; Ling, Y.-C.; Tan, W. H. *Chem. Commun.* **2005**, 1092.

[43] Nie, Z. H.; Fava, D.; Kumacheva, E.; Zou, S.; Walker, G. C.; Rubinstein, M. *Nat. Mater.* **2007**, *6*, 609.

[44] Nie, Z. H.; Fava, D.; Rubinstein, M.; Kumacheva, E. *J. Am. Chem. Soc.* **2008**, *130*, 3683.

[45] Zhang, L.; Chen, H. J.; Wang, J. F.; Li, Y. F.; Wang, J.; Sang, Y.; Xiao, S. J.; Zhan, L.; Huang, C. Z. *Small* **2010**, *6*, 2001.

[46] Ni, W. H.; Kou, X. S.; Yang, Z.; Wang, J. F. *ACS Nano* **2008**, *2*, 677.

[47] Ropers, C.; Park, D. J.; Stibenz, G.; Steinmeyer, G.; Kim, J.; Kim, D. S.; Lienau, C. *Phys. Rev. Lett.* **2005**, *94*, 113901.

[48] Christ, A.; Ekinci, Y.; Solak, H. H.; Gippius, N. A.; Tikhodeev, S. G.; Martin, O. J. F. *Phys. Rev. B* **2007**, *76*, 201405.

[49] Christ, A.; Martin, O. J. F.; Ekinci, Y.; Gippius, N. A.; Tikhodeev, S. G. *Nano Lett.* **2008**, *8*, 2171.

[50] Verellen, N.; Van Dorpe, P.; Huang, C. J.; Lodewijks, K.; Vandenbosch, G. A. E.; Lagae, L.; Moshchalkov, V. V. *Nano Lett.* **2011**, *11*, 391.

Chapter 5

Position-Resolved Plasmon Coupling in Gold Nanorod–Nanosphere Heterodimers

In the previous chapters (Chapter 1 and Chapter 4), I have introduced the plasmonic coupling in metal nanostructures, which has been extensively explored due to its potentials in various applications.[1] The near-field interactions in coupled metallic nanostructures enable the excitation of new plasmon modes, such as high-order electric multipole and magnetic dipole plasmon modes.[2] The interferences between different plasmon modes thereafter result in fascinating phenomena in coupled metal nanostructures, such as spectral splitting,[3] plasmonic Fano resonance,[4] and electromagnetically induced transparency.[5] Due to their unique plasmonic features, coupled metal nanostructures can serve as one- and three-dimensional plasmon rulers[6,7] owing to the strong dependence of the scattering spectrum on the interparticle spacing as well as the spatial configuration. Plasmon coupling-induced spectral changes and Fano resonances have been employed for developing ultrasensitive biological and chemical sensors, optical switches, metamaterials and novel optical media.

Heterodimers of metal nanocrystals, as I have mentioned in Chapter 4, exhibit richer plasmon coupling behaviors arising from symmetry breaking. In these heterodimers, multipolar plasmon modes can be excited through near-field interactions and the Fano interference between subradiant and superradiant plasmon modes can usually be observed. These heterodimers exhibit light responses that are dependent on the incident direction [8–10] and possess unique electric field distributions at different plasmon modes.[11] They therefore have potentials for nanoscale directional color router[10] and subwavelength imaging.

The plasmon coupling in metal nanocrystal heterodimers is expected to be dependent not only on the metal type and the size difference but also on the spatial arrangement of the two components. Nearly all of the plasmonic heterodimers investigated previously are rotationally symmetric about the interparticle axis, where the spatial symmetry is not completely broken. Breaking the rotational symmetry will undoubtedly provide more freedom for controlling the plasmonic properties of heterodimers. In this chapter, I will investigate the plasmon coupling in the heterodimers made of a large Au nanorod and a small Au nanosphere, where the nanosphere is located at different positions on the nanorod surface, as shown schematically in Figure 5.1. Au nanorods are chosen due to their synthetically adjustable plasmon energies and polarization-sensitive optical responses. The anisotropic geometry of the nanorod causes the rotational symmetry to be broken as the nanosphere is moved around the nanorod.

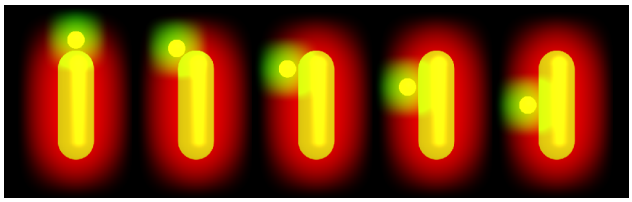

Figure 5.1 Schematic showing the plasmon resonance of a Au nanorod perturbed by the plasmon resonance of an adjacent small Au nanosphere that is located at different positions around the nanorod.

The small spatial perturbation introduced by the nanosphere can generate dramatic changes in the scattering spectrum of the heterodimer. Such dramatic spectral variation has already been presented in my MPhil thesis [12] and will be briefly discussed in Section 5.1 here. My further investigation indicates that the dipole of the nanosphere rotates around that of the nanorod in the bonding dipole–dipole mode when the nanosphere is moved around the nanorod. Like the Au nanorod heterodimers I have shown in Chapter 4, the Au nanorod–nanosphere heterodimers exhibit Fano resonance. The Fano interference strength was found to be strongly dependent of the geometrical configuration. Details will be presented in Section 5.2. Compared to more complex metal nanostructures supporting symmetry breaking, such as trimers and tetramers, the

Au nanorod–nanosphere heterodimers are easier to prepare, which is attractive for their practical applications. In Section 5.3, I will explore the potential of the heterodimers for designing plasmon rulers of two spatial coordinates. All the contents of this chapter have been published in *Nano Letters* in 2012.[13]

5.1 Distinct Plasmonic Manifestation Induced by Spatial Perturbation

The Au nanorods and nanospheres stabilized with cetyltrimethylammonium bromide (CTAB) were synthesized following the growth method introduced in Chapter 3. The scanning electron microscopy (SEM) image of the nanorod sample and the transmission electron microscopy (TEM) image of the nanosphere sample are shown in Figure 5.2a and b. The nanorod sample exhibits a longitudinal plasmon resonance wavelength of 654 nm in aqueous solutions and has an average length of 85 ± 6 nm, diameter of 38 ± 4 nm, and aspect ratio of 2.2 ± 0.2. The nanosphere sample has an average diameter of 24 ± 2 nm, with the plasmon resonance wavelength at 527 nm in an aqueous environment. For the formation of the heterodimers, the two nanocrystal samples were mixed and dispersed in a mixture of H_2O and CH_3CN. 1,8-octanedithiol, as a link between the nanorods and nanospheres,[14,15] was then added in the mixture solution. The assembly process in the solution was monitored spectrally (Figure 5.2g). The assembled nanocrystals were deposited on conductive indium tin oxide (ITO)-coated glass slides. Figure 5.2c–e show the TEM images of representative Au nanorod–nanosphere heterodimers. The position of the nanosphere relative to the nanorod varies among different heterodimers. The spacing between the two nanocrystals was estimated from high-resolution TEM images (Figure 5.2f) to be ~1 nm, which is consistent with the values obtained in the previous studies.[14,15]

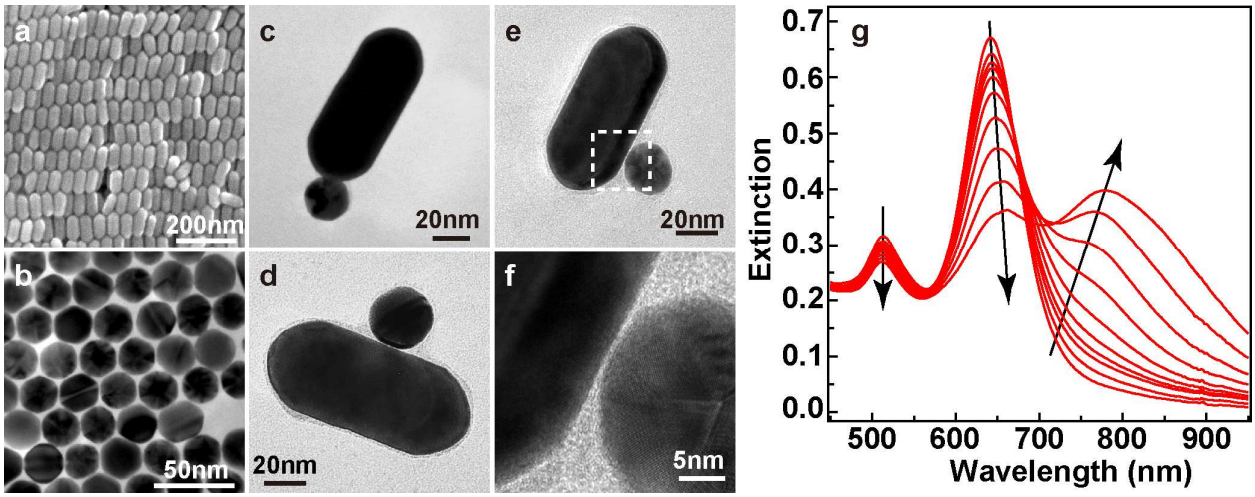

Figure 5.2 Preparation of the Au nanorod and nanosphere monomers and heterodimers. (a) SEM image of the Au nanorods. (b) TEM image of the Au nanospheres. (c–e) TEM images of three representative nanorod–nanosphere heterodimers. (f) High-resolution TEM image of the area indicated with a dashed box in (e). The image shows the presence of a gap between the two nanocrystals. (g) Extinction spectra of the Au nanorod–nanosphere solution recorded as a function of time after the addition of the dithiol molecules. The arrows indicate the time-increasing direction. The particle concentrations of the nanorods and nanospheres in the solution were ~0.006 and 0.1 nM. The dithiol concentration was 1 μM. The interval between two consecutive spectra was 2 min.

I utilized the pattern-matching method introduced in Chapter 3 to correlate the single-particle dark-field scattering spectrum of each heterodimer with its geometry revealed by SEM imaging. Figure 5.3 shows the SEM images of four representative nanorod–nanosphere heterodimers with the nanosphere located at different positions on the nanorod and the corresponding scattering spectra. The scattering spectra are observed to vary systematically as a function of the position of the nanosphere on the nanorod (Figure 5.3e). When the nanosphere is located at the end of the nanorod, two scattering peaks are detected, with the higher-energy one much weaker than the lower-energy one. In comparison, a single Au nanorod exhibits only one strong scattering peak.[12,14] The two scattering peaks of the heterodimer arise from the plasmon coupling between the nanorod and nanosphere. When the nanosphere is moved from the end through the shoulder to the side of the nanorod at a fixed gap distance, the intensity of the higher-energy peak gets relatively stronger, and the two peaks become closer spectrally. When

the nanosphere is at the exact central side of the nanorod, the two scattering peaks coalesce into one. A small bump is present around 530 nm on all the scattering spectra. This weak peak is contributed mainly by the coupling between the heterodimers and the substrate and excited by light polarized perpendicular to the substrate plane.

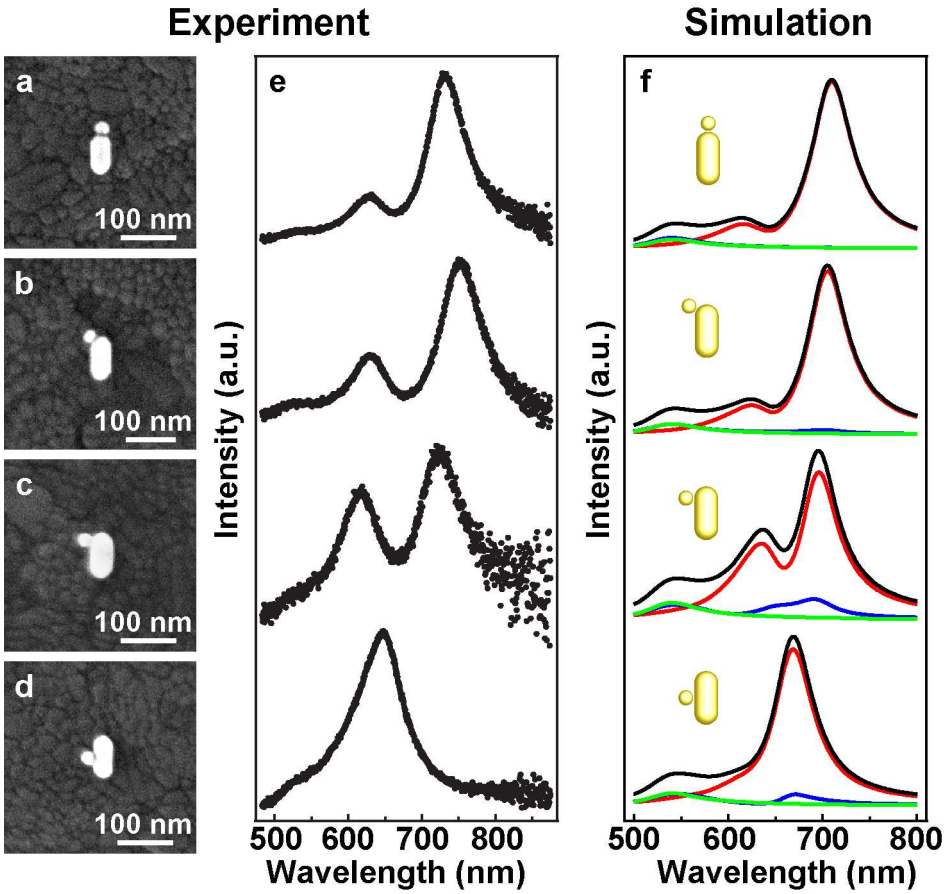

Figure 5.3 Plasmonic responses of four representative Au nanorod–nanosphere heterodimers. (a–d) SEM images. (e) Corresponding experimental scattering spectra. Each spectrum is normalized and shifted vertically for clarity. (f) Calculated scattering spectra. The red, blue, and green curves represent the scattering spectra when the excitation light is polarized longitudinally, transversely, and vertically, respectively. The black curves are the sums.

I measured the scattering spectra of more than 100 heterodimers. The position of the nanosphere on the nanorod is statistically randomly distributed in these heterodimers. More than 80% of the heterodimers with the nanosphere off the exact central side of the nanorod show the two peaks on their scattering spectra. The overall shapes of the scattering spectra vary systematically, as described above, although the positions and relative intensities of the two

peaks also fluctuate among the heterodimers with the same geometrical arrangement under the SEM imaging resolution. The fluctuations can be ascribed to the size distributions of both the Au nanorod and nanosphere samples and the slight variation in the gap distance caused by the flexibility of the linking molecules. To exclude the conductive coupling between the nanorod and nanosphere in the heterodimers, I performed a control experiment, where the heterodimers deposited on the ITO substrates were thermally treated. The scattering spectra of the heterodimers after the thermal treatment are dramatically different from those before the treatment (results are not shown here; please refer to the discussions in my MPhil thesis [12] for more details). Such spectral changes result from the formation of conductive contacts caused by the thermal treatment.[12,14,16,17] The results from this control experiment verify the existence of a gap in the nanorod–nanosphere heterodimers. Moreover, in order to reveal the origin of the different scattering peaks, I also excited the heterodimers with polarized white light. The experiment setup can be found in a related thesis.[18,19] The polarization measurement reveals that the two scattering peaks are excited when the white light source is polarized along the length axis of the Au nanorod (results are not shown here; please refer to the discussions in my MPhil thesis [12] for more details). This finding is consistent with the previous result for the plasmon modes in Au nanosphere–nanoshell heterodimers.[8] The plasmon response excited by the light source polarized perpendicular to the length axis of the nanorod is too weak to be detected in my experiments.

Finite-difference time-domain (FDTD) calculations were carried out to understand the plasmonic properties of a nanorod perturbed by a nanosphere at varying spatial positions. Our previous studies have shown that ITO substrates only induce a weak scattering peak in the spectral region of 500–550 nm for relatively small Au nanostructures.[12,14,16,18,19] The simulations were therefore performed in a homogeneous medium with a refractive index of 1.45 in order to clearly unravel the involved plasmon modes. Both the nanocrystal monomers and heterodimers were considered. The Au nanorod was modeled as a cylinder capped with a

hemisphere at each end. The Au nanosphere was modeled as an exact sphere. The gap distance between the nanorod and nanosphere was set at 1 nm. The nanocrystal sizes were adjusted slightly within the experimentally measured range to reach a good agreement between the calculated and measured scattering spectra. The final sizes used in the calculations were 79 nm in length and 42 nm in diameter for the nanorod and 24 nm in diameter for the nanosphere. The calculated scattering spectra of the four heterodimers with their geometrical arrangements shown in Figure 5.3a–d are plotted in Figure 5.3f for different excitation polarizations. The scattering for the excitation polarized parallel to the substrate and along the nanorod length axis (longitudinal polarization) is much stronger than that for the excitation polarized parallel to the substrate and along the direction perpendicular to the nanorod length axis (transverse polarization) and that for the excitation polarized perpendicular to the substrate (vertical polarization). The longitudinally polarized light can excite two scattering peaks, which agrees with the experimental results. A weak peak is observed around 540 nm for both the transversely and vertically polarized excitation. Taking into account of the ITO substrate will only increase the scattering intensity of this peak under the vertically polarized excitation owing to the coupling between the heterodimers and the substrate.[12,14,16] The overall variation trend in the calculated scattering spectra agrees qualitatively with that observed experimentally. The differences between the measured and calculated spectra are ascribed to the nanocrystal size distributions and small fluctuation in the interparticle gap distance in the experiments, the use of a homogeneous dielectric environment in the calculations, and the dissimilar excitation and collection geometries between the calculations and measurements. In particular, the higher-energy scattering peaks on the measured spectra are stronger than those on the simulated spectra. The stronger scattering peaks on the measured spectra can be attributed to smaller-than-1-nm gap distances.

5.2 Hybridized Plasmonic Mode Assignments, Rotating Plasmonic Dipole

Phenomenon, and Fano Resonance

The distinct plasmonic response of the Au nanorod–nanosphere heterodimers has been observed. The plasmonic scattering spectra are quite sensitive to the spatial perturbation of the small Au nanosphere. To further understand this phenomenon, more simulations were carried out and the results are provided in Figure 5.4a, which illustrates how the scattering spectrum evolves as the Au nanosphere is moved from the end to the central side of the Au nanorod. A vertical displacement, *h*, was employed to designate the position of the nanosphere on the nanorod. *h* equals 0 when the nanosphere is located at the exact central side of the nanorod, and it assumes the maximal value of 52.5 nm when the nanosphere is at the end of the nanorod. Only the longitudinally polarized excitation was considered. As *h* gradually decreases from 52.5 to 0 nm, the lower-energy scattering peak blue-shifts from 709 to 669 nm, while the higher-energy one first red-shifts from 616 to 647 nm and then becomes submerged under the lower-energy peak.

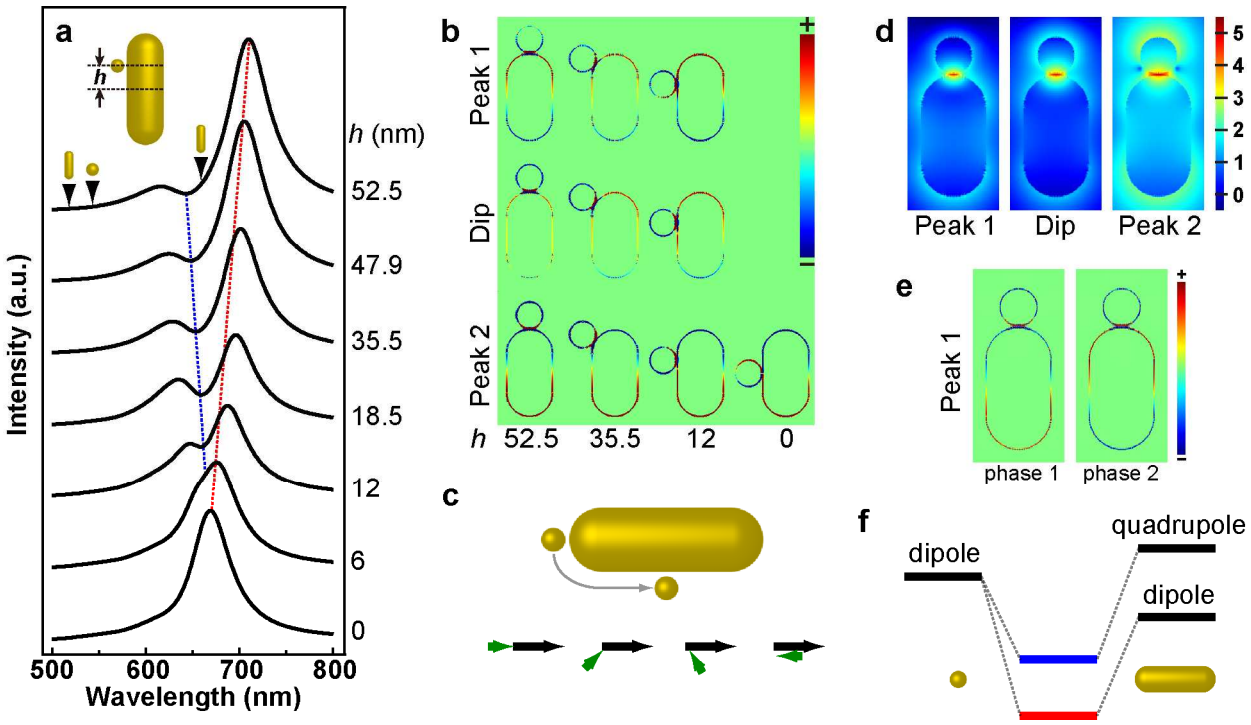

Figure 5.4 Scattering spectral evolvement and plasmon hybridization in the Au nanorod–nanosphere heterodimers. (a) Calculated scattering spectra of the heterodimers under the longitudinally polarized excitation. The inset shows the definition of the displacement, *h*, of the nanosphere. The spectral positions of the dipolar and quadrupolar plasmon modes of the naonrod and the dipolar plasmon mode of the nanosphere are indicated with the downward

arrows. The blue and red dotted lines indicate the dip and lower-energy peak positions. (b) Charge distributions on the central cross sections of the heterodimers for the higher- (Peak 1) and lower-energy (Peak 2) scattering peaks and the dip between them. (c) Schematic elucidating how the plasmonic dipole of the nanosphere rotates around that of the nanorod as the nanosphere is moved from the end to the exact central side of the nanorod. (d) Electric field intensity enhancement contours obtained from the FDTD calculations for the nanorod–nanosphere heterodimer with the nanosphere placed at the end of the nanorod. The excitation light was polarized along the nanorod length axis. The contours were calculated at the Peak 1, Peak 2 and the dip wavelength. The enhancement is drawn at the logarithmic scale. (e) Plots of the charge distributions (red, positive; blue, negative) on the central cross section of the heterodimer at the Peak 1 wavelength. The nanosphere is located at the end of the nanorod. The charge distributions were obtained from the electric field intensity contours captured during the FDTD simulation. The two charge plots were acquired under the same excitation frequency at two different time points with a corresponding phase difference of 90°. They exhibit a dipole–dipole (left) and dipole–quadrupole (right) bonding mode. (f) Plasmon hybridization diagram for the nanorod–nanosphere heterodimer.

To assign the hybridized plasmon modes in the heterodimers, I determined the charge distributions at different excitation wavelengths from the calculated electric field contours. The dipolar plasmon modes of the nanosphere and nanorod are at 543 nm (2.28 eV) and 659 nm (1.88 eV), respectively. The wavelength of the quadrupolar plasmon mode of the nanorod was calculated by using a dipole source [20] to be 518 nm (2.39 eV), following the same method introduced in Chapter 4. When the nanosphere is located at the end of the nanorod, the two scattering peak wavelengths of the heterodimer were obtained to be 709 nm (1.75 eV) and 616 nm (2.01 eV). The charge distributions (Figure 5.4b), as well as the electric field intensity enhancement contours (Figure 5.4d), on the central cross section of the heterodimer indicate that the two scattering peaks and the dip in between result from the hybridization of the plasmon modes of the nanorod and nanosphere. The two nanocrystals exhibit unambiguously an attractive dipole–dipole interaction at the lower-energy peak, suggesting the dominance of the bonding dipole–dipole mode at the lower-energy peak. The charge distributions of the nanosphere remain to be dipolar at both the higher-energy peak and the dip, while those of the nanorod turn out to contain both dipolar and multipolar characteristics. At the dip, the nanorod mainly exhibits a

quadrupolar charge distribution. At the higher-energy peak, both dipole-dominated and quadrupole-dominated charge contours are obtained, depending on the phase angle of the excitation light wave (Figure 5.4e). The two nanocrystals in the heterodimer, no matter what type of hybridization behaviors they present, always display an attractive manner. Therefore the heterodimer exhibits a bonding dipole–dipole pattern at the lower-energy peak, a bonding dipole–quadrupole one at the dip, and a mixture of them at the higher-energy peak. Since the Au nanosphere in the heterodimer is much smaller than the nanorod, it exhibits only a dipolar plasmon mode. Due to the closeness in the plasmon energy levels of the monomers, the dipolar plasmon mode (2.28 eV) of the nanosphere can hybridize largely with both the dipolar (1.88 eV) and quadrupolar (2.39 eV) plasmon modes of the nanorod, forming the bonding dipole–dipole (~1.75 eV) and dipole–quadrupole (~1.93 eV) hybridized modes, as shown in Figure 5.4f.

When the nanosphere is moved away from the nanorod end and the displacement *h* is reduced, the nanosphere and nanorod both maintain their dipolar charge patterns at the lower-energy peak, which blue-shifts gradually (Figure 5.4a). The nanosphere rotates its plasmonic dipole as it is moved from the end to the central side of the nanorod. At the exact central side, the dipoles of the nanosphere and nanorod are oriented oppositely. Throughout the positional changes of the nanosphere on the nanorod, the two dipoles are always in attractive bonding configurations (Figure 5.4b and c), and the energy of the bonding dipole–dipole mode increases slightly as *h* is decreased. The rotating plasmonic dipole phenomenon is consistent with the hot spots observed in the electric field intensity enhancement contours (Figure 5.5). No matter where the nanosphere is placed on the nanorod, the gap region between the two nanocrystals always exhibits a large electric field enhancement at the lower-energy scattering peak, forming a so-called "hot spot" (Figure 5.5). This result is different from the reduction in the electric field in the gap region exhibited by Au nanorod dimers.[12,14] At the dip, the heterodimers always exhibit a bonding dipole–quadrupole mode. The slight red shift of the dip

on the scattering spectra with decreasing h (Figure 5.4a) suggests the strengthening of the attractive interaction between the dipole of the nanosphere and the quadrupole of the nanorod.

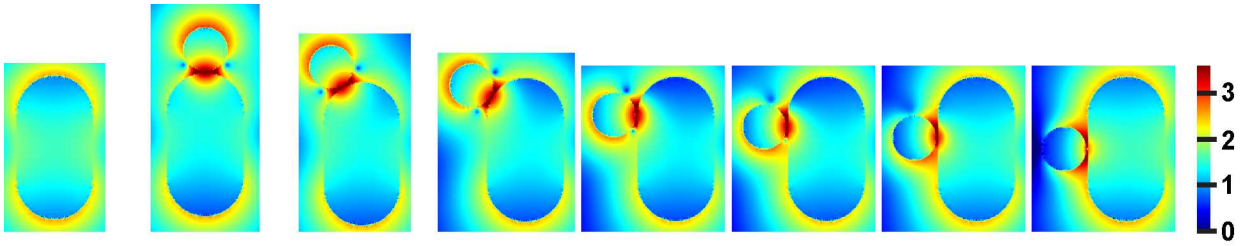

Figure 5.5 Electric field intensity enhancement contours obtained from the FDTD calculations for the nanorod monomer and nanorod–nanosphere heterodimers with the nanosphere placed at different positions. The excitation light was polarized along the nanorod length axis. The contour for the nanorod monomer was calculated at its longitudinal plasmon wavelength. The contours for the heterodimers were calculated at their respective lower-energy scattering peak wavelengths. The enhancement is drawn at the logarithmic scale.

The pronounced dips observed in both the measured and simulated scattering spectra are attributed to the Fano interference between the superradiant bonding dipole–dipole and the subradiant bonding dipole–quadrupole plasmon modes. The charge contours in Figure 5.4b indicate that the quadrupolar mode of the nanorod can be excited through near-field interaction in the presence of the nanosphere. It can thus hybridize with the dipolar mode of the nanosphere. Because the energies of the bonding dipole–dipole and dipole–quadrupole modes are close to each other and the former mode has a broad line width, the two modes interfere destructively at their common frequency. The destructive interference produces a Fano resonance, which is reflected by the dips on the scattering spectra.

The Fano profiles of the calculated scattering spectra of the nanorod–nanosphere heterodimers can be well reproduced by the classical two-oscillator model that has been introduced in Chapter 2. The bonding dipole–dipole and dipole–quadrupole plasmon modes are modeled as two interacting one-dimensional mechanical oscillators of energies ω_1 and ω_2 with an interacting strength of ν_{12} (Figure 5.6a). The oscillator with an energy of ω_1, corresponding to

the superradiant mode, is driven by a periodic harmonic force $F(t) = F_0 e^{-i\omega t}$. The equations of motion of the two oscillators are described by

$$\ddot{x}_1 + \gamma_1 \dot{x}_1 + \omega_1^2 x_1 - \nu_{12} x_2 = F_0 e^{-i\omega t} \tag{5.1}$$

$$\ddot{x}_2 + \gamma_2 \dot{x}_2 + \omega_2^2 x_2 - \nu_{12} x_1 = 0 \tag{5.2}$$

where x_i specifies the displacement from the equilibrium position of the oscillator, and γ_i represents the friction coefficient accounting for the energy dissipation of the oscillator. The equations can be solved in the form $x_i = c_i e^{-i\omega t}$. The scattering power of the system is expressed by $P(\omega) = |\ddot{x}_1 + \ddot{x}_2|^2$. The scattering spectra calculated from the two-oscillator model fit the FDTD simulation results very well (Figure 5.6b,c). Figure 5.6a shows the variations of ω_1, ω_2, and ν_{12} as a function of h. The variation trends of ω_1 and ω_2 agree well with the FDTD simulation results. As the nanosphere is moved away from the rod end, the dipole–dipole bonding energy ω_1 increases and the dipole–quadrupole bonding energy ω_2 decreases. I also find that ω_1 and ω_2 change rapidly after the nanosphere enters into the cylindrical body region of the nanorod ($h \leq$ 18.5 nm). In addition, the interaction strength between the two bonding plasmon modes ν_{12} generally becomes weaker with decreasing h. The reduction in the ν_{12} can be attributed to the decrease in the oscillator strengths of the two bonding modes. The Fano dip disappears when the nanosphere arrives at the exact central side of the nanorod, where h equals 0. Despite nearly the same energy of the two bonding plasmon modes at this position, the quadrupolar mode of the nanorod can hardly be excited, owing to the increase in the symmetry of the system. As a result, the oscillator strength of the bonding dipole–dipole mode is much larger than that of the dipole–quadrupole mode, and the interaction strength ν_{12} becomes very small.

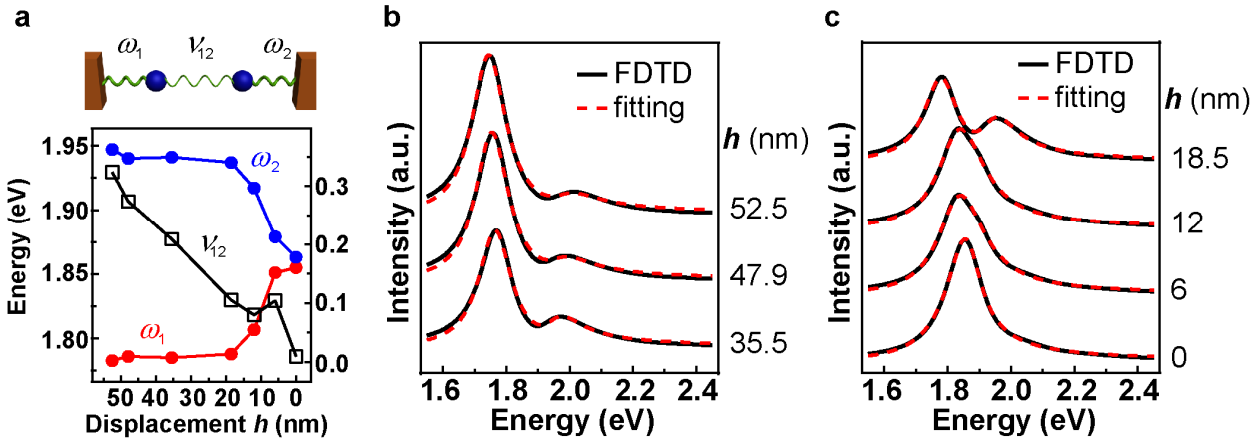

Figure 5.6 Coupled harmonic oscillator model for the plasmonic response of the Au nanorod–nanosphere heterodimer. (a) Schematic showing the model. Oscillator 1 is driven by a periodic harmonic force. The eigenenergies of the two oscillators, ω_1 and ω_2 (red and blue, respectively, left axis), and their coupling strength, V_{12} (black, right axis), are plotted against the displacement of the nanosphere. (b,c) FDTD-simulated scattering spectra (black solid curves) that have been shown in Figure 5.4a for the Au nanorod–nanosphere heterodimers and the fittings (red dashed curves) based on the two-harmonic oscillator model.

5.3 Potential for Improved Plasmon Rulers

The evolving mechanism of the scattering spectrum as a function of the position of the nanosphere on the nanorod has been understood above. I next studied the effects of the gap distance and the nanocrystal dimensions on the plasmonic response of the nanorod perturbed by the nanosphere by placing the nanosphere at the end of the nanorod. Figure 5.7a shows how the scattering spectrum of the nanorod–nanosphere heterodimer changes as the gap distance *d* is varied. At a very small *d* value of 0.5 nm, the heterodimer displays a distinct Fano profile on its scattering spectrum. As *d* is increased, the higher-energy scattering peak gets weaker while the lower-energy peak becomes stronger, indicating the gradual weakening of the destructive Fano interference between the bonding dipole–dipole and dipole–quadrupole plasmon modes. The double-peak spectral feature vanishes when *d* is larger than 1.5 nm. The gap distance-dependent result indicates that the perturbation caused by the nanosphere is remarkably sensitive to the gap distance. I then fixed the gap distance at 1 nm and changed the nanorod length *L*. The lower-energy peak increases in intensity and exhibits a gradual red shift with increasing *L*, while

the higher-energy peak decreases slightly in intensity and red-shifts slightly (Figure 5.7b). The red shift of the bonding dipole–dipole mode is mainly caused by the red shift of the longitudinal dipolar mode of the nanorod as its aspect ratio is increased. The intensity increase of the lower-energy peak results from the increase in the polarizability of the nanorod as *L* gets larger. I further fixed the gap distance *d* at 1 nm and the nanorod length *L* at 79 nm and varied the nanosphere diameter *D*. The gradual enlargement of the nanosphere leads to the red shift of its dipolar plasmon mode and consequently the red shift of the bonding dipole–dipole mode of the heterodimer, but the higher-energy scattering peak wavelength remains nearly unchanged (Figure 5.7c). Both the lower- and higher-energy scattering peaks increase slightly in intensity with *D* due to the increase in the polarizability of the nanosphere. Moreover, I examined the effect of the gap distance on the scattering spectra of the heterodimers with the nanosphere placed at different vertical displacements. The lateral displacement *s* of the nanosphere, defined by the distance from the nanosphere center to the nanorod length axis, was increased gradually to enlarge the gap distance *d*. As an example, Figure 5.7d shows how the scattering spectrum of the heterodimer changes as *s* is varied while the vertical displacement *h* is fixed at 35.5 nm. Similar to the case shown in Figure 5.7a, the heterodimer only displays a distinct Fano profile on its scattering spectrum at small gap distances. As *s* is increased, the lower-energy scattering peak blue-shifts gradually. The double-peak spectral feature vanishes when *s* reaches 30.5 nm, which corresponds to a gap distance of d = 1.9 nm. The spatial perturbation of the nanosphere on the plasmonic response of the nanorod is thereafter found to be extraordinarily sensitive to the gap distance and affected by the nanorod dimension. It is less sensitive to the size of the nanosphere. These results further explain the origins of the differences between our measured and calculated scattering spectra. In the experiments, the plasmonic features reflected on the scattering spectra are affected by the fluctuations in the gap distance and the nanocrystal sizes.

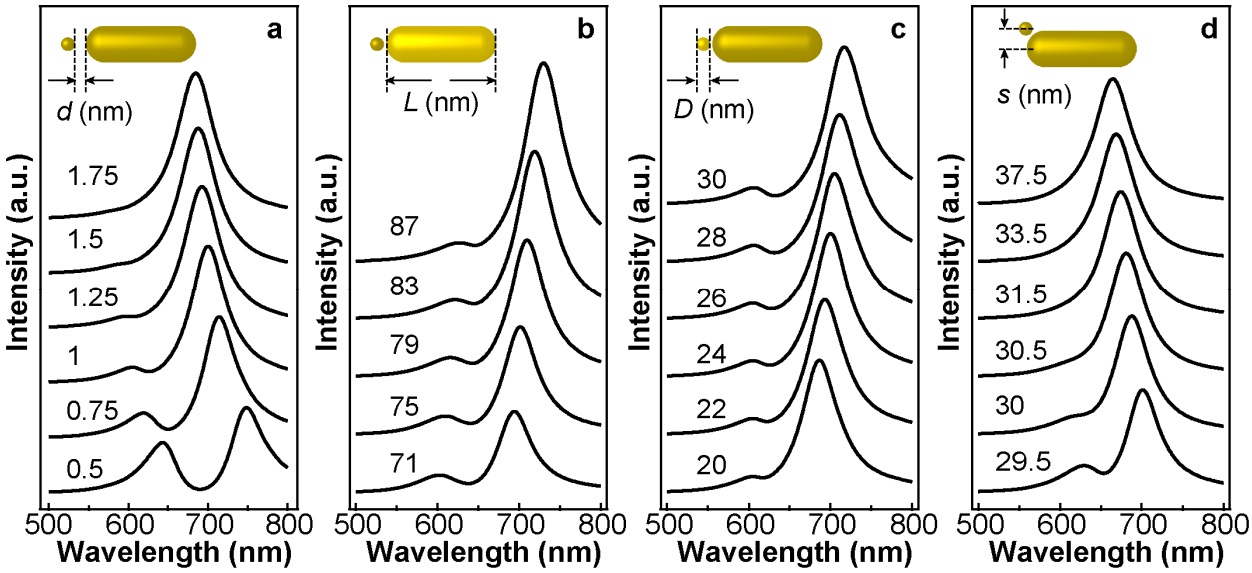

Figure 5.7 Calculated scattering spectra of the Au nanorod–nanosphere heterodimers. (a) The nanosphere is at the end of the nanorod. The gap distance *d* is varied. (b) The nanosphere is at the end of the nanorod with a gap distance of 1 nm. The nanorod length *L* is varied. (c) The nanosphere is at the end of the nanorod with a gap distance of 1 nm. The nanosphere diameter *D* is varied. (d) The vertical displacement *h* is fixed at 35.5 nm. The lateral displacement *s* is varied. The excitation light is longitudinally polarized. The insets show the schematics of the heterodimers.

Finally I extracted the scattering peak wavelengths and intensities from the calculated scattering spectra and plotted them versus the positions of the perturbing nanosphere in Figure 5.8. As described above, when the gap distance *d* is fixed at 1 nm, the wavelength of the lower-energy scattering peak becomes shorter and that of the higher-energy one gets longer with decreasing vertical displacement *h* (Figure 5.8a). The intensity of the lower-energy peak first decreases as the nanosphere is moved away from the end of the nanorod and then increases after the nanosphere enters into the cylindrical body region of the nanorod. The intensity of the higher-energy peak, in contrast, exhibits a monotonic increase. I also integrated the scattering intensity, which is an easy-to-measure quantity, from 500 to 800 nm and plotted it as a function of the vertical displacement *h* of the nanosphere in Figure 5.8b. The integrated intensity exhibits first a decrease and then an increase as the nanosphere is moved away from the end of the nanorod. The turning point also occurs when the nanosphere enters into the cylindrical body of the nanorod. On the other hand, when *h* is fixed at 35.5 nm, the wavelength of the lower-energy

scattering peak becomes shorter and thereafter closer to the longitudinal plasmon wavelength of the nanorod as the lateral displacement *s* is increased (Figure 5.8c). The integrated intensity first rises rapidly and then falls down slowly as *s* is increased from 29.5 to 38.5 nm (Figure 5.8d). The rapid intensity increase results from the fast weakening of the destructive Fano interference between the two bonding plasmon modes as the gap distance is increased. The subsequent decrease of the intensity originates from the reduction of the plasmon coupling strength between the two nanocrystals. The wavelength of the lower-energy scattering peak and the integrated scattering intensity of the heterodimer are further plotted as functions of both the vertical displacement *h* and the lateral displacement *s* (Figure 5.8e–g). The continuous blue shift of the peak wavelength indicates the weakening of the plasmon coupling as the nanosphere is moved away from the nanorod. The scattering intensity generally exhibits a rapid decrease when the nanosphere gets very close to the nanorod. These dependences allow for the determination of the spatial position of the perturbing nanosphere relative to the nanorod by monitoring the scattering peak wavelength and the total scattering intensity. The Au nanorod–nanosphere heterodimers therefore offer a potential means for measuring nanometric distance changes that are involved in biological and nanoelectromechanical systems.

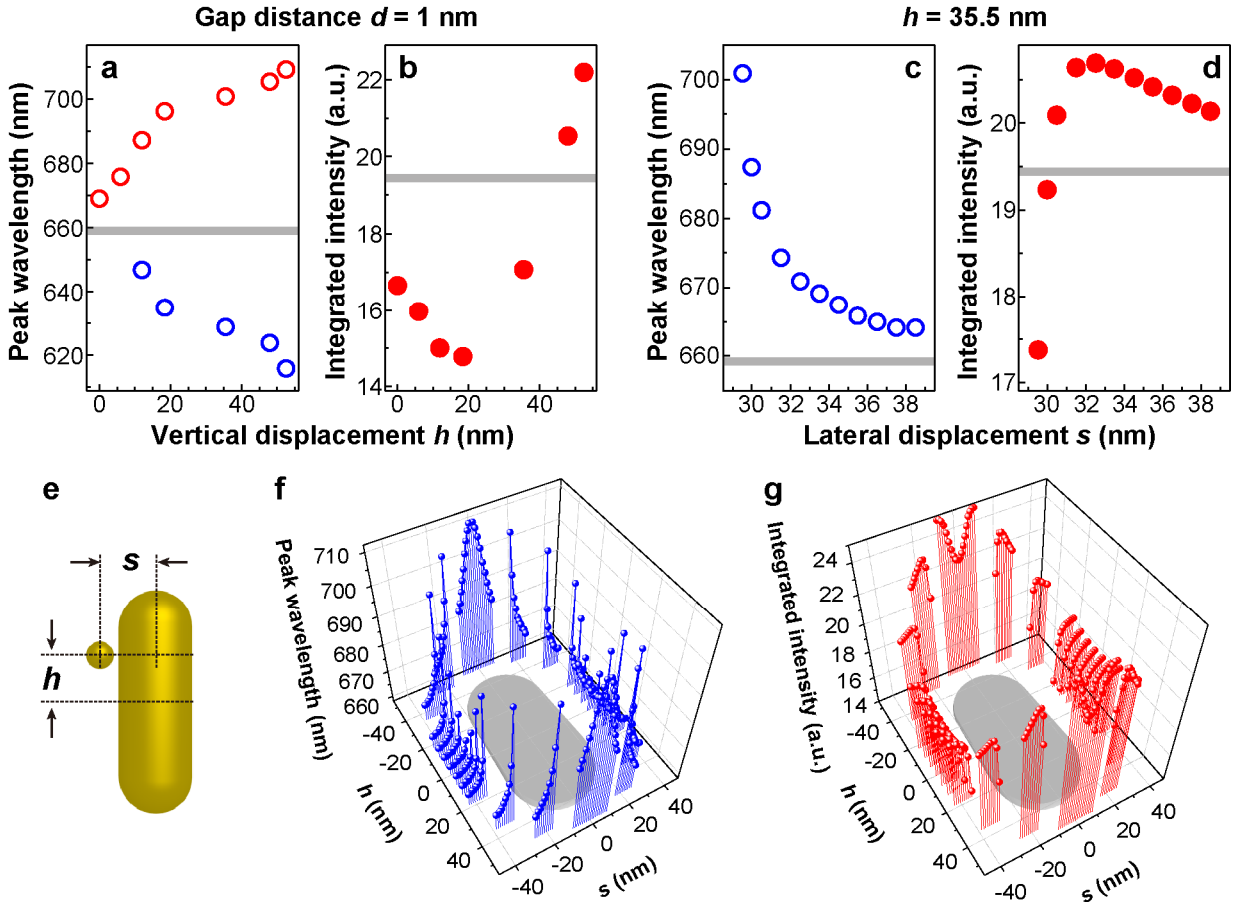

Figure 5.8 Dependence of the plasmon peak wavelength and the integrated scattering intensity on the nanosphere spatial coordinates in the Au nanorod–nanosphere heterodimers. (a) Wavelengths of the two scattering peaks as a function of the vertical displacement *h* when the gap distance *d* between the nanorod and nanosphere is fixed at 1 nm. The data were extracted from the calculated scattering spectra shown in Figure 5.4a. The red and blue colors denote the data points for the lower- and higher-energy peaks, respectively. (b) Integrated scattering intensity of the heterodimer versus *h* when *d* is fixed at 1 nm. (c) Wavelength of the lower-energy scattering peak as a function of the lateral displacement *s* when *h* is fixed at 35.5 nm. The data were extracted from the calculated scattering spectra shown in Figure 5.7d. (d) Integrated scattering intensity of the heterodimer versus *s* when *h* is fixed at 35.5 nm. The gray bars in (a–d) represent the corresponding values of a single Au nanorod. (e) Schematic of the coordinate system. (f) Wavelength of the lower-energy scattering peak as a function of both *h* and *s*. (g) Integrated scattering intensity as a function of both *h* and *s*. The gray elliptical shadows in (f) and (g) indicate the positions of the nanorods. The excitation light is longitudinally polarized.

As I have shown, the optical response of the heterodimer system varies with both the vertical and lateral displacements of the nanosphere. In particular, it is extremely sensitive to the movement of the nanosphere when the gap distance between the two nanocrystals is less than ~2

nm. I therefore expect that the nanorod–nanosphere system will offer a useful means for measuring the transformations of macromolecules in soft-matter systems. Molecules can be conjugated to small Au nanospheres. Molecular transformations can then be detected in real time by monitoring the plasmon coupling between the nanospheres and Au nanorods deposited or lithographically fabricated on substrates. A lookup database will be needed for determining the positions of the nanospheres relative to the nanorods accurately. As a result, the distinct plasmonic manifestations on Au nanorods induced by the spatial perturbations of Au nanospheres enable the use of dark-field scattering spectroscopy to identify the spatial movements of a metal nanocrystal at nanometric precision. The Au nanorod–nanosphere heterodimers can therefore be utilized as a potential plasmon ruler of two spatial coordinates.

5.4 Summary

In summary, I have shown in this chapter that the spatial perturbation of a Au nanosphere attached to a Au nanorod induces distinct variations on the scattering spectrum of the heterodimer. The plasmon resonance of the Au nanorod is strongly modulated by that of the small nanosphere. As the nanosphere is moved around the nanorod, the rotational symmetry of the Au nanorod–nanosphere heterodimer is broken, causing the coupled plasmon modes and their Fano interference to vary. The dipole of the nanosphere rotates around that of the nanorod and maintains favorable attractive configurations for the bonding dipole–dipole mode. The gap region between the two nanocrystals therefore always exhibits an electric field "hot spot". In addition, the plasmonic responses of the heterodimers are found to be highly sensitive to the gap distance and affected by the sizes of the constituting monomers. The breaking of the rotational symmetry provides an additional freedom for controlling the plasmonic properties of metal nanocrystal heterodimers. The optical response of the heterodimer system strongly depends on the position of the nanosphere. Therefore the Au nanorod–nanosphere can be potentially employed as a plasmon ruler to monitor the molecule transformations in biological systems.

References

[1] Halas, N. J.; Lal, S.; Chang, W.-S.; Link, S.; Nordlander, P. *Chem. Rev.* **2011**, *111*, 3913.

[2] Fan, J. A.; Wu, C.; Bao, K.; Bao, J. M.; Bardhan, R.; Halas, N. J.; Manoharan, V. N.; Nordlander, P.; Shvets, G.; Capasso, F. *Science* **2010**, *328*, 1135.

[3] Liu, N.; Guo, H. C.; Fu, L. W.; Kaiser, S.; Schweizer, H.; Giessen, H. *Nat. Mater.* **2008**, *7*, 31.

[4] Luk'yanchuk, B.; Zheludev, N. I.; Maier, S. A.; Halas, N. J.; Nordlander, P.; Giessen, H.; Chong, C. T. *Nat. Mater.* **2010**, *9*, 707.

[5] Liu, N.; Langguth, L.; Weiss, T.; Kästel, J.; Fleischhauer, M.; Pfau, T.; Giessen, H. *Nat. Mater.* **2009**, *8*, 758.

[6] Sönnichsen, C.; Reinhard, B. M.; Liphardt, J.; Alivisatos, A. P. *Nat. Biotechnol.* **2005**, *23*, 741.

[7] Liu, N.; Hentschel, M.; Weiss, T.; Alivisatos, A. P.; Giessen, H. *Science* **2011**, *332*, 1407.

[8] Brown, L. V.; Sobhani, H.; Lassiter, J. B.; Nordlander, P.; Halas, N. J. *ACS Nano* **2010**, *4*, 819.

[9] Pakizeh, T.; Käll, M. *Nano Lett.* **2009**, *9*, 2343

[10] Shegai, T.; Chen, S.; Miljković, V. D.; Zengin, G.; Johansson, P.; Käll, M. *Nat. Commun.* **2011**, *2*, 481.

[11] Sheikholeslami, S.; Jun, Y.-W.; Jain, P. K.; Alivisatos, A. P. *Nano Lett.* **2010**, *10*, 2655.

[12] Shao, L. *Angle-, Energy- and Position-Resolved Plasmon Resonance Coupling between Gold Nanocrystals.* MPhil. Thesis, Department of Physics, The Chinese University of Hong Kong, 2008.

[13] Shao, L.; Fang, C. H.; Chen, H. J.; Man, Y. C.; Wang, J. F.; Lin, H.-Q. *Nano Lett.* **2012**, *12*, 1424.

[14] Shao, L.; Woo, K. C.; Chen, H. J.; Jin, Z.; Wang, J. F.; Lin, H.-Q. *ACS Nano* **2010**, *4*, 3053.

[15] Pramod, P.; Thomas, K. G. *Adv. Mater.* **2008**, *20*, 4300.

[16] Chen, H. J.; Sun, Z. H.; Ni, W. H.; Woo, K. C.; Lin, H.-Q.; Sun, L. D.; Wang, J. F.; Yan, C. H. *Small*, **2009**, *5*, 2111.

[17] Slaughter, L. S.; Wu, Y.; Willingham, B. A.; Nordlander, P.; Link, S. *ACS Nano* **2010**, *4*, 4657.

[18] Chen, H. J. Localized Surface Plasmon Resonances of Gold Nanocrystals: Refractive Index Sensitivity, Plasmon Coupling, and Photothermal Conversion. Ph.D Thesis, Department of Physics, The Chinese University of Hong Kong. 2010.

[19] Chen, H. J.; Shao, L.; Ming, T.; Woo, K. C.; Man, Y. C.; Wang, J. F.; Lin, H.-Q. *ACS Nano* **2011**, *5*, 6754.

[20] Woo, K. C.; Shao, L.; Chen, H. J.; Liang, Y.; Wang, J. F.; Lin, H.-Q. *ACS Nano* **2011**, *5*, 5976.

Chapter 6

Graphene-Mediated Plasmon Coupling

Plasmon coupling between neighboring noble metal nanostructures can compress light into nanoscale regions, where the electromagnetic field intensity is enhanced by several orders of magnitude.[1] The greatly enhanced electromagnetic field intensity near the coupled nanostructures will permit strong light−matter interaction. In addition, the plasmon coupling is sensitively dependent on the interparticle spacing, the plasmon energy of each component, the nanocrystal shape, the spatial arrangement, and the surrounding dielectric environment.[1,2] In Chapters 4 and 5, I have systematically investigated the plasmon coupling in Au nanorod-based dimer structures. In these studies, I have found that slight perturbation in coupled plasmonic structures can give rise to rich changes on light scattering and absorption spectra.[2] As a result, coupled plasmonic structures can act as favorable candidates for ideal light absorbers with tunable absorption windows,[3] biosensing components,[4] and electromagnetically-induced transparency materials.[5] The high-sensitivity feature brought by plasmon coupling enables the use of slight external driving forces to control optical responses of artificial metal nanostructures. To actively modulate the plasmonic spectral features of coupled metal nanostructures can further facilitate the manipulation of light at the nanoscale and are strongly desired for future novel optoelectronic applications.[6]

Graphene is a promising two-dimensional material with a linear band structure with carries behaving like massless Dirac fermions, which therefore gives rise to many unique physical phenomena, ranging from anomalous quantum Hall effect, universal optical absorption, chiral Klein tunneling to fascinating plasmon excitation.[7] In addition to its impressive exotic band

structure, its optical interband transitions are strongly carrier-density-dependent.[8,9] Benefiting from its electrical and chemical adjustability, graphene has been widely studied for optical and photonic functions, such as optical modulation, photodetection, and tuning of surface plasmon polaritons.[10–12] Moreover, the gate electric potentials or external doping can be applied to graphene to adjust the Fermi energy of graphene, and as a result to introduce the tuning of the interband transitions in graphene.[9,13] It is thereafter possible to tune the dielectric properties of graphene, enabling the use of graphene to modulate the optical response of photonic and noble metal-based plasmonic structures.[14–17] However, the one-atomic-layer thickness of graphene makes light–graphene interaction very weak, which results in indistinctive light modulation and therefore the requirement of sophisticated device structures to increase the interaction.[18–21] It is still quite difficult to experimentally achieve a deep modulation of the plasmonic responses of metal nanostructures by graphene. Moreover, currently realized optical modulations by graphene are limited at the mid-infrared region. The gate electric potentials that can currently be applied to graphene even through state-of-the-art high-*k* dielectrics are still insufficient for inducing interband transitions at high energies.[13] This limit on the gate potentials has so far prevented graphene from being active in the visible-to-near-infrared (NIR) range, yet to push the optical response of graphene to this spectral range, though challenging, can further yield myriad applications, such as in molecular sensing, energy harvesting, and communications.

The key point for pushing graphene to be active in the visible-to-NIR region is to increase light–graphene interaction. The electromagnetic hot spots in the coupled plasmonic metal structures, where the electric field intensity can be enhanced by up to 10^5 times,[1,2,22] can provide a strategy for strengthening light–graphene interaction at the visible-to-NIR region. Additionally, since the plasmonic coupling between noble metals is quite sensitive to environmental perturbations, graphene interacting with coupled plasmonic structures is expected to be able to remarkably modulate plasmonic spectral features, because the dielectric properties of graphene can be varied by external stimuli.[14]

In this chapter, I will describe the use of coupled plasmonic structures to focus visible-to-NIR light for strengthening light–graphene interaction and therefore realize graphene-mediated plasmon coupling. In Section 6.1, the scattering responses of graphene-covered Au nanorod dimers are examined. No apparent change has been observed in the scattering spectra of the dimers when different gate voltages are applied onto the graphene sheet. The poor tunability might come from the weak interaction between graphene and the coupled metal structures, since the graphene sheet cannot be exactly placed into the nanorod–nanorod gap region where the electromagnetic field is greatly enhanced. We therefore propose an improved structure design in Section 6.2. Nanoantennas composed of colloidal Au nanospheres and a supporting Au film with sandwiched graphene are constructed by loading graphene into the sphere–film gap area. The graphene-loaded nanoantenna supports a series of cavity resonance-like responses at visible-to-NIR wavelengths. We show that our graphene–nanoantenna platform offers a great opportunity for circumventing the problems met in previous light–graphene interaction investigations. Graphene fills in the nanocavity formed between the Au nanosphere and film, where the electromagnetic field is greatly concentrated. The large field enhancement allows visible-to-NIR light with frequencies far away from the interband optical transitions of graphene to be squeezed in the nanocavity. As a result, the interaction between visible-to-NIR light and ultrathin, nearly transparent graphene is remarkably reinforced. Moreover, apart from the interband transition variations at infrared frequencies, electrical gating or chemical doping of graphene can also cause large changes in the real part (ε'_G) of its dielectric function in the visible-to-NIR region, which arises from the intraband transition variations. This optical response change caused by the tunable screening effect (tunable ε'_G) can further be amplified by the plasmonic nanoantenna. As a result, the reinforced light–graphene interaction together with the tunable screening effect of graphene enables the modulation of the plasmonic response of the graphene-loaded nanoantenna at visible-to-NIR frequencies.[13] A brief summary will be given in Section 6.3. The contents in this chapter have not been published.

6.1 Graphene-Covered Gold Nanorod Dimers

The Au nanorods stabilized with cetyltrimethylammonium bromide (CTAB) were first synthesized following the growth method introduced in Chapter 3.[22] The TEM image of the nanorod sample are shown in Figure 6.1a. The average diameter, length, and aspect ratio of the Au nanorods are (32 ± 3) nm, (63 ± 5) nm, and 2.0 ± 0.2, respectively. The Au nanorods were then dispersed in a mixture of H_2O and CH_3CN, and assembled by a linking molecule, 1,8-octanedithiol, to form Au nanorod dimers (Figure 6.1b–f). The two Au nanorods are connected in an end-to-end manner, and the spacing between them was estimated from the high-resolution TEM images (Figure 6.1e) to be ~1 nm. I have employed the same structure to study the dependence of the plasmon coupling between two Au nanorods on their interparticle angles during my MPhil study. Readers can referred to my MPhil thesis and some published works for more details about the preparation of the Au nanorod dimers.[22–24] The formed Au nanorod dimers in solutions were then deposited by drop-casting onto a HfO_x/Si substrate. The HfO_x/Si substrate was composed of a highly p-doped Si wafer and a 16-nm HfO_x coating layer, which was prepared by atomic layer deposition.

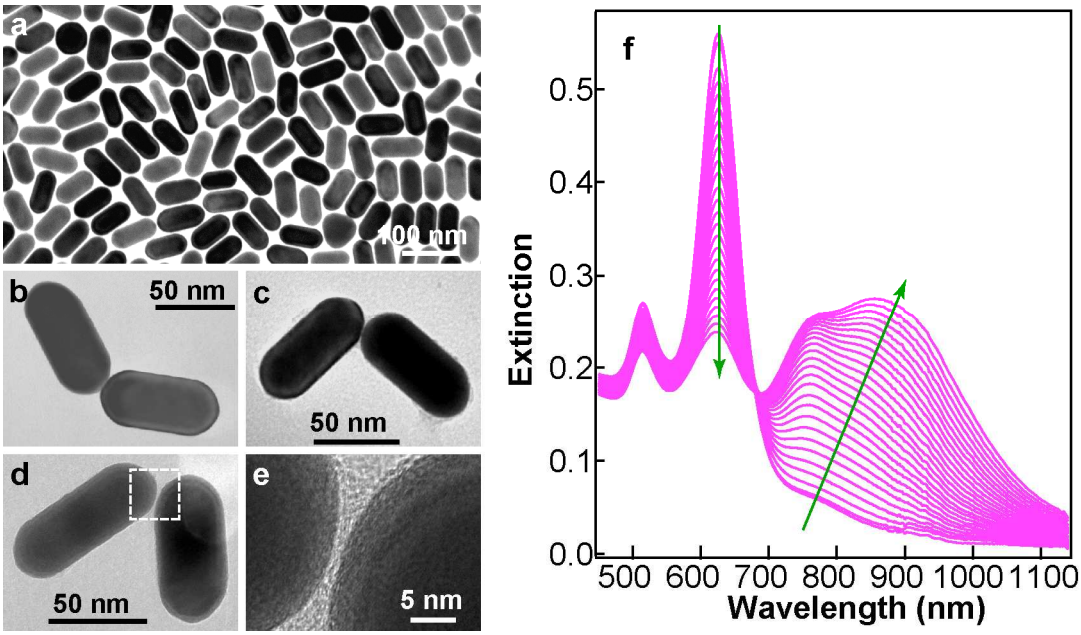

Figure 6.1 Au nanorod dimers. (a) TEM image of the Au nanorods. (b–d) TEM images of three nanorod dimers. The angles between the two nanorods are 128°, 97°, and 58°, respectively. (e) High-resolution TEM image of the area indicated with a dashed box in (d), showing the presence

of a gap between the two nanorods. (f) Extinction spectra of the Au nanorod solution recorded as a function of time after the addition of the dithiol molecules. The particle concentration of the nanorods in the solution was ~0.02 nM, and the dithiol concentration was 1 μM. The interval between two consecutive spectra was 4 min.[22]

Large-area monolayer graphene was provided by our collaborators from both The Chinese University of Hong Kong and Peking University. The monolayer graphene was grown on copper by chemical vapor deposition (CVD) method. The high quality of the obtained graphene sheets was verified by micro-Raman spectroscopy and field-effect transport measurements. A typical Raman spectrum of a graphene sheet is shown in Figure 6.2a. The joint occurrence of a large intensity ratio, $I(G')/I(G)$, and a weak D peak indicates a low doping level and high quality of the graphene sheets. The transport curve of a typical field-effect transistor made of a graphene sheet with a channel width of 20 μm and length of 5 μm is shown in Figure 6.2b. The details about the field-effect transport measurements can be found in a related Ph. D thesis.[25] We employed a phenomenological model to extract the mobility from the experimental data.[26] The total carrier density n in the channel was determined by both the gate coupling and graphene chemical potential, which can be described by the gate capacitance and the quantum capacitance, respectively. The expression is

$$n\frac{e}{C}+\frac{\hbar v_F}{e}\sqrt{n}=\left|V_g-V_{Dirac}\right| \tag{6.1}$$

where C is the gate capacitance, v_F is the Fermi velocity, V_g is the gate voltage, and V_{Dirac} is the voltage of Dirac point. Then the total resistance R_{tot} is described by

$$R_{tot}=R_{contact}+\frac{L}{W}\frac{1}{e\mu\sqrt{\left(n^*\right)^2+n^2}} \tag{6.2}$$

In equation (6.2), $R_{contact}$ is the contact resistance. W, L, μ and n^* stand for the channel width and length, carrier mobility, and the residue carrier concentration induced by impurities. Fitting our data to this model, we obtained the mobilities of μ_h = 3715 cm^2/(V·s) and μ_e = 2783 cm^2/(V·s).

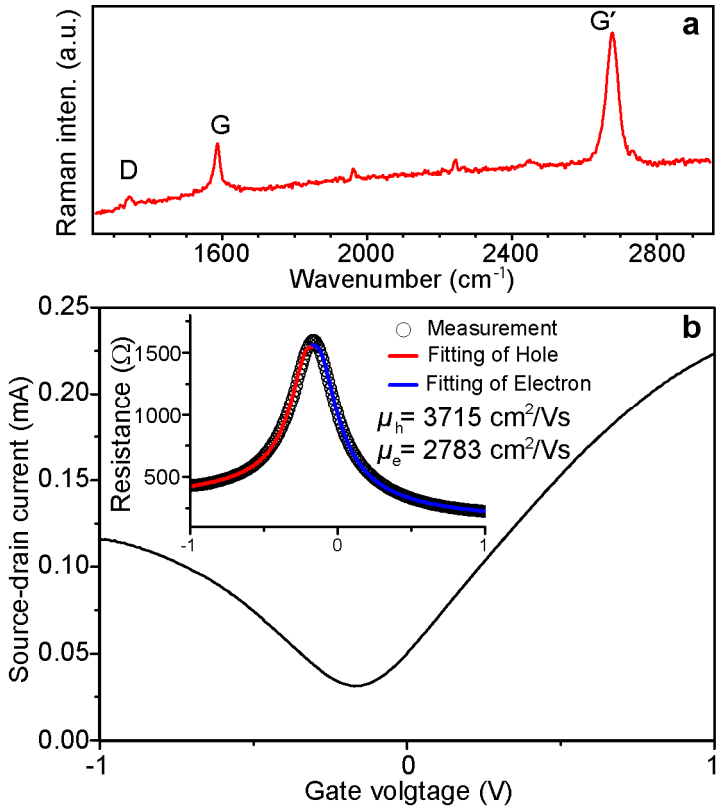

Figure 6.2 Characterization of the CVD-grown monolayer graphene sheets. (a) Raman spectrum. (b) Field-effect transport curve. The inset is the variation of the resistance as a function of the gate voltage. The red and blue curves are the fits for holes and electrons, respectively.

The large-area graphene sheet was subsequently transferred onto the HfO_x/Si substrate with Au nanorod dimers, following a reported method.[27] The Au nanorod dimers on the HfO_x/Si substrate were then covered by monolayer graphene (Figure 6.3b,c). The graphene sheet on the large dielectric-constant HfO_x layer therefore can be electrically gated, with two Au contacts serving as the source and drain (can be both grounded) and the silicon wafer as the backgate, following a reported technique (Figure 6.3a).[20,25] We then recorded the scattering spectra of individual Au nanorod dimers using the pattern matching method introduced in Chapter 3. The scattering spectra of one Au nanorod dimer at varying gate voltages are shown in Figure 6.3d. For comparison, the same dimer without graphene coating was also given. Two scattering peaks are observed, with the lower-energy one (centered at ~770 nm) corresponding to the attractive bonding plasmon mode and the higher-energy one (centered at ~570 nm) corresponding to the repulsive antibonding plasmon mode, respectively.[22,23] The bonding and antibonding plasmon modes are excited under the light polarized perpendicular and along the bisector of the angle

formed by the two nanorods, respectively. After the graphene sheet coating is added, no apparent spectral changes have been found, indicating that the interaction between graphene and the Au nanorod dimers is not strong enough. When different gate voltages are applied to the graphene sheet, we haven't observed any significant spectral evolution. This observation is consistent with the experimental results of recently reported works.[17]

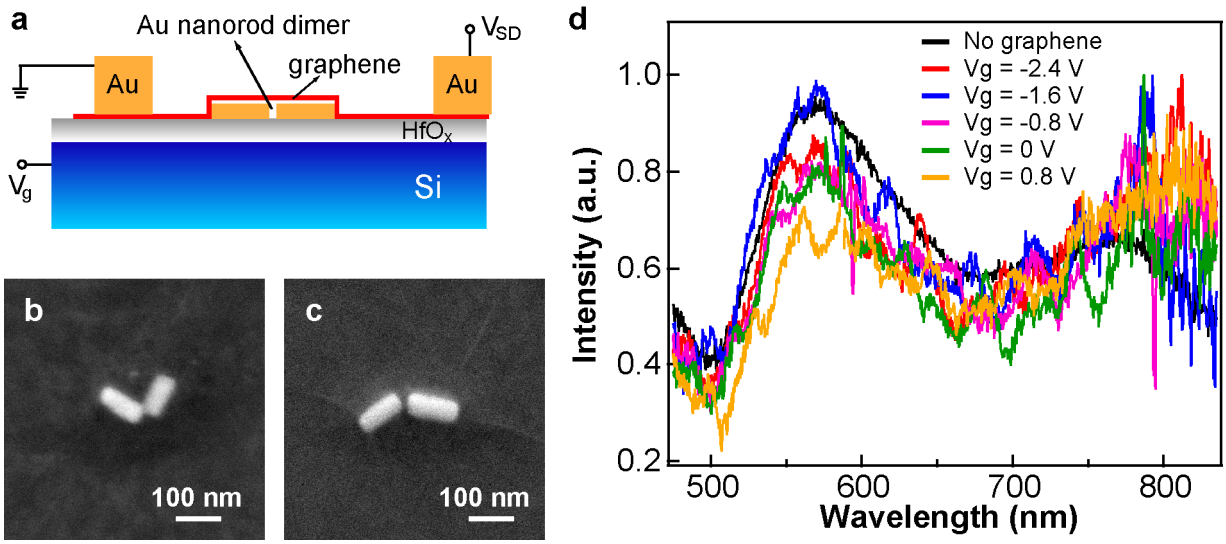

Figure 6.3 Effect of graphene on the plasmon resonances of Au nanorod dimers. (a) Illustration of a typical device with graphene placed on top of a Au nanorod dimers. Grounded Au electrodes (only one is shown) are placed on graphene, serving as the source and drain. The Si substrate is employed as the gate while the 16-nm HfO_x layer acts as the high-*k* dielectric. Different gate voltages are applied and the scattering of the Au nanorod dimer–graphene hybrid system is collected. (b,c) SEM images of two representative nanorod dimers coated with graphene. (d) Dark-field scattering spectra of the Au nanorod dimer–graphene hybrid system when different gate voltages are applied. No apparent changes have been observed.

The little change of the plasmonic response of the graphene-coated Au nanorod dimers results from insufficient coupling between graphene optical transitions and the plasmon resonances of Au nanorod dimers. The gate voltage we applied in our experiments can only shift the Fermi level of graphene by less than 0.5 eV. The permitted graphene optical transition energies are therefore less than 1 eV. These low-energy optical transitions are far away from the plasmon resonances of the Au nanorod dimers in the visible-to-NIR region. More importantly, as Figure 6.4 shows, the enhancements of the electromagnetic fields surrounding the Au nanorod

dimers (~10^2 times) are not large enough to allow for a strong light–graphene interaction. A huge electromagnetic field enhancement (up to 10^4 times) can be supported in the gap (Figure 6.4), but it is quite difficult to place graphene exactly into the small gap region (less than 1 nm) in our experiments. We then therefore cannot observe a distinct spectral tuning with graphene. To achieve the modulation of plasmon resonances by graphene at the high-energy visible-to-NIR frequencies, improved structure designs are required to place graphene into the electromagnetic hot spots to significantly increase light–graphene interaction. We then thereafter proposed a sandwiched structure to place graphene into the cavity formed between a Au nanosphere and a Au film, which will be discussed in the following section.

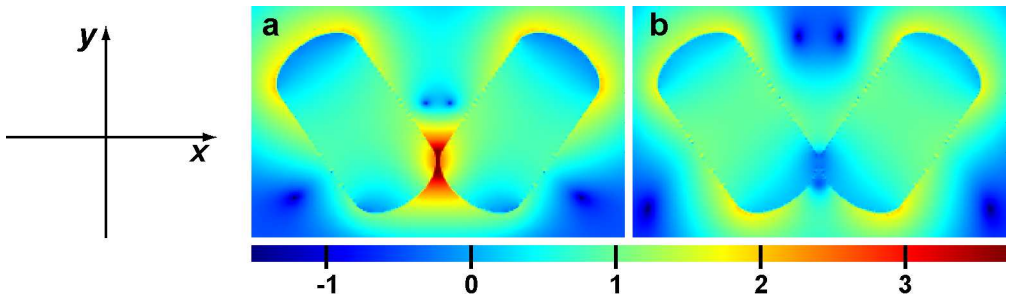

Figure 6.4 Electric field intensity enhancement contours obtained from FDTD calculations for a Au nanorod dimer with an interparticle angle of 70°.[22,23] The contours were calculated at the wavelengths of the plasmon peaks excited by the *x*-polarized (a) and the *y*-polarized light (b), respectively. The enhancement is drawn at the logarithmic scale.

6.2 Film-Coupled Nanoantennas with Graphene Loading

To increase light–graphene interaction, we then proposed a structure by inserting graphene into a sub-nm cavity formed by a Au nanosphere and a Au film. Our film-coupled colloidal Au nanoantennas (Figure 6.5a) were constructed by depositing chemically grown Au nanospheres on thermally evaporated, flat Au films that were pre-covered with graphene. Compared with lithographically fabricated Au nanostructures, the colloidal Au nanospheres possess high crystallinity with reduced plasmon damping and therefore show outstanding plasmonic performances. The Au films were pre-evaporated (100-nm, thermally evaporated at a speed of 0.4 nm·min^{-1}) on Si substrates and cut into pieces at ~1 mm × 100 μm. The obtained Au films

were then carefully transferred onto a HfO_x/Si substrate with a micromanipulator under an optical microscope.[25] Large-area CVD-grown graphene was subsequently transferred onto the Au film pieces supported by the HfO_x/Si substrate, following the method introduced in Section 6.1.[27] The geometrical configuration of the film-coupled nanoantennas allows graphene to be placed at a nanometer electromagnetic hot spot. We first employed the CVD-grown monolayer graphene, whose transport performance was examined previously (Section 6.1). It was carefully transferred to minimize folding (Figure 6.5b,c). The thickness of the transferred graphene sheets was measured with atomic force microscopy (AFM) to be 1 ± 0.25 nm. Under SEM imaging, the edges of the transferred Au films are clearly observable, and those of the transferred graphene sheets are seen to be suspended from the Au film to HfO_x/Si surface (Figure 6.5c). When excited with white light, the nanoantennas loaded with graphene exhibit significantly different scattering spectra from the unloaded ones (Figure 6.5d,e). In the spectral range of our optical detector (~450–850 nm), a new strong scattering peak is observed around 800 nm for the graphene-loaded nanoantennas. The resonance features near 625 and 700 nm also change to ~545 and ~605 nm after the nanoantennas are loaded with graphene. It is remarkable that a monolayer graphene sheet can cause such a large variation in the scattering spectrum of the film-coupled Au nanosphere antenna in the visible-to-NIR range.

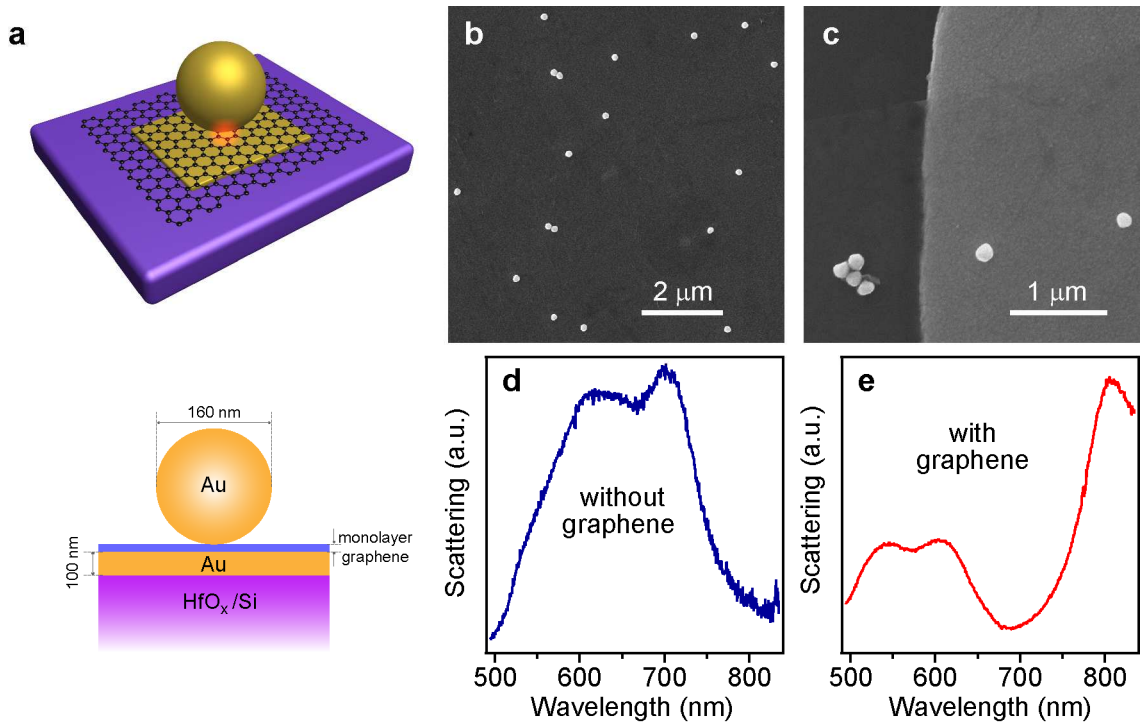

Figure 6.5 Graphene-loaded plasmonic nanoantennas working in the visible-to-NIR region. (a) Schematic of a graphene-loaded plasmonic nanoantenna. Top: a perspective view. Bottom: a side view. (b,c) SEM images of the graphene-loaded, film-coupled colloidal Au nanosphere antennas at low and high magnification, respectively. The low-magnification image in (b) shows ripples on a transferred, CVD-grown monolayer graphene sheet, where the entire imaged area contains graphene on a Au film that is supported on HfO_x/Si. The high-magnification image in (c) shows the edge of a graphene sheet (indicated with the dashed line) and the edge of a Au film (indicated with the solid line) on HfO_x/Si. The average diameter of the Au nanospheres is 155 ± 9 nm. In aqueous solutions, the nanosphere sample has a dipolar plasmon peak at 694 nm and a quadrupolar one at 545 nm (see Chapter 3 for the growth method of these nanospheres). The Au film has a thickness of 100 nm and a root-mean-squared roughness of 0.44 nm. (d,e) Experimentally measured scattering spectra of a film-coupled Au nanosphere antenna in the absence and presence of graphene, respectively.

The strong plasmon coupling between the individual Au nanospheres and Au film plays a vital role in giving rise to the dramatic scattering spectral changes. Our control experiments show that the scattering spectra of the Au nanospheres deposited on HfO_x/Si in the absence of graphene are similar to those with graphene (Figure 6.6). Slight blue shifts (~30 nm) in the lowest-energy scattering peak are observed after graphene loading. The blue shifts are attributed to the weakened plasmon coupling between the Au nanospheres and substrate, which arises in turn from the raise of the Au nanospheres from the substrate by graphene.[28] In addition, in a

recent study, the raise of 60-nm Au nanospheres from a Au film with a molecular layer has been reported to result in ~80-nm blue shifts in the dipolar plasmon resonance peak of the coupled system as the thickness of the dielectric molecular layer is increased from 0.5 to 2 nm.[29] In contrast, in our study, under the intense plasmon coupling between the Au nanospheres and the Au film, the unique dielectric response of graphene itself plays a much more important role than the heightening effect. It causes the excitation of the plasmon resonance around 800 nm for the Au film-coupled Au nanosphere antennas. This plasmon resonance in the presence of loaded graphene is red-shifted in comparison to the lowest-energy plasmon mode in the absence of graphene. On the other hand, the scattering peaks observed at higher energies irrespective of the presence or absence of graphene can be ascribed to the excitation of higher-order plasmon modes owing to the retardation effect of the large, ~160-nm Au nanospheres as well as symmetry breaking brought by the Au film.[30]

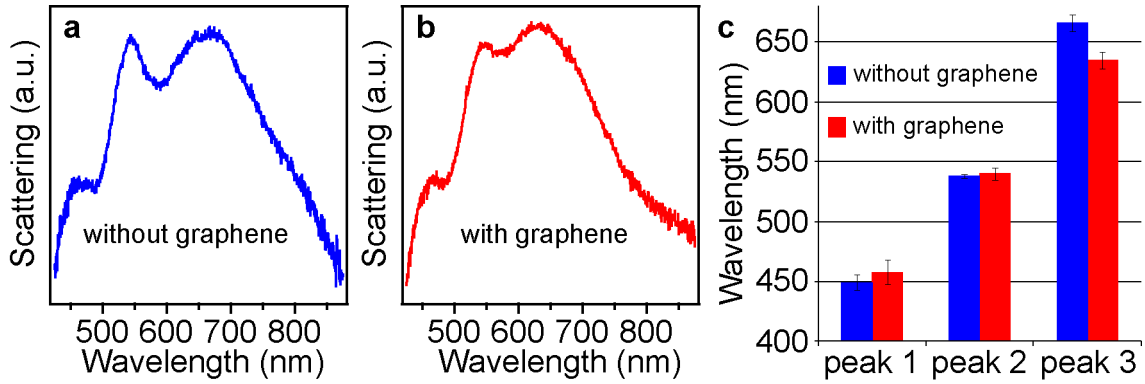

Figure 6.6 Scattering spectra of the Au nanosphere antennas deposited on HfO_x/Si in the absence of the Au film. (a) Scattering spectrum of a Au nanosphere in the absence of graphene. (b) Scattering spectrum of a Au nanosphere in the presence of graphene. The scattering spectral shape of the nanoantennas remains nearly unchanged when graphene is loaded in the gap between the Au nanosphere and the substrate. (c) Wavelengths of the three scattering peaks for the nanoantennas without and with graphene. The error bar heights represent double standard deviations. The two higher-energy peaks, peaks 1 and 2, exhibit slight shifts. Peak 3, which corresponds to a dipolar plasmon resonance, shows a larger blue shift. The ~30-nm blue shift is attributed to the raise of the Au nanosphere by graphene.

To reveal clearly the plasmon modes in the Au film-coupled, graphene-loaded Au nanosphere antennas, we measured the polarization-dependent scattering spectra on the

individual nanoantennas and compared them with those recorded on the nanoantennas without graphene (Figure 6.7a–d). The light polarized parallel to the substrate (s-polarized light) can excite three plasmon resonance modes for the Au nanospheres deposited directly on the Au film without graphene at around 528 nm, 587 nm, and 687 nm, respectively (Figure 6.7c). The plasmon resonance wavelengths vary slightly among the different Au nanospheres owing to the fluctuations in the nanosphere size and gap distance. After graphene is loaded, the overall shape of the scattering spectrum is changed. There are also three plasmon resonance modes. They are centered at 539 nm, 629 nm, 820 nm, respectively (Figure 6.7d). In contrast to the slight blue shift of the lowest-energy plasmon mode caused by the loading of graphene for the Au nanospheres deposited on HfO_x/Si without a Au film, the strong plasmon coupling between the Au nanospheres and Au film enables graphene to interact with the largely plasmon-enhanced local electric field, leading to a distinct red shift in the lowest-energy plasmon mode. The small blue shift caused by the heightening effect of graphene is readily overcome by the large red shift induced by the strong interaction between the plasmonic field and graphene. We therefore hypothesize that the loaded graphene sheet provides a screening effect to the coupled plasmonic cavity. In analogy with resonant circuits, where the increase in the capacitance of a system will reduce the resonance frequency, the loading of graphene increases the effective 'capacitance' of the film-coupled nanoantenna. As a result, the resonance frequency of the nanoantenna is decreased, which results in the observed red shift of the plasmon resonance mode.

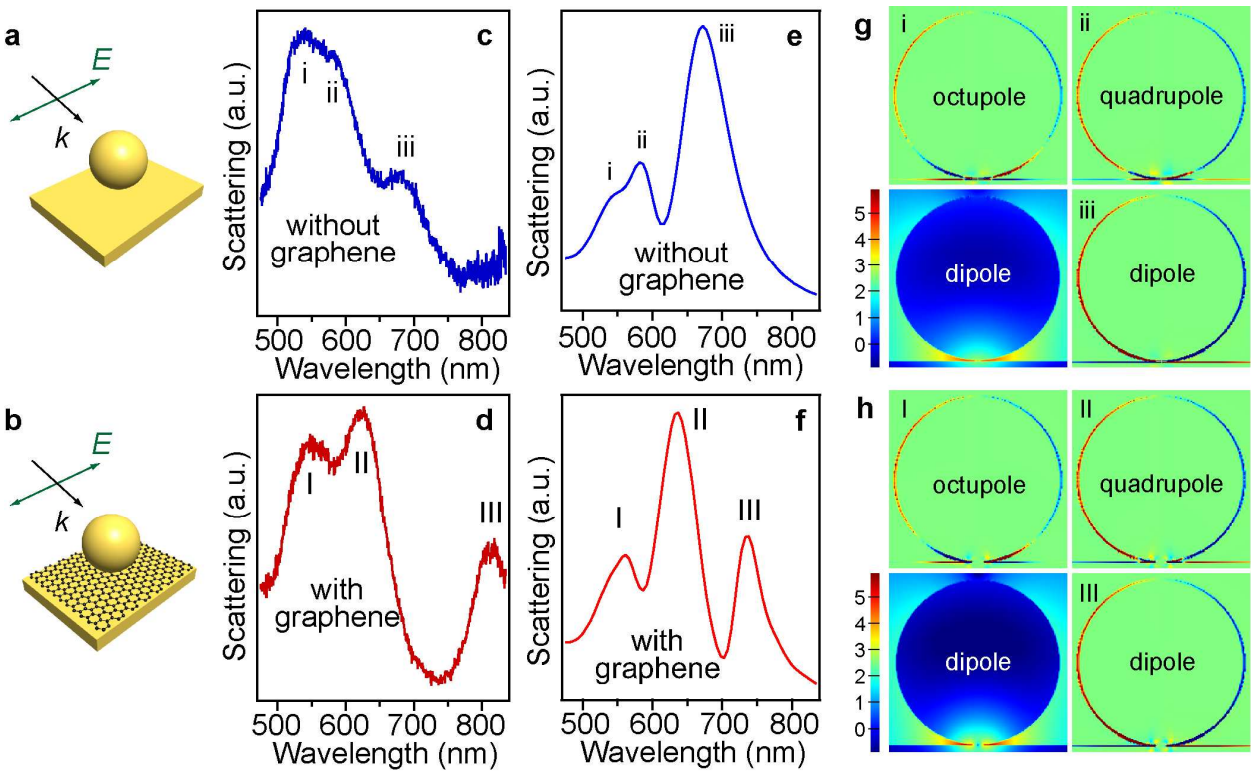

Figure 6.7 Plasmon modes of the film-coupled Au nanosphere antennas. (a,b) Schematics showing a Au nanosphere on a Au film under s-polarized excitation in the absence and presence of graphene, respectively. (c,d) Measured scattering spectra of the film-coupled Au nanosphere antennas without and with graphene, respectively. (e,f) FDTD calculated scattering spectra of the film-coupled Au nanosphere antennas without and with graphene, respectively. (g) Calculated charge distributions and electric field intensity contour (bottom left) for the plasmon modes labeled as i, ii, and iii in (c,e). (h) Calculated charge distributions and electric field intensity contour (bottom left) for the plasmon modes labeled as I, II, and III in (d,f). The field intensity contours are at the logarithmic scale.

To confirm the role played by loaded graphene, we performed FDTD calculations to unveil the different plasmon modes excited for the film-coupled Au nanosphere antenna without and with graphene loading, respectively. For simplicity, a perfect Au sphere of 160 nm in diameter was considered, and the gap distance between the Au nanosphere and the Au film substrate was assumed to be 1 nm owing to the remaining organic stabilizing molecules on the Au nanosphere. The gap was filled with either air (refractive index = 1) or graphene to simulate the situations without and with graphene. Graphene was modeled as a sheet with a thickness of 1 nm in order to reduce the computational load. The dielectric function of gold was represented with the fitting from Johnson & Christy data. Graphene was treated as an isotropic dielectric material and its

dielectric function was obtained by calculating its relative permittivity ε_G as a function of optical frequency ω as follows:

$$\varepsilon_G(\omega) = \frac{i\sigma(\omega)}{\omega\varepsilon_0 d} \tag{6.3}$$

where ε_0 and d are the vacuum permittivity and the graphene thickness (0.33 nm), respectively. $\sigma(\omega)$ is the conductivity of graphene, which can be expressed as:

$$\sigma(\omega) = \frac{2e^2\omega_T}{\pi\hbar} \times \frac{i}{\omega + i\tau^{-1}} \log\left[2\cosh\left(\frac{\omega_F}{2\omega_T}\right)\right] + \frac{e^2}{4\hbar}\left[H\left(\frac{\omega}{2}\right) + i\frac{2\omega}{\pi}\int_0^\infty \frac{H(\omega'/2) - H(\omega/2)}{\omega^2 - \omega'^2} d\omega'\right] \tag{6.4}$$

$$H(\omega) = \sinh(\omega/\omega_T)/[\cosh(\omega/\omega_T) + \cosh(\omega_F/\omega_T)] \tag{6.5}$$

where $\omega_T = k_B T/\hbar$, τ is the carrier scattering time. The Fermi frequency is defined as $\omega_F = E_F/\hbar$, where E_F is the Fermi energy. The influence of the gate voltage V_g on the Fermi energy level can be expressed by [15]

$$E_F = \hbar v_F \sqrt{\pi\left(n_0 + \frac{C|V_g|}{q_e}\right)} \tag{6.6}$$

where v_F is the Fermi velocity for graphene (v_F = 10^6 m/s), n_0 is the intrinsic carrier concentration, C is the effective capacitance per unit area of the dielectric spacer (HfO_x), and q_e is the electronic charge. Here, any intrinsic carrier concentrations can be neglected.

The occurrence of the three plasmon resonance peaks and the trend of the plasmon shifts caused by the loading of graphene are well reproduced by the computed scattering spectra (Figure 6.7e and f). In the absence of graphene, the three plasmon resonances obtained from the simulations are located at 535 nm, 580 nm, and 677 nm, respectively. Analysis of the charge distributions reveals that the Au nanosphere exhibits octupolar, quadrupolar, and dipolar plasmon resonances (Figure 6.7g) at the three peak wavelengths, respectively. After the loading of graphene, the calculated three plasmon resonances shift to 546 nm, 637 nm, and 741 nm, respectively. According to the charge distributions (Figure 6.7h), these three plasmon resonances on the Au nanosphere are also octupolar, quadrupolar, and dipolar, respectively. The

discrepancies in the peak intensities and positions between the experiments and simulations might result from a number of factors, including the difficulty in obtaining the accurate values of the gap distance between the Au nanosphere and film, deviation of the Au nanocrystal from a perfectly spherical shape, remaining surfactant molecules on the Au nanosphere surface, dissimilar excitation and collection geometries between the simulations and measurements, imperfect fitting of the dielectric values of graphene by the FDTD software, and possible quantum effect due to the small gap distance. Despite the discrepancies between the measured and calculated scattering spectra under s-polarized excitation, the FDTD simulations confirm that the spectral modulation is induced by the presence of graphene in the gap. The observed ~100-nm red shift (133 nm in the experiments, 64 nm in the simulations) of the dipolar plasmon mode indicates a strong interaction between visible-to-NIR light and the graphene sheet in the coupled plasmonic nanocavity. The quadrupolar and octupolar plasmon resonances are less sensitive to the loading of graphene. They exhibit red shifts of 42/57 nm and 11/11 nm in the experiments/simulations, respectively. The simulations also reveal that the electromagnetic energy is extremely concentrated in the nanocavity (Figure 6.7g and h), enabling strong light–graphene interaction. Careful examination of the electric field intensity enhancement contours discloses that the existence of graphene makes the electric field even more concentrated in the gap region at the dipolar plasmon resonance wavelength. The increase in light confinement indicates that more charges are induced by capacitive plasmon coupling. The effective 'capacitance' of the resonator is increased by loading graphene into the gap between the Au nanosphere and film. The simulation results therefore suggest that our hypothesis of the screening effect and the use of the resonant-circuit model (see below for further discussion) as an analogy are appropriate for interpreting the large resonance red shift brought by graphene.

We also measured the scattering spectra of the Au film-coupled Au nanosphere antennas excited with p-polarized light (Figure 6.8). In the experiments, the excitation white light is incident on the nanoantennas at an angle of 64.2° owing to the used dark-field objective, which

causes the existence of an electric field component that is oriented parallel to the Au film plane. Therefore, the scattering spectra measured under p-polarized excitation contain a partial contribution from those acquired under s-polarized excitation. Three plasmon resonance peaks are observed. They are located at 541/559 nm, 597/617 nm, and 704/821 nm for the nanoantennas without/with graphene. These peak wavelengths are very close to the respective ones (528/539 nm, 587/629 nm, 687/820 nm) observed on the scattering spectra under s-polarized excitation. In addition, there might also be plasmon resonance peaks in the low-energy region beyond the detection limit of our optical system, as suggested by the rising intensities in the low-energy spectral region. For the nanoantennas without graphene, previous studies by others have shown that ~60-nm Au nanospheres deposited on Au films at a gap distance of ~1 nm exhibit a plasmon resonance peak at ~700 nm under p-polarized excitation.[29] According to this result, our ~160-nm Au nanospheres deposited on the Au film in the absence of graphene are estimated to display a plasmon peak beyond 850 nm. For the nanoantennas containing graphene in the gap, this plasmon peak is believed to overlap largely with the plasmon peak that is excited under s-polarized excitation. We also carried out FDTD simulations on the nanoantennas with the excitation light polarized perpendicular to the Au film plane. However, the enormous difference between the large size of the overall system and the involved small features (gap and graphene) makes such simulations difficult to converge even on our 64-CPU cluster. Owing to both the experimental and simulation difficulties mentioned above, we did not deal further with p-polarized excitation in our study. In addition, the electric field under unpolarized excitation contains dominantly the component that is polarized parallel to the Au film plane. The plasmon modes observed under unpolarized excitation (Figure 6.5e) are nearly the same in wavelength as those observed under s-polarized excitation. Therefore, we only considered the scattering responses under unpolarized excitation below.

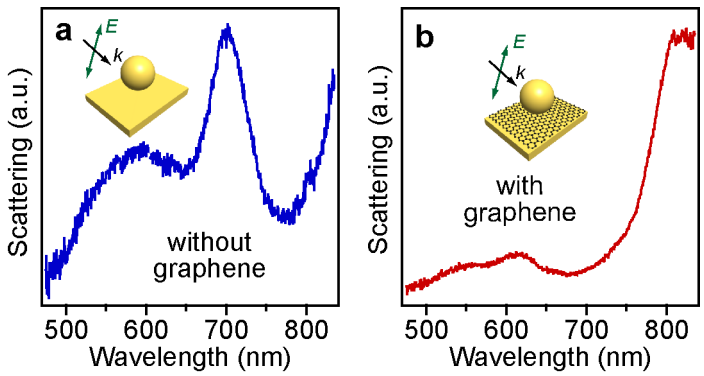

Figure 6.8 Scattering spectra of the Au film-coupled Au nanosphere antennas under p-polarized excitation. (a) Without graphene. (b) With graphene. Because a dark-field objective with a numerical aperture of 0.9 is employed in the experiments for excitation, the incidence angle is 64.2°. Therefore, there is an electric field component that is polarized parallel to the Au film plane. As a result, the scattering spectra measured experimentally under p-polarized excitation contain a partial contribution from those measured under s-polarization excitation.

We tried to modulate the coupled plasmon resonances of the nanoantennas loaded with graphene by varying the doping level in graphene. The FDTD simulations show that both p- and n-type doping of graphene can lead to blue shifts of the coupled plasmon resonances. Specifically, when a gate voltage of −10 V, which corresponds to a chemical potential of 0.8 eV, is applied to the loaded graphene sheet to achieve a high level of hole-doping, the three plasmon modes of the nanoantenna under s-polarized excitation blue-shift from 546 nm, 637 nm, and 741 nm to 540 nm, 615 nm, and 714 nm, respectively (Figure 6.9a). However, owing to the insufficient doping level achievable with HfO_x as the gate dielectric, we chose thermal annealing to realize a high level of p-doping. SEM and Raman characterizations (results not shown) indicate that the shape of the Au nanospheres and the graphene sheets are maintained after the thermal treatment. The annealing induced p-type doping is estimated at 4×10^{13} cm^{-2} from the intensity ratio between G and G' peaks on the Raman spectrum (Figure 6.9b).[31] The corresponding chemical potential is therefore ~0.8 eV. The scattering measurements were performed on the same Au nanosphere in the presence of graphene before and after annealing. A large blue shift of the dipolar plasmon resonance from 761 nm to 687 nm is observed (Figure 6.9c). The octupolar plasmon mode shifts from 544 nm to 525 nm. The quadrupolar resonance overlaps with the dipolar one. The experimental result agrees qualitatively with the simulation

one. As mentioned above, quantitative prediction by FDTD simulations is difficult, which is even exacerbated by the possible annealing-induced change in the gap distance and the inaccurate description of the dielectric function of graphene at high doping levels. For comparison, the scattering spectra of the nanoantennas without graphene loading were also recorded (Figure 6.9d), where a conductive plasmon coupling between the Au nanosphere and film was observed, owing to the partial fusion of the nanosphere and film caused by the thermal treatment. Doping graphene at a high level pushes the real part of its dielectric function to a more negative value at visible-to-NIR wavelengths (400–1300 nm). Such a change causes the observed blue shifts in the plasmon resonances (see below for further discussion with the resonant-circuit model). We believe that similar modulation of the screening effect of graphene can be achieved by electrical gating with dielectrics that have sufficiently large dielectric constants,[32] such as Y_2O_3, and therefore that the coupled plasmon resonances can be electrically switched by changing the gate voltage.

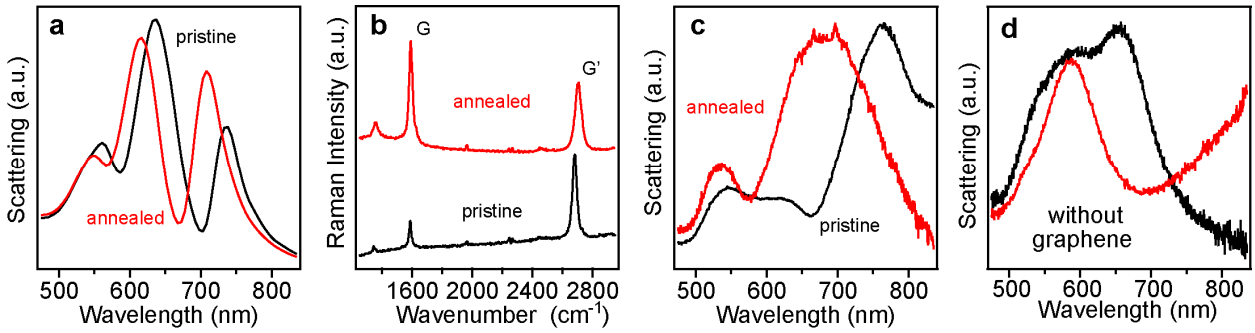

Figure 6.9 (a–c) Annealing-induced change of the scattering spectrum of the Au film-coupled Au nanosphere antennas in the presence of graphene. (a) FDTD-calculated scattering spectra of the pristine (black) and p-doped (red) nanoantenna under s-polarized excitation. (b) Raman spectra of a graphene sheet on the Au film before and after the thermal treatment. (c) Measured scattering spectra of the nanoantenna before (pristine) and after (red) the thermal treatment. The spectra were taken on the same nanoantenna. The excitation light was unpolarized. (d) Annealing-induced change of the scattering spectrum of the Au film-coupled Au nanosphere antennas in the absence of graphene.

We further studied the effect of the number *n* of graphene layers on the plasmonic response of the Au film-coupled Au nanosphere antennas by loading graphene with different layers. The

screening effect of graphene varies greatly as a function of *n*,[33] which in turn affects the coupled plasmons of the nanoantennas. Few-layer graphene (FLG) was obtained by cleaving graphite with scotch tape.[7] The nanoantennas were constructed similarly by transferring the cleaved FLG sheets onto the Au film and then depositing the Au nanospheres. Particularly, the FLG sheets were first transferred from the tape onto Si wafers that were covered with thermally grown SiO_2 at a thickness of 300 nm. The Au film was then directly evaporated onto the transferred FLG sheets. A poly(methylmethacrylate) (PMMA) layer was subsequently spin-coated onto the obtained Au film/FLG/SiO_2/Si sample, followed by the etching of the SiO_2 layer in an hot aqueous KOH solution (80 °C, 1.0M) for ~10 min to release the PMMA/Au film/FLG layer. The suspended PMMA/Au film/FLG layer was rinsed and transferred to the HfO_x/Si substrate, with the PMMA layer in contact with the HfO_x layer. The FLG/Au film structure supported on the HfO_x/Si substrate was finally obtained by removing PMMA with acetone. The number of graphene layers *n* was determined according to the optical contrasts and Raman spectra (Fig. 6.10). The Au film-coupled Au nanosphere antennas as a result can be constructed by depositing Au nanospheres onto the FLG/Au film structure supported on the HfO_x/Si substrate. Figure 6.10 shows the bright-field optical micrograph and SEM images of the obtained nanoantennas.

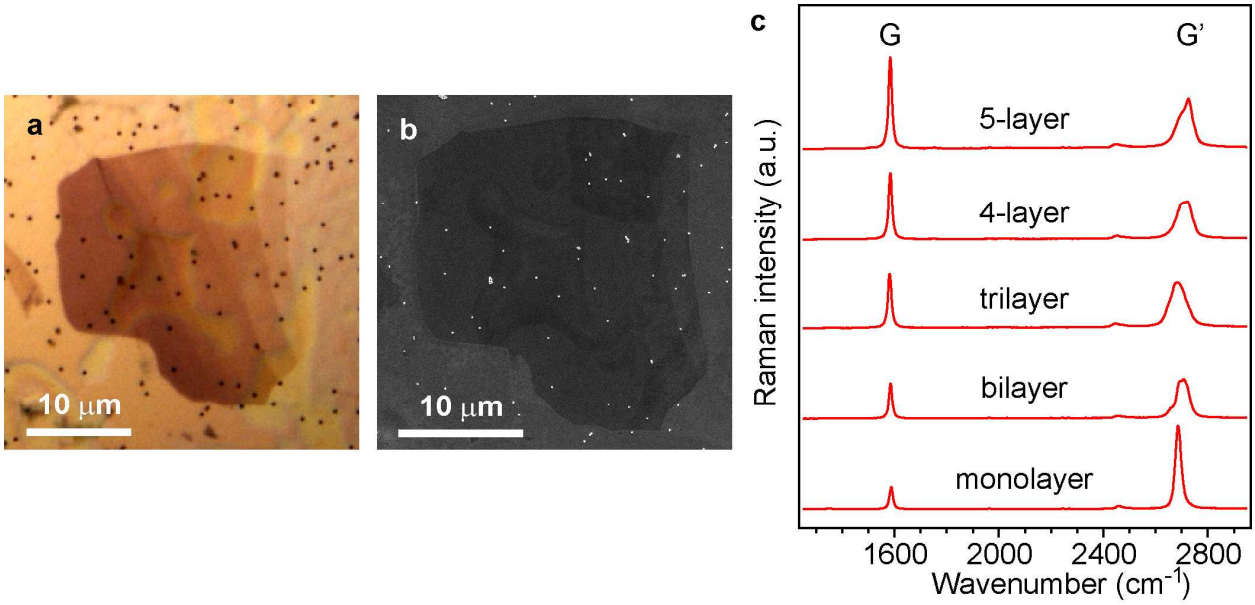

Figure 6.10 Au film-coupled Au nanosphere antennas loaded with different numbers of graphene layers. (a) Optical micrograph of the colloidal Au nanospheres deposited on the cleaved FLG sheets that are placed on the Au film. (b) SEM image acquired from the same area as in (a). (c) Raman spectra of graphene sheets with different number of layers.

SEM and optical imaging were jointly employed to make sure that only the nanoantennas that were far away from the suspending and bulging part of the FLG sheets were examined (Fig. 6.10a,b). When a cleaved, monolayer-thick graphene sheet is loaded between the Au nanospheres and film, the nanoantennas display scattering spectra (Figure 6.11a) that are nearly the same as those measured on the counterparts above that contain the CVD-grown monolayer graphene sheets. As *n* is increased, the quadrupolar plasmon mode disappears, the dipolar and octupolar resonances blueshift. When *n* is varied from 1 to 6, the thickness of FLG increases from 0.33 to ~2 nm. Since the gap distance between the Au nanosphere and film separated by monolayer graphene is estimated to be ~1 nm, we infer that the gap distance for the nanoantennas increases from ~1 to ~2.7 nm as *n* is varied from 1 to 6. The dipolar plasmon resonance is seen to show a large blue shift of ~100 nm when *n* is changed from 1 to 6 (Figure 6.11b). The increase in the gap spacing cannot fully explain such a large blue shift, suggesting that the screening effect of FLG plays a role. The screening effect of FLG becomes more remarkable as *n* is increased, resulting in a large increase in the resonance frequency of the nanoantenna. Compared with the dipolar plasmon mode, the higher-order octupolar mode exhibits slight shifts while the

quadrupolar mode can only be detected for the nanoantennas loaded with monolayer graphene.

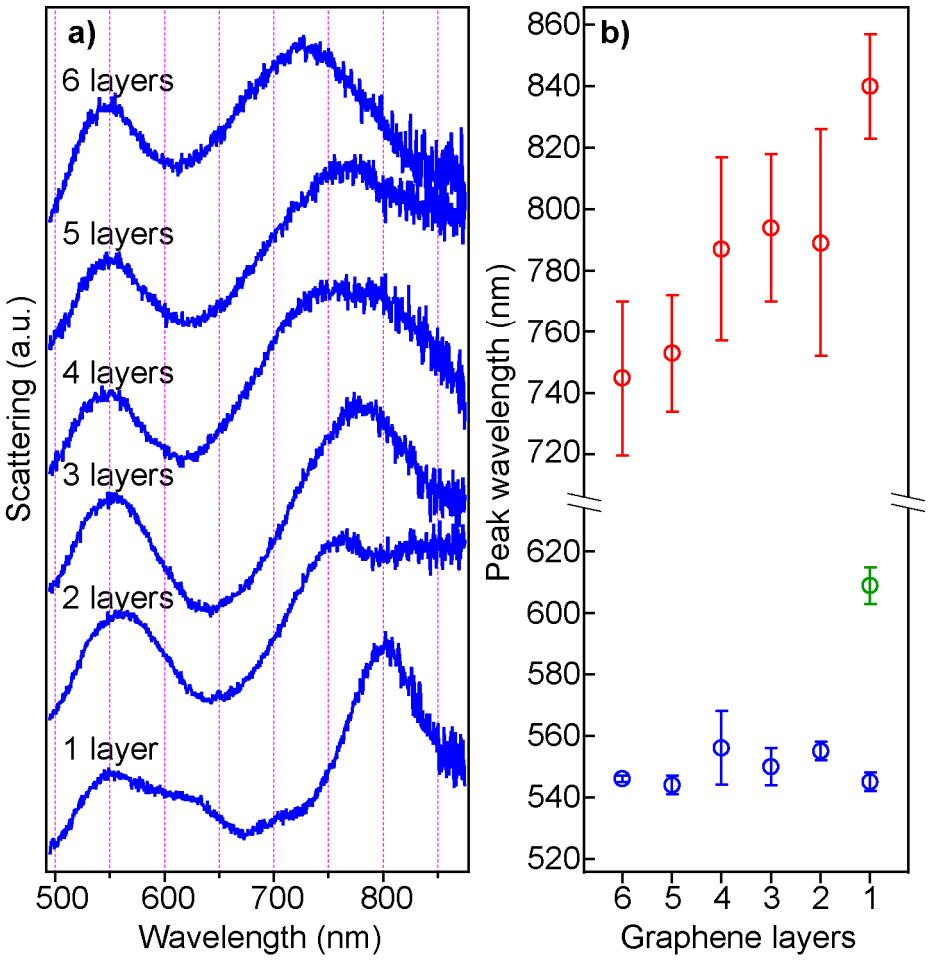

Figure 6.11 Scattering response of the Au film-coupled Au nanosphere antennas loaded with different numbers of graphene layers. (a) Scattering spectra of the nanoantennas loaded with the number of graphene layers n increasing from 1 to 6. (b) Scattering peak wavelengths of the dipolar (red), quadrupolar (green), and octupolar (blue) plasmon resonances as functions of n. The error bar heights represent double standard deviations.

A resonant-circuit model was employed to help in understanding the graphene-modulated dipolar plasmon resonance of the Au film-coupled Au nanosphere antennas. The nanoantenna without graphene is modeled with a simple circuit consisting of one inductor and one capacitor (Figure 6.12a). The air gap with a distance of d_1 between the Au nanosphere and film has a capacitance of C_1. The inductance of the entire system is assumed to be L. After graphene is loaded, an additional capacitor with a capacitance of C_G is connected in series with the existent inductor and capacitor. For simplicity, C_1 and L are assumed to remain unchanged after graphene loading. The capacitance of the entire circuit changes to C_2 after graphene loading. C_1, C_G, and

C_2 can be expressed as

$$C_1 = \varepsilon_0 \frac{S}{d_1} \tag{6.7}$$

$$C_G(\lambda) = \varepsilon_0 \varepsilon'_G(\lambda) \frac{S}{d_2} \tag{6.8}$$

$$C_2(\lambda) = \frac{1}{1/C_1 + 1/C_G(\lambda)} \tag{6.9}$$

where ε_0 is vacuum permittivity, S is the effective area of the capacitor, and d_2 is the effective separation of the graphene capacitor. C_G is a function of wavelength λ. ε'_G is the real part of the dielectric function of graphene. The imaginary part of the dielectric function of graphene in the visible-to-NIR region is nearly zero and is not considered in our modeling. The dipolar plasmon resonance wavelengths of the nanoantenna in the absence and presence of graphene, which are denoted as λ_1 and λ_2, respectively, can be derived from the effective circuit model as

$$\lambda_1 = 2\pi c\sqrt{LC_1} \tag{6.10}$$

$$\lambda_2 = 2\pi c\sqrt{LC_2(\lambda_2)} \tag{6.11}$$

where c is light velocity in free space. Both the experiments and FDTD simulations show that λ_1 is ~677 nm and λ_2 is dependent on the doping level of graphene. By solving equations (6.7)–(6.11), we can obtain the following equation at the dipolar plasmon resonance wavelength of the graphene-loaded nanoantenna

$$\varepsilon'_G(\lambda_2) = \frac{d_2}{d_1} \cdot \frac{1}{\left(\frac{\lambda_1}{\lambda_2}\right)^2 - 1} \tag{6.12}$$

We define the right side of equation (6.12), which is also a function of λ_2, as $F(\lambda_2)$. As a result, the criterion of the dipolar plasmon resonance of the graphene-loaded nanoantenna becomes

$$\varepsilon'_G(\lambda) = F(\lambda) \tag{6.13}$$

By plotting the curves of $\varepsilon'_G(\lambda)$ and $F(\lambda)$ versus λ in the same graph (Figure 6.12b), we can readily locate the dipolar plasmon wavelength of the graphene-loaded nanoantenna from the

intersection between the two curves. Since the real part, $\varepsilon'_G(\lambda)$, of the dielectric function of graphene is always negative in the wavelength range of 400–1000 nm, $\varepsilon'_G(\lambda)$ can only intersect with the negative part of hyperbolic $F(\lambda)$, giving rise to the red shift of the dipolar plasmon resonance after graphene loading. The coefficient d_2/d_1 in $F(\lambda)$ is determined to be 2.9 by letting the plasmon resonance wavelength of the nanoantenna loaded with pristine graphene be 741 nm. After graphene is thermally annealed, its ε'_G is pushed to more negative values. As a result, the intersection between $\varepsilon'_G(\lambda)$ and $F(\lambda)$ blue-shifts to ~700 nm, which is in good agreement with our experiments and FDTD simulations. Our resonant-circuit model can also explain the slight blue shift of the dipolar plasmon observed on the FLG-loaded nanoantennas. In comparison to pristine graphene, FLG possesses a stronger screening effect,[33] which makes the real part of its dielectric function more negative and therefore results in blue shifts in the dipolar plasmon resonance of the nanoantenna in comparison to that of the nanoentanna loaded with monolayer pristine graphene.

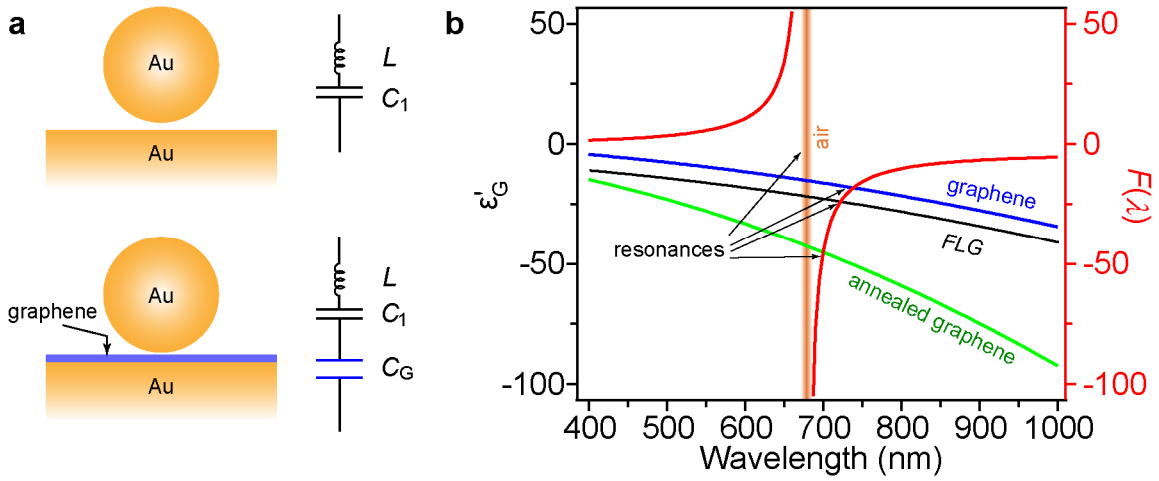

Figure 6.12 Resonant-circuit model for interpreting the dipolar plasmon shifts of the Au film coupled Au nanosphere antenna with loaded graphene at varying screening effect. (a) Schematics showing the effective circuits of the nanoantenna in the absence (top) and presence (bottom) of graphene. L is the inductance, C_1 is the capacitance corresponding to the air gap, and C_G is the capacitance of the graphene sheet. (b) Plots of ε'_G and $F(\lambda)$ *versus* wavelength. The dipolar plasmon wavelengths are indicated by the intersections between the curves of the real part of the dielectric function of graphene (left axis, blue: monolayer graphene, black: FLG, green: annealed graphene) and the hyperbolic curve $F(\lambda)$ (right axis, red). The vertical bar (orange) indicates the

asymptotic position of the hyperbolic curve, representing the plasmon wavelength, λ_1, of the nanoantenna without graphene loading. ε'_G of annealed graphene is calculated by assuming an effective gate voltage of −10 V to account for high-level hole doping. ε'_G of FLG is a schematic curve, only showing that FLG has a larger screening effect than pristine graphene.

6.3 Summary and Outlook

In this chapter, I have investigated the interaction between graphene and coupled plasmonic Au nanostructures to examine whether graphene can be employed for modulating plasmonic resonances. Two different coupled plasmonic structures have been proposed to interact with graphene, including the Au nanorod dimers and the Au film-coupled Au nanosphere structures.

The Au nanorod dimers in my experiments cannot realize strong light–graphene interaction. After coating graphene, the scattering spectra of Au nanorod dimers rarely change. In addition, the scattering response of the dimer varies little when the graphene optical transitions are adjusted by electrostatic gating. The weak coupling is attributed to (1) the inability to place graphene into the gap between two Au nanorods where the light energy is greatly concentrated, and (2) the energy mismatch between the graphene optical transitions and the dimer plasmon resonances.

By contrast, the Au film-coupled colloidal Au nanosphere antenna provides a simple but effective strategy for accomplishing strong light–graphene interaction at visible-to-NIR frequencies. Loading graphene in the nanocavity between the Au nanosphere and film greatly modulates the scattering response of the plasmonic nanoantenna. The scattering response of the graphene-loaded nanoantenna is further varied by changing the doping level through thermal treatment or the number of graphene layers. The spectral modulation has been qualitatively understood by employing a simple resonant-circuit model. Our graphene-loaded nanoantenna is expected to enable various applications based on graphene–light interaction at visible-to-NIR frequencies in sensing and ultrafast photodetection. Moreover, the spectral modulation realized by tuning graphene forms the basis for electrically controlling and manipulating light at

visible-to-NIR frequencies by integrating graphene with rich plasmonic structures at different length scales. Our rapid, inexpensive, and readily scalable wet-chemistry approach and the distinct modulation of the scattering response for the graphene-loaded nanoantenna will boost the flourishing research activities on graphene as well as facilitate the cost-effective construction of active plasmonic devices.

It should also be pointed out here that p-polarized light can excite plasmon resonances of the Au film-coupled Au nanosphere at the NIR region, where we currently cannot perform measurements. However, these resonances are supposed to be quite sensitive to the gap dielectric, since (1) they exhibit bonding manners between the nanosphere dipole standing on the film and its image beneath the film, and (2) the electric field intensity enhancement would be larger than that under the s-polarized excitation. These plasmon resonances therefore can also be tuned by graphene loading. By employing electrical gating on graphene with dielectrics that have sufficiently large dielectric constants (e.g. Y_2O_3), the plasmon modes excited by p-polarized light would be more easily tuned than the modes under s-polarized excitations. To investigate these plasmon modes requires the use of IR CCDs. An alternative approach to investigating such plasmon modes is to use smaller Au nanospheres, whose plasmon wavelength will appear in shorter wavelengths.[29]

Further investigation on the graphene–metal nanostructure coupling can be focused on the following aspects. (1) The first is to study the plasmonic properties of Au film-coupled Au nanorods with graphene loading. The use of Au nanorods to replace Au nanospheres in Section 6.2 will provide several advantages. The plasmon energy of Au nanorods can be varied over a wide range. We therefore can examine the effect of graphene on the Au nanorod–Au film coupling at different wavelengths. Besides, large Au nanorods (~188 × 118 nm) on Au film can support Fano resonances, which has great potential for plasmonic switching and electro-optical modulation.[28] Graphene can help to tune the Fano resonances supported by the Au nanorod–Au film structures and facilitate their electro-optical applications. (2) The second is to

examine the quantum effect of graphene embedded in the gap between Au nanoparticle and the Au film. Graphene provides an ultra-small, but controllable gap distance between metal nanostructures. The tunneling effect mediated by graphene can be examined by monitoring the spectral change under different applied voltages between the Au nanocrystal and the substrate. We then therefore can investigate the graphene-mediated tunneling plasmonics in the coupled Au nanocrystal-substrate system, which is fundamentally important and can bring intriguing novel electro-optical applications.

References

[1] Halas, N. J.; Lal, S.; Chang, W.-S.; Link, S.; Nordlander, P. *Chem. Rev.* **2011**, *111*, 3913.

[2] Shao, L.; Fang, C. H.; Chen, H. J.; Man, Y. C.; Wang, J. F.; Lin, H.-Q. *Nano Lett.* **2012**, *12*, 1424.

[3] Moreau, A.; Ciracì, C.; Mock, J. J.; Hill, R. T.; Wang, Q.; Wiley, B. J.; Chilkoti, A.; Smith, D. R. *Nature* **2012**, *492*, 86.

[4] Liu, N.; Hentschel, M.; Weiss, T.; Alivisatos, A. P.; Giessen, H. *Science* **2011**, *332*, 1407.

[5] Liu, N.; langguth, L.; Weiss, T.; Kästel, J.; Fleischhauer, M.; Pfau, T.; Giessen, H. *Nat. Mater.* **2009**, *8*, 758.

[6] Large, N.; Abb, M.; Aizpurua, J.; Muskens, O. L. *Nano Lett.* **2010**, *10*, 1741.

[7] Novoselov, K. S.; Geim, A. K.; Morozov, S. V.; Jiang, D.; Zhang, Y.; Dubonos, S. V.; Grigorieva, I. V.; Firsov, A. A. *Science* **2004**, *306*, 666.

[8] Li, Z. Q.; Henriksen, E. A.; Jiang, Z.; Hao, Z.; Martin, M. C.; Kim, P.; Stormer, H. L.; Basov, D. N. *Nat. Phys.* **2008**, *4*, 532.

[9] Wang, F.; Zhang, Y. B.; Tian, C. S.; Girit, C.; Zettl, A.; Crommie, M.; Shen, Y. R. *Science* **2008**, *320*, 206.

[10] Xia, F. N.; Mueller, T.; Lin, Y.-M.; Valdes-Garcia, A.; Avouris, P. *Nat. Nanotechnol.* **2009**, *4*, 839.

[11] Ju, L.; Geng, B. S.; Horng, J.; Girit, C.; Martin, M.; Hao, Z.; Bechtel, H. A.; Liang, X. G.; Zettl, A.; Shen, Y. R.; Wang, F. *Nat. Nanotechnol.* **2011**, *6*, 630.

[12] Liu, M.; Yin, X. B.; Ulin-Avila, E.; Geng, B. S.; Zentgraf, T.; Ju, L.; Wang, F.; Zhang, X. A

Nature **2011**, *474*, 64.

[13] García de Abajo, F. J. *Science* **2013**, *339*, 917.

[14] Kim, J.; Son, H.; Cho, D. J.; Geng, B. S.; Regan, W.; Shi, S. F.; Kim, K.; Zettl, A.; Shen, Y.-R.; Wang, F. *Nano Lett.* **2012**, *12*, 5598.

[15] Majumdar, A.; Kim, J.; Vuckovic, J.; Wang, F. *Nano Lett.* **2013**, *13*, 515.

[16] Yao, Y.; Kats, M. A.; Genevet, P.; Yu, N. F.; Song, Y.; Kong, J.; Capasso, F. *Nano Lett.* **2013**, *13*, 1257.

[17] Mousavi, S. H.; Kholmanov, I.; Alici, K. B.; Purtseladze, D.; Arju, N.; Tatar, K.; Fozdar, D. Y.; Suk, J. W.; Hao, Y. F.; Khanikaev, A. B.; Ruoff, R. S.; Shvets, G. *Nano Lett.* **2013**, *13*, 1111.

[18] Engel, M.; Steiner, M.; Lombardo, A.; Ferrari, A. C.; v. Löhneysen, H.; Avouris, P.; Krupke, R. *Nat. Commun.* **2012**, *3*, 906.

[19] Furchi, M.; Urich, A.; Pospischil, A.; Lilley, G.; Unterrainer, K.; Detz, H.; Klang, P.; Andrews, A. M.; Schrenk, W.; Strasser, G.; Mueller T. *Nano Lett.* **2012**, *12*, 2773.

[20] Konstantatos, G.; Badioli, M.; Gaudreau, L.; Osmond, J.; Bernechea, M.; Garcia de Arquer, F. P.; Gatti, F.; Koppens, F. H. L. *Nat. Nanotechnol.* **2012**, *7*, 363.

[21] Echtermeyer, T. J.; Britnell, L.; Jasnos, P. K.; Lombardo, A.; Gorbachev, R. V.; Grigorenko, A. N.; Geim, A. K.; Ferrari, A. C.; Novoselov, K. S. *Nat. Commun.* **2011**, *2*, 458.

[22] Shao, L.; Woo, K. C.; Chen, H. J.; Jin, Z.; Wang, J. F.; Lin, H.-Q. *ACS Nano* **2010**, *4*, 3053.

[23] Shao, L. *Angle-, Energy- and Position-Resolved Plasmon Resonance Coupling between Gold Nanocrystals*. MPhil. Thesis, Department of Physics, The Chinese University of Hong Kong, 2008.

[24] Pramod, P.; Thomas, K. G. *Adv. Mater.* **2008**, *20*, 4300.

[25] Wang, X. M. *Graphene Interface Engineering: Surface/Substrate Modifications cum Metal contact Exploration*. Ph.D Thesis, Department of Electronic Engineering, The Chinese University of Hong Kong, 2008.

[26] Kim, S.; Nah, J.; Jo, I.; Shahrjerdi, D.; Colombo, L.; Yao, Z.; Tutuc, E.; Banerjee, S. K. *Appl. Phys. Lett.* **2009**, *94*, 062107.

[27] Gao, L. B.; Ren, W. C.; Xu, H. L.; Jin, L.; Wang, Z. X.; Ma, T.; Ma, L.-P.; Zhang, Z. Y.; Fu, Q.; Peng, L.-M.; Bao, X. H.; Cheng, H.-M. *Nat. Commun.* **2011**, *3*, 699.

[28] Chen, H. J.; Shao, L.; Ming, T.; Woo, K. C.; Man, Y. C.; Wang, J. F.; Lin, H.-Q. *ACS Nano* **2011**, *5*, 6754.

[29] Ciracì, C.; Hill, R. T.; Mock, J. J.; Urzhumov, Y.; Fernández-Domínguez, A. I.; Maier, S. A.; Pendry, J. B.; Chilkoti, A.; Smith, D. R. *Science* **2012**, *337*, 1072.

[30] Kottmann, J. P.; Martin, O. J. F. *Opt. Lett.* **2001**, *26*, 1096.

[31]Das, A.; Pisana, S.; Chakraborty, B.; Piscanec, S.; Saha, S. K.; Waghmare, U. V.; Novoselov, K. S.; Krishnamurthy, H. R.; Geim, A. K.; Ferrari, A. C.; Sood, A. K. *Nat. Nanotechnol.* **2008**, *3*, 210.

[32] Xu, H. L.; Zhang, Z. Y.; Xu, H. T.; Wang, Z. X.; Wang, S.; Peng, L.-M. Top-Gated *ACS Nano* **2011**, *5*, 5031.

[33] Nilsson, J.; Castro Neto, A. H.; Guinea, F.; Peres, N. M. R. *Phys. Rev. B* **2008**, *78*, 045405.

Chapter 7

Plasmonic Properties of Macroscale Gold Nanorod Arrays

As I have introduced in Chapter 1, gold nanorods are very promising for a great number of optical and biochemical applications.[1] However, great efforts are still required to put Au nanorods (and other noble metal nanocrystals) into practical applications where dense macroscale arrays are needed, such as plasmonic photovoltaic solar cells,[2] plasmon-facilitated solar water splitting,[3,4] ultra-high-density optical data storage,[5] controlled reflection/absorption metamaterial surface,[6] plasmon-enhanced light-emitting diodes,[7] and plasmon-enhanced multicolor photodetectors.[8] High density of nanocrystal arrays is important for utilizing and concentrating light as efficiently as possible in the above optical-related applications. However, unpredictable plasmon coupling in nanocrystals that are spaced too closely with random gap distances will lead to the loss of plasmonic features in their absorption/scattering spectral responses. The nanocrystals in the arrays therefore should be simultaneously dense enough to efficiently employ light and well-separated to make the macroscale arrays maintain the plasmonic responses of individual nanocrystals. Usually ordered metal nanocrystal structures are not a necessary for the intriguing applications mentioned above. For instance, periodic and pseudorandom arrays of silver nanostructures result in nearly undistinguishable efficiency improvement of thin-film a-Si:H solar cells.[9] Lithographical methods, such as electron beam lithography (EBL), focused ion beam lithography, soft nanoimprint lithography,[10] and nanosphere lithography techniques,[11] are reliable approaches for achieving nanostructure arrays on substrate surfaces, with controllable morphologies, orders,

and separation gap distances. However, the high cost of the time-consuming lithographical methods prevents their large-scale production of nanostructure patterns, the resolution limit of the lithographical processes inhibits fine control of nanostructure corner sharpness and interparticle spacing, and indispensable adhesive layers and polycrystalline metal structures obtained from deposition procedures can degrade their plasmonic performances due to increased plasmon damping. Besides the lithographical techniques, the Langmuir–Blodgett technique is able to deposit colloidal plasmonic nanocrystal arrays onto substrates at large scales.[12,13] Electrostatic methods have also been employed to assembly colloidal gold nanocrystals onto charged surfaces.[14] Nevertheless, it has remained challenging to deposit chemically-grown metal nanocrystals uniformly and densely on substrates while keeping the nanocrystals well-separated to eliminate the random plasmon coupling effect.

Additionally, although lithographically fabricated Au nanocrystals suffer from a poor plasmonic performance compared with their chemically grown counterparts, there have been no reports on investigating how severe the plasmonic performance degradation is. To quantitatively determine the degradation effect is of vital importance, since the plasmonic properties should be considered when evaluating the device performance of lithographically fabricated Au nanocrystals in various plasmonic applications. In this chapter, I will first compare the plasmonic properties of Au nanorods with the same dimensions that are fabricated by EBL as well as by seed-mediated growth approaches in Section 7.1. Then I will introduce, in Section 7.2, a novel approach for the uniform deposition of gold nanocrystals onto various surfaces to form dense, macroscale nanocrystal arrays. Au nanorods, Au nanospheres, Au nanobipyramids, and (Au core)/(Ag shell) nanorods have been successfully deposited from solution onto substrates by controlling the surfactant concentration in solution. Nanocrystals in the dense arrays are well-separated and as a result the arrays maintain the plasmonic response of an individual nanocrystal with plasmon coupling effect eliminated. In the end, in Section 7.3, I will characterize the refractive index sensing performances of the Au nanorod arrays deposited on

glass slides, mesoporous silica and titania films. The effects of the supporting substrate and the capping molecules on the index sensitivity are examined.

7.1 Comparison of Plasmonic Properties between Lithographically-Written and Chemically-Grown Au Nanorods

Au nanorods were prepared by seed-mediated and EBL writing methods separately according to the procedures in Chapter 3. The chemically-grown colloidal Au nanorods have an average dimension of (96 ± 9) × (40 ± 4) nm (Figure 7.1a). They were deposited by drop-casting onto ITO substrates. The EBL-written Au nanorods were fabricated on ITO substrates with a 4.5-nm thick Cr adhesive layer between gold and the ITO substrate (Figure 7.1b). The average length and width of the Au nanorods were 98 ± 4 and 43 ± 3 nm, respectively. The thickness of the Au nanorods was around 40 nm, which was controlled during the thermal evaporation. The EBL-written Au nanorods on ITO substrates were subjected under thermal treatment (200 °C, 2h) before their plasmonic properties were characterized.

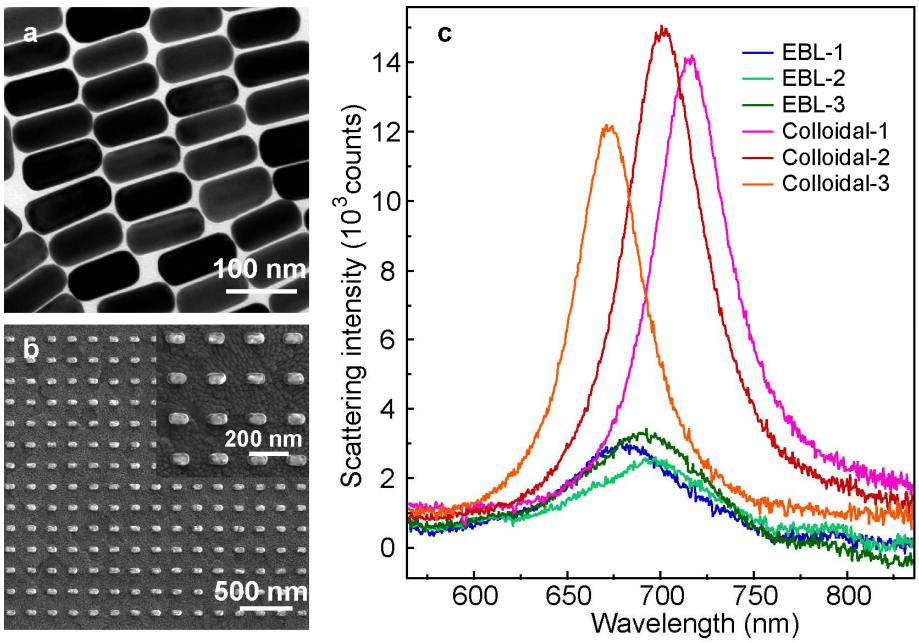

Figure 7.1 Scattering of both the chemically-grown and EBL-written Au nanorods. (a) TEM image of the chemically-grown colloidal Au nanorods. (b) SEM image of the EBL-written Au

nanorods. The inset is the SEM image at a large magnification. (c) Dark-field scattering spectra of the individual Au nanorods fabricated by the different methods.

We have measured the scattering spectra of both the colloidal and EBL-written Au nanorods. The scattering of more than 15 individual nanorods obtained from each preparation approach were recorded and compared. Figure 7.1c shows the scattering spectra of some representative Au nanorods. For the colloidal nanorods, their plasmon wavelength, scattering peak intensity, and plasmon width (full-width at half maximum) were measured to be 697 ± 22 nm, 13804 ± 1501 counts, and 48 ± 4 nm (or 0.12 eV), respectively. In comparison, the EBL-written Au nanorods have their plasmon wavelength, scattering peak intensity, and plasmon width at 714 ± 22 nm, 3051 ± 612 counts, and 87 ± 10 nm (or 0.23 eV), respectively. The Au nanorods prepared by the two methods have nearly the same size. The plasmon energies of the EBL-written Au nanorods are slightly lower than that of their colloidal counterparts. The small difference might come from the size deviation and the end shape difference. In my MPhil thesis, I have shown that Au nanorods with blunter ends have lower plasmon energies.[15,16] The colloidal Au nanorods usually have rounded ends while the EBL-written ones have blunter ends. The scattering peak intensities, on the other hand, of the EBL-written Au nanorods were much lower than that of the colloidal nanorods. Such an intensity decrease was also accompanied with the broadening of the scattering peak. The plasmon width of the EBL-written Au nanorods was measured to be twice the value of the colloidal ones. The weaker plasmon peak and the broader plasmon width can be attributed to the use of the Cr adhesive layers and the multi-crystalline nature of the EBL-written Au nanorods. To disclose the role of the adhesive Cr layers, I have performed FDTD calculations. The simulations results showed that, for a Au nanorod with a dimension of (90 nm × 40 nm × 40 nm), a 3-nm and 6-nm Cr layer would blue shift the scattering peak from 610 nm to 595 nm and 577 nm, respectively (Figure 7.2). This blue shift further confirms that the longer plasmon wavelength of the EBL-written Au nanorods observed in the experiments comes from their blunter ends. The 3-nm and 6-nm Cr layer would decrease the scattering intensity to 27.8% and 25.5% of that without Cr layer, respectively. The plasmon width would become ~2.2 times that

of the nanorods without Cr. In comparison, the experiments indicated that the scattering intensity and plasmon width of the EBL-written Au nanorods with a 4.5-nm Cr layer was 22.1% and 1.8 times that of the colloidal nanorods, respectively. Our simulation and experimental results reveal that the effect of a Cr layer dominates in plasmon damping of the EBL-written Au nanorods. More simulations to replace Cr with Ti gave similar results. To overcome the negative role played by the metal adhesive layer, one can resort to an organic adhesive layer such as (3-mercaptopropyl)trimethoxysilane (MPTMS) [17], but a lot of efforts should still be made to simplify the fabrication procedures in order to facilitate the applications of EBL-fabricated plasmonic structures. As a result, if ordering is not required, it is highly desired to fabricate Au nanorod arrays using the colloidal nanorods to replace the EBL-written ones, since the colloidal Au nanorods exhibit much better plasmonic performances.

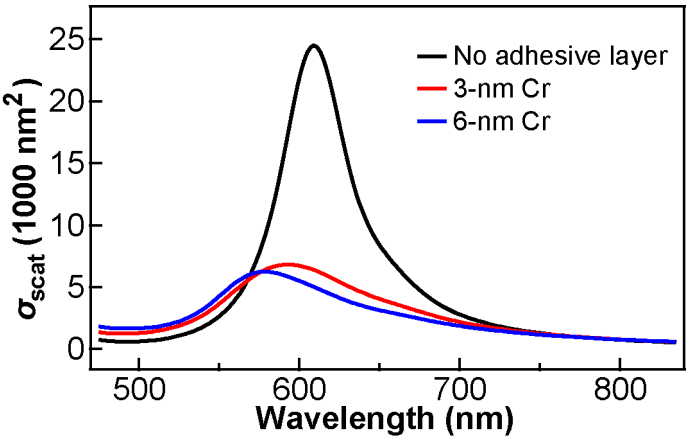

Figure 7.2 Calculated scattering cross sections of a Au nanorod with a dimension of (90 × 40 × 40) nm in the absence and presence of a Cr adhesive layer of different thicknesses. In the simulation, the metal nanostructures were embedded in an ambient dielectric environment (refractive index = 1).

7.2 Deposition of Macroscale Colloidal Noble Metal Nanocrystal Arrays

Previously reported spin-coating,[5] electrostatic,[14] and Langmuir–Blodgett techniques[12,13] to deposit metal nanocrystals onto substrates are limited by inadequate particle densities, too many procedures, or uncontrolled inter-particle gap distances. I developed a

one-step method to deposit metal nanocrystals directly from the CTAB-stabilized nanocrystal solutions onto substrate surfaces, to form dense and uniform nanocrystal monolayers with well-separated interparticle distances. Our strategy is based on the electrostatic interactions between colloidal metal nanocrystals and the substrate surfaces, which can be controlled by tuning the CTAB concentration.[18] By decreasing the CTAB concentration to a certain value, the metal nanocrystals can be deposited densely onto a negatively charged surface.

Figure 7.3 illustrates the deposition procedure and one example of the deposition results. A Au nanorod sample with its ensemble transverse and longitudinal plasmon wavelengths at 536 nm and 699 nm in aqueous solutions was deposited from colloidal solutions onto glass slides. The average length, width and aspect ratio of the nanorod sample were measured respectively to be 111 ± 7 nm, 50 ± 4 nm, and 2.2 ± 0.2, from the TEM images (Figure 7.3a). The as-grown Au nanorod sample, which was dispersed in an aqueous CTAB solution (0.1 M), was washed twice by centrifugation and redispersion into deionized water at the same volume. The CTAB concentration in the resultant solution was estimated to be ~2 μM. This concentration is high enough to prevent the Au nanorods from aggregation, but low enough to allow for dense deposition. Glass slides were treated under ultrasonication in ethanol for at least 30 min, followed by plasma cleaning to remove organic contaminants on the surface of glass slides before deposition. The cleaned glass slides were then immersed in the washed Au nanorod solution, as shown schematically in Figure 7.3b, and left undisturbed for 4 h. In neutral aqueous solutions, the surface of glass slides is negatively charged owing to the dissociated hydroxyl groups that are existent on the glass surface. The CTAB-stabilized, positively charged Au nanorods are therefore attracted onto the negatively charged glass surface, producing a dense monolayer. The Au nanorods in the resultant arrays are disordered. The surface number density can reach 70 particles per μm^2, as revealed by SEM imaging (Figure 7.3c). Such a high surface number density makes the Au nanorod monolayer arrays exhibit a clearly green color, which is easily visible by naked eyes (Figure 7.3d). The average spacing between neighboring Au

nanorods on the glass surface was determined to be ~120 nm. Slight aggregation of the Au nanorods in the arrays is also observed from the SEM images. The formation of the aggregates can be attributed to the possible slight aggregation of the Au nanorods in the solution due to the reduced CTAB concentration and the incomplete cleanness of the glass surface. The well-separated Au nanorods allow the deposited large-scale arrays to maintain the plasmonic properties of the individual Au nanocrystals. The extinction spectral shape of the Au nanorod arrays is very similar to that of the Au nanorod solution (Figure 7.3e), with the transverse and longitudinal plasmon peaks shifted to 518 and 610 nm, respectively. This blueshift is also confirmed by the single-particle scattering spectral measurements. The peak extinction value of two Au nanorod monolayers, with one on each side of the glass slide, reaches 0.4. A weak bump that is centered around 950 nm is also present in the longer-wavelength region on the extinction spectrum of the nanorod arrays. This bump arises from the plasmon coupling between closely-spaced Au nanorods in various geometrical configurations,[16,19,20] which is caused by the slight aggregation of the Au nanorods in the arrays. The weak extinction intensity of the bump confirms the low aggregation level of Au nanorods in the arrays. Our one-step deposition technique is simple, fast, of very low cost, and not limited in surface areas. The fabrication of the Au nanorod arrays can be readily scaled up, by utilizing larger substrates and more colloidal solutions. Figure 7.3d shows a Au nanorod array deposited on a glass slide at a dimension of 10 $\times$ 10 cm^2. The distribution of the Au nanorods in the array is uniform. The entire glass slide exhibits a nearly unvarying green color. Moreover, the deposited Au nanorod arrays are stable and remain on glass slides after they are immersed in aqueous solutions. The extinction peak values of the Au nanorod arrays on glass slides were found to vary only slightly after the arrays were immersed in ethanol or water (Figure 7.4). Such a stability is beneficial for applying the Au nanorod arrays in sensing applications in liquid environments.

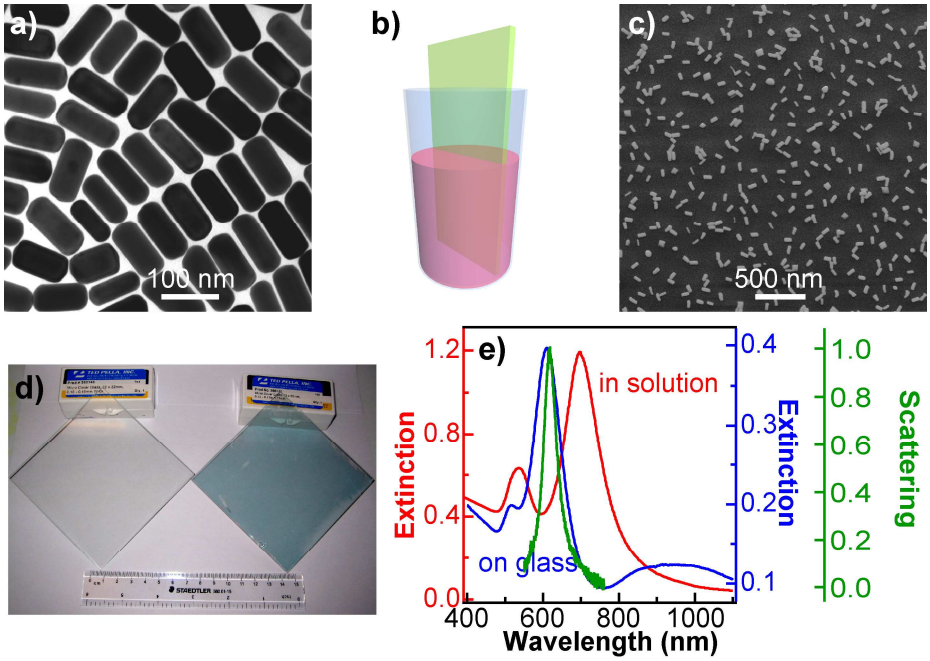

Figure 7.3 Deposition of colloidal metal nanocrystals onto substrates to give macroscale arrays. (a) TEM image of a Au nanorod sample. (b) Schematic showing the deposition of Au nanocrystals on glass slides by immersing a substrate into the nanocrystal solution. (c) Backscattering SEM image of the Au nanorod sample deposited on a glass slide. (d) Photograph of a blank glass slide (left) and one (right) deposited with the Au nanorods. The glass slides are 10×10 cm^2. A 15-cm ruler is also included for reference. (e) Extinction spectra of the Au nanorod sample dispersed in an aqueous solution (red, left axis) and deposited on a glass slide (blue, right axis). Scattering spectrum of one single Au nanorod on glass is also given for reference.

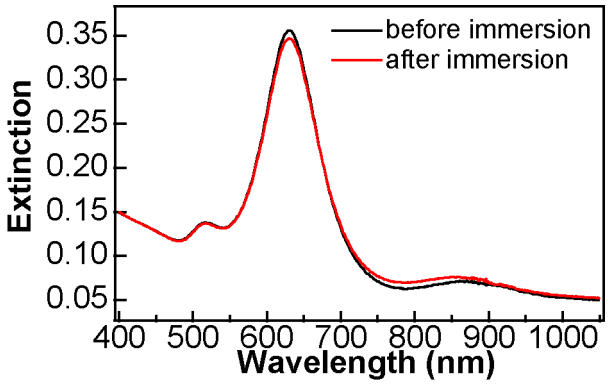

Figure 7.4 Extinction spectra of a Au nanorod array deposited on a glass slide. The black spectrum was recorded before the prepared array was immersed in ethanol, and the red one was recorded after the array was immersed in ethanol, taken out, and dried gently with flowing N_2. The slight decrease in the extinction peak intensity suggests that only a small number of Au nanorods were removed from the glass slide after the immersion process. The small intensity increase in the spectral region from 700 nm to 900 nm suggests that the immersion process also caused slight aggregation of Au nanorods.

The CTAB concentration in the Au nanocrystal solution plays a crucial role in the deposition of CTAB-stabilized Au nanocrystals onto substrates. The effect of the CTAB concentration was studied by characterizing the particle densities of the Au nanorod arrays obtained at varying CTAB concentrations. The results reveal that the particle density of the Au nanorod arrays can be roughly controlled by changing the CTAB concentration. When the CTAB concentration is varied from 2 mM to 20 μM, the Au nanorods were deposited uniformly on the glass surface, with their surface number densities remaining nearly unchanged, as shown by the dark-field scattering images (Figure 7.5). The Au nanorod densities in the arrays are estimated to be 0.3 particles per μm^2 and the corresponding spacing between neighboring Au nanorods is ~ 2 μm on average. As the CTAB concentration is further reduced from 20 μM to 2 μM, the Au nanorod density in the formed arrays suddenly increases to 70 particles per μm^2, more than two orders of magnitude higher than those at higher CTAB concentrations. The average interparticle spacing shows an abrupt decrease from ~2 μm to ~120 nm. The nanorods are so closely positioned that we cannot distinguish each individual Au nanorod on their dark-field scattering images, because their separation is below the diffraction limit. Our experiments therefore suggests that 2 μM is an approximate critical CTAB concentration for dense and uniform deposition of CTAB-stabilized Au nanocrystals. We accordingly surmise that the formation of the Au nanocrystal arrays is driven by the attractive electrostatic interaction between the CTAB-capped, positively charged Au nanocrystals and the negatively charged glass surfaces in neutral aqueous environments. The repulsive electrostatic force between the individual positively charged Au nanocrystals prevents their aggregation. When CTAB exceeds the critical concentration, there exist many CTAB micelles in the solution. These 'free' CTAB micelles, which are also positively charged, compete with the CTAB-capped nanocrystals in being attracted by the negatively charged surface, and, as a result reduce the deposition density of the Au nanocrystals.

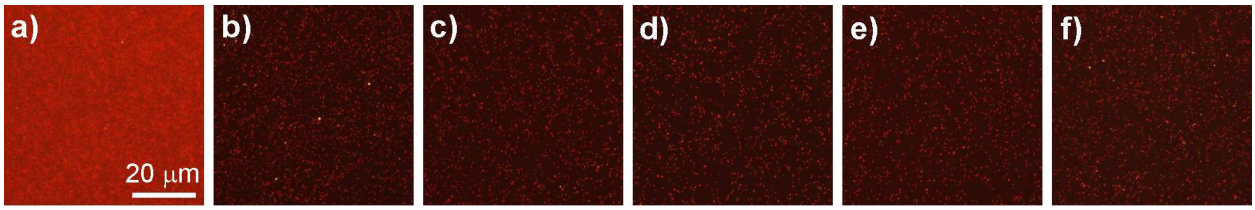

Figure 7.5 Dependence of the particle density in the Au nanorod array deposited on glass slides on the CTAB concentration in the Au nanorod solution. (a) Dark-field scattering image of a high-density Au nanorod array obtained at a CTAB concentration of 2 μM. (b–f) Darkfield scattering images of the low-density Au nanorod arrays obtained at CTAB concentrations of 20 μM, 80 μM, 0.4 mM, 0.8 mM, and 2 mM, respectively. All of the images have the same scale bar as that shown in (a).

Our deposition method is applicable to various metal nanocrystals with different compositions, shapes and sizes. Besides Au nanorods, we have achieved the successful deposition of Au nanospheres, Au nanobipyramids, and (Au core)/(Ag shell) nanorods onto glass slides to form macroscale dense arrays. The Au nanobipyramids and (Au core)/(Ag shell) nanorods were prepared following the similar seed-mediated method introduced in Chapter 3. Detailed synthesis procedures can be found in reported works.[21,22] Figure 7.6 shows the electron microscopy images of the three types of the as-grown metal nanocrystals and their arrays formed on glass surfaces, the photograph of the metal nanocrystal arrays, and the extinction spectra of both the metal nanocrystal solutions and arrays on glass slides. Both the Au nanosphere and (Au core)/(Ag shell) nanorod samples are in high yields, while the Au nanobipyramid sample is limited in number yields to be ~50%. In aqueous solutions, the Au nanosphere sample with an average diameter of 100 ± 8 nm shows a single plasmon peak at 572 nm. The plasmon peak blue-shifts to 526 nm after the Au nanospheres are supported on glass slides. The average length and waist diameter of the Au nanobipyramid sample are 158 ± 7 nm and 35 ± 2 nm, respectively. The longitudinal plasmon peak of the nanobipyramid sample is located at 1045 nm in solution. It blue-shifts to 921 nm after deposition. The (Au core)/(Ag shell) nanorod sample and their Au nanorod cores have average dimensions of (90 ± 9) nm × (52 ± 6) nm and (73 ± 8) nm × (18 ± 2) nm, respectively. The two main plasmon peaks of the (Au core)/(Ag shell) nanorod sample blue-shift from 581 and 507 nm in solutions to 520 nm and 425

nm on glass slides, respectively. The metal nanocrystals in the obtained arrays are all relatively uniform and dense. The metal nanocrystal arrays on glass slides are transparent and show different colors (Figure 7.6g) owing to the different plasmon resonance wavelengths. The Au nanosphere, nanorod, nanobipyramid, and (Au core)/(Ag shell) nanorod arrays display distinct red, green, purple, and yellow colors, respectively. The plasmon wavelength of the metal nanocrystal arrays on glass slides can therefore be tailored from ~500 to 920 nm, with relatively narrow plasmon resonance peaks. Moreover, our solution-based deposition approach allows for large-scale production of colloidal metal nanocrystal arrays. These plasmonic metal nanocrystal arrays are expected to be of great potential for building optical components, trapping light for solar energy conversion, manufacturing high-density optical recording materials, and constructing meta-surfaces to control the reflection and transmission of light.

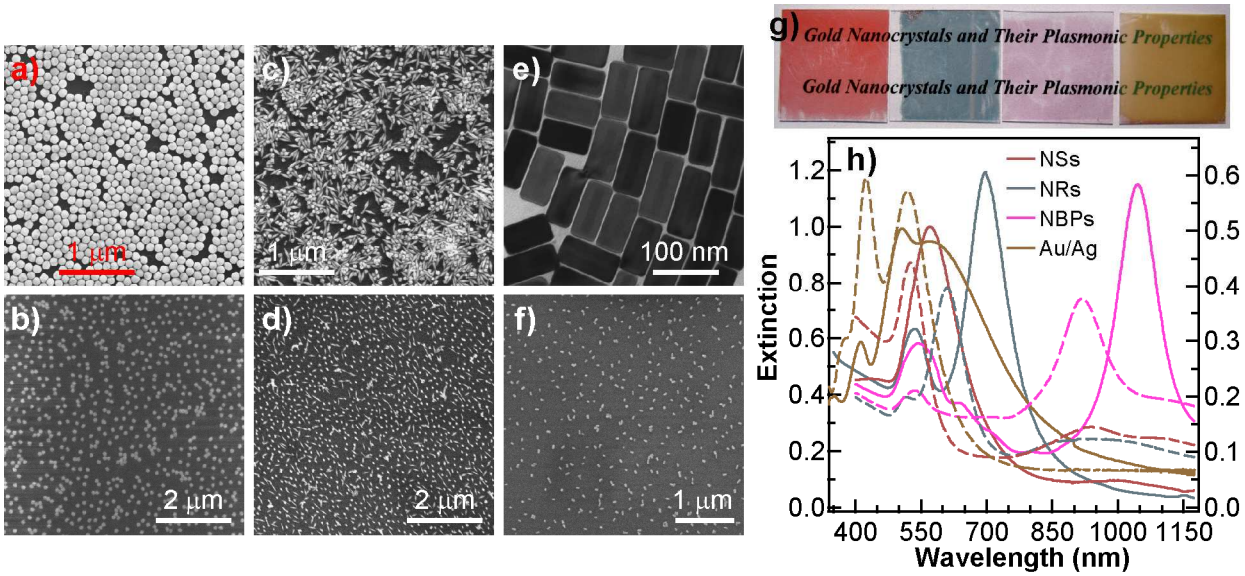

Figure 7.6 Deposition of different colloidal noble metal nanocrystals on glass slides to produce macroscale arrays. (a) SEM image of the Au nanosphere sample. (b) SEM image of the Au nanosphere sample deposited on a glass slide. (c) SEM image of the Au nanobipyramid sample. (d) SEM image of the Au nanobipyramid sample deposited on a glass slide. (e) TEM image of the (Au core)/(Ag shell) nanorod sample. (f) SEM image of the (Au core)/(Ag shell) nanorod sample deposited on a glass slide. (g) Photograph of the Au nanocrystal arrays formed on glass slides. The red, green, purple, and yellow colors result from the Au nanosphere, Au nanorod, Au nanobipyramid, and (Au core)/(Ag shell) nanorod arrays, respectively. (h) Extinction spectra of the metal nanocrystal samples in solutions (solid lines, left axis) and their corresponding arrays on glass slides (dashed lines, right axis). The "NSs", "NRs", "NBPs", and "Au/Ag" labels

represent the Au nanosphere, nanorod, nanobipyramid, and (Au core)/(Ag shell) nanorod samples, respectively.

We further tested different substrates for the formation of high-density metal nanocrystal arrays from solutions. Mesostructured silica and titania thin films were first coated on glass slides following the reported evaporation-induced self-assembly procedures through dip coating.[23–25] In particular, tetraethyl orthosilicate (TEOS) and tetraethyl orthotitanate (TEOT) were used as the inorganic precursors for the preparation of silica and titania films, respectively. Poly(ethylene oxide)-poly(propylene oxide)-poly(ethylene oxide) triblock copolymer ($EO_{20}PO_{70}EO_{20}$, P123) was used as the structure-directing agent. For mesostructured silica films, P123 (0.32 g) was first dissolved in ethanol (12.69 g). Separately, TEOS (1.19 g) was prehydrolyzed in a solution containing dilute HCl (0.617 g, pH 2) and ethanol (0.914 g) by vigorous stirring at room temperature for 20 min. These two solutions were thereafter mixed together. The final molar composition of the precursor solutions was 1 TEOS: 0.0097 P123: 6 H_2O: 0.001 HCl: 51.8 ethanol. After the precursor solutions were stirred for 2 h at room temperature, they were dip-coated onto cover glass slides at a speed of 10 $mm \cdot min^{-1}$.The resultant mesostructured silica films were dried in an oven at 60 °C overnight before further treatment. For mesostructured titania films, P123 (0.5 g) was first dissolved in ethanol (12 g). Separately, TEOT (1.85 g) was added to concentrated HCl (1.62 g, ≈12.1 M) and prehydrolyzed under vigorous stirring at room temperature for 5 min. The two solutions were thereafter mixed together. The final molar composition in the precursor solution was 1 TEOT: 0.01 P123: 7 H_2O: 2 HCl: 32.1 ethanol. After the precursor solutions were stirred at room temperature for 10 min, they were dip-coated onto cover glass slides at a speed of 10 $mm \cdot min^{-1}$. The produced films were dried in a refrigerator at 5 °C overnight before further treatment. The organic templating surfactants in the films were removed by thermal calcination at 400 °C for 5 hours.

The resultant mesoporous silica and titania films were characterized by TEM and SEM imaging. For the mesoporous silica films, it has been reported that the pore channels in the film form a distorted two-dimensional hexagonal mesostructure.[25] TEM imaging reveals parallel

fringes and distorted hexagonally packed pore channels when the small pieces of the mesoporous silica films that were scratched off the substrates were observed along the [110] and [001] axes, respectively (Figure 7.7a and b). The pore channels in mesoporous silica films are generally aligned parallel to the film plane. The mesoporous titania films have a body-centered-cubic mesostructure. The TEM image (Figure 7.7c), taken along the [111] zone axis shows hexagonally organized pores. Hexagonally organized pores are also observable on high-resolution SEM images and their fast Fourier transform patterns (Figure 7.7d). The thermally calcined, mesoporous silica and titania films are both hydrophilic, with dangling hydroxyl groups present on their surfaces. The hydroxyl groups make the surfaces negatively charged in neutral aqueous solutions. Without any further treatments, both mesoporous silica and titania films can be readily deposited with uniform and dense colloidal noble metal nanocrystal arrays, by immersing the films into the metal nanocrystal solutions. Figure 7.7e and f shows the SEM images of Au nanorod arrays deposited on mesoporous silica and titania films, respectively. The same Au nanorod samples as above were employed. Owning to the crystallization of the inorganic pore framework caused by thermal calcination, the mesoporous titania films are relatively conductive.[25–27] The conductivity of the mesoporous titania films can reduce electron accumulation, which enables large-scale SEM imaging without the occurrence of distortion induced by electrostatic charging. The Au nanorod arrays formed on the mesoporous silica and titania films exhibit the similar bright green colors to the arrays formed on glass slides. Their longitudinal plasmon peak wavelengths are 589 nm and 613 nm respectively. The successful deposition of colloidal noble metal nanocrystals on different substrates further expands the application of metal nanocrystal arrays. With our method, we could fabricate multilayered metal nanocrystal arrays by repeatedly depositing monolayer metal nanocrystal arrays and mesostructured silica/titania spacer layers. The potential of fabricating multilayered metal nanocrystal structures, together with the unique plasmonic properties of noble metal nanocrystals, makes our method promising for constructing three-dimensional media to achieve

multidimensional optical data storage at ultrahigh densities.[5] The capability of depositing noble metal nanocrystals onto different substrates can also facilitate the utilization of dense noble metal nanocrystal arrays in various plasmon-assisted optoelectronic devices, such as plasmon-enhanced light-emitting diodes,[7] plasmonic photovoltaic solar cells,[2] and plasmon-enhanced photodetectors.[8]

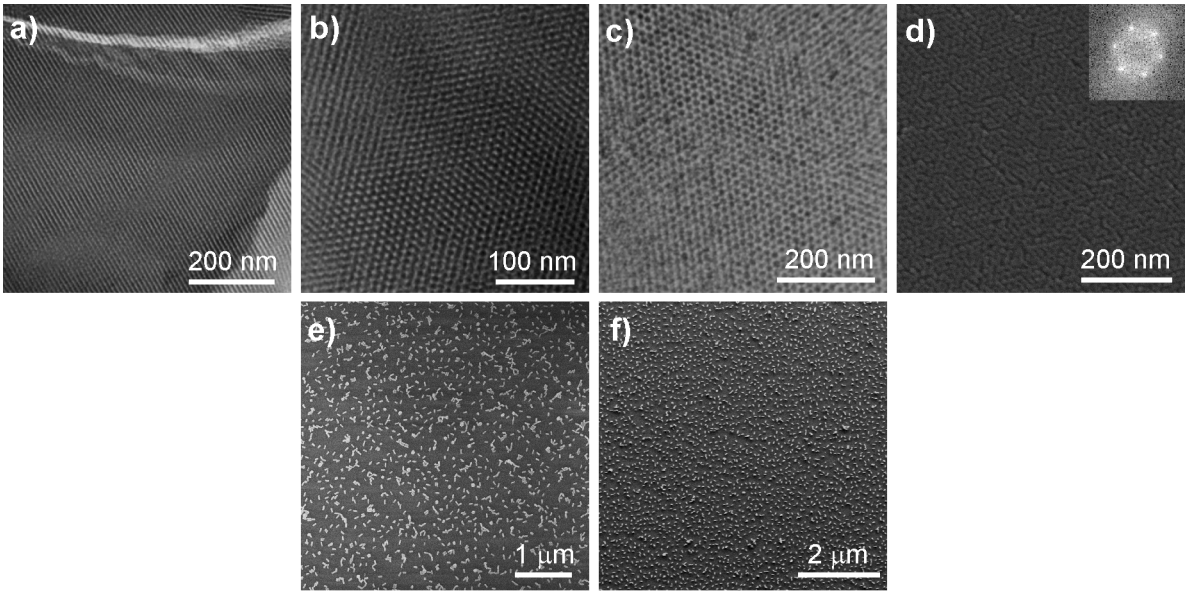

Figure 7.7 Colloidal metal nanocrystal arrays formed on the mesoporous silica and titania thin films. (a,b) TEM images of the mesoporous silica thin film taken along the [110] and [001] zone axes, respectively. (c) TEM image of the mesoporous titania thin film taken along the [111] zone axis. (d) High-resolution SEM image of the top surface of the mesoporous titania thin film. The inset is the fast Fourier transform pattern of the SEM image. (e,f) SEM images of the Au nanorod arrays deposited on the mesoporous silica and titania thin films, respectively.

7.3 Refractive Index-Based Sensing of Gold Nanorod Arrays

We further conducted refractive index sensitivity measurements for the Au nanorod arrays deposited on glass slides to explore the potential of macroscale noble metal nanocrystal arrays for building portable sensing devices. As has been reported previously,[28,29] the plasmon peak shift, $\Delta\lambda$, in response to refractive index changes can be approximately described as

$$\Delta\lambda \approx m\left(n_{\text{adsorbate}} - n_{\text{medium}}\right)\left(1 - e^{-2d/l_{\text{d}}}\right) \tag{7.1}$$

where m is the refractive index sensitivity, $n_{\text{adsorbate}}$ and n_{medium} are the refractive indices of the

adsorbate and surround medium, respectively, l_d is the electromagnetic field decay length and d is the effective thickness of the adsorbate layer. The refractive index sensitivity is usually determined by measuring the plasmon peak wavelengths when metal nanocrystals are dispersed in different uniform dielectric environments. According to Equation (7.1), noble metal nanocrystals are ideal candidates for sensing molecules adsorbed on them. The refractive index sensitivity is an essential factor in determining ultimate detection resolutions. In our experiments, glass slides carrying Au nanorods were cut into small pieces, which were then immersed into ethanol–glycerol mixture solvents of varying volume ratios.[30,31] The volume percentage of glycerol was varied from 0% to 100% at a step of 20%. The color of the Au nanorod-deposited glass slides turns from green in ambient environment to dark red in the mixture solvents (Figure 7.8a). The extinction spectra (Figure 7.8b) of the Au nanorod arrays kept in air and immersed in the mixture solvents show that both the longitudinal and transverse plasmon resonance peaks are red-shifted as the refractive index of the surrounding environment is increased. Because the longitudinal plasmon resonance is more sensitive than the transverse plasmon resonance, we considered only the longitudinal plasmon resonance in this study. The longitudinal plasmon shift was plotted against the refractive index change from air to the liquid mixture. The refractive index sensitivity was then determined by linear fitting (Figure 7.8c) to be 230 nm per refractive index unit (RIU). We note that the refractive index sensitivity determined in our experiments are actually an apparent one, because the Au nanorods are capped with CTAB molecules and supported on glass slides. The contribution of the capping CTAB molecules and supporting glass slide to the refractive index of the surrounding environment is fixed. This causes the measured index sensitivity to be smaller than the true sensitivity of the bare, unsupported Au nanorods. However, to measure the true index sensitivity of metal nanocrystals experimentally has been challenging, because metal nanocrystals are required to be stable in solutions without any capping species or supports. For simplicity, in our study, we will use the term of refractive index sensitivity. The figure of merit (FOM), which is defined as the ratio of the plasmon sensitivity to

the plasmon peak width, was calculated to be 2.29. For comparison, the index sensitivity of the same Au nanorod sample in solutions was examined by first centrifuging the CTAB-stabilized Au nanorod solution and then dispersing them into water–glycerol mixtures with varying glycerol concentrations. Water–glycerol mixture solvents are more viscous than ethanol–glycerol solvents, but do not cause the aggregation of the Au nanorods. The index sensitivity of the Au nanorod sample in solutions was determined to be 349 nm/RIU (Figure 7.9) and the FOM was 3.7. The index sensitivity of the Au nanorod arrays on glass slides is therefore much smaller than that of the Au nanorod sample dispersed in solutions, exhibiting a reduction by 34%.

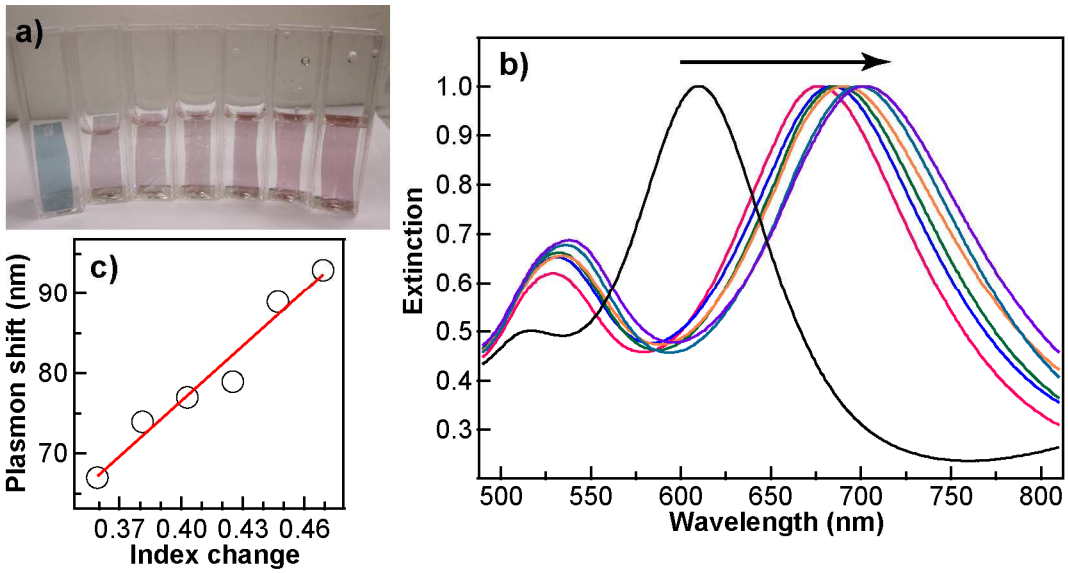

Figure 7.8 Refractive index sensitivity of the Au nanorod arrays deposited on glass slides. (a) Photograph of the Au nanorod arrays kept in an ambient environment (leftmost) and immersed in the mixture solvents of ethanol and glycerol. The volume percentage of glycerol in the liquid mixture was varied from 0% to 100% at a step of 20%. (b) Normalized extinction spectra of the Au nanorod arrays kept in an ambient environment and immersed in the mixture solvents at varying compositions. (c) Dependence of the longitudinal plasmon shift on the refractive index change from air to the liquid mixture. The plasmon shift is relative to the longitudinal plasmon resonance wavelength measured when the Au nanorod array is in air. The red line is a linear fit.

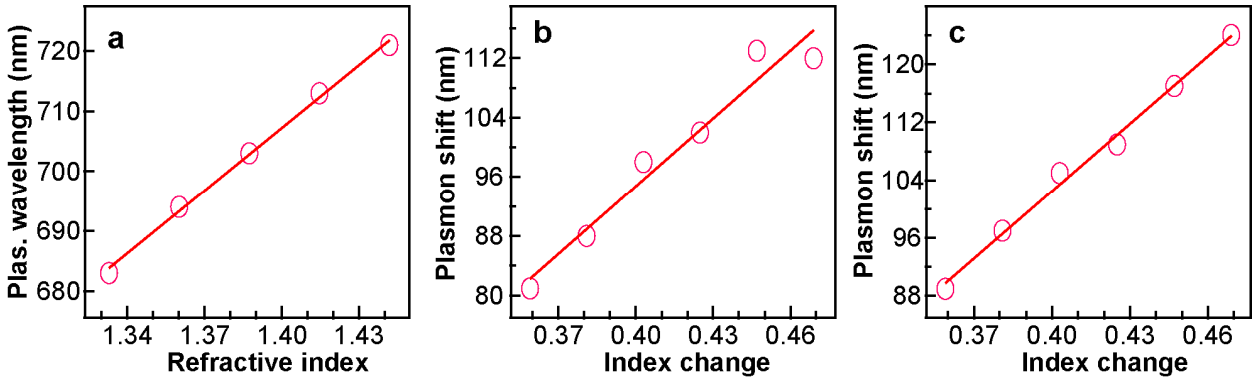

Figure 7.9 (a) Variation of the longitudinal plasmon wavelength of the CTAB-stabilized Au nanorod sample dispersed in the mixture solvents with the refractive index of the mixture solvent. (b,c) Variations of the longitudinal plasmon shifts of the Au nanorod arrays deposited on mesoporous silica and titania thin films, respectively, with the refractive index change of the mixture solvent relative to the refractive index of air. The plasmon shifts are relative to the longitudinal plasmon wavelengths measured when the Au nanorod arrays were in an ambient environment. The red lines are linear fits.

We further determined the refractive index sensitivities of the Au nanorod arrays that were deposited on the mesoporous silica and titania thin films. The index sensitivities of the Au nanorod arrays increase to 304 and 310 nm/RIU when being deposited on the mesoporous silica and titania films, respectively (Figure 7.9b,c and Figure 7.10a). The FOM values increase to 3.09 and 3.03, respectively (Figure 7.10b). The use of mesoporous films can therefore remarkably improve the sensing performance of the Au nanorod arrays. The sensing performances are comparable to those of the Au nanorods in solutions, with the reductions in the index sensitivity being 13% and 11% for the arrays on the silica and titania films, respectively. The substrate effect on the index sensitivity can be understood as follows. The refractive indices of the substrates employed in our study are not large enough to induce new plasmon modes of the Au nanorods.[32] The longitudinal plasmon peak widths of the Au nanorod arrays on glass slides, the silica and titania films increase only slightly in comparison to that of the Au nanorod sample in solutions, which is attributed to the probability that the gap distances among a small fraction of the Au nanorods in the arrays are small enough to cause weak plasmon coupling. On the other hand, the fixed refractive index of the supporting substrate can reduce the overall index sensitivity of the metal nanocrystals, since the spatial overlap between the liquid environment

and the locally enhanced electric field around the nanocrystals at their plasmon resonance is reduced owing to the presence of the substrate.[33] Another way of understanding the reduction of the index sensitivity is to consider that the overall net change in the refractive index of the entire surrounding environment is smaller in the presence of the supporting substrate. The mesoporous films help in lifting the metal nanocrystals from the glass surface (Figure 7.10c and d). When the Au nanorods are supported on the mesoporous films, the liquid solvent can penetrate into the pores, increasing the overlap between the liquid solvent and the locally enhanced electric field around the Au nanorods. As a result, the use of the mesoporous films as the substrates can increase the refractive index sensitivity of the Au nanorod arrays in comparison to the use of solid glass slides as the substrates. Our observed effect of the mesoporous films on the index sensitivity is similar to the result of a previous study, where the index sensitivity of Au nanodisks is doubled by lifting them with dielectric silica nanopillars.[34]

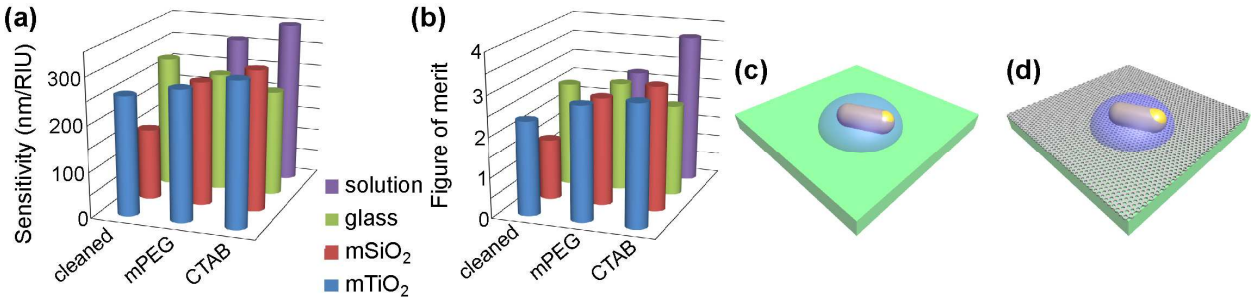

Figure 7.10 Refractive index sensing performances of the Au nanorods in solutions and deposited on the different substrates. The Au nanorods were capped with CTAB, PEGylated, or plasma-cleaned. (a) Refractive index sensitivities of the Au nanorod sample. (b) FOM values of the Au nanorod sample. (c,d) Schematic showing one Au nanorod supported on a glass slide and on a mesoporous film, respectively. The "$mSiO_2$", "$mTiO_2$", and "mPEG" labels represent the mesoporous silica films, mesoporous titania films, and Au nanorods functionalized with mPEG-SH, respectively.

CTAB-stabilized Au nanocrystals have been found to cause cytotoxicity, allergic response and eryptosis/erythroptosis, probably owing to the presence of free CTAB molecules that are desorbed from Au nanocrystals and/or left from the incomplete purification of Au nanocrystal products. In comparison, Au nanocrystals functionalized with thiol-terminated methoxy

poly(ethylene glycol) (mPEG-SH) are less cytotoxic. They have also been employed for biological sensing. We therefore functionalized both the Au nanorod sample dispersed in solutions and deposited on the different substrates with mPEG-SH and examined the index sensitivities of the functionalized Au nanorods. After PEGylation, mPEG-SH molecules with a long carbon chain cover the surface of the Au nanorods. The refractive index sensitivities of the Au nanorods are expected to be reduced, because a larger volume fraction of the surrounding environment around the Au nanorods is occupied by mPEG-SH molecules in comparison to the case for the CTAB-capped Au nanorods. We characterized the sensing performances of the mPEG-SH coated Au nanorods in solution and their arrays supported by different substrates. The Au nanorod-deposited substrates were first immersed in 1 μM mPEG-SH (MW = 5000, Rapp Polymere GmbH) aqueous solution for overnight to saturate the adsorption of mPEG-SH molecules on the Au surface. The sensitivity measurement results can be found in Figure 7.10 and 7.11. The index sensitivity (309 nm/RIU) of the PEGylated Au nanorods in solutions is smaller than that of the CTAB-capped ones (349 nm/RIU), which is in agreement with our expectation. Similarly, on the mesoporous silica and titania films, the index sensitivities of the PEGylated Au nanorod arrays are also smaller than the respective values of the CTAB-capped Au nanorod arrays. In contrast, on glass slides, the index sensitivity of the PEGylated Au nanorod arrays is larger than that of the CTAB-capped Au nanorod arrays. This increase could be ascribed to the lifting effect caused by the bonding of the large mPEG-SH molecules on the Au nanorods.[34]

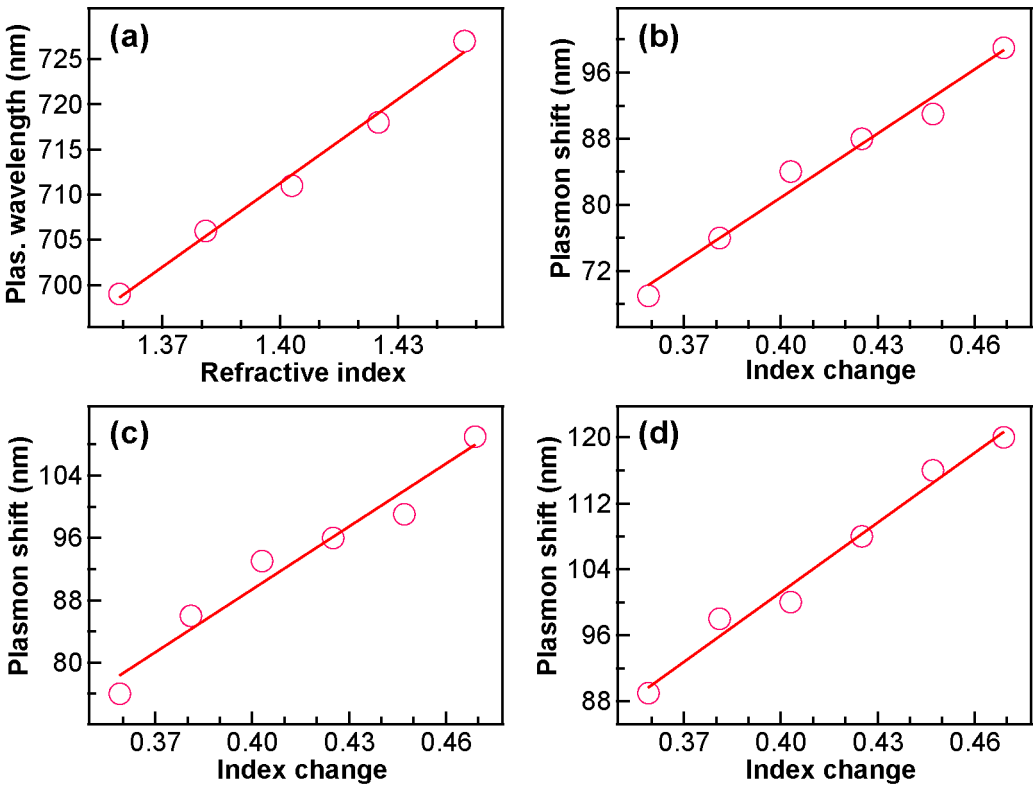

Figure 7.11 (a) Variation of the longitudinal plasmon wavelength of the PEGylated Au nanorod sample dispersed in the mixture solvents with the refractive index of the mixture solvent. (b–d) Variations of the longitudinal plasmon shifts of the PEGylated Au nanorod arrays deposited on glass slides, mesoporous silica films, and mesoporous titania films, respectively, on the refractive index change of the mixture solvent relative to the refractive index of air. The plasmon shifts are relative to the longitudinal plasmon wavelengths measured when the Au nanorod arrays were in an ambient environment. The red lines are linear fits.

Our deposition of the metal nanocrystals on the substrates allowed for the use of plasma treatment to remove the capping CTAB molecules on the surface of the nanocrystals. Removal of the capping organic molecules is expected to boost the refractive index sensitivity, since the net index change caused by the adsorption of molecules that are involved in sensing will be larger for the bare metal nanocrystals than for the CTAB-capped ones. The conditions for plasma cleaning to remove the capping CTAB molecules were adapted from a previous study.[35] The longitudinal plasmon wavelength of the Au nanorod arrays is blue-shifted by ~9 nm after plasma cleaning, suggesting the removal of the capping CTAB molecules and possible slight change of the Au nanorod morphology. The index sensitivities of the plasma-cleaned Au nanorod arrays on glass, the mesoporous silica and titania films were characterized (Figure 7.12). The index

sensitivity (283 nm/RIU) of the plasma-cleaned Au nanorod arrays on glass slides is larger than that (230 nm/RIU) of the CTAB-capped ones. The cleaned Au nanorod arrays supported on the mesoporous silica and titania films, however, show reductions in the index sensitivity. We reason that the bombardment of the charged species during plasma cleaning causes the Au nanorods to be partially embedded in the mesoporous silica and titania films due to the porous nature of the films. The partial embedding reduces the contact of the liquid solvent with the Au nanorods, which, as a result, results in the reductions in the measured index sensitivities.

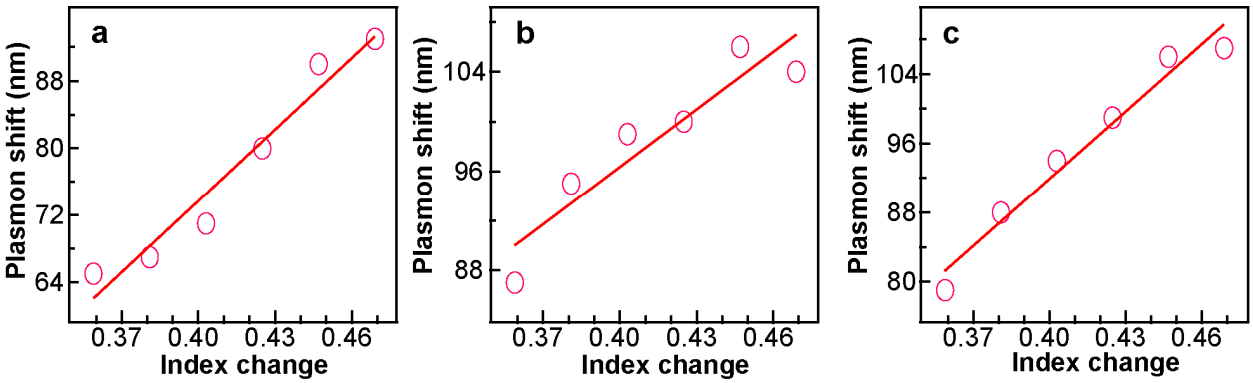

Figure 7.12 Variations of the longitudinal plasmon shifts of the plasma-cleaned Au nanorod arrays with the refractive index change of the mixture solvent relative to the refractive index of air. The Au nanorod arrays were deposited on (a) glass slides, (b) mesoporous silica fims, and (c) mesoporous titania films, respectively. The plasmon shifts are relative to the longitudinal plasmon wavelengths measured when the Au nanorod arrays were in an ambient environment. The red lines are linear fits.

7.4 Summary

In this chapter, I have first compared the plasmonic properties between chemically-grown and EBL-written Au nanorods. Compared with their chemically-grown counterparts, EBL-written Au nanorods suffer from much poorer plasmonic performances. The scattering intensity of EBL-written Au nanorods was found to be only a quarter of that of chemically-grown ones. The large plasmon damping of EBL-written Au nanorods is mainly attributed to the employment of an adhesive metal layer. To overcome the drawbacks of lithographically-fabricated Au nanorod arrays, we therefore further developed a general approach

for depositing noble metal nanocrystals from aqueous colloidal solutions onto substrates. Au nanorods, Au nanospheres, Au nanobipyramids, and (Au core)/(Ag shell) nanorods have been successfully deposited to form macroscale random arrays with high densities. We have acquired nanocrystal arrays on glass slides and mesoporous silica and titania films. The size of the nanocrystal arrays can be up to 10 cm by 10 cm and can be further increased. The noble metal nanocrystal arrays have distinct plasmonic properties and are promising candidates for a number of plasmonic applications. In addition, we employed Au nanorod arrays for studying the refractive index-based sensing characteristics. The sensing performance of Au nanorod arrays supported by mesoporous films is comparable to that of Au nanorods in solutions. The effects of plasma cleaning and mPEG-SH coating on the refractive index sensitivity of Au nanorod arrays have also been examined. We believe our method will greatly facilitate the plasmonic applications that require the formation of large-area arrays of metal nanocrystals.

References

[1] Chen, H. J.; Shao, L.; Li, Q.; Wang, J. F. *Chem. Soc. Rev.* **2013**, *42*, 2679.

[2] Atwater, H. A.; Polman, A. *Nat. Mater.* **2010**, *9*, 205.

[3] Linic, S.; Christopher, P.; Ingram, D. B. *Nat. Mater.* **2011**, *10*, 911.

[4] Warren, S. C.; Thimsen, E. Plasmonic Solar Water Splitting. *Energy Environ. Sci.* **2012**, *5*, 5133.

[5] Zijlstra, P.; Chon, J. W. M.; Gu, M. *Nature* **2009**, *459*, 410.

[6] Moreau, A.; Ciracì, C.; Mock, J. J.; Hill, R. T.; Wang, Q.; Wiley, B. J.; Chilkoti, A.; Smith, D. R. *Nature* **2012**, *492*, 86.

[7] Kim, B.-H.; Cho, C.-H.; Mun, J.-S.; Kwon, M.-K.; Park, T.-Y.; Kim, J. S.; Byeon, C. C.; Lee, J.; Park, S.-J. *Adv. Mater.* **2008**, *20*, 3100.

[8] Liu, Y.; Cheng, R.; Liao, L.; Zhou, H. L.; Bai, J. W.; Liu, G.; Liu, L. X.; Huang, Y.; Duan, X. F. *Nat. Commun.* **2011**, *2*, 579.

[9] Ferry, V. E.; Verschuuren, M. A.; van Lare, M. C.; Schropp, R. E. I.; Atwater, H. A.; Polman, A. *Nano Lett.* **2011**, *11*, 4239.

[10] Lucas, B. D.; Kim, J.-S.; Chin, C.; Guo, L. J. *Adv. Mater.* **2008**, *20*, 1129.

[11] Malinsky, M. D.; Kelly, K. L.; Schatz, G. C.; Van Duyne, R. P. J. *J. Am. Chem. Soc.* **2001**, *123*, 1471.

[12] Tao, A.; Sinsermsuksakul, P.; Yang, P. D. *Nat. Nanotechnol.* **2007**, *2*, 435.

[13] Mahmoud, M. A.; Chamanzar, M.; Adibi, A.; El-Sayed, M. A. *J. Am. Chem. Soc.* **2012**, *134*, 6434.

[14] Guo, L.; Huang, Y. J.; Kikutani, Y.; Tanaka, Y.; Kitamori, T.; Kim, D.-H. *Lab Chip* **2011**, *11*, 3299.

[15] Shao, L. *Angle-, Energy- and Position-Resolved Plasmon Resonance Coupling between Gold Nanocrystals.* MPhil. Thesis, Department of Physics, The Chinese University of Hong Kong, 2008.

[16] Shao, L.; Woo, K. C.; Chen, H. J.; Jin, Z.; Wang, J. F.; Lin, H.-Q. *ACS Nano* **2010**, *4*, 3053.

[17] Toury, T.; DE LA CHAPELLE, M. L.; Shen, H.; GUELORGET, B. *Multilayer Structure Comprising a Precious Metal Stuck onto a Dielectric Substrate, and an Associated Method and Use.* U. S. Patent Appl. No. 13/272,000, filed Oct. 12, 2011.

[18] Pramod, P.; Thomas, K. G. *Adv. Mater.* **2008**, *20*, 4300.

[19] Halas, N. J.; Lal, S.; Chang, W.-S.; Link, S.; Nordlander, P. *Chem. Rev.* **2011**, *111*, 3913.

[20] Woo, K. C.; Shao, L.; Chen, H. J.; Liang, Y.; Wang, J. F.; Lin, H.-Q. *ACS Nano* **2011**, *5*, 5976.

[21] Kou, X. S.; Ni, W. H.; Tsung, C.-K.; Chan, K.; Lin, H.-Q.; Stucky, G. D.; Wang, J. F. *Small* **2007**, *3*, 2103.

[22] Jiang, R. B.; Chen, H. J.; Shao, L.; Li, Q.; Wang, J. F. *Adv. Mater.* **2012**, *24*, OP200.

[23] Yang, Z.; Ni, W. H.; Kou, X. S.; Zhang, S. Z.; Sun, Z. H.; Sun, L.-D.; Wang, J. F.; Yan, C.-H. *J. Phys. Chem. C* **2008**, *112*, 18895.

[24] Wang, J. F.; Stucky, G. D. *Adv. Funct. Mater.* **2004**, *14*, 409.

[25] Zhao, L.; Ming, T.; Li, G. S.; Chen, H. J.; Wang, J. F.; Yu, J. C. *Small*, **2010**, *6*, 1880−1885.

[26] Tsung, C.-K.; Fan, J.; Zheng, N. F.; Shi, Q. H.; Forman, A. J.; Wang, J. F.; Stucky, G. D. *Angew. Chem. Int. Ed.* **2008**, *47*, 8682.

[27] Yang, P. D.; Zhao, D. Y.; Margolese, D. I.; Chmelka, B. F.; Stucky, G. D. *Nature* **1998**, *396*, 152.

[28] Anker, J. N.; Hall, W. P.; Lyandres, O.; Shah, N. C.; Zhao, J.; Van Duyne, R. P. *Nat. Mater.* **2008**, *7*, 442.

[29] Rindzevicius, T.; Alaverdyan, Y.; Käll, M.; Murray, W. A.; Barnes, W. L. *J. Phys. Chem. C* **2007**, *111*, 11806.

[30] Chen, H. J.; Kou, X. S.; Yang, Z.; Ni, W. H.; Wang, J. F. *Langmuir* **2008**, *24*, 5233.

[31] Chen, H. J.; Shao, L.; Woo, K. C.; Ming, T.; Lin, H.-Q.; Wang, J. F. *J. Phys. Chem. C* **2009**, *113*, 17691.

[32] Chen, H. J.; Shao, L.; Ming, T.; Woo, K. C.; Man, Y. C.; Wang, J. F.; Lin, H.-Q. *ACS Nano* **2011**, *5*, 6754.

[33] Miller, M. M.; Lazarides, A. A. *J. Phys. Chem. B* **2005**, *109*, 21556.

[34] Dmitriev, A.; Hägglund, C.; Chen, S.; Fredriksson, H.; Pakizeh, T.; Käll, M.; Sutherland, D. S. *Nano Lett.* **2008**, *8*, 3893.

[35] Camargo, P. H. C.; Rycenga, M.; Au, L.; Xia, Y. N. *Angew. Chem. Int. Ed.* **2009**, *48*, 2180.

Chapter 8

Conclusions and Outlook

In this thesis, I report on my studies on the plasmon coupling in Au nanorod-based dimers, the use of graphene to mediate the plasmon coupling between Au nanocrystals, the comparison of the plasmonic properties between lithographically-written and chemically-grown Au nanorods, and the fabrication of macro-scale colloidal Au nanorod arrays.

To obtain a thorough understanding of the plasmon coupling behavior, I have performed systematic studies on the plasmon coupling in heterodimers composed of two different Au nanorods or one Au nanorod and one Au nanosphere. First, extensive simulations were performed to unravel the plasmon coupling in heterodimers of nanorods aligned along their length axes. I found that the plasmon coupling between two arbitrarily varying Au nanorods can be well described using a coupled mechanical oscillator model. The coupled plasmon energy can be easily, but accurately predicted with a universal hyperbolic formula. The nanorod heterodimers also exhibit Fano interference, which can be adjusted by controlling the gap distance and monomer plasmon energies. Second, the plasmon coupling between a Au nanorod and a small Au nanosphere has been studied with scattering measurements, electrodynamic simulations, and model analysis. The spatial perturbation of the nanosphere leads to distinct spectral changes of the heterodimer. Interestingly, the nanosphere dipole is found to rotate around the nanorod dipole to achieve favorable attractive interaction for the bonding dipole–dipole mode. The sensitive spectral response of the heterodimer to the spatial perturbation of the nanosphere offers an approach to designing plasmon rulers of two spatial coordinates for sensing and high-resolution measurements of distance changes.

Furthermore, plasmon coupling can be modulated by an ultra-thin monolayer graphene. I have explored the interaction between graphene and two different coupled plasmonic structures, including Au nanorod dimers and Au film-coupled Au nanosphere structures. For the nanorod dimers, no apparent spectral modulation can be acquired through graphene due to the weak interaction between the nanorod dimer and graphene. By contrast, remarkable modulation on Au nanosphere scattering can be achieved by adding graphene into the cavity between the nanosphere and the supporting film. The graphene-loaded nanosphere antennas exhibit significant resonance redshifts, which can further be modulated when the graphene screening effect is varied. This graphene-decorated plasmonic nanocavity not only pushes the optical response of graphene into the visible-to-near-infrared region but also naturally exemplifies an electro-plasmonic system. These findings thus open an avenue on effectively operating graphene photonic devices at the visible-to-near-infrared range and pave a way for electrically controlling light by plasmonic structures.

Practical applications of Au nanorods usually require their assembly into coupled or uncoupled macro-scale arrays. I have fabricated Au nanorod arrays by electron beam lithography (EBL) and further developed a method for preparing macro-scale colloidal nanocrystal arrays. The plasmonic properties of Au nanorods prepared from different methods are compared. The EBL-written Au nanorods suffer from a poor plasmonic performance, which is found to be mainly attributed to the employment of an adhesive metal layer. The chemical method, on the other hand, can achieve Au nanocrystals with excellent plasmonic responses at a very low cost but appears difficult to assembly into ordered structures. In particular, I have succeeded in directly depositing colloidal metal nanocrystals onto different substrates to form arrays. The resultant nanocrystal arrays are uniform and dense, with the single-layer absorbance value reaching 0.2 and the size up to one decimeter square. The refractive index sensitivities of the obtained Au nanorod arrays have also been characterized. The macro-scale metal nanocrystal arrays can overcome the poor stability of the colloidal solutions and the high cost of

single-particle spectroscopy that hinders the practical applications of plasmonic nanocrystals for sensing. This method is expected to greatly facilitate the plasmonic applications that require the formation of large-area metal nanocrystal arrays.

I believe that the improved understanding on the plasmonic response of Au nanorod-based oligomers, the exploration of using graphene to modulate the plasmon coupling, and the efforts towards the fabrication of macro-scale nanocrystal arrays in this thesis are important for designing and fabricating complex assemblies, hierarchical structures, and macroscopic materials out of noble metal nanocrystal building blocks, much similar to the formation of molecules and macroscopic materials out of atoms, with desired plasmon-derived functions. The results here will promote the applications of Au nanorods in optics, optoelectronics, and biotechnology. However, it still requires great efforts to further improve the understanding of coupled plasmonic system, to use plasmonic structures to realize the electronic and all-optical control of photonic signals on sub-wavelength scale (so called active plasmonics), and to unleash the full potential of plasmonic metal nanostructures as novel functional nanomaterials. Based on the results shown here, further explorations can be focused in the following aspects.

First, in analogy to the cases of wave function interactions between electrons to from electronic band structures, the plasmon coupling in two- or three-dimension periodic arrays of plasmonic nanocrystals can form plasmonic band structures. These metal nanocrystal arrays can support novel plasmonics properties, such as collective plasmon resonances,[1] plasmonic Fano resonances, and extraordinary optical transmission.[2] They are ideal candidates to achieve tunale plasmonic analogues of electronic structures of specific materials, e.g. graphene, and to realize nanoplasmonic sensors with ultra-high figure of merit values. Two- or three-dimension metal nanocrystal periodic arrays in small areas can be simply fabricated through evaporation-driven self-assembly processes. Novel assembling techniques are required to achieve large-area arrays of colloidal nanocrystals. Both experimental and theoretical efforts need to be developed for understanding the plasmonic coupling in these metal nanocrystal

arrays.

Second, the high sensitivity of the plasmonic responses of coupled plasmonic structures to the spatial perturbations permits both the monitoring of molecular transformations by optical means and the use of specific molecules that can allow reversible configuration changes to construct plasmonic switches. To fabricate reliable and robust plasmonic biosensors and plasmonic switches, extensive efforts are still required to find coupled plasmonic structures that can react sensitively and reproducibly to spatial perturbations.

Third, the interaction between plasmonic noble metal nanostructures and two-dimensional materials, such as graphene and molybdenum disulfide, can bring strong interaction between light and two-dimensional materials and result in novel physical phenomena, enabling new developments in the investigation of two-dimensional materials and active plasmonics. The investigation is in its infancy. To understand the physics behind, we need to design smart experiments to reveal the quantum effects in the interaction between metal nanostructures and two-dimensional materials. The applications of the hybrid structures composed of noble metals and two-dimensional materials can also be extended by making use of the unique properties of two-dimensional materials, such as strong photoluminescence (monolayer MoS_2: monolayer MoS_2 is a direct-bandgap semiconductor due to the quantum effect while bulk MoS_2 is an indirect-bandgap semiconductor),[3] gate voltage-controlled metal–insulator transitions (monolayer MoS_2),[4] gate-controlled dielectric property variations (graphene),[5] and the negative differential thermal resistance (graphene).[6,7] For instance, the light trapping and light antenna effects of plasmonic metal nanostructures can boost the development of monolayer MoS_2 as an ultra-compact single-photon source; The photothermal conversion capability of plasmonic nanocrystals enables the employment of graphene to construct ultra-high density optoelectric storage memories by utilizing their negative differential thermal resistance responses; The gate-tunable dielectric properties of graphene/MoS_2 permit their hybrids with noble metal nanostructures as active plasmonic devices and ultrafast plasmonic switches. Extensive

explorations are required to transform the above proposals into realities.

In the end, the successful deposition of colloidal metal nanocrystals into large-area arrays in this thesis paves the way to fabricate low-cost plasmon-enhanced thin-film solar cells and photodetectors. Experimental challenges are waiting for us to overcome to release the potentials of the colloidal mental nanocrystal arrays in practical applications.

Reference

[1] Auguié, B.; Barnes, W. L. *Phys. Rev. Lett.* **2008**, *101*, 143902.

[2] Ebbesen, T. W.; Lezec, H. J.; Ghaemi, H. F.; Thio, T.; Wolff, P. A. *Nature* **1998**, *391*, 667.

[3] Splendiani, A.; Sun, L.; Zhang, Y. B. Li, T. S.; Kim, J.; Chim, C.-Y.; Galli, G.; Wang, F. *Nano Lett.* **2010**, *10*, 1271.

[4] Radisavljevic, B.; Kis, A. *Nat. Mater.* doi:10.1038/nm3687.

[5] Majumdar, A.; Kim, J.; Vuckovic, J.; Wang, F. *Nano Lett.* **2013**, *13*, 515.

[6] Chen, S. S.; Moore, A. L.; Cai, W. W.; Suk, J. W.; An, J.; Mishra, C.; Amos, C.; Magnuson, C. W.; Kang, J. Y.; Shi, L.; Ruoff, R. S. *ACS Nano* **2011**, *5*, 321.

[7] Balandin, A. A. *Nat. Mater.* **2011**, *10*, 569.

Curriculum Vitae

Lei Shao

lshao@phy.cuhk.edu.hk
TEL: +852-51655042
https://sites.google.com/site/lei2kevin

RM G26, Science Centre North Block
The Chinese University of Hong Kong
Shatin, N. T., Hong Kong

Education

Aug. 2010 – Present	Ph. D candidate, Physics, The Chinese University of Hong Kong, expected to graduate in July 2013.
Aug. 2008 – July 2010	MPhil., Physics, The Chinese University of Hong Kong
Sep. 2004 – July 2008	B.S., Applied Physics, University of Science and Technology of China

Research Interests:

- Design and fabrication of plasmonic nanostructures
- Plasmon coupling between noble metal nanocrystals
- Plasmonic nanostructures for sensing applications
- Graphene–noble metal hybrid nanostructures for active plasmonics
- Application of plasmonic nanocrystals in microfluidic chips
- Plasmon enhanced chemical reactions

Publications:

1. **L. Shao**, Q. F. Ruan, R. B. Jiang, J. F. Wang,* "Macroscale colloidal noble metal nanocrystal arrays and their refractive index-based sensing characteristics", Manuscript submitted.
2. **L. Shao**, X. M. Wang, H. T. Xu, J. F. Wang,* J.-B. Xu,* L.-M. Peng, H.-Q. Lin, "Nanoantenna-sandwiched graphene with giant spectral tuning in the visible-to-near-infrared region", Manuscript submitted.
3. **L. Shao**, C. H. Fang, H. J. Chen, Y. C. Man, J. F. Wang,* H.-Q. Lin, "Distinct plasmonic manifestation on gold nanorods induced by the spatial perturbation of small gold nanospheres", *Nano Lett.* **12**: 1424-1430 (2012).
4. **L. Shao**, A. S. Susha, L. S. Cheung, T. K. Sau, A. L. Rogach,* J. F. Wang,* "Plasmonic properties of single multi-spiked gold nanostars: correlating modeling with experiments", *Langmuir* **28**: 8979-8984 (2012).
5. **L. Shao**, K. C. Woo, H. J. Chen, Z. Jin, J. F. Wang,* H. Q. Lin, "Angle- and energy-resolved surface plasmon coupling between gold nanorods", *ACS Nano* **4**: 3053-3062 (2010).
6. C. H. Fang, **L. Shao** (*equal contribution*), Y. H. Zhao, J. F. Wang,* H. K. Wu,* "A gold nanocrystal/poly(dimethylsiloxane) composite for plasmonic heating on microfluidic chips",

Adv. Mater. **24**: 94-98 (2012).

7. K. C. Woo, **L. Shao** (*equal contribution*), H. J. Chen, Y. Liang, J. F. Wang,* H.-Q. Lin,* "Universal scaling and Fano resonance in the plasmon coupling between gold nanorods", *ACS Nano* **5**: 5976-5986 (2011).
8. H. J. Chen, **L. Shao**, Q. Li, J. F. Wang,* "Gold nanorods and their plasmonic properties", *Chem. Soc. Rev.* **42**:2679-2724 (2013).
9. R. B. Jiang, S. Cheng, L. Shao, Q. F. Ruan, J. F. Wang,* "Mass-based photothermal comparison among gold nanocrystals, PbS nanocrystals, organic dyes, and carbon black", *J. Phys. Chem. C.* DOI: 10.1021/jp400770x (2013).
10. H. J. Chen, **L. Shao**, K. C. Woo, J. F. Wang,* H.-Q. Lin, "Plasmonic-molecular resonance coupling: plasmonic splitting versus energy transfer", *J. Phys. Chem. C* **116**:14088-14095 (2012).
11. R. B. Jiang, H. J. Chen, **L. Shao**, Q. Li, J. F. Wang,* "Unraveling the evolution and nature of the plasmons in (Au core)-(Ag shell) nanorods", *Adv. Mater.* **24**: OP200-OP207 (2012).
12. L. Zhao, T. Ming, **L. Shao**, H. J. Chen, J. F. Wang,* "Plasmon-controlled Förster resonance energy transfer", *J. Phys. Chem. C* **116**: 8287-8296 (2012).
13. H. J. Chen, **L. Shao**, Y. C. Man, C. M. Zhao, J. F. Wang,* B. C. Yang, "Fano resonance in gold core-dielectric shell nanostructures without symmetry breaking", *Small* **8**: 1503-1509 (2012).
14. H. J. Chen, **L. Shao**, T. Ming, K. C. Woo, Y. C. Man, J. F. Wang,* H.-Q. Lin,* "Observation of the Fano resonance in gold nanorods supported on high-dielectric-constant substrates", *ACS Nano* **5**: 6754-6763 (2011).
15. M. D. Xiao, H. J. Chen, T. Ming, **L. Shao**, J. F. Wang,* "Plasmon-modulated light scattering from gold nanocrystal-decorated hollow mesoporous silica microspheres", *ACS Nano* **4**: 6565-6572 (2010).
16. H. J. Chen, **L. Shao**, T. Ming, Z. H. Sun, C. M. Zhao, B. C. Yang, J. F. Wang,* "Understanding the photothermal conversion efficiency of gold nanocrystals", *Small* **6**: 2272-2280 (2010).
17. H. J. Chen, **L. Shao**, K. C. Woo, T. Ming, H.-Q. Lin, J. F. Wang,* "Shape-dependent refractive index sensitivities of gold nanocrystals with the same plasmon resonance wavelength", *J. Phys. Chem. C* **113**: 17691-17697 (2009).

Conference presentations:

1. **L. Shao**, Q. F. Ruan, J. F. Wang, "Macro-scale colloidal noble metal nanocrystal arrays for refractive index-based sensing applications." Oral presentation, The 245th ACS National Meeting, New Orleans, Louisiana, U. S. A., April 2013.
2. **L. Shao**, J. F. Wang, "Plasmon coupling of gold nanorods." Poster presentation, Gordon Research Conference: Noble Metal Nanoparticles, South Hadley, Massachusetts, U. S. A., June 2012.

3. **L. Shao**, J. F. Wang, "Nanoantennas for directing light & quantum plasmon resonances." Oral presentation, "Frontiers in Plasmonics" Workshop, Suzhou, P. R. China, May 2012.
4. **L. Shao**, J. F. Wang, "Plasmon coupling between Au nanorods: angle dependence, universal scaling behavior, and Fano resonance." Poster presentation, 2nd Nano Today Conference, Hawaii, U. S. A, December 2011.
5. **L. Shao**, K. C. Woo, J. F. Wang, H.-Q. Lin, "Study on the plasmon coupling between two Au nanorods." Oral presentation, 14th Annual Conference of The Physical Society of Hong Kong, Hong Kong S. A. R., June 2011.
6. **L. Shao**, J. F. Wang, "Angle- and position-resolved plasmon coupling in gold nanocrystal dimers." Poster presentation, APS March Meeting, Dallas, Texas, U. S. A, March 2011.
7. **L. Shao**, K. C. Woo, H. J. Chen, J. F. Wang, H.-Q. Lin, "Angle- and energy-resolved plasmon coupling between gold nanorods." Poster presentation, MRS Spring Meeting, San Francisco, California, U. S. A., April 2010.

Hornors and Awards:

C N Yang Scholarship, The Chinese University of Hong Kong (2013)
Outstanding Graduate Honor, University of Science and Technology of China (2008)